MODEL PREDICTIVE CONTROL TECHNIQUES WITH APPLICATION TO PHOTOVOLTAIC, DC MICROGRID, AND A MULTI-SOURCED HYBRID ENERGY SYSTEM

A Dissertation

by

MOHAMMAD BAGHER SHADMAND

Submitted to the Office of Graduate and Professional Studies of
Texas A&M University
in partial fulfillment of the requirements for the degree of

DOCTOR OF PHILOSOPHY

Chair of Committee,	Robert S. Balog
Co-Chair of Committee,	Haitham Abu-Rub
Committee Members,	Shankar P. Bhattacharyya
	Prasad Enjeti
	Natarajan Gautam
Head of Department,	Miroslav M. Begovic

December 2015

Major Subject: Electrical Engineering

ABSTRACT

Renewable energy sources continue to gain popularity. However, two major limitations exist that prevent widespread adoption: availability and variability of the electricity generated and the cost of the equipment. The focus of this dissertation is Model Predictive Control (MPC) for optimal sized photovoltaic (PV), DC Microgrid, and multi-sourced hybrid energy systems. The main considered applications are: maximum power point tracking (MPPT) by MPC, droop predictive control of DC microgrid, MPC of grid-interaction inverter, MPC of a capacitor-less VAR compensator based on matrix converter (MC).

This dissertation firstly investigates a multi-objective optimization technique for a hybrid distribution system. The variability of a high-penetration PV scenario is also studied when incorporated into the microgrid concept. Emerging (PV) technologies have enabled the creation of contoured and conformal PV surfaces; the effect of using non-planar PV modules on variability is also analyzed.

The proposed predictive control to achieve maximum power point for isolated and grid-tied PV systems speeds up the control loop since it predicts error before the switching signal is applied to the converter. The low conversion efficiency of PV cells means we want to ensure always operating at maximum possible power point to make the system economical. Thus the proposed MPPT technique can capture more energy compared to the conventional MPPT techniques from same amount of installed solar panel. Because of the MPPT requirement, the output voltage of the converter may vary.

Therefore a droop control is needed to feed multiple arrays of photovoltaic systems to a DC bus in microgrid community. Development of a droop control technique by means of predictive control is another application of this dissertation.

Reactive power, denoted as Volt Ampere Reactive (VAR), has several undesirable consequences on AC power system network such as reduction in power transfer capability and increase in transmission loss if not controlled appropriately. Inductive loads which operate with lagging power factor consume VARs, thus load compensation techniques by capacitor bank employment locally supply VARs needed by the load. Capacitors are highly unreliable components due to their failure modes and aging inherent. Approximately 60% of power electronic devices failure such as voltage-source inverter based static synchronous compensator (STATCOM) is due to the use of aluminum electrolytic DC capacitors. Therefore, a capacitor-less VAR compensation is desired. This dissertation also investigates a STATCOM capacitor-less reactive power compensation that uses only inductors combined with predictive controlled matrix converter.

DEDICATION

To

My father; Jalal and My Mother; Shahin

ACKNOWLEDGEMENTS

I would like to thank my committee chair, Dr. Balog, my committee co-chair Dr. Abu Rub, and my committee members, Dr. Enjeti, Dr. Bhattacharyya, and Dr. Gautam, for their guidance and support throughout the course of this research.

Thanks also go to my friends and colleagues and the department faculty and staff for making my time at Texas A&M University a great experience. Finally, thanks to my mother and father for their encouragement.

This dissertation was made possible by NPRP grant # [4- 077-2-028] (Sections 7, 8, and 9) and NPRP-EP grant # [X-033-2-007] (Sections 3, 4, 5, 6) from the Qatar National Research Fund (a member of Qatar Foundation). The statements made herein are solely the responsibility of the authors.

TABLE OF CONTENTS

Page

LIST OF FIGURES

Page

LIST OF TABLES

Page

1. INTRODUCTION

1.1 Hybrid electrical distribution systems

With the depletion of fossil fuels and skyrocketing levels of CO_2 in the atmosphere, renewable energy sources continue to gain popularity as a long-term sustainable energy source. However, two major limitations exist that prevent widespread adoption: availability and variability of the electricity generated and the cost of the equipment. Figure 1 illustrates the future of hybrid distribution system which demonstrates the integration of renewable energy sources into DC microgrid and current AC distribution system.

DC electrical systems are gaining popularity due in part to high efficiency, high reliability and ease of interconnection of the renewable sources compared to alternating current (AC) systems [1, 2]. DC microgrids have been proposed to improve point-of-load energy availability and to integrate disparate renewable energy sources with energy storage [3]. Various renewable energy sources such as photovoltaic (PV) systems have natural DC couplings; therefore it is more efficient to connect these sources directly to DC microgrid by using DC/DC converters.

A DC microgrid system with distributed PV and wind generation and employing centralized battery storage, illustrated in Figure 1, is an attractive technology solution for communities to "go-green" while simultaneously ensures reliable electricity. DC distributed generation (DG), grid-tied PV-wind systems with centralized battery back-up, illustrated in Figure 1, have been proposed for community-scale microgrids such as the Pecan Street project in Austin Texas [4] and other communities [5]. The US

Department of Defense is pursuing similar concepts to improve energy surety and increase renewable energy penetration for military installation. It turns out that in addition to improving reliable energy to the loads in the microgrid, this concept also mitigates the variability of the microgrid as seen by the utility, existing AC distribution system, at the point of common coupling (PCC). An example of the power electronic interface between the DC microgrid and current AC distribution system bus is the solid state transformer [6, 7] being developed by the FREEDM Center at NC State, Figure 1. The control and management of the islanded PV-wind and storage systems have been proposed in [8-11].

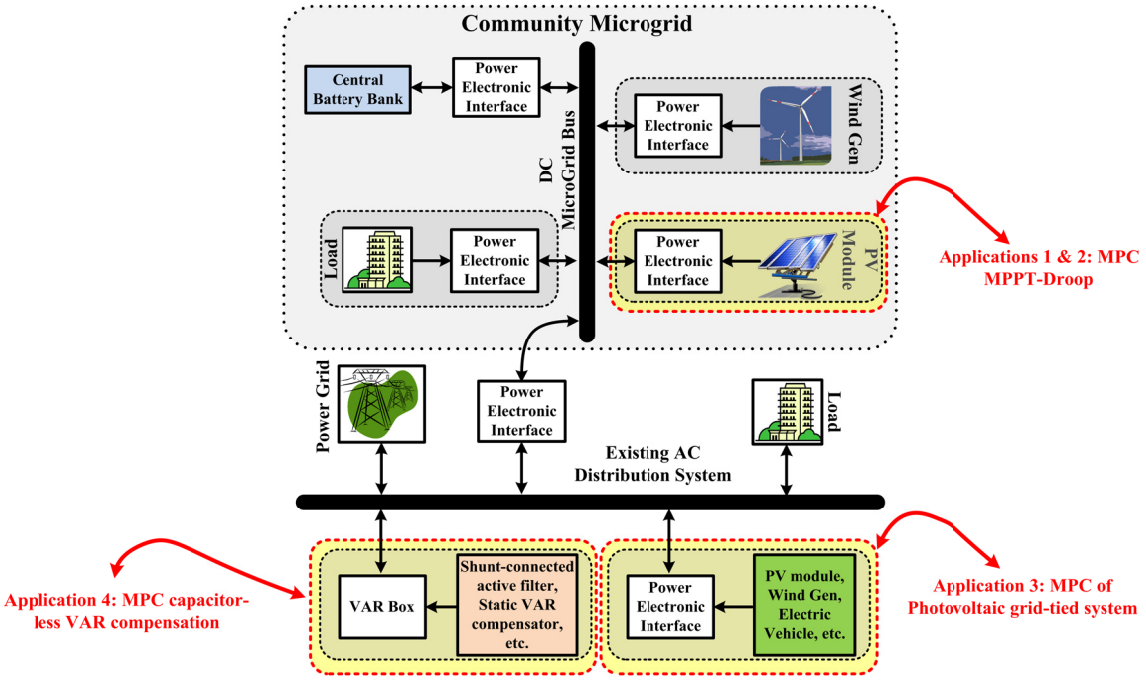

Figure 1: Hybrid distribution system of the future and considered applications in this dissertation

The focus of this dissertation is Model Predictive Control (MPC) for optimal sized photovoltaic (PV), DC Microgrid, and multi-sourced hybrid energy systems. The main considered applications are:

1. Maximum Power Point Tracking (MPPT) by MPC
2. Droop predictive control of DC Microgrid
3. MPC of grid-interaction inverter
4. MPC of a capacitor-less VAR compensator based on a matrix converter (MC)

The considered applications have direct impact on efficiency and performance of renewable energy systems. This dissertation firstly investigates an optimization technique base on a Multi-Objective Genetic Algorithm for the hybrid distribution system illustrated in Figure 1. The proposed methodology employs a techno-economic approach to determine the system design optimized by considering multiple criteria including size, cost, and energy availability. The variability of a high-penetration PV scenario also studied when incorporated into the microgrid concept. Emerging (PV) technologies have enabled the creation of contoured and conformal PV surfaces, the effect of using non-planar PV modules on variability also analyzed.

1.2 Control of power electronic interface in hybrid electrical distribution systems

The use of power electronics converters are increasing for wide range of applications such the applications illustrated in hybrid electrical distribution system in Figure 1. Literature investigated numerous control techniques for power converters and drives; Figure 2 demonstrates several control schemes that have been investigated in literature for power electronics converters. Among these, non-linear controllers based on

hysteresis and linear controller, using pulse width modulation, techniques are mostly used and developed in literature [12-14]. These techniques go back to the investigation of controllers by analog hardware. Digital control platforms such as DSPs and dSpaces are widely accepted by the industry standards for digital implementations of controllers. Digital control platforms based on floating point processor are commonly accepted by academic world; however platforms based on fixed-point processor because of low cost and adequate computation power are accepted by industry world [14, 15].

These classical controllers are commonly associated with dynamic performance and stability of the system needs. By increasing the industry demand for technical specifications, constraints, regulations, and codes trend has driven the investigation of more advanced control techniques. The design of power electronic interfaces for the hybrid distribution system in Figure 1 can be define as an optimization problem where multiple objectives must be achieved simultaneously while considering specific constraints.

In last couple of decade, development of powerful microprocessor made possible implementation of more complex control techniques for power electronics converters and drives. Some of these new control techniques are sliding mode, predictive, and artificial intelligence as illustrated in Figure 2. Slide mode controllers such as current and voltage mode controller are considering the switching nature of the converter, they demonstrate robust controllers. Artificial intelligence controllers such as fuzzy logic are appropriate for applications with unknown system parameters. Predictive control techniques are easy to understand, they can be applied to wide range of applications.

One of the main advantages of predictive control is that several constraints and nonlinearities can be easily included and implemented. The main drawback of predictive controller is requirement for high number of calculation which necessitates using fast microprocessors for implementation of this group of controllers.

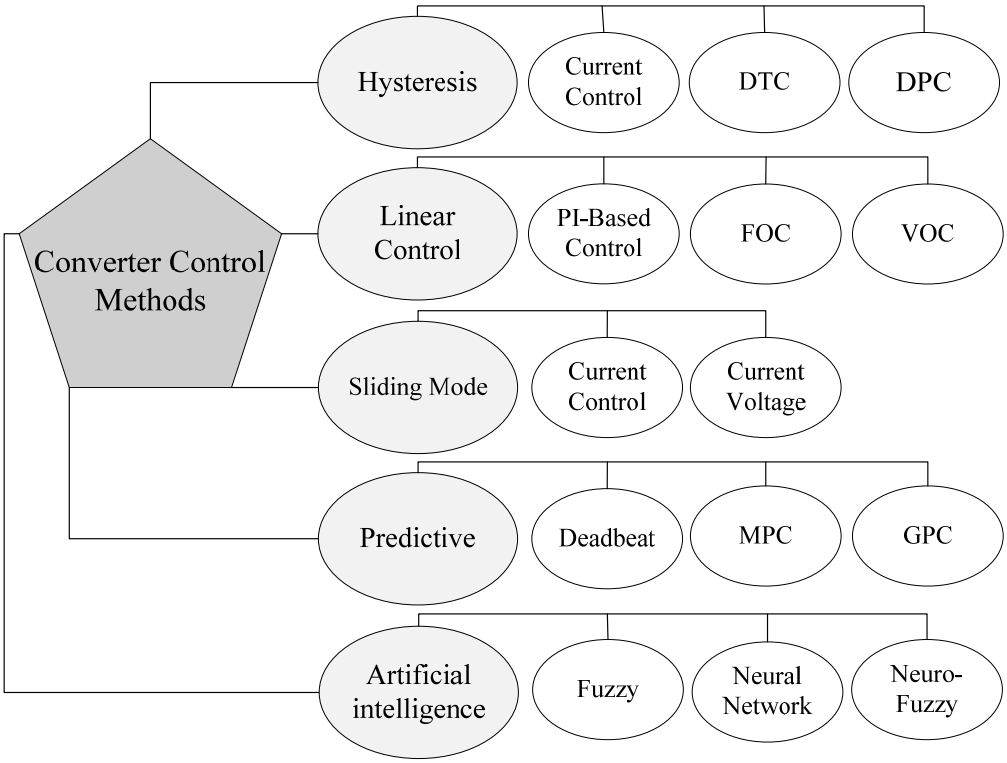

Figure 2: General schematic of different control techniques for power electronics converters and drives

1.2.1 Classical control techniques

Linear controllers using pulse width modulation (PWM) as well as hysteresis controllers are the most common traditional control techniques for power converters [16]. Hysteresis control techniques are commonly implemented using analog electronics, the switching states is determined by comparing the measured control

variable to its commanded value while considering a given hysteresis width for the error. The nature of this type of controller demonstrates that they have variable switching frequency characteristics. This characteristic may cause undesired resonance issues in some applications, thus bulky filters are required in some applications. Hysteresis control techniques can be applied for several applications as an example current control, direct power control (DPC) [17], and direct torque control (DTC) [18] as illustrated in Figure 2 [15]. In order to implement hysteresis current control by digital platform, very small sampling time is required.

Proportional Integral (PI) controller with a modulation stage is one of the most common linear controller techniques for the power converters, Figure 2. A common linear controller for grid-tied converters is voltage oriented control (VOC) for the current [19]. Field oriented control (FOC) is one of the well-known linear controller technique for drives [18, 20]. Linear controllers for power electronics converters commonly required some coordinate transformations. In order to implement linear controller by digital control platforms, sampled data process is required which is an approximation of the continuous-time behavior of the system control variables. All these require further design steps and consideration in linear controller in order to achieve an appropriate controller.

These design steps and considerations are sometimes challenging for some power converters applications such as matrix converters. In addition, if constraints are desired to be included in the control algorithm, it is not straight forward to include directly constraints into linear controller design. The constraints such as switching frequency,

total harmonic distortion, maximum switching happening, and etc are commonly desired in control of power converters. Thus by taken into consideration the increase in demand of high performance and efficiency controller for power converter, the investigation of new control techniques should be consider that are simple to implement and have high performance for wide range of applications.

1.2.2 Predictive control techniques

Literature has investigated predictive control applications in power electronics as early as the 1980's for high-power systems with low switching frequency [21]. The use of higher switching frequencies was not possible at that time due to the large calculation time required for the control algorithm. During last couple of decades by improvement of high speed and powerful microprocessors, interests in predictive control in power electronics considerably increased [22-25].

Power electronics converters are nonlinear system with finite number of switching devices. Characteristics of power converters and drives such as nonlinear behavior, finite number of switching states, and constraints lead to the application of model predictive controls. In addition, predictive control techniques are coincident by the characteristics of present day control platforms such as discrete-time implementation and model knowledge based.

Predictive controllers can be divided into four main methods, these classification of predictive controllers are illustrated in Figure 3. The main difference between these methods of control is that the model predictive control and deadbeat control with continuous control set are working with a modulator, thus they have fixed switching

frequency. However the hysteresis based and trajectory based predictive controller generating the switching signals directly and therefore they have variable switching frequency. The main focus of this dissertation is model predictive control as highlighted in Figure 3. The main characteristics of all of the predictive controllers are to use the system (power converter) model to predict the future behavior of the controlled variables. This information is utilized by the controller algorithm to determine the optimal actuation by predefined optimization criteria.

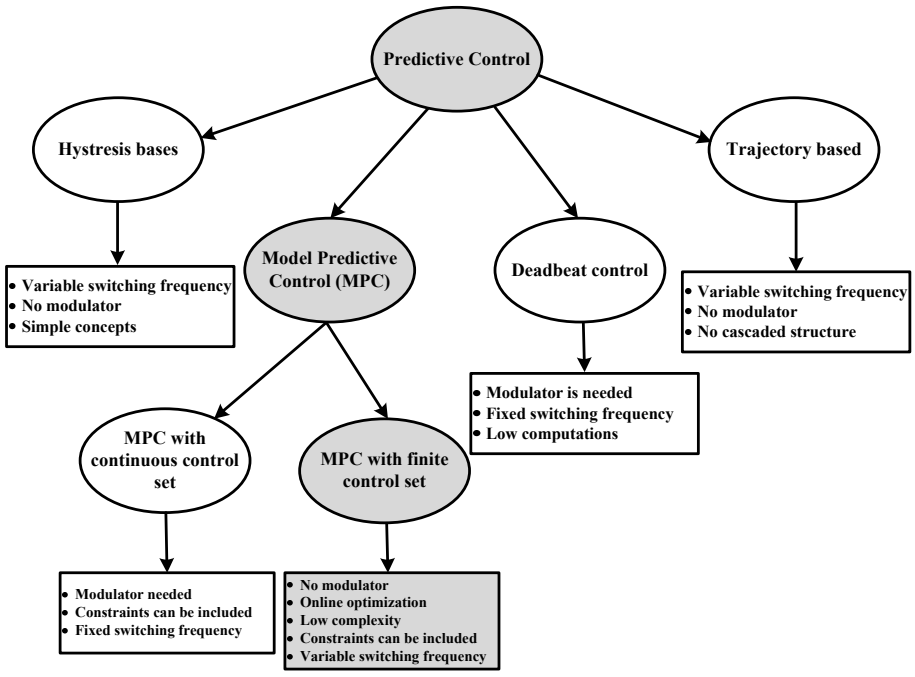

Figure 3: Classifications of predictive controllers

Predictive controllers eliminate the need of cascaded structure which is common in linear control techniques, thus very fast transient response can be achieved. This characteristic is observed and verified through the applications considered in this

dissertation. Nonlinearities can be included in the system thus linearizing the model can be eliminated. All of these advantages can be simply implemented in predictive controllers such as model predictive controls.

In hysteresis based predictive controller, the optimal actuation is determined by keeping the desired control variable within certain boundaries known as hysteresis area or space [26, 27]. This principle is also known as bang-bang controller in literature, however commonly they are not called predictive controller, but they have characteristics of predictive controller. The predictive current controller by hysteresis principle proposed in [27] is an improved form of conventional bang-bang controller. As an example for hysteresis based predictive current control the optimal switching state is determined by suitable error boundaries as illustrated in Figure 4. This figure demonstrates a circular form boundary, where its location is determined by the reference current $\vec{i}^*$ as shown in Figure 4 by dotted line. The next switching state is determined by optimization once the predicted current vector, $\vec{i}$, hits the boundary line [28].

Trajectory based predictive control the control variables are subject to follow a predefined trajectory [29]. This method force system control variables to pre-calculated trajectories. Several control strategies according to this method is proposed within literature such as direct self-control (DSC) [30], direct mean torque control (DMTC) [31], and direct speed control (DSPC) [29]. DSPC algorithm is a good example that shows the main principle of trajectory based predictive control, where the optimal switching state is determined by the pre-known of the drive system. A brief explanation of DSPC is presented in [28].

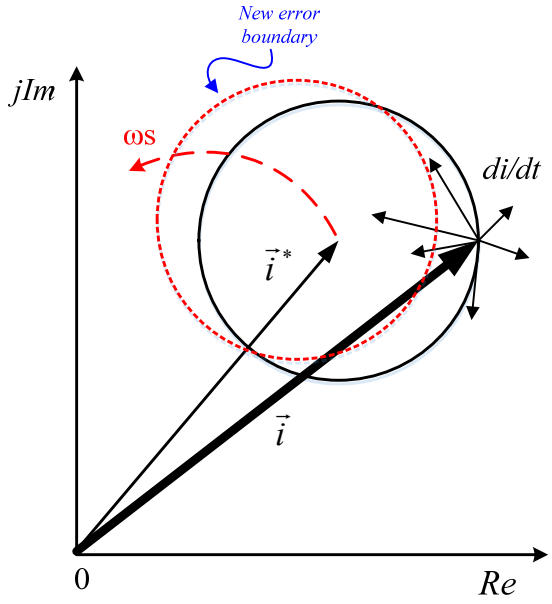

Figure 4: Hysteresis based predictive current control

The optimal actuation in deadbeat predictive control is the one that make the error merge to zero in the next sampling in horizon of time. Then the value of the control variable that makes the error zero is applied using a modulator. This predictive control strategy is widely applied for applications such as current control in inverters [32], active filters [33], rectifiers [33], uninterruptible power supplies [34], dc-dc converters [35], and etc. The general principle of operation of deadbeat predictive current control is illustrated in Figure 5. The existence present error between the current, i, and its reference, i^*, is used for calculation of reference voltage v^*; this voltage is applied to the load at next sampling time k+1. In ideal case of operation, the error between the current and its reference should be zero at time k+1.

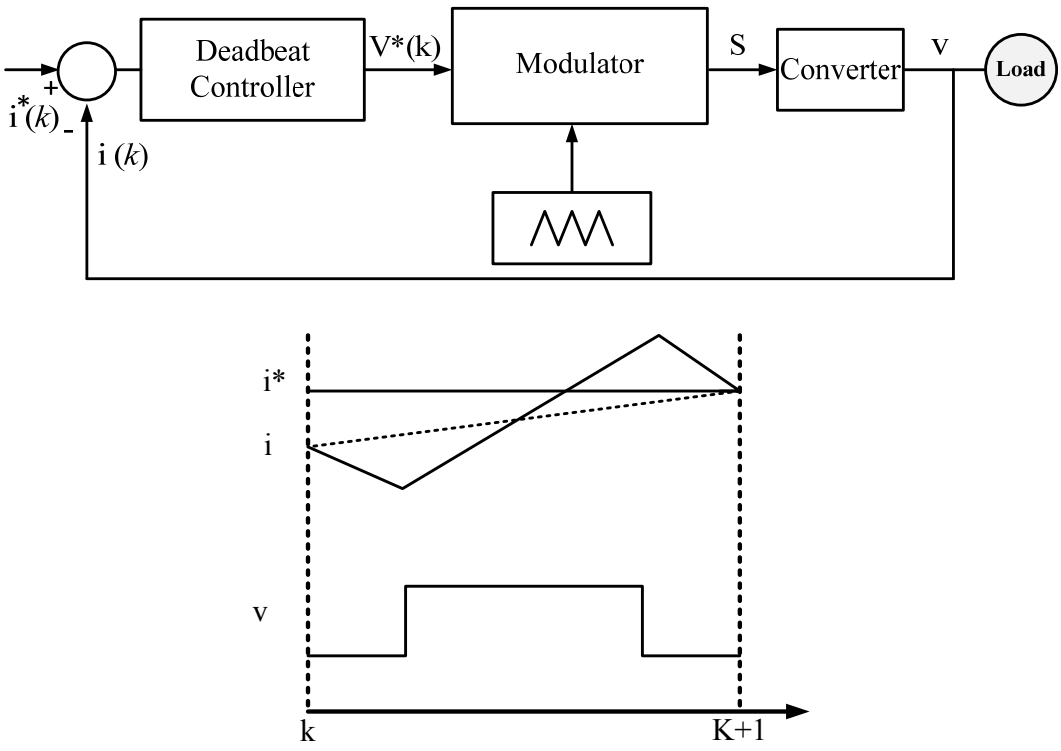

Figure 5: Deadbeat based predictive current control

The model predictive control (MPC) which is the main focus of this dissertation has more flexible criterion, where a cost function is defined subject to minimization. The optimal actuation is the one that minimized the predefined cost function. This class of predictive controller is also known as receding horizon control which is the one of the advanced control techniques compared to the others that usually understood as more advanced than PID controller. MPC has been highly considered successfully for wide range of application in last couple of decades [14, 15, 36-40]. MPC can simply take into consideration constrained nonlinear systems with multiple inputs and outputs. The detail formulation and analysis of MPC will be presented in Section 3 of this dissertation.

1.3 Dissertation overview

This dissertation deals with the multi-criteria design and control of hybrid electrical distribution systems. The thesis can be divided into two main aspects: (1) Techno-Economic multi-objective optimization of hybrid power and energy system; (2) Model predictive control techniques for hybrid electrical distribution systems. In order to conduct the stated research goals, the remainder of this dissertation is organized as follows.

In section 2, a techno-economic multi-objective optimization tool is developed using Prato Front for hybrid power and energy system design. A decision making procedure is proposed to determine a single solution based on user preferences. Variability of high penetration PV scenario is analyzed using flat and non-flat PV modules. The effect of geographical distribution of PV arrays on variability of high-penetration PV scenario in community microgrid is analyzed.

In section 3, the model predictive control state of art for power electronics application is presented. A comprehensive framework and strategy is presented in this section that is used as the basis for designing of MPC in this disseretation.

In section 4, a high effective and rapid Maximum Power Point Tracking of PV systems by means of model predictive control techniques is presented for multilevel boost converter topology. The high control effectiveness in steady state with small oscillation around maximum power point and fast dynamic response to change in solar irradiance are the main outcomes of this section. The proposed technique is compared to conventional Incremental Conductance technique.

In section 5, a high efficient maximum power point tracking using model predictive control for grid-tied PV application is presented. A two-step model predictive control is developed for multilevel DC-DC boost converter cascaded with multilevel DC-AC converter to feed the PV power to grid. The performance of the proposed method compared to conventional Incremental Conductance.

In section 6, a current oriented model predictive based maximum power point tracking is proposed for flyback converter. The load model is eliminated in this section to reduce the sensitivity of MPC to load disturbances. The dynamic EN-50530 standard test is used to analyze the performance of the proposed method under rapidly changing weather condition.

In section 7, a droop predictive control is presented for multiple PV arrays connected to a single DC distribution bus in community microgrid. The maximum power extracted from PV arrays using the method presented in section 6, and then they are connected in parallel to a DC bus. Back-to-back DC-DC converters control both the input current from the PV module, known as maximum power point tracking, and the droop characteristics of the output current injected into the distribution bus.

In section 8, a reactive power compensation technique is presented using model predictive control of a direct matrix converter. The objective of this section is to develop a capacitor less reactive power compensator by using only inductors and matrix converter controlled by MPC. A novel online optimization of cost function by auto-tuning of weight factor in the cost function of MPC is presented in this section.

In section 9, a decoupled direct real and reactive power predictive control for grid-tied single phase inverter is presented. The proposed decouple direct power predictive control is further developed in this section by modifying the MPC cost function to minimize the switching losses by minimizing the switching events with harmonics constraints.

2. OPTIMIZATION OF HYBRID ELECTRICAL SYSTEMS*

Renewable energy sources continues to gain popularity. However, two major limitations exist that prevent widespread adoption: availability of the electricity generated and the cost of the equipment. Distributed generation, (DG) grid-tied photovoltaic-wind hybrid systems with centralized battery back-up, can help mitigate the variability of the renewable energy resource. The downside, however, is the cost of the equipment needed to create such a system. Thus, optimization of generation and storage in light of capital cost and variability mitigation is imperative to the financial feasibility of DC microgrid systems.

PV and wind generation are both time dependent and variable but are highly correlated, which make them ideal for a dual-sourced hybrid system. This section presents an optimization technique base on a Multi-Objective Genetic Algorithm (MOGA) which uses high temporal resolution insolation data taken at 10 seconds data rate instead of more commonly used hourly data rate. The proposed methodology employs a techno-economic approach to determine the system design optimized by considering multiple criteria including size, cost, and availability. The result is the baseline system cost necessary to meet the load requirements and which can also be used

*Part of this section is reprinted with permission from M. B. Shadmand and R. S. Balog, "Multi-Objective Optimization of Photovoltaic-Wind hybrid System for Community Smart DC Microgrid," IEEE Transactions on Smart Grid, September, 2014, © 2014 IEEE and M. B. Shadmand, R. S. Balog, and M. D. Johnson, "Predicting Variability of High-Penetration Photovoltaic Systems in a Community Microgrid by Analyzing High-Temporal Rate Data," IEEE Transactions on Sustainable Energy, October, 2014, © 2014 IEEE and M. B. Shadmand and R. S. Balog, "Mitigating Variability of High Penetration Photovoltaic Systems in a Community Smart Microgrid using Non-flat Photovoltaic Modules," Energy Conversion Congress and Exposition (ECCE), September, 2013, © 2013 IEEE.

to monetize ancillary services that the smart DC microgrid can provide to the utility at the point of common coupling (PCC) such as voltage regulation. The hybrid smart DC microgrid community system optimized using high-temporal resolution data is compared to a system optimized using lower-rate temporal date to examine the effect of the temporal sampling of the renewable energy resource.

2.1 DC distribution system

DC distribution systems are ideal for integrating distribute renewable energy sources and energy storage into point-of-use energy systems [1, 41, 42]. Renewable energy adoption has increased with 60% annual growth in the installed capacity of photovoltaic (PV) systems from 2004 to 2009, and a growth factor of 68% from 2010 to 2013 [43]. However, two major fundamental limitation exists that prevent truly widespread adoption: availability of electricity generated and cost of equipment. At the same time, DC systems have been gaining popularity because of the high efficiency, high reliability and easy interconnection of renewable sources compared to AC systems [1, 5]. A DC microgrid system with distributed PV and wind generation and employing centralized battery storage, illustrated in Figure 1, is an attractive technology solution for communities to "go-green" while simultaneously ensures reliable electricity.

To mitigate fluctuations in the generation portion of the hybrid system, a battery bank is used for energy storage. This will absorb the surplus power and supply deficit power under different operating conditions. The proposed methodology has been previously used for assessing standalone distributed photovoltaic systems and has been experimentally verified through long-term field testing [44].

DC distributed generation (DG), grid-tied PV-wind systems with centralized battery back-up, illustrated in Figure 1, have been proposed for community-scale microgrids such as the Pecan Street project in Austin Texas [4] and other communities [5]. An example of the power electronic interface between the utility-power grid and the community distribution bus is the solid state transformer [6, 7] being developed by the FREEDM Center at NC State, Figure 1. The control and management of the islanded PV-wind and storage systems have been proposed in [8-11].

Due to the stochastic behavior of wind and solar energy, one of the most vital factors in optimal sizing of the hybrid systems is the temporal resolution of collected data to provide sufficient resolution [45], particularly on cloudy days, Figure 6. Optimization techniques such as Multi-Objective Genetic Algorithm (MOGA) [46-48] are able to take advantage of high temporal resolution data for renewable resources instead of relying only on mathematical probabilistic models. The main contribution of this paper is to employ an energy availability technical assessment in conjunction with economic assessment to optimize the sizing of the PV panel, wind turbine, battery storage, and the power imported from grid in order to determine the system that would guarantee a reliable energy supply with the lowest investment.

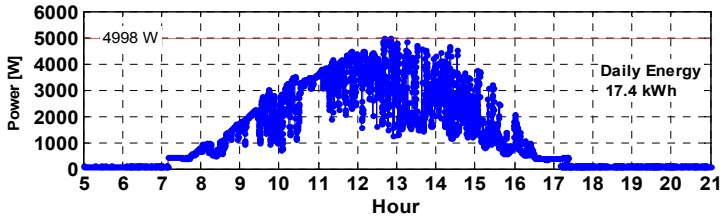

Figure 6: Example of high temporal resolution PV data on a cloudy day

The objective of this section is to simultaneously maximize the power availability and minimize the cost which will optimize system size with highest availability. The problem is firstly visualized based on MOGA technique and Pareto Front for purpose of engineering trade off when analyzing high temporal resolution data. Then a utility function will be determined in order to do a decision making for the multi-objective problem. Uncertainty analysis is added because of the stochastic behavior of the insolation and wind speed data.

The "average month" technique [49, 50] is not used in this paper because the system designed in this way may not be able to satisfy the load during some periods of real-work operation. On the other hand, the calculation of each subsystem (wind, photovoltaic, storage, and ratio of power imported from grid) separately for the worst month in each resource makes the total system oversized. The optimized hybrid system, based on accurate and enhanced 10 seconds insolation data rate of photovoltaic system, is compared to conventional PV-Wind optimized systems based on hourly insolation data. Using MOGA as the optimization technique when analyzing high temporal resolution insolation data shows that the system availability is maximized for lowest possible cost comparing to conventional hybrid system sizing [51-53].

Due to the different operating life of various components, reliability analysis is critical [54, 55]. In this paper, though no reliability analysis details will be discussed, the results of the extra cost overhead to the owner due to maintenance and repairs will be included. In addition, the mathematical modeling of the system considers the economic

aspects such as inflation, interest, and escalation rates which makes the model more realistic.

The case study is a grid-tied community living environment in College Station, Texas. The case study uses high temporal resolution data collected from a 27.6 kW PV system installed on Texas A&M University campus [56]. The system, configured as five independent residential-scale arrays, has the PV generation (ac output) data sampled every 10 seconds, Figure 6. Details of the hybrid system and selected site are:

- The apartment complex consists of 70 units with 28 two story buildings, the load schedule is shown in Table 1
- The monthly average load requirement for the apartment complex is approximately equal to 82,920 kWh
- There is 5.27 kWh/m^2 of available incident solar energy
- The site has class-1 wind [57], and Wind Finder [58] is used to gather wind resource data

Table 1. Summary of apartment complex energy usage

Summary of Apartment Units		
Type of Units	***No. of Units***	***Average Energy Usage (KWh)***
Efficiency	2	830
1bed 1bath	20	940
2bed 1bath	10	1150
2bed 1.5bath	32	1330
2bed 2bath	6	1410

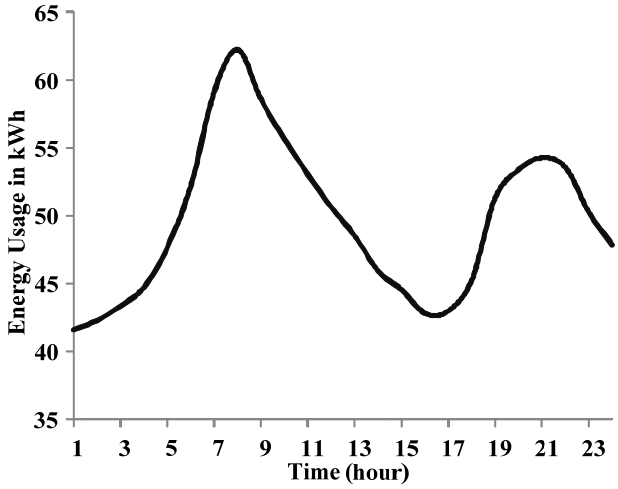

Figure 7: Daily load profile

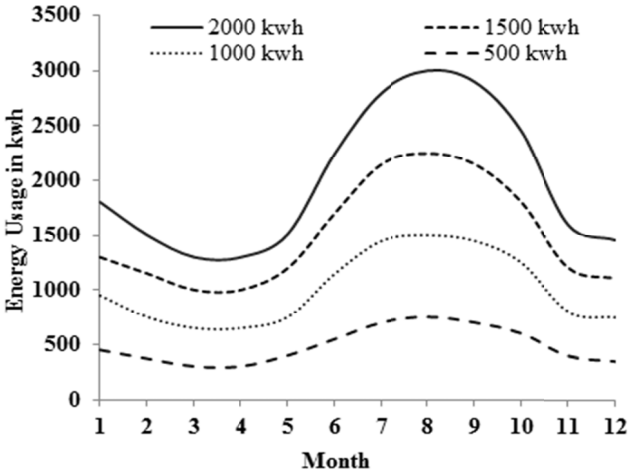

Figure 8: Estimated monthly residential load profiles

The hourly demand of the case study is illustrated in Figure 7. The load profile of each apartment is estimated over an entire year as it is illustrated in Figure 8. A center of mass approach is utilized to estimate the load profiles for apartment units which lie between energy profiles. For example the unit with 1150 kWh which is between 1000 kWh and 1500 kWh, we get 1000P + 1500(1-P) = 1150, where P=70%. Therefore 1150

kWh has 70% resemblance to 1000 kWh load pattern and 30% to 1500 load pattern. By using this methodology and base on the information provided in Table 1, the monthly average load requirement for the apartment complex is determined to be approximately 82,920 kWh.

2.2 Problem statement

In this section, the objectives of the system will be mathematically formulated for optimization. These objectives are to simultaneously maximize the power availability and minimize the cost which minimizes the system size with highest possible availability. The output power of PV and wind generators has the highest priority to feed the DC bus, and if the power generated is inadequate, the battery bank can be discharged to a certain amount to feed the bus. If there is still insufficient power, a certain amount of power can be purchased from grid to feed the load. Thus the power imported from grid has the lowest priority.

2.2.1 Cost

Major component of the system cost consists of the price of PV panels, Wind turbines, and Battery bank. The total system cost ($/year) includes initial cost and Operational & Maintenance cost (O&M), this can be formulated as

$$Cost = C_{Grid} + \frac{\sum_{i=PV,Wind,Batt} (I_i + OM_i)}{N} \qquad (1)$$

where I_i and OM_i indicate the initial cost and Operation & Maintenance (O&M) cost of each individual components respectively. N and C_{Grid} are the life cycle of the system and

cost of power imported from grid respectively. So the first objective can be formulated as

$$\underset{Minimize}{Cost}\ (A_{PV}, A_{Wind}, P_{CapBatt}, \Psi) \tag{2}$$

where A_{PV}, A_{Wind}, $P_{CapBatt}$ and Ψ are the design parameters in this project.

For the photovoltaic, the initial and O&M cost can be formulated as

$$I_{PV} = \lambda_{PV} \times A_{PV} \tag{3}$$

$$OM_{PV} = OM_{yearly} \times A_{PV} \times \sum_{i=1}^{N} \left(\frac{1+\upsilon}{1+\gamma} \right)^{i} \tag{4}$$

For the wind turbine, the initial and O&M cost can be similarly formulated as

$$I_{wind} = \lambda_{wind} \times A_{wind} \tag{5}$$

$$OM_{wind} = OM_{yearly} \times A_{wind} \times \sum_{i=1}^{N} \left(\frac{1+\upsilon}{1+\gamma} \right)^{i} \tag{6}$$

For the battery bank, the initial cost and O&M cost can be formulated as

$$I_{Batt} = \lambda_{Batt} \times P_{Cap\_Batt} \tag{7}$$

$$OM_{Batt} = OM_{yearly-Batt} \times P_{yearl-Batt} \times \sum_{i=1}^{T_b} \left(\frac{1+\upsilon}{1+\beta} \right)^{(i-1)N_{Batt}} \tag{8}$$

For the battery bank, since their life cycle is less than the life cycle of PVs and Wind turbines, they should be replaced several times during the project life span. This replacement cost taken into consideration as O&M costs in (8).

The cost of importing power from the grid can be formulated as

$$C_g = \sum_{i=1}^{T} P_{grid,t} \times \lambda_{Grid} \tag{9}$$

2.2.2 Electrical energy availability

Availability, the fraction of the time when energy is available, is a key figure of merit for the proposed system. It is important to make a clear distinction between availability and reliability. Reliability is the ability of the system to operate without failure; availability is the ability of the system to supply power to the load. As an example, a highly reliable photovoltaic energy system, where the components are not prone to failure, can have low availability if there is insufficient energy storage to support the load's power requirements during the night or during an overcast day.

A specified level of availability can be achieved with many configuration of a system. The availability can be formulated for duration under consideration *T* as

$$A = 1 - \frac{DNM}{D} \tag{10}$$

The *DNM* can be formulated as

$$DNM = \sum_{t=1}^{T} \begin{pmatrix} P_{\underset{MIN}{Batt}}(t) - P_{\underset{SOC}{Batt}}(t) - \\ \left(P_{PV}(t) + P_{Wind}(t) + P_{Grid}(t) - P_{D}(t)\right) \times u(t) \end{pmatrix} \tag{11}$$

where *u(t)* is a step function which is zero if the supply power is greater or equal demand and one if the demand is not met.

The imported power from grid is:

$$P_{Grid} = \Psi \times \left(P_D(t) - P_{PV}(t) - P_{Wind}(t) - P_{Batt}(t)\right) \tag{12}$$

where

$$P_{Wind} = P_{WTG} \times A_{Wind} \times \eta_{Wind} \tag{13}$$

$$P_{PV} = Insolation \times A_{PV} \times \eta_{PV} \tag{14}$$

The second objective can be formulated as:

$$\underset{A}{Maximize}\ (A_{PV}, A_{Wind}, P_{CapBatt}, \Psi) \tag{15}$$

The hybrid system parameters values are given in

Table 2.

Table 2. Numerical value of hybrid system parameters

Parameters	Values
Life cycle of the project N	20 *years*
Battery life cycle N_{Batt}	5 *years*
Inflation rate β	8%
Interest rate γ	12%
Escalation rate υ	12%

2.3 Multi-objective optimization

2.3.1 Design constraints

A physical constraint which must be added to the optimization algorithm is the available area for PV panels and wind generators installation:

$$A_{\underset{Min}{PV}} < A_{PV} < A_{\underset{Max}{PV}} \qquad (16)$$

$$A_{\underset{Min}{Wind}} < A_{Wind} < A_{\underset{Max}{Wind}} \qquad (17)$$

Obviously the lower bounds can be zero, but in order to make the system more reliable for the purpose of uncertain analysis, the lower bound for wind turbines is decided to be about 100 m^2. For the selected apartment complex the upper bound was determined to be approximately 12% of the available area, which was approximately 4,221 m^2.

The imported power from the grid should be within a certain range:

$$P_{\underset{Min}{Grid}} < P_{Grid} < P_{\underset{Max}{Grid}} \qquad (18)$$

$$0 < \Psi < 1$$

The fraction of the power Ψ to be imported from grid can vary from zero to one, this can be seen from (12).

Finally, the total generated power should not exceed the demand in order to avoid oversizing the system and adding excessive cost. This constraint is formulated as:

$$P_{PV}(t) + P_{Wind}(t) + P_{Batt}(t) + P_{Grid}(t) \leq P_D(t) \qquad (19)$$

The numerical values of design constraints are given in Table 3 for the presented case study.

Table 3. Constraints numerical data

Parameters	Values
$A_{PV_{Min}}$	0 m^2
$A_{PV_{Max}}$	4,221 m^2
$A_{Wind_{Min}}$	100 m^2
$A_{Wind_{Max}}$	4,221 m^2

2.3.2 NSGA-II optimization for the hybrid system

Multi Objective Genetic Algorithm (MOGA) which is commonly called Non-dominated Sorting Genetic Algorithm-II (NSGA-II) [48, 59] is used as an optimization algorithm or search method to find a set of equally good solutions for the objectives mentioned in section III as a form of a Pareto frontier. However other optimization techniques can be used, but this method has been one of the most popular heuristic search methods for multi-objective optimization [48]. Genetic Algorithm is a well-known non-gradient-based search method which mimics the natural evolution process.

The key distinction between single-objective and multi-objective optimization is that in the case of multi-objective optimization, there may be multiple feasible solutions that satisfy the optimization criterion. Further, may not be possible to identify one

solution as being *better* than another if neither is *dominated* by the other in some sense. In other words, in multi-objective optimization, there could exist a set of equally-good solutions rather that a single solution as we expect in single-objective optimization problems. The results of multi-objective optimization can be also be described as a set of non-dominated solutions, the so called Pareto frontier.

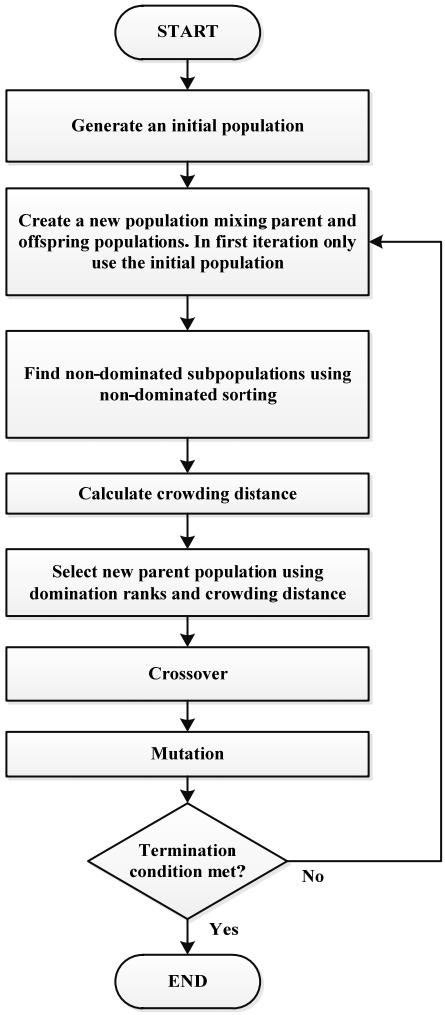

Figure 9: MOGA (NSGA-II) optimization algorithm for hybrid system.

MOGA uses Genetic Algorithm (GA) as its core with two important new concepts in order to achieve good multi-objective optimization. These two concepts are non-dominated sorting and crowding distance as described in [46, 48]. By using these two concepts and GA principle, MOGA algorithm can be formed which is called Non-dominated Sorting Genetic Algorithm-II (NSGA-II) [48]. This algorithm is briefly explained in this section.

A sorting process is then performed by selecting solutions with the lowest rank and then solutions with the next lowest rank and so on. This process continues until the number of solutions in the parent population exceeds *N*. Then, for the latest sorted subpopulation included in the parent population, only the solutions with a larger crowding distance are selected until parent population has exactly *N* solutions. Crossover and mutation operators are then performed to find the next offspring population. Figure 9 illustrates the flowchart of NSGA-II algorithm used in this section for optimizing the hybrid system.

The comprehensive design procedure of the hybrid system for DC smart microgrid is illustrated in Figure 10. Without loss of generality, the models of the various components, including the wind generator, solar cells, and power electronics interfaces can be made arbitrarily complex to improve the fidelity of the model. In a PV-wind hybrid energy harvesting system, there are many factors which contribute to the overall conversion efficiency. One of the most important conditions is the geographical location where the system is deployed which determines the latitude and the meteorological conditions. Therefore the first step in the design procedure is to specify

the geographical location. Based on the location, conditions such as available wind and solar resources and weather data are used to determine the ratings for the PV array and wind generator. Usable roof area, desired availability of power (loss of load probability), desired lifetime, and limits on maximum imported grid power are considered as design constraints for the objective functions. Finally, by using the optimization tool illustrated in Figure 9, a set of equally good solutions, the Pareto Frontier, is found that maximize the availability and minimize the cost of the hybrid system.

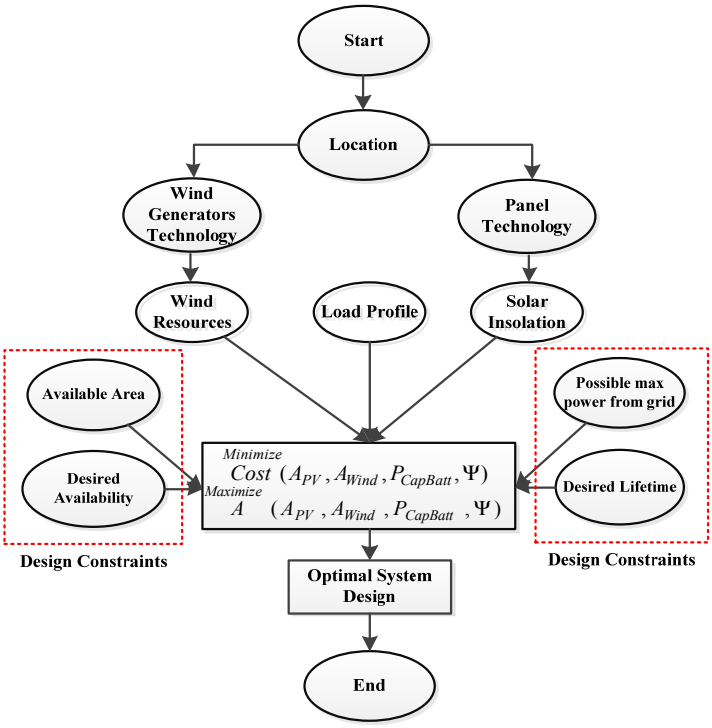

Figure 10: Comprehensive design and optimization procedure of the hybrid system for smart DC microgrid.

Figure 11 illustrates a set of optimal design solution for the hybrid system. The PV panel cost (λ_{PV}), wind turbine cost (λ_{Wind}), battery bank cost (λ_{Batt}), and price of grid power (λ_{Grid}) are assumed 450 \$/m^2, 100 \$/m^2, 100 \$/kWh, and 0.10 \$/kWh respectively.

Figure 11 illustrates the trade-off between cost and availability. This is due primarily from the need to supply the peak load during as determined by the system energy availability. Thus the Pareto Frontier is a tool that enables engineering tradeoff analysis to choose the unique design from the set of feasible designs based on particular preferences.

Due to stochastic behavior of the solar and wind, in this paper the decision making is done for two scenarios: without uncertainty and with uncertainty. A more detail discussion on uncertainty analysis is presented in the next section.

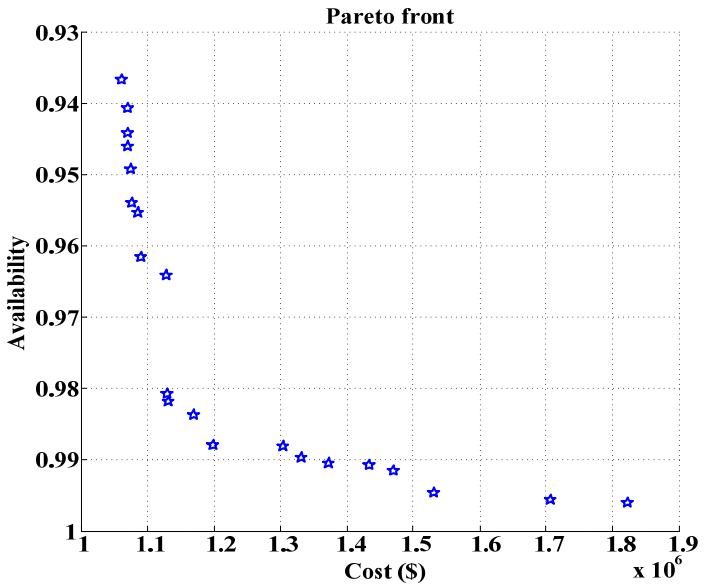

Figure 11: Pareto frontier reveals the set of optimal solutions found from the evaluation of (1)-(15) for the proposed hybrid system.

2.4 Decision making

The set of optimal solution given by the Pareto Frontier is illustrated in Fig. 7 can be used to visualize the optimal solutions and perform engineering tradeoff studies. In this paper the utility theory [60, 61] is used to decide the optimal solution based on the

preferences for the smart DC microgrid. Therefore a function need to be defined to clearly rank-order the alternatives for decision making, this function is commonly called the *utility* or *value* function [61]. Usually the term "*value function*" denotes the decision under certainty and the term "*utility function*" denotes a decision under uncertainty.

Two decision making scenarios are investigated in this paper: with and without uncertainty in the solar radiation, wind speed, and demand data. Firstly a utility function will be formulated for decision on system design without uncertainty, then the expected value of utility function will be used for decision by taking into consideration the uncertainties.

2.4.1 Decision making without uncertainty

Objectives and attributes are used as tools for modeling the preferences or the utility function, and then an irrevocable allocation of resources will be done. An attribute, or figure of merit (FOM), is the measure of progress toward an objective. The attributes in this paper are the availability and cost. So a function needs to be defined that relates every point in an n-dimensional attribute space to a scalar value or utility as follow

$$\begin{aligned} u &= u(z) \\ z &= [Cost \quad A] \end{aligned} \tag{20}$$

which allow the designer to rank order the alternatives. The next step is to convert all attributes to same scale, frequently called "pricing out". The summary of the decision modeling without uncertainty is illustrated in Figure 12. By using the procedure illustrated in Figure 12, the general form of value function for the hybrid system optimization is given by

$$u(Cost, A) = \lambda_1 \frac{Cost - (Min(Cost))}{Max(Cost) - Min(Cost)} - \lambda_2 \frac{A - (Min(A))}{Max(A) - Min(A)} \quad (21)$$

where λ_1 and λ_2 are the weighing factors that can be defined by the designer. If $\lambda_1 = \lambda_2$, it means the designer are indifferent between the availability and cost of the hybrid system for the DC distribution systems. Consequently, the proposed value function provides the designer the ability to perform the engineering trade study. Finally by minimizing *u (Cost, A)* using GA optimization toolbox in MATLAB, the irrevocable decision on the design variables can be obtained.

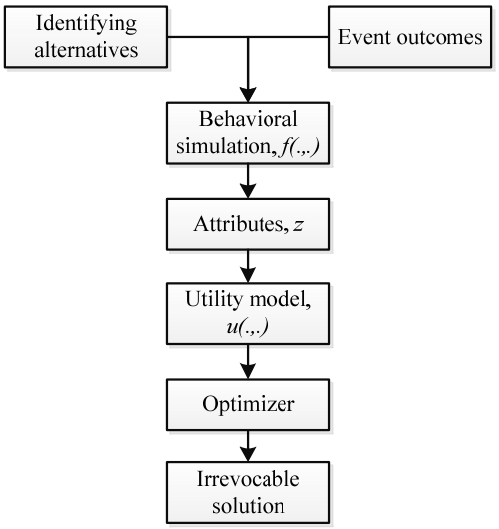

Figure 12: Decision model without uncertainty.

The optimized design variables of the hybrid system for two scenarios are given in Table 4. In the first design scenario, λ_1 is assumed to be equal to λ_2 which means an indifference to cost and availability. For the second design scenario, more weight is given to the availability than cost (λ_1=0.3, λ_2=0.7) in the *u(Cost, A)* function. As expected, inspection of the Pareto Front of the optimal solutions of the system (Figure 11), reveals that the cost of the system increased significantly.

Table 4. Optimized hybrid system design variables for two scenarios without uncertainty

Design Scenario	A_{PV} (m^2)	A_{Wind} (m^2)	P_{Cap_Batt} (kWh)	Ψ	A	Cost
1	2102.61	376.74	248.78	13%	98.5%	$1,164,523
2	2911.95	662.8	395.31	17%	99.3%	$1,526,928

2.4.2 Decision making with uncertainty

A normal probability distribution is assumed over the attribute vectors. The solar insolation, wind speed, and demand have the following normal distribution:

$$\varepsilon_{PV}, \varepsilon_{Wind} \sim N(0,0.2) \quad (22)$$

$$\varepsilon_{Demand} \sim N(0,40) \quad (23)$$

Now their corresponding parameter in system modeling should be modified as:

$$P_{Wind} = (P_{WTG} + \varepsilon_{Wind}) \times A_{Wind} \times \eta_{Wind} \quad (24)$$

$$P_{PV} = (Insolation + \varepsilon_{PV}) \times A_{PV} \times \eta_{PV} \quad (25)$$

$$P_{Demand} = (Demand + \varepsilon_{Demand}) \quad (26)$$

In order to optimize the utility function (21) under uncertainty, the expected value of the utility function must be determined. In this paper Monte Carlo is used for uncertainty propagation purpose. The proposed methodology is illustrated in Figure 13. The simulation is performed for 100 iterations; the results are given in Table 5 for the two design scenarios discussed in the previous section. As shown, the cost of the system is increased significantly when considering uncertainties. Interestingly, the analysis revels similar availability comparing to results given in Table 4, but the cost of the system what is increased substantially.

It is important to note that an optimization design based on collected data does not guarantee worst case system availability. A worst case optimized system design specifying absolute limits on availability such as two days without solar insolation is possible, but will result in a larger and more costly system. Thus, the main contribution of this paper is to introduce a step by step optimization design procedure for desired availability and cost.

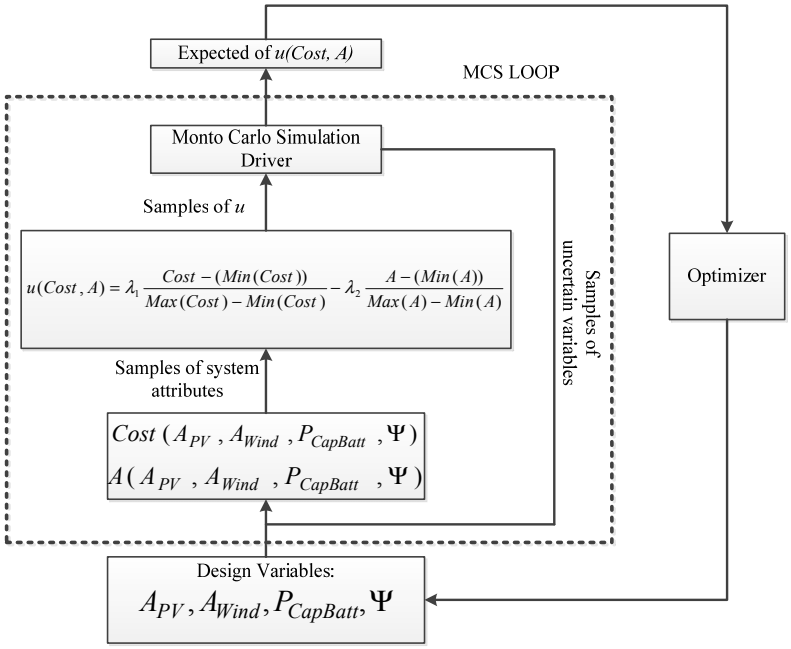

Figure 13: Procedure of optimizing the utility function with uncertainty on solar insolation, wind speed, and demand data.

Table 5. Optimized hybrid system design variables for two scenarios with uncertainty

Design Scenario	A_{PV} (m^2)	A_{Wind} (m^2)	P_{Cap_Batt} (kWh)	Ψ	A	Cost
1	2865.33	711.30	371.80	21%	97.8%	$1,477,528
2	3465.73	871.2	399.37	27%	99.1%	$1,788,931

2.5 Mitigating variability

2.5.1 High penetration photovoltaic systems

The high penetration photovoltaic system variability presents considerable challenges for maintaining system balance [62-66]. The focus of this section is to analyze the variability of a high-penetration PV scenario using flat and non-flat PV modules when incorporated using the microgrid concept illustrated in Figure 1.

Within the literature numerous papers can be found dealing with variability PV systems [67], single location, PV systems. Most of them demonstrates that analyzing high-frequency irradiance data, such as 5 minutes, can reduce the variability comparing to more commonly hourly data [68, 69]. This dissertation proposes a new idea to mitigate further variability of generated power from the PV system using non-flat photovoltaic modules as well as geographical distribution of PV arrays in microgrid concept of Figure 1.

2.5.2 Non-flat photovoltaic modules

Emerging PV cell technologies no longer impose the requirement of a rigid, flat, planar PV module [70-74] and can be processed on flexible substrates [74-76], screen printed [77], or embedded into fabric [78] as illustrated in Figure 14 [79] which opens new applications [80] for energy scavenging from the environment using non-planar PV surfaces.

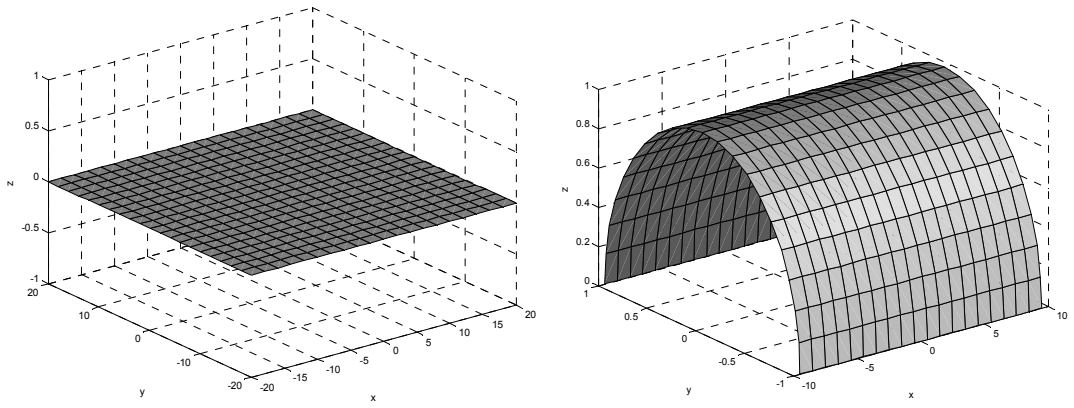

(a) (b)

Figure 14: Candidate geometries for PV modules: a) traditional flat plat (planar) PV collection surface b) proposed semi cylinder PV modules

The proposed methodology in this section shows that using non-flat PV modules can mitigate further variability of the power generated when analyzing high-temporal resolution solar radiation data illustrated in Figure 6. It turns out that in addition to improving reliable energy supply in the Microgrid, the concept of using non-flat PV modules, Figure 14, also mitigates the variability of the entire Microgrid as seen by the utility at the point of common coupling. Thus in addition to optimization of generation and storage, mitigation of variability is imperative to the financial feasibility and power quality of such Microgrid systems [81-83].

In a solar energy harvesting system, there are many factors which contribute to the overall conversion efficiency. One of the most important conditions is the geographical location where the system is deployed which determines the latitude and the weather pattern. This factor will be analyzed in the next section. The second factor is the geometry and alignment of the solar module itself which determines the amount of sunlight reaching individual cell of the PV module. An earlier paper [70] investigated

the amount of power and overall energy harvested from different PV geometries. The geometries in [70] were suitable for different application based on the total energy harvest requirements. A key design goal in this section of dissertation is to select a geometry which performs best in the selected location as well as mitigate the variability of power generated power.

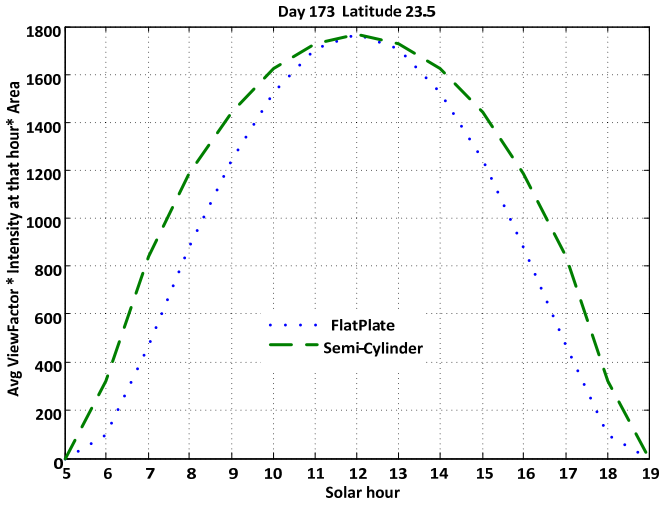

Figure 15: Comparison of flat plate vs. semi-cylinder panels energy harvest.

One way to compare PV geometries is by considering their two-dimensional projection (ie, footprint.). Figure 15 compares the power generated by a semi-cylinder to the generated by a flat panel of the same footprint. The semi-cylinder harvests more energy (difference in the area under the curves) during early morning and evening hours. This is advantageous in a stand-alone power system in which energy available to the load is more important than power generated. Figure 15 is taken during the summer solstice, when the sun is directly overhead. As such, it is no surprise that at solar noon both the semi-cylinder and the flat panel generate the same amount of electrical power,

because the sun "sees' the same effective footprint. During other days of the year, when the sun's apex does not reach as high above the horizon, the total energy generated over the diurnal cycle of the semi-cylinder compared to the flat plate is even greater than what is shown in Figure 15.

After optimization of the hybrid system using the method presented in this section, three candidate geometries of PV modules are evaluated: normal flat PV module, semi-cylinder PV module with same surface area as flat, and semi-cylinder PV module with same footprint area as flat. Simulation results in Figure 16-Figure 18 shows that for a 7 days interval, using the semi-cylinder PV modules with same footprint area as flat modules predict less power imported from grid than the other two PV modules, operationally this means the system becomes easier to dispatch and control.

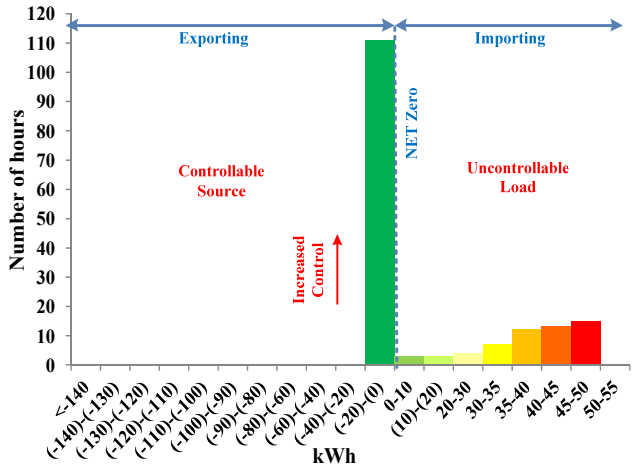

Figure 16: Baseline histogram of power flow for 7 days from Microgrid to main grid using flat PV modules

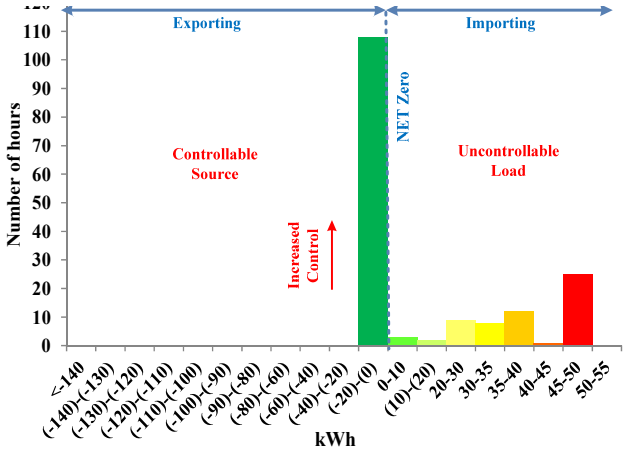

Figure 17: Histogram of power flow for 7 days from Microgrid to main grid using semi-cylinder PV modules with same surface area as flat

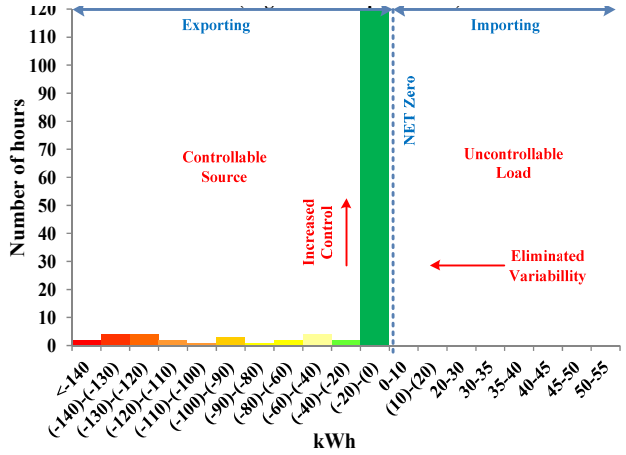

Figure 18: Histogram of power flow for 7 days from Microgrid to main grid using semi-cylinder PV modules with same foot print area as flat

Overlaying the capability of a smart grid communication system, the excess energy generated, shown as "exporting" can be selectively injected into the utility grid by adjusting the power point tracking of each solar array [84]. It is interesting to note that when the semi-cylinder PV modules with same foot print area as flat plate modules combined with energy storage, the variability is eliminated and net zero importing power

from the grid can be achieved. Thus the high penetration PV Microgrid can be made to operate and a nearly constant power load on the main ac power grid.

2.5.3 Geographical distribution of photovoltaic arrays

The focus of this section is to analyze the variability of a high-penetration PV scenario when incorporated into the microgrid concept of Figure 1. The proposed approach is to demonstrate that the variability of the PV resource can be quantified and mitigate by determining the number of PV arrays and their corresponding distance in the microgrid.

Within the literature some papers can be found dealing with understanding the variability of centrally located PV systems [67, 85] when analyzing high temporal resolution irradiance data, such as 5 minutes [68, 69]. Most of the existing literature [86-89] focuses on the effect of variability on the ac electrical grid and the operational implications of spinning reserves. This dissertation choses a different perspective. Instead, we analyses the problem from the perspective of how to mitigate the variability at the point of common coupling. As such, the PV variability determines the amount of storage that our local system would need to maintain a PV variation-free node on the utility perspective. From this perspective, we study the effect of the distance between PV arrays as one way to mitigate variability and thus lower the amount of energy storage. Of course, this only works in transient atmospheric conditions, but this is also the scenario that is hardest to plan for in the utility operations. Our implicit assumption is that a uniformly cloudy day would be easier to forecast and plan.

A comprehensive analysis to understand the effect of distributed PV arrays on variability of system when analyzing high temporal resolution data, such as few seconds, is missing in the literature. Much of them uses stochastic mathematical models [90, 91]. The main contribution of this section is to experimentally analyze the variability of a high-penetration point-of-load PV scenario using the microgrid concept illustrated in Figure 1. The result shows that the variability of high penetration PV is not as large as if the PV was centrally located, and that only a small amount of community energy storage is needed to arbitrarily mitigate this variability as well as reduce energy intensity through demand reduction including peak shaving and demand shifting.

The distributed PV system in this section consists of N identical PV arrays equally spaced, D, as illustrated in Figure 19. If D is small, less than five meters for example, the system behaves more like a centralized PV generation than distributed generation. A detail plot of the three PV arrays with distance D of approximately 100 meters, near noon, is illustrated in Figure 20, which reveals an interesting observation – the physical distribution of the arrays results in a time shift; a delay in the effect of the cloud transient. Figure 21 compares the total generated power from the three distributed PV arrays with the generated power if they were centrally located; the variability of output power is significantly reduced when the PV arrays are co-located.

Variability can be defined as PV output power changes over a selected time interval under study. The variability of the PV system can be determined by calculating the standard deviation of the system over specified period of time as

$$\sigma_{\bar{T}}^{\sum_N} \qquad (27)$$

where N is number of arrays and T is period under consideration, and by definition

$$\sigma_T^{\sum N} = \frac{1}{P_{Peak}} \sqrt{Var\left[\sum_{n=1}^{N} \Delta P_T^n\right]} \qquad (28)$$

where P_{Peak} is the installed peak power of the PV arrays and $^{\Delta P_T^n}$ is the time series of changes in power at the n^{th} PV installation in time interval T. More specifically $^{\Delta P_T^n}$ can be defined as:

$$\Delta P_T^n = P_t^n - P_{t+\Delta t}^n \qquad (29)$$

In this section a relative variability is defined to do the variability analysis. A relative variability is the ratio of the variability of N co-located PV arrays to the variability of centralized PV system with same number of arrays, ranges from 0 to 1 and can be defined as:

$$\text{Relative variability} = \frac{\sigma_T^{\sum N}}{\sigma_T^1} \qquad (30)$$

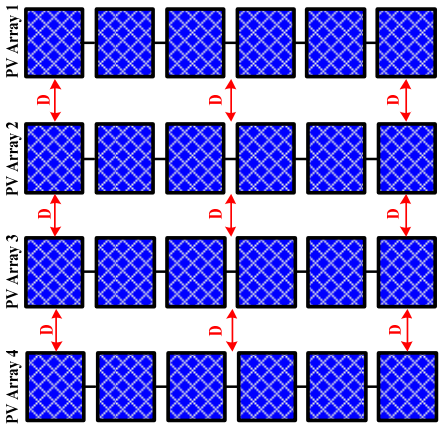

Figure 19: Distributed photovoltaic arrays.

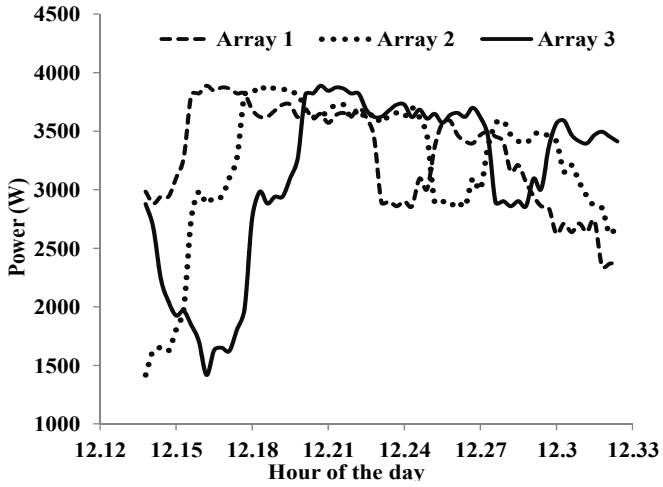

Figure 20: Zoomed-in plot of data of three PV arrays with distance of 100 meters near noon.

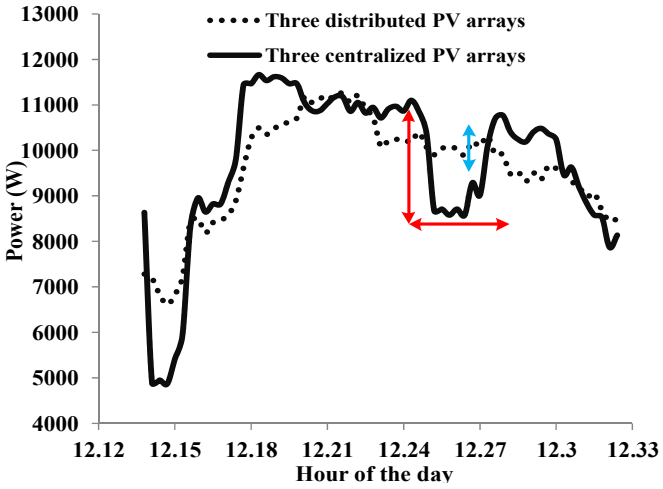

Figure 21: Zoomed-in plot of data of three PV arrays near noon. The 100 meter separation reduces the variability compared to if they were located side-by-side.

As illustrated in Figure 21, the variability of output power of three PV arrays when geographically distributed is significantly reduced comparing to the centralized arrays. It is interesting to see the change in relative variability by varying the distance *D* and number of arrays in the system *N*. In this analysis the cloud transit speed assumed

constant. Figure 22 illustrates the behavior of the relative variability of a system with 3 and 5 PV arrays when varying the distance *D* between them, the cloud transient speed is assumed to be constant "x".

As it can be seen in Figure 22, the relative variability doesn't have a pure convex shape, but for *D* more than 150 meters we can see slightly increase in the relative variability which is undesirable. Therefore the optimal distance between the five PV arrays system is 150 meters. Theoretically the optimal point can be achieved when the cloud disturbance affecting one PV array in exactly one time interval, *T*, for the selected case study this optimal distance is approximately 150 meters based on experimental measurements. A more clear observation of this phenomenon can be seen in Figure 23, when the cloud transient speed is varying. Assuming the cloud transient speed, *V*, of the actual measured data of Figure 22 is known to be "*V*=*x*".

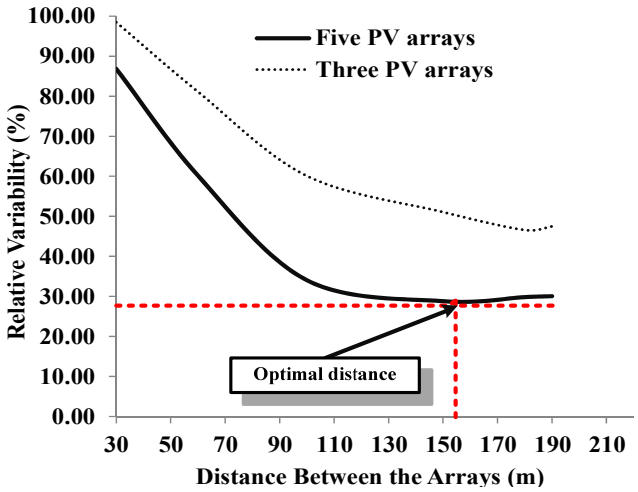

Figure 22: Relative variability vs distance between the arrays for *N=3* and *N=5*.

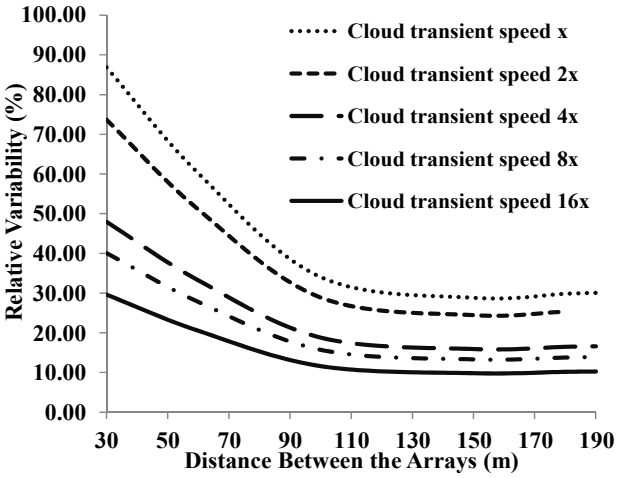

Figure 23: Relative variability vs distance between the arrays for *N=5* and different cloud transient speed.

If the irradiance level of the PV array 1 is I_t at time t, then the irradiance level at the adjacent PV array with distance D will be:

$$I_{t_1}^{D} = I_t \tag{31}$$

where the t_1 is:

$$t_1 = t + \frac{D}{V} \tag{32}$$

This formulation can be extended for the five adjacent PV arrays case study presented in this paper. Now by knowing the distance between the arrays and their corresponding irradiance levels with cloud transient speed of x (based on actual measured data), the irradiance level of each PV array can be determined for any other cloud transient speed than cloud transient speed of x. By using this phenomenon the results illustrated in Figure 23 is determined. Two assumptions are made for this phenomenon: a) the cloud transient vector is assumed to be in the direction of the PV

arrays location; b) the cloud area and its density are approximately unchanged while moving above the PV arrays.

It can be seen that when the cloud transient speed is 16 times more comparing to its speed in Figure 22, the relative variability is much lower as depicted in Figure 23. The worst case scenario in co-locating PV arrays happens when the distance between them are less than a certain value, this cause two or more partially shaded PV array in one time interval which diminish the effectiveness of the proposed model.

The tail of the plots in Figure 23 suggests that the relative variability increases once the distance exceeds a minimizing length. Since the system of interest in this paper is a microgrid, which by its very nature is a small-scale system, points to the right of the minimizing distance are not practical. In a community neighborhood, or a military base, we are interested in how closely together we can group the PV and the required minimum distance to achieve the lowest energy storage in the system.

It should be noted that maximizing distance D for fixed number of PV arrays doesn't minimize the relative variability, while this may add additional wiring and communicating cost of the system. Similarly as illustrated in Figure 24, adding more PV arrays within a crowded region doesn't decrease the relative variability.

As shown in Figure 24, by assuming constant amount of installed power and distance D, the relative variability reduced significantly by increasing the number of co-located PV arrays and then saturated. It is interesting to see the effect of co-locating more PV arrays on the variability of system. Figure 25 illustrates the daily output power

of five co-located versus centralized PV arrays, as it is shown the variability substantially decreased when the PV arrays distributed geographically.

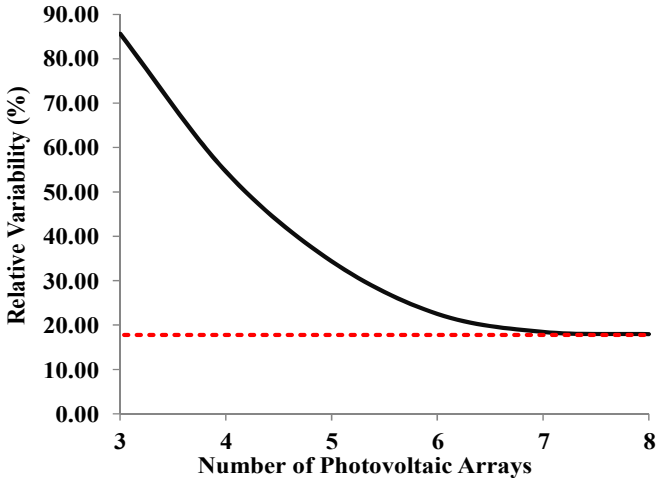

Figure 24: Relative variability vs number of photovoltaic arrays with constant distance between arrays.

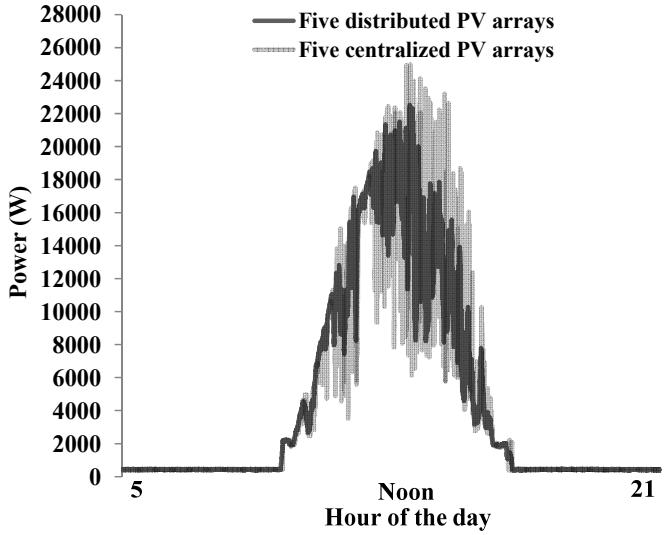

Figure 25: Daily output power of five co-located vs centralized PV arrays.

It should be noted that the proposed model and experimental analysis done for a uni-dimensional PV system installation.

2.6 Conclusion

An important contribution of this section is a sizing model that considers desired availability and cost simultaneously. The proposed methodology avoids oversizing the system for high percentage of availability by using accurate and enhanced high-temporal resolution data. The main objective of this section is to provide a general model that quantifies the availability and cost of hybrid renewable energy systems for smart DC microgrid.

In this paper high temporal resolution data for PV system is used to optimize the hybrid system based on Multi-Objective Genetic Algorithm (MOGA). MOGA is used to plot the Pareto Front in order to visualize the problem for engineering tradeoff. A utility function based on availability and cost formulated to find the final optimal solution. The optimization is done for two scenarios: with certainty and uncertainty on available resource. The proposed methodology guarantees a reliable energy supply with lowest investment.

In addition this section investigates how to address the inherent variability of solar energy. A general model that quantifies the variability of different PV configuration systems by analyzing high-temporal resolution solar radiation data is investigated. It is always important from utility point of view to obtain a better understanding of the impact of the PV system variability on utility systems operation.

This section investigates experimentally the parameters that affect the system variability such as number of PV arrays, geometry of PV panels, and distance between adjacent PV arrays. The proposed analysis in this section is based on an optimally sized

hybrid system as a realistic model framework. When storage is considered, results from analyzing High-temporal resolution data show that the variability of the hybrid system can significantly decreased if the PV arrays in the proposed microgrid system co-located instead of more commonly centrally located PV arrays. The centralized PV system can be viewed as closely spaced PV arrays.

3. PRINCIPLE OF MODEL PREDICTIVE CONTROL

3.1 Model predictive control techniques for power electronics

3.1.1 Background and literature review

Application of model predictive control (MPC) in power electronics with low switching frequency goes back to the 1980's for high power applications [15, 21]. Since high switching frequencies for the MPC algorithm required long calculation time, widespread adoption was not feasible at that time. Though the theory of MPC was developed in 1970s, in the past decade, with the improvement of high speed microprocessors, interest in the application of MPC in power electronics with high switching frequency has increased considerably [22, 24, 92-95].

The main characteristic of MPC is predicting the future behavior of the desired control variables [15, 22] until a specific time in the horizon. The predicted control variables are used to obtain the optimal switching state by minimizing a cost function.

One of the major advantages of predictive controllers is that the concept is simple and straight forward to implement as an example finite control set MPC for two-level converters. When considering continuous control set MPC, the implementation of MPC for some application is more complex. Considering little time available due to small sampling time for calculation of MPC algorithm and optimization of MPC algorithm, it is common to do most of calculations offline using the system parameters and model. This technique is known as explicit MPC where the resulting optimal actuations are in form of look-up table. This look-up table is containing optimal solution as a function of

the state of the system. Explicit MPC is applied for wide range of power electronics converter in literature [96-98].

In explicit MPC method, the model of power electronic converter is approximated in form of a linear system by a modulator to eliminate the need of online optimization. The main drawback of this method is that the discrete characteristics of power electronics converters are not taken into account. The online implementation and optimization problem can be considered when including the discrete characteristics of power converters and finite number of switching states. More flexibility of implementation and desired constraints for controller can be achieved when considering online optimization of cost function in MPC method. In the following section more detail will be discussed about this technique which is the main focus of this dissertation.

3.1.2 Basic principle

The MPC for power electronics converters can be designed using the following steps [22]:

- Modeling of the power converter identifying all possible switching states and its relation to the input or output voltages or currents.
- Defining a cost function that represents the desired behavior of the system.
- Obtaining discrete-time models that allow one to predict the future behavior of the variables to be controlled.

The designed controller should consider the following tasks:

- Predict the behavior of the controlled variables for all possible switching states.
- Evaluate the cost function for each prediction.

- Select the switching state that minimizes the cost function.

The model used for prediction is a discrete-time model which can be presented as state space model as follow [15]:

$$x(k+1) = Ax(k) + Bu(k) \tag{33}$$

$$y(k) = Cx(k) + Du(k) \tag{34}$$

Then a cost function that takes into consideration the future states, references and future actuations can be defined:

$$g = f\left(x(k), u(k), \cdots, u(k+N)\right) \tag{35}$$

The defined cost function g should be minimized for a predefined horizon in time N; the result is a sequence of N optimal actuations:

$$u(k) = \begin{bmatrix} 1 & 0 & \cdots & 0 \end{bmatrix} \arg \min_{u} g \tag{36}$$

Despite the fact that $u(k)$ contains feasible plants inputs over the entire horizon of time only the first element is used in conventional MPC. At next sampling time (k+1), the system states are calculated using the system model, the horizon is shifted by one step, and another optimization is applied. As demonstrated in Figure 26 for a horizon length N=3, the horizon taken into consideration in the minimization of g slides forward as k increases. Therefore, MPC amounts to an open-loop-optimal feedback control methodology.

At each sampling time the optimization problem is solved again by using new set of measured data to obtain a new sequence of optimal actuation. The MPC principle of

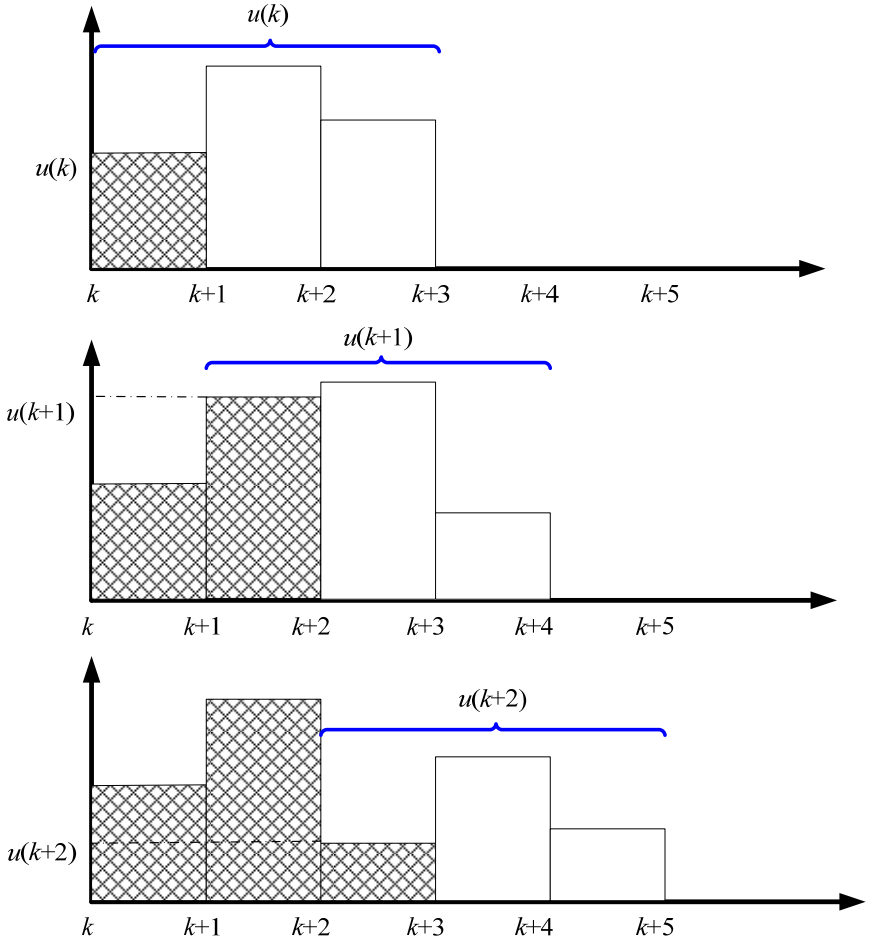

(a) Moving in horizon of time principle (N=3)

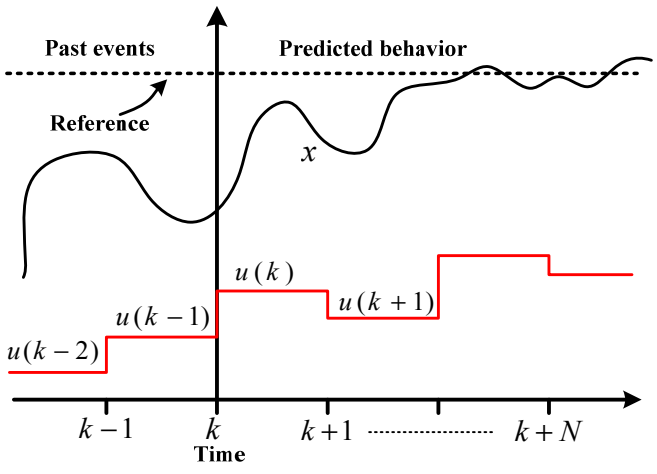

(b) Principle of working

Figure 26: Model Predictive Control (MPC).

working is illustrated graphically in Figure 26. As it is shown by using the measured information and system model until time k, the future value of the system state is predicted until time ($k + N$) in horizon. Then the optimal actuation is calculated by optimizing the cost function (35).

3.2 Controller design

In designing stage and modeling of the MPC for a power converter, the basic element is the power switch. Considering ideal operation of power switches such IGBT, they have only two states "ON" and "OFF". Thus number of different combination of switching states minus the impossible states is the total number of switching states. These impossible switching states are the ones that may cause for example short-circuit. Generally, the number of switching states *NSS* is determined as following

$$NSS = \chi^{NP} \qquad (37)$$

where χ is the number of possible states of each phase or leg of the power converter and the number of phases or legs is presented by *NP*. As an example, a three phase, three level converter has 3^3=27 switching states.

In design of MPC for power converters another factor that should be considered is the switching states relation with voltage vectors and voltage levels in multi-phase converters and single phase converters respectively. Similarly if current source converter is the application, the relation of switching states to current vectors should be considered. Figure 27 illustrates the relation between the individual voltage vectors and their corresponding switching state of a typical three-phase, two level converter.

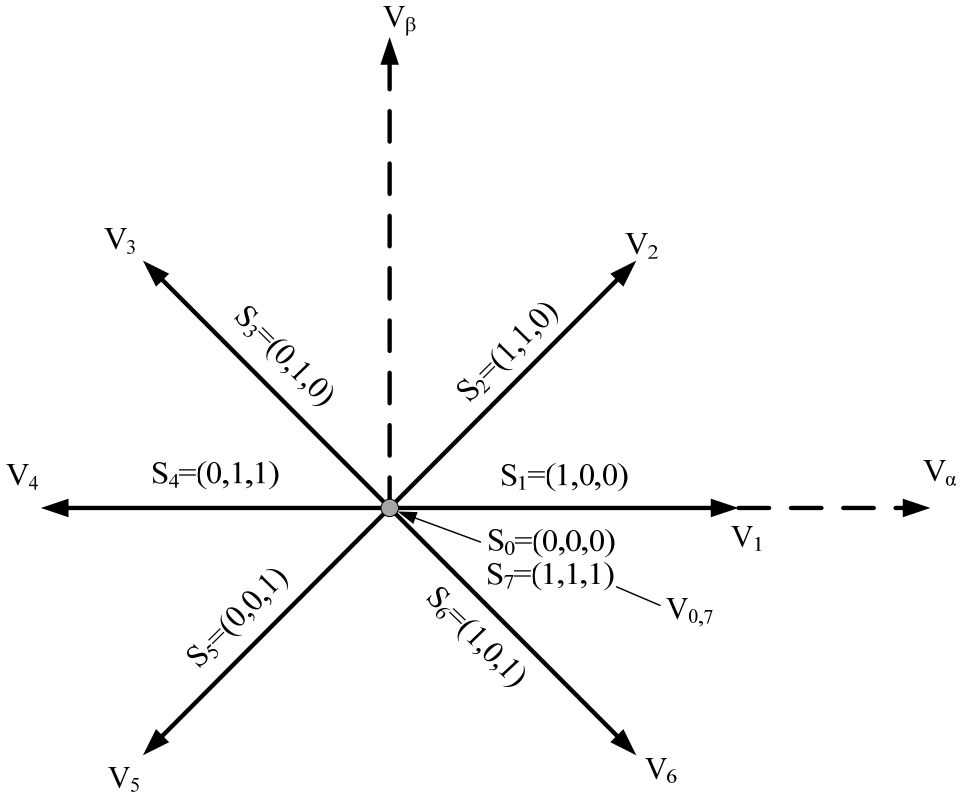

Figure 27: Voltage vectors of a three-phase two-level converter.

As mentioned in previous section, discrete-time model of the control variables should be considered in order to determine their predicted values in future sample time. Several discretization methods exist to determine the discrete-time model of the system. As an example, for first order systems, Euler forward method can be used to approximate the derivatives:

$$\frac{dx}{dt} = \frac{x(k+1) - x(k)}{T_S} \qquad (38)$$

where T_s is the sampling time. For higher order system, Euler forward method does not have accurate approximation and the error is higher for these systems. Thus an exact discretization should be used.

As mentioned earlier in this section, the control requirement such as torque, current, power, and etc control can be included in a single cost function, *g*, subject to minimization. One of the main advantages of MPC is that characteristics where several control variables with different nature and units can be included into single cost function. Each term in the cost function is multiplied by a weight factor to deal with units and magnitudes of the control variables.

Weight factors in the cost function in addition to accommodation of different units and scales, enable prioritization of specific control variables. However, selection of these weight factors is not straight forward [15]. Several empirical approaches to determine a fix weight factor using trial and error have been investigated in the literature [99]. However, a fixed weight factor is not robust to parameter variation and other uncertainties of the system. One of the main contributions of this dissertation is the introduction of a technique to select optimal values for the weight factors in the MPC cost function for each sampling time.

The general scheme of MPC for power electronics converters is illustrated in Figure 28 [22]. In this scheme measured variables, $X(K)$, are used in the model to calculate predictions, $\tilde{X}(K+1)$, of the controlled variables for each one of the *N* possible actuations, that is, switching states, voltages, or currents. Then these predictions are evaluated using a cost function which considers the reference values, $X^*(K+1)$, design

constraints, and the optimal actuation, *S*, is selected and applied to the converter. The general form of the cost function, *g*, subject to minimization can be formulated as

$$g = \left[\tilde{X}_1(K+1) - X_1^*(K+1)\right] + \lambda_1\left[\tilde{X}_2(K+1) - X_2^*(K+1)\right] \qquad (39)$$
$$+ \ldots + \lambda_n\left[\tilde{X}_n(K+1) - X_n^*(K+1)\right]$$

where λ is the weighting factor for each objective. To select the switching state which minimizes the cost function *g*, all possible states are evaluated and the optimal value is stored to be applied next. The power converter can be from any topology and number of phases, while the generic load shown in Figure 28 can represent an electrical machine, the grid, or any other active or passive load.

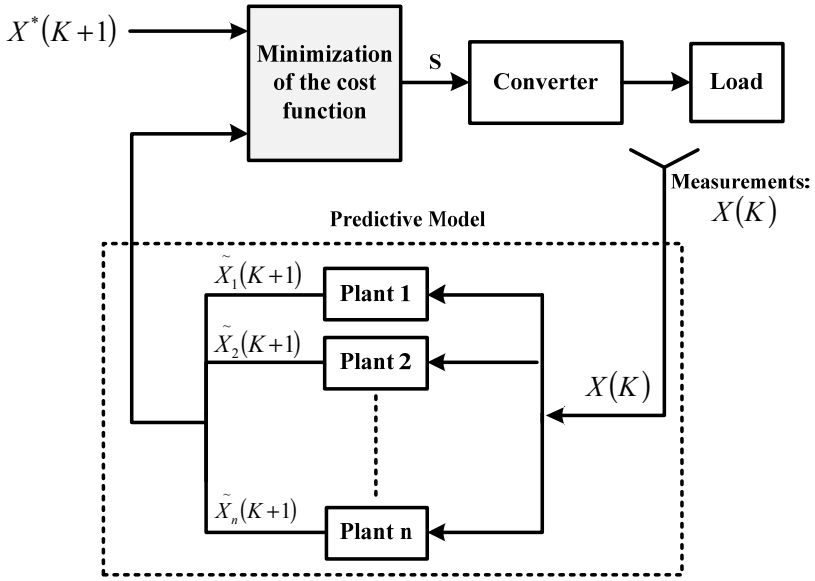

Figure 28: MPC general schematic for power electronics converters.

3.3 Conclusion

The general principle of MPC for power electronics converters is presented in this section and will be considered for all of the applications in the following sections of this dissertation.

4. MAXIMUM POWER POINT TRACKING BY MODEL PREDICTIVE CONTROL FOR HIGH GAIN DC-DC CONVERTER*

This section demonstrates a high effective and rapid Maximum Power Point Tracking (MPPT) of Photovoltaic (PV) systems by means of Model Predictive Control (MPC) techniques. The high variability and stochastic nature of solar energy necessitates MPPT control technique of PV arrays to continuously operate at true maximum power point. The PV array can feed power to the load through a DC/DC converter boosting the output voltage. Extracting the maximum power from PV systems has been widely investigated within the literature. The main contribution of this paper is to increase the effectiveness of the Incremental Conductance (INC) method through a fixed step predictive control under measured fast solar radiation variation. Consequently, the efficiency of the overall PV system is increased. The proposed control to achieve Maximum Power Point (MPP) speeds up the control loop since it predicts error before the switching signal is applied to the selected high gain multilevel DC-DC converter. Comparing the developed technique to the conventional INC method shows substantial improvement in MPPT effectiveness and PV system performance. Experimental validation is presented using the dSpace DS1103 to implement the proposed MPC-MPPT.

*Part of this section is reprinted with permission from M. B. Shadmand, M. Mosa, R. S. Balog, and H. Abu Rub, "An improved MPPT Technique of High Gain DC-DC Converter by Model Predictive Control for Photovoltaic Applications," Applied Power Electronics Conference & Exposition (APEC), March, 2014, © 2014 IEEE.

Many MPPT techniques have been suggested over the past few decades [100-104]; the relative merits of these various approaches are discussed in [105]. The critical operating regime is at low solar irradiance. Capturing all of the available solar power during low solar irradiance periods can substantially improve system performance and minimize the power loss. An effective MPPT controller and converter can use available energy to significantly reduce the amount of installed PV.

Considering the MPPT techniques listed in [105], candidate techniques include Incremental Conductance (INC) [106], Perturb-and-Observe (P&O) [101], fractional Open-Circuit Voltage (Voc) [107], and Best Fixed Voltage (BFV) [108]. Each approach has certain advantages and disadvantages for the present application. INC is a well-known technique with relatively good performance; however, INC method cannot always converge to the true maximum power point.

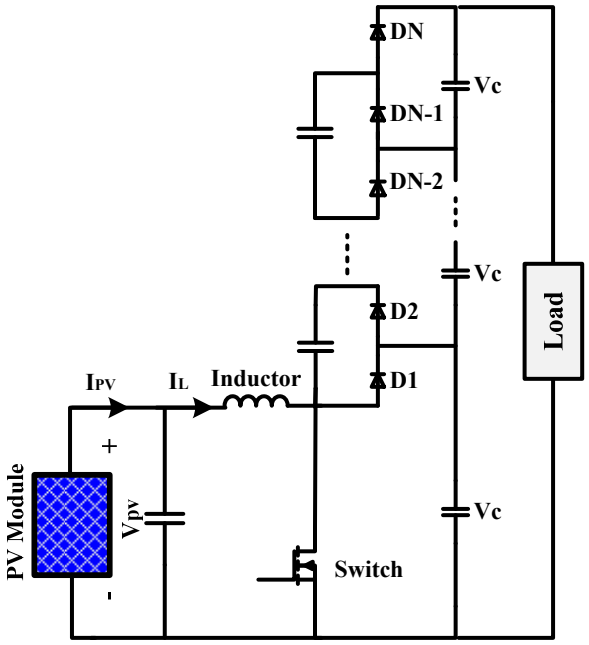

Figure 29: Multilevel DC-DC boost converter topology for PV application.

Also, INC is relatively slow, which limits its ability to track transient insolation conditions [105, 106]. The main contribution of this paper is to improve the INC method performance by predicting the error one step in horizon of time through model predictive control technique for the proposed multilevel boost converter, Figure 29. The proposed method has faster dynamic response than conventional INC method and solves some of the effectiveness limitation of the conventional INC approach under rapidly changing atmospheric conditions such as Figure 6. The efficiency analysis of the proposed predictive control based MPPT approach shows that it has rapid dynamic response and high tracking efficiency at steady state.

4.1 Principle of predictive model-based controller

The general form of the cost function, *g*, subject to minimization can be formulated as

$$g_{\xi} = \lambda_1 \left| X_{ref}^{\alpha=1}(K+1) - \tilde{X}_{\xi}^{\alpha=1}(K+1) \right| + \lambda_2 \left| X_{ref}^{\alpha=2}(K+1) - \tilde{X}_{\xi}^{\alpha=2}(K+1) \right| + \ldots + \lambda_n \left| X_{ref}^{\alpha=n}(K+1) - \tilde{X}_{\xi}^{\alpha=n}(K+1) \right| \quad (40)$$

where λ is the value or weight factor for each control objective (X^{α}), α corresponds to the different control variables, and ξ corresponds to the switching states.

In this paper we use a predictive controller to not just determine switch actuation of the converter, but also to find the maximum power operating point of the PV. This is similar in concept to ripple correlation control technique (RCC) [109], but the difference is in the formulation of the predicted control variables.

The scheme of predictive model-based controller for this application is illustrated in Figure 30. In this block diagram measured variables (PV voltage and current in this

application), $X^{\alpha}(K)$, are used in the model to estimate predictions, $\tilde{X}^{\alpha}_{\xi}(K+1)$, of the controlled variables for all of the ξ possible switching state. Then based on these predictions the reference value of voltage or current to achieve maximum power point operation will be determined. Then the predicted control variable will be evaluated based on the calculated reference control variable in form of a cost function subject to minimization. Finally the optimal actuation is selected and applied to the converter.

The schematic of Figure 30 without loss of generality can be applied to any power converter topology and the generic load illustrated in Figure 30 can represent the grid or any other active/passive load. In this section the multilevel boost converter (MLBC) topology illustrated in Figure 29 has been selected for the proposed MPPT technique, the detail analysis of this converter topology and its advantages for the application in this section are presented in the next section.

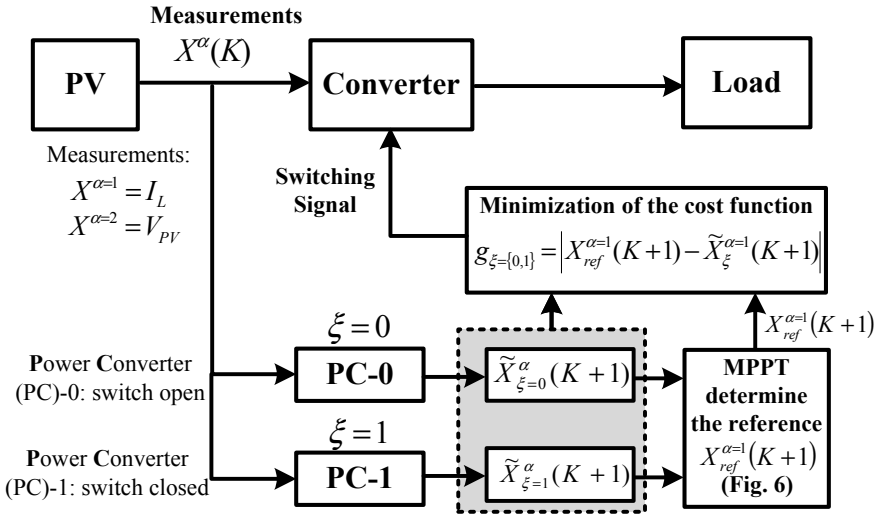

Figure 30: Predictive model-based controller block diagram for maximum power point tracking.

4.2 Analysis of multilevel boost converter

The multilevel boost converter (MLBC) topology for MPPT is illustrated in Figure 29 [110, 111]; the output voltage of the converter is proportional to the number of levels, which can be increased by adding two additional capacitors and diodes. Since only one switch is used in the selected MLBC topology, the control procedure is simpler than other topologies such as switched capacitor converter with a boost stage [112].

In this paper MLBC with two levels is used for MPPT. Figure 31 illustrates the graphical analysis of the converter when the switch is "ON" and "OFF." As shown in Figure 31 (a) when the switch is turned ON, the inductor conducts and capacitor C_1 keeps charging capacitor C_3 through diode D_2 while voltage of C_3 is smaller than voltage of C_1. Simultaneously capacitors C_1 and C_2 supply the load. When the switch is turned OFF, the diode D_1 starts conducting, and the inductor keeps charging capacitor C_1 till its voltage is equal to the summation of the PV module and inductor voltages, Figure 31 (b). Then diode D_3 turns on and the capacitors C_1 and C_2 start charging while the voltage across C_1+C_2 is equal to the summation of PV module, inductor, and capacitor C_3 voltages, Figure 31 (c).

The small-ripple approximation, the inductor volt-second balance principle, and capacitor charge balance principle are used to find the steady-state output voltage and inductor current of the MLBC. When the switch is ON in the first subinterval, Figure 31 (a), the inductor's voltage and capacitor's current are given by

$$L\frac{di}{dt} = V_{PV} - I_L R_L - R_{on-sw}\left[I_L + C_3\frac{dV_{C_3}}{dt}\right] \qquad (41)$$

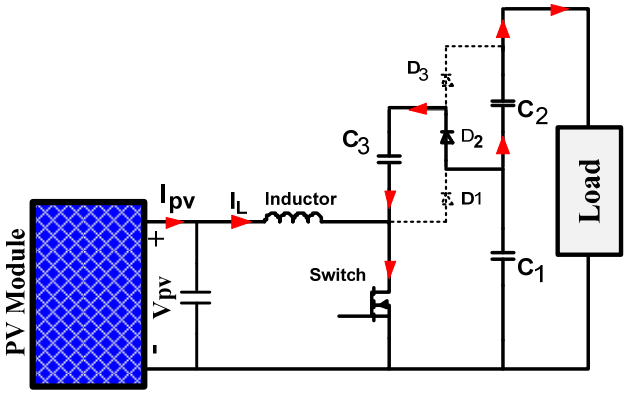

(a)

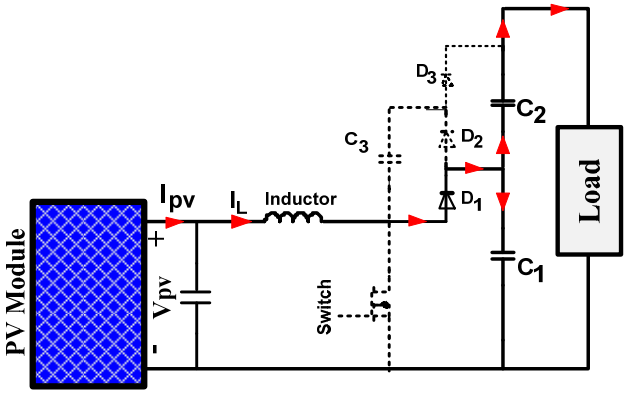

(a)

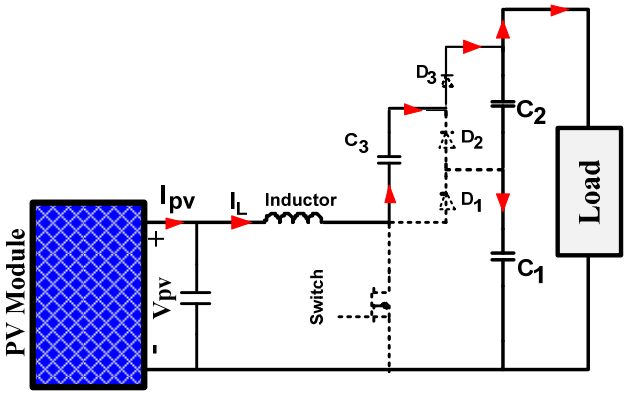

(c)

Figure 31: Multilevel Boost Converter: a) switch is ON b) switch is OFF c) switch is OFF

$$C_1 \frac{dV_{C_1}}{dt} = \frac{-V_{C_1} + V_d + V_{C_3}}{R_{C_1}} + C_3 \frac{dV_{C_3}}{dt} + \frac{R_{on-sw}}{R_{C_1}} (I_L + C_3 \frac{dV_{C_3}}{dt}) \quad (42)$$

$$C_2 \frac{dV_{C_2}}{dt} = \frac{-V_{C_2}}{R_{C_2}} + C_3 \frac{dV_{C_3}}{dt} \tag{43}$$

$$C_3 \frac{dV_{C_3}}{dt} = \frac{V_{C_1} - V_d - V_{C_3} - I_L R_{on-sw} - I_o R_C}{2R_{C_3} + R_{on-sw}} \tag{44}$$

For the next subinterval when switch is OFF, Figure 31 (b) and (c), the inductor's voltage and capacitor's current are

$$L \frac{di}{dt} = V_{PV} - I_L R_L - V_d - R_{C_1} C_1 \frac{dV_{C_1}}{dt} \tag{45}$$

$$C_1 \frac{dV_{C_1}}{dt} = I_L - I_o \tag{46}$$

$$C_2 \frac{dV_{C_2}}{dt} = \frac{V_{C_3} - V_{C_1}}{R_{C_2}} + C_3 \frac{dV_{C_3}}{dt} \tag{47}$$

$$C_3 \frac{dV_{C_3}}{dt} = \frac{V_{C_2} - V_{C_3}}{2R_{C_3}} - \frac{I_o}{2} \tag{48}$$

During the first subinterval, V_L is equal to the dc input voltage. Since, in steady-state, the total volt-seconds applied over one switching period must be zero, negative volt-seconds must be applied during the second subinterval. Therefore, the inductor voltage during the second subinterval must be negative. The volt-seconds and charge balance applied to the inductor and capacitor over one switching period are given by

$$\begin{aligned} L \frac{di}{dt} = v_{in} - I_l \times \mathrm{A} + v_d \left[\frac{R_{sw}(2D-1) + 2R_c(1-D)}{2R_c + R_{sw}} \right] \\ - R_{sw} D \left[\frac{v_{c1} - v_{c4} - I_0 R_c}{2R_c + R_{sw}} \right] - v_{c1}(1-D) + I_0 R_c \end{aligned} \tag{49}$$

where A is

$$\mathrm{A} = R_l + \frac{2R_c R_{sw}}{2R_c + R_{sw}} + R_c(1-D) \tag{50}$$

$$C_1 \frac{dV_c}{dt} = \frac{V_{pv}}{(1-D)} - I_o \left[\begin{array}{l} \dfrac{2R_c}{(1-D)} + \dfrac{2R_L}{(1-D)^2} + \dfrac{4R_{sw}R_c D}{(1-D)^2(2R_c + R_{sw})} \\ + \dfrac{DR_{sw}}{D(1-D)^2(2R_c + R_{sw})}\left(R_c(3(1-D)-D) - 1 + R_{sw}(1+2D)\right) \end{array} \right] \tag{51}$$

$$C_2 \frac{dV_c}{dt} = \frac{V_{pv}}{(1-D)} - V_d - I_o \left[\begin{array}{l} \dfrac{R_c(3+D)}{(1-D)} + \dfrac{2R_L}{(1-D)^2} + \dfrac{4R_{sw}R_c D}{(1-D)^2(2R_c + R_{sw})} \\ + \dfrac{2R_c(1-D) + R_{sw}}{(2R_c + R_{sw})}\left(\dfrac{4(1-D)R_c + 2(1+D)R_{sw}}{D(1-D)^2} - \dfrac{R_{sw} + (2-D)R_c}{D(1-D)} \right) \end{array} \right] \tag{52}$$

where C is the value of the capacitors, R_c is parasitic dc resistance of the capacitor, R_{sw} is the ON resistance of the switch, V_d is the forward voltage of any diodes, R_L is the dc resistance of the inductor.

The dc component of the inductor current is derived by using of the principle of capacitor charge balance. During the first subinterval, the capacitors supply the load current and it is partially discharged. During the second subinterval, the inductor current supplies the load and recharges the capacitors. The output voltage is given by

$$v_o = v_{c1} + v_{c2} = \frac{2V_{pv}}{(1-D)} - V_d - I_o \left[\begin{array}{l} R_c\left(\dfrac{5+D}{(1-D)}\right) + \dfrac{4R_L}{(1-D)} + \dfrac{8R_{sw}R_c D}{(1-D)^2(2R_c + R_{sw})} \\ + \dfrac{DR_{sw}}{D(1-D)^2(2R_c + R_{sw})}\left(R_c(3(1-D)-1) + R_{sw}(1+2D)\right) \\ + \dfrac{2R_c(1-D) + R_{sw}}{(2R_c + R_{sw})}\left(\dfrac{4(1-D)R_c + 2(1+D)R_{sw}}{D(1-D)^2} - \dfrac{R_{sw} + (2-D)R_c}{D(1-D)} \right) \end{array} \right] \tag{53}$$

The theoretical analysis in this paper is based on non-ideal components; therefore it is interesting to see the effect of the Equivalent Series Resistance (ESR) and switch

turn on resistance on the efficiency against the output power. As it is illustrated in Figure 32, at high power, efficiency is highly dependent on the capacitor, inductor, and the switch turn on ESRs. As shown, the ESR of the inductor has the highest effect on the efficiency because the input current is high due to high gain of the converter which is passing through the inductor. This means that the efficiency is more effective by the inductor ESR.

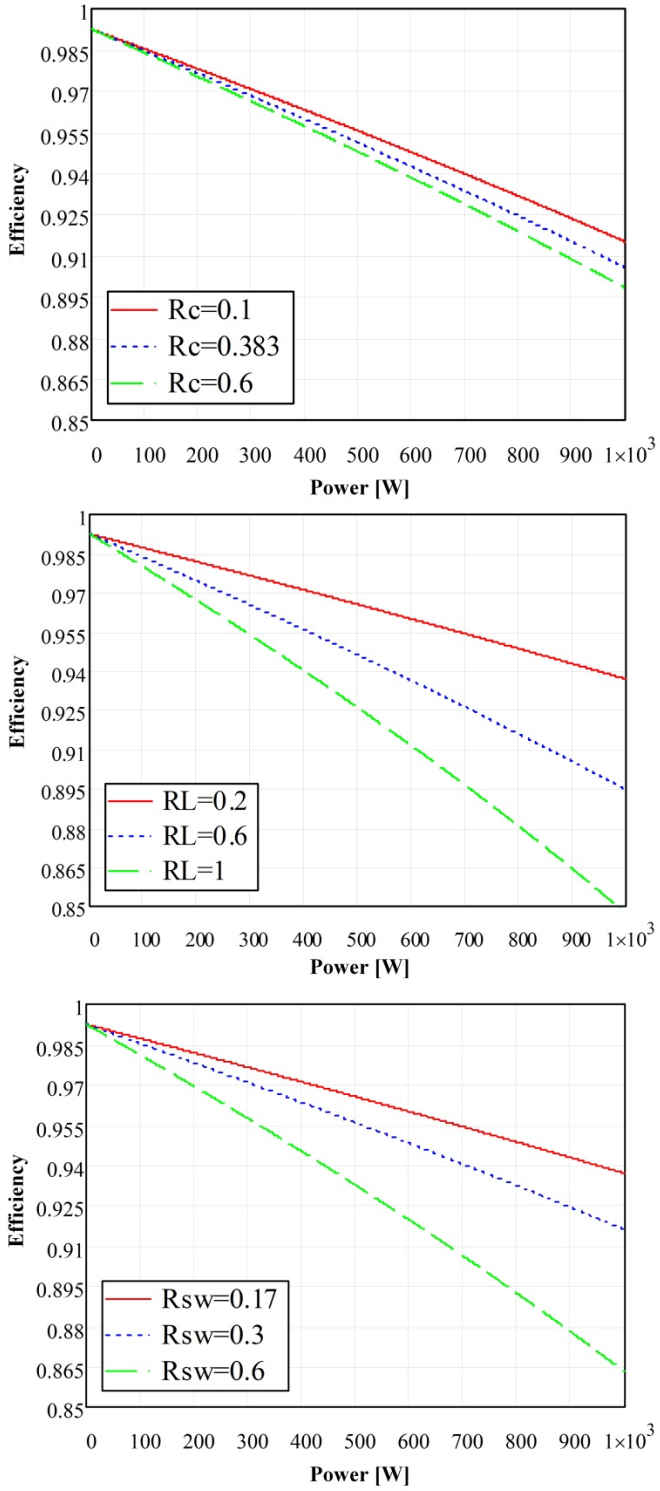

Figure 32: Effect of Equivalent Series Resistance (ESR) of capacitor, inductor, and switch turn on resistance (from top to bottom) on efficiency versus output power

4.3 Voltage oriented maximum power point tracking by model predictive control

The main characteristic of model predictive control is predicting the future behavior of the desired control variables [22]. The predicted variables will be used to obtain the optimal switching state. The proposed MPPT algorithm is illustrated in Figure 33. The inputs to the algorithm are the PV system voltage and inductor current.

The inductor current and PV voltage when the switch is ON ($\xi = 0$) are given by

$$L\frac{dI_L(t)}{dt} = V_{PV}(t) - I_L(t)R_L \qquad (54)$$

$$C\frac{dV_{PV}(t)}{dt} = I_{PV}(t) - I_L(t) \qquad (55)$$

and when the switch is OFF ($\xi = 1$) are given by

$$L\frac{dI_L(t)}{dt} = V_{PV}(t) - I_L(t)R_L - V_{C1}(t) \qquad (56)$$

$$C\frac{dV_{PV}(t)}{dt} = I_{PV}(t) - I_L(t) \qquad (57)$$

By using the Euler forward method, the derivatives in (54)-(57) can be approximated as

$$\frac{d\psi(t)}{dt} \approx \frac{\psi(k+1) - \psi(k)}{T_S} \qquad (58)$$

where Ψ is the parameter for discretization, T_s is the sampling period and k is discretized t.

By the deriving discrete time set of equations, the behavior of control variable can be predicted at next sampling time K. By using (54)-(57) and (58), the discrete time model of the converter is given by (59)-(62), when the switch is ON ($\xi = 0$):

$$I_L(K+1) = I_L(K)\left[1 - R_L \times \frac{T_s}{L}\right] + V_{PV}(K) \times \frac{T_s}{L} \qquad (59)$$

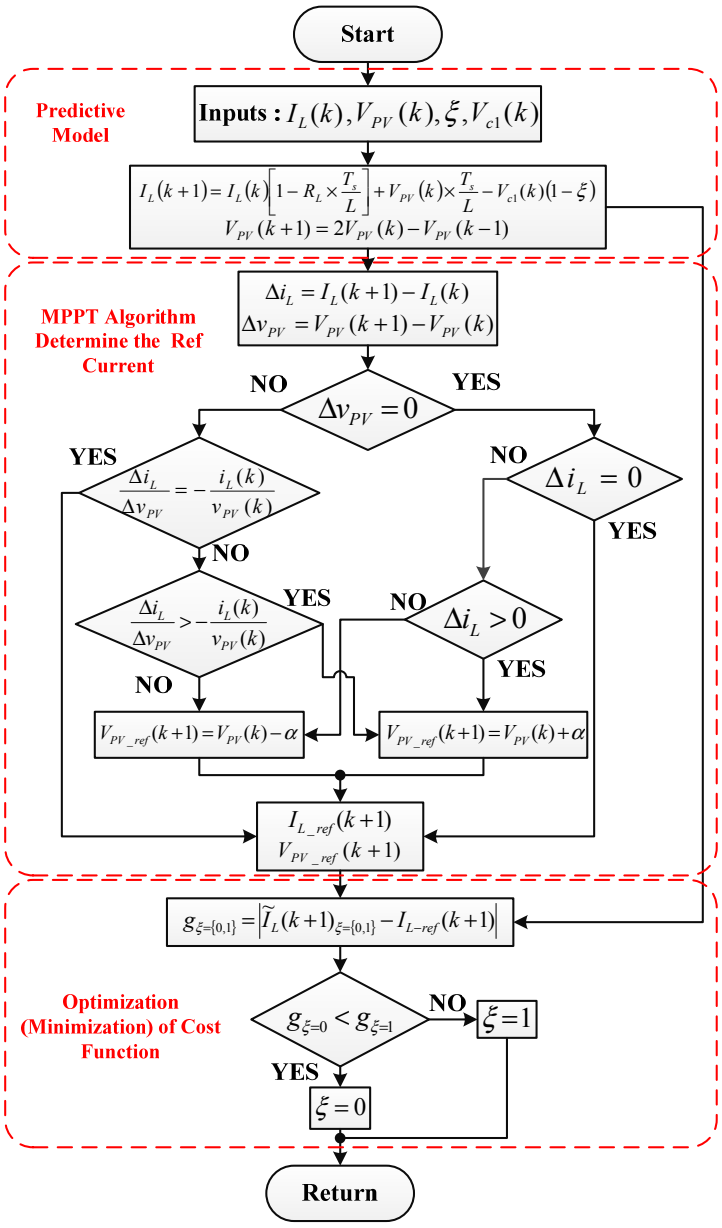

Figure 33: Maximum power point tracking by MPC

$$V_{PV}(K+1) = V_{PV}(K) + [I_{PV}(K) - I_L(K)] \times \frac{T_s}{C} \qquad (60)$$

and when the switch is turned OFF ($\xi = 1$):

$$I_L(K+1) = I_L(K)\left[1 - R_L \times \frac{T_s}{L}\right] + V_{PV}(K) \times \frac{T_s}{L} - V_{c1}(K) \quad (61)$$

$$V_{PV}(K+1) = V_{PV}(K) + [I_{PV}(K) - I_L(K)] \times \frac{T_s}{C} \quad (62)$$

It can be seen from (59)-(62) that there are four inputs I_L, V_{pv}, I_{pv}, and V_{C1}. In order to reduce the number of required sensors we can rearrange these equations by decreasing the number of input variables. Therefore (60), (61), and (62) can be represented as following

$$V_{PV}(K+1) = 2V_{PV}(K) - V_{PV}(K-1) \quad (63)$$

$$I_L(K+1) = I_L(K) \quad (64)$$

The derived equations can be expressed in matrix form by (65) and (66) when the switch is ON and OFF ($\xi = \{0,1\}$) respectively

$$\begin{bmatrix} I_L(K+1) \\ V_{PV}(K+1) \end{bmatrix} = \begin{bmatrix} 1 - R_L \times \frac{T_s}{L} & \frac{T_s}{L} \\ 0 & 2 \end{bmatrix} \times \begin{bmatrix} I_L(K) \\ V_{PV}(K) \end{bmatrix} + \begin{bmatrix} 0 \\ -1 \end{bmatrix} \times V_{PV}(K-1) \quad (65)$$

$$\begin{bmatrix} I_L(K+1) \\ V_{PV}(K+1) \end{bmatrix} = \begin{bmatrix} 1 & 0 \\ 0 & 2 \end{bmatrix} \times \begin{bmatrix} I_L(K) \\ V_{PV}(K) \end{bmatrix} + \begin{bmatrix} 0 \\ -1 \end{bmatrix} \times V_{PV}(K-1) \quad (66)$$

The detail of proposed maximum power point tracking methodology using model predictive control is illustrated in Figure 33. The present switching state (ζ) is added as an input to the algorithm to determine the inductor current ($I_L(k+1)$) if the switch is ON or OFF and then using this value for determination of reference current/voltage to be tracked. The MPPT algorithm is based on the fact that the slope of the PV array power curve is zero at the predicted MPP, positive on the left and negative on the right of the

predicted MPP. Therefore the voltage and current at MPP can be determined by comparing the predicted incremental and instantaneous conductance as illustrated in Figure 33, the increment of the PV system voltage at each sampling time is presented by (α) in Figure 33. This calculated current is the reference current for the cost function subject to minimization. The cost function subject minimization is given by

$$g_{\xi=\{0,1\}} = \left|\widetilde{I}_L(k+1)_{\xi=\{0,1\}} - I_{L-ref}(k+1)\right| \qquad (67)$$

The final switching state is the state that minimizes (67); the complete procedure of the controller is summarized in Figure 33.

4.4 Results and discussion

In this section the model predictive control for MPPT is compared to the commonly used incremental conductance method with fixed variation of the duty cycle of the converter. Directly comparing two control algorithms is challenging to create a fair comparison. However in this section, not only the proposed predictive controller technique has faster dynamic response to step change in solar irradiance level, but also it has smaller steady-state ripple power. The detail performance comparison of both controllers is presented in the following section.

The I-V and P-V characteristic of the PV systems for different irradiance levels are illustrated in Figure 34. The SUNPOWER SPR-305-WHT is used as PV module type. The PV module characteristics under standard test condition (STC: solar irradiance = 1 kW/m^2, cell temperature = 25 deg. C) are:

- Open circuit voltage (*Voc*) = 64.2 V
- Short-circuit current (*Isc*) = 5.96 A

- Voltage at MPP (V_{MP}) = 54.7 V
- Current at MPP (I_{MP}) = 5.58 A

The control algorithm is implemented in Matlab/Simulink; the sampling time T_S is 10 μs. The detail descriptive results are illustrated in Figure 35-Figure 37. By considering continuous operation of the PV systems over the year, the extra amount of energy captured by the proposed MPPT technique is significant, particularly under the cloudy sky condition such as solar irradiance level of Figure 6. Combination of the proposed MPPT technique with high efficient inverters can enhance the total efficiency of grid connected PV systems.

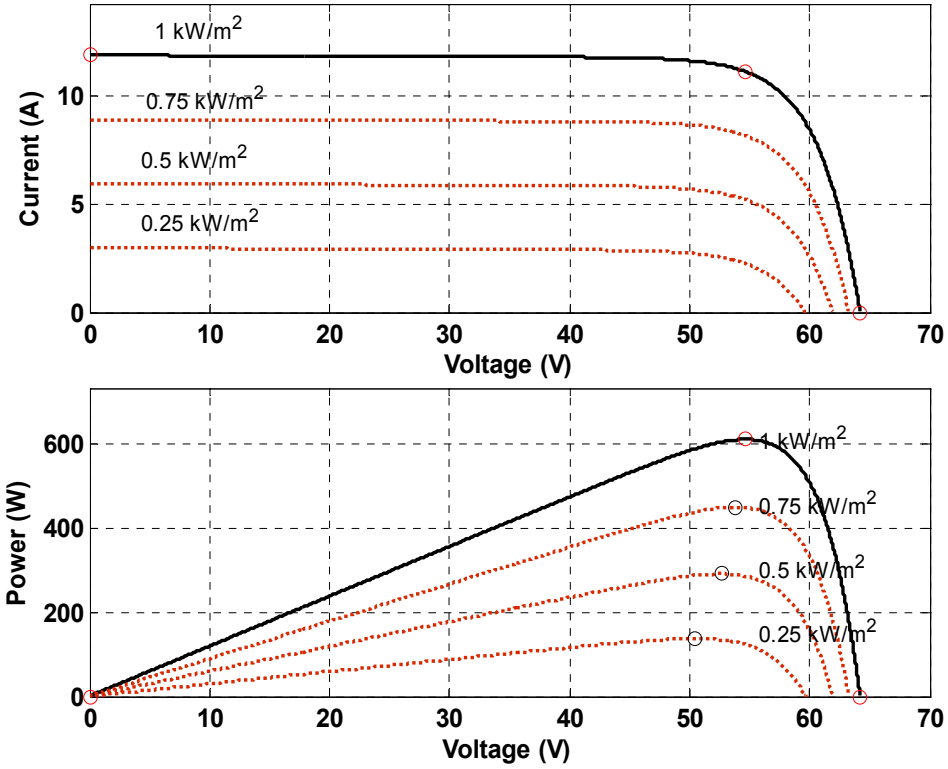

Figure 34: I-V and P-V characteristics of the array.

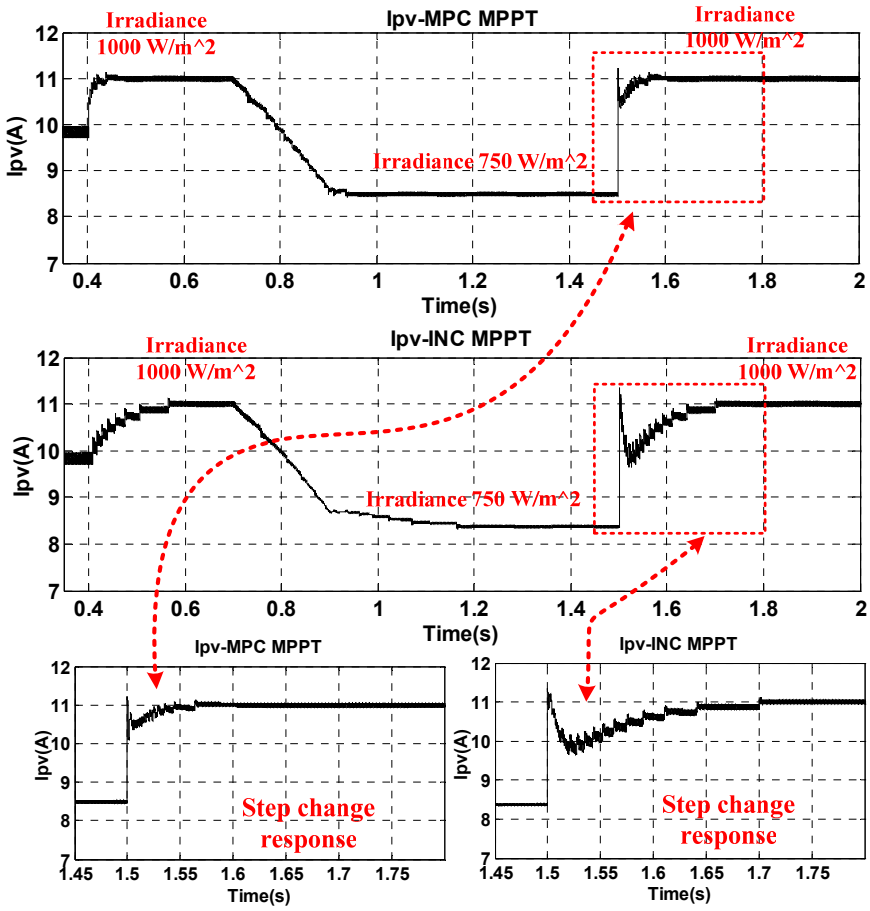

Figure 35: PV current Simulation results comparison of the MPC versus INC method under irradiance level change.

Figure 35 and Figure 36 illustrate the simulation results of the proposed MPC and INC method. The MPPT is enabled at t=0.4 s, the system is tested under three irradiance levels changes. The irradiance level of the case study is illustrated in Figure 37. The irradiance was initially 1000 W/m^2 until time 0.7 s, then the irradiance decreases gradually at time 0.7 s from 1000 W/m^2 to 750 W/m^2, and finally there is a step change

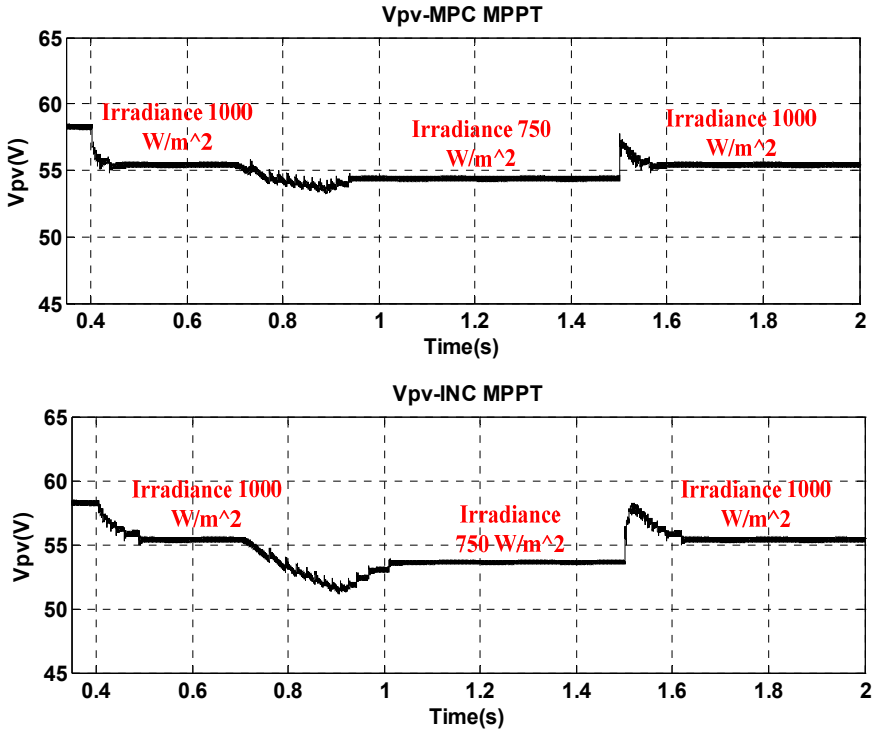

Figure 36: PV voltage simulation results comparison of the MPC versus INC method under irradiance level change.

in irradiance level at time 1.5 s from 750 W/m^2 to 1000 W/m^2. As shown in Figure 35 the dynamic performance of the MPC method is better than the conventional INC method. More specifically by applying a step change in the irradiance level from 750 W/m^2 to 1000 W/m^2 at time 1.5 s, when using the proposed MPC method the MPP is achieved 0.05 s after the step change. Conversely it is about 0.15 s for conventional INC method, which shows the proposed MPPT technique by MPC is much faster and more efficient than the conventional INC method. The PV power of MPC and INC method are presented in Figure 37, it demonstrate that for approximately similar steady state power value the convergence time to MPP of the proposed MPC method is much smaller comparing to the conventional INC method.

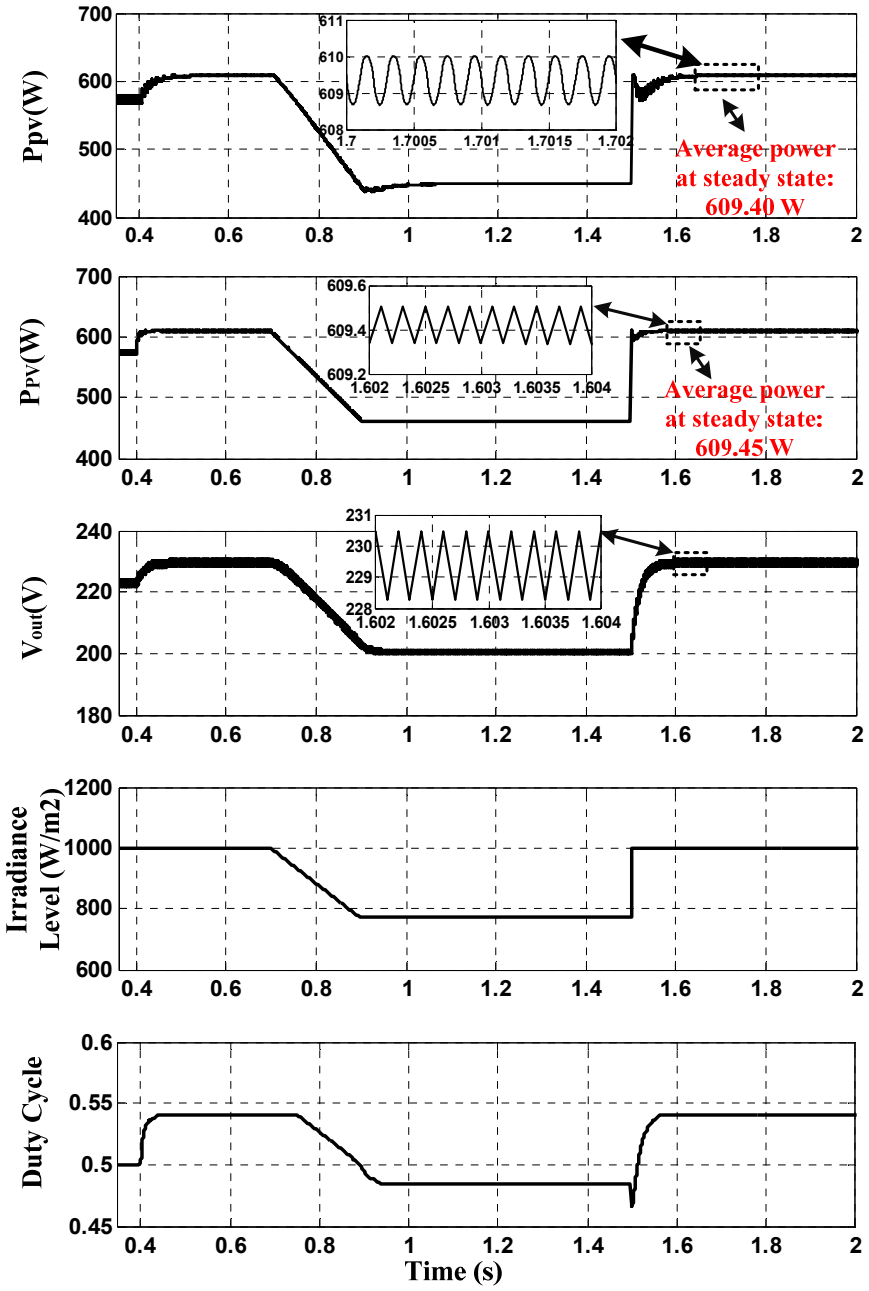

Figure 37: (From top to bottom) PV power by INC-MPPT, PV power, output voltage of the converter, irradiance level, and duty cycle of the converter switch by MPC-MPPT.

Agilent E4360A solar array simulator (SAS), Matlab/Simulink, and dSpace DS1103 are used for the experimental results. The control algorithm implemented in Matlab/Simulink and applied to the hardware prototype by using dSpace DS1103 platform. The experimental prototype is illustrated in Figure 38. GeneSiC Semiconductor GA35XCP12-247 used as a switch for the experimental setup. The capacitor and inductor of 470 µF and 1 mH are used respectively. The experimental implementation of the MPC-MPPT and INC-MPPT are illustrated in Figure 39-Figure 41and Figure 42-Figure 44 respectively to validate the simulation results. As it is shown, they confirm the simulation results.

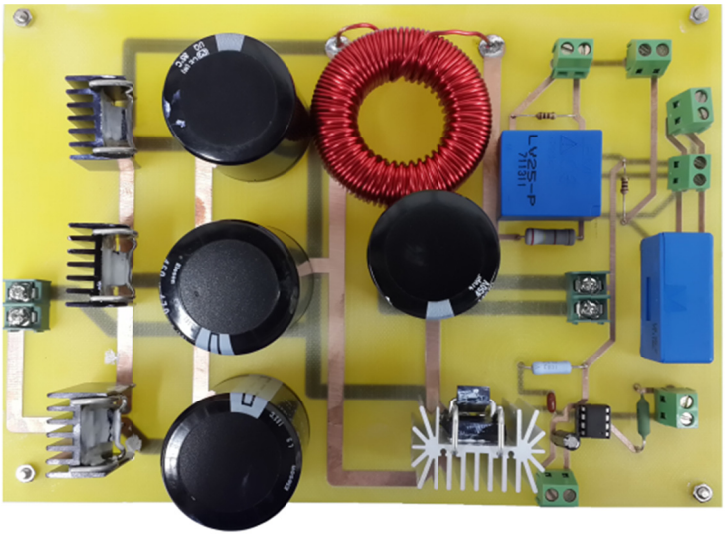

Figure 38: Experimental Setup.

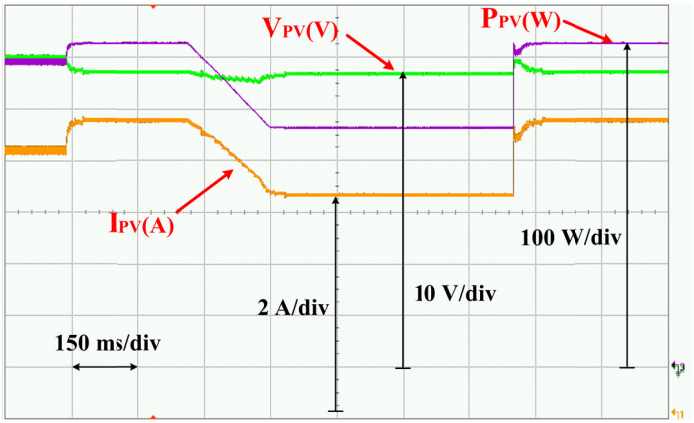

Figure 39: PV current, voltage, and power of MPC-MPPT.

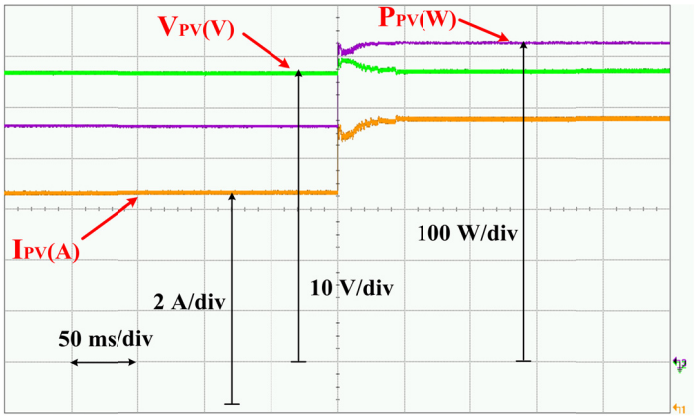

Figure 40: Zoomed in plot of PV current, voltage, and power by proposed MPC-MPPT when the step change in irradiance level at time 1.5 s occur.

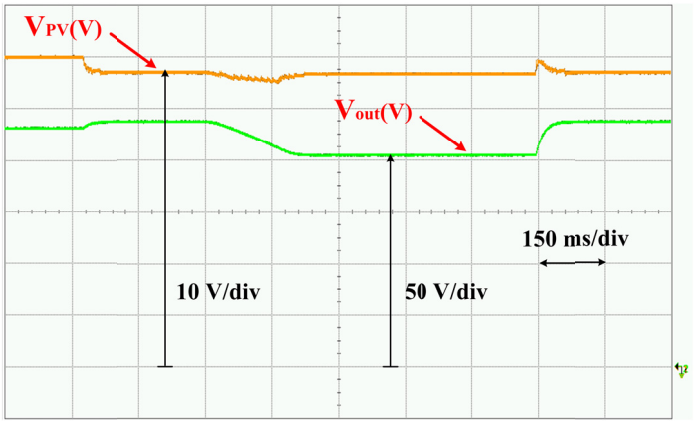

Figure 41: Output to input voltage ratio using MPC-MPPT.

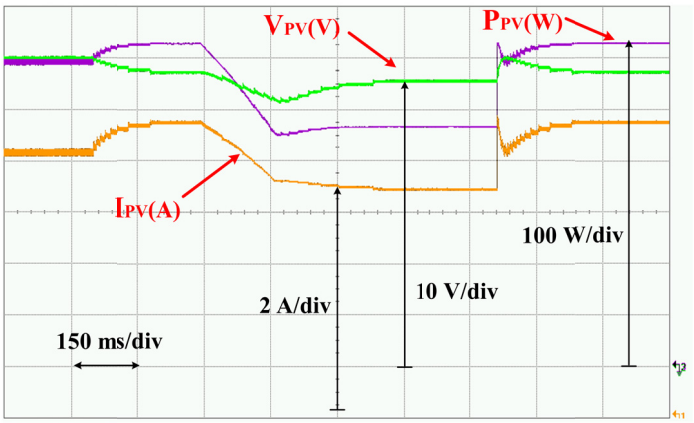

Figure 42: PV current, voltage, and power of INC-MPPT.

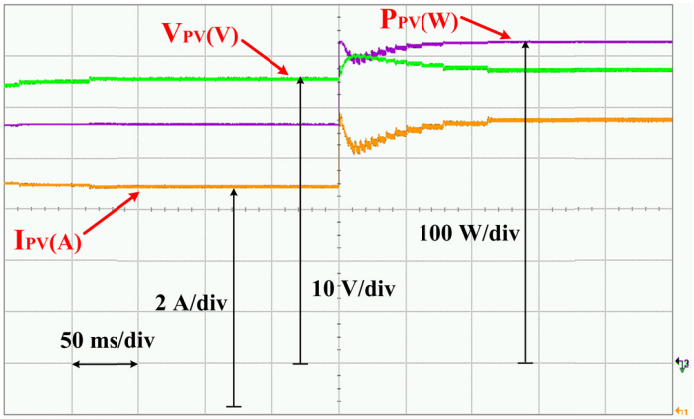

Figure 43: Zoomed in plot of PV current, voltage, and power by proposed INC-MPPT when the step change in irradiance level at time 1.5 s occur.

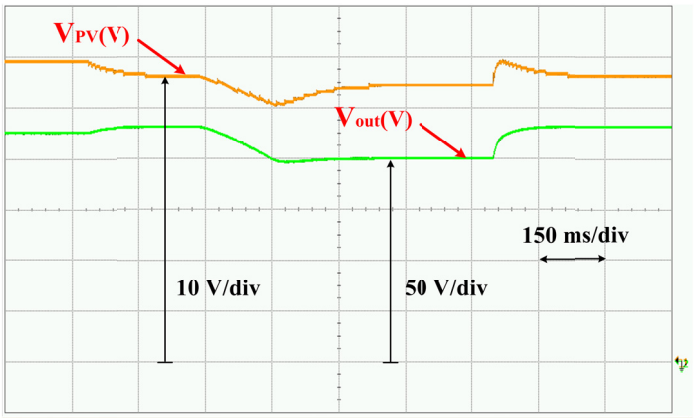

Figure 44: Output to input voltage ratio using INC-MPPT.

4.5 Efficiency analysis

The output power of the Agilent E4360A solar array simulator (converter input power) and the converter output power for solar irradiance levels of 100 W/m^2 to 1000 W/m^2 are measured using YOKOGAWA WT1600 digital power meter. The expected power from the solar array simulator at maximum power point is determined using its P-V characteristics curve; these P-V curves for four irradiance levels are illustrated in Figure 34. By using these information, the control effectiveness and converter efficiency of the proposed MPC-MPPT procedure is investigate for solar irradiance levels of 100 W/m^2 to 1000 W/m^2, the results are illustrated in Figure 45. The MPPT control effectiveness is calculated by dividing the measured output power of the solar array simulator by the expected power at MPP from solar array simulator at each solar irradiance level. The converter efficiency is calculated by dividing the measured output power of the converter by the measured output power of the solar array simulator. The results demonstrate that the true maximum power point has been tracked with high efficacy, the worst case scenarios are for the solar irradiance levels of less than 400 W/m^2 which have control effectiveness of 93%-94%. The output power level of solar array simulator and converter at the corresponding solar irradiance level are also plotted in Figure 45.

Similarly, the efficiency and control effectiveness analysis are done for INC-MPPT method, Figure 46. By comparing the effectiveness of MPC-MPPT to INC-MPPT, it can be observed that the proposed method based on predictive controller is

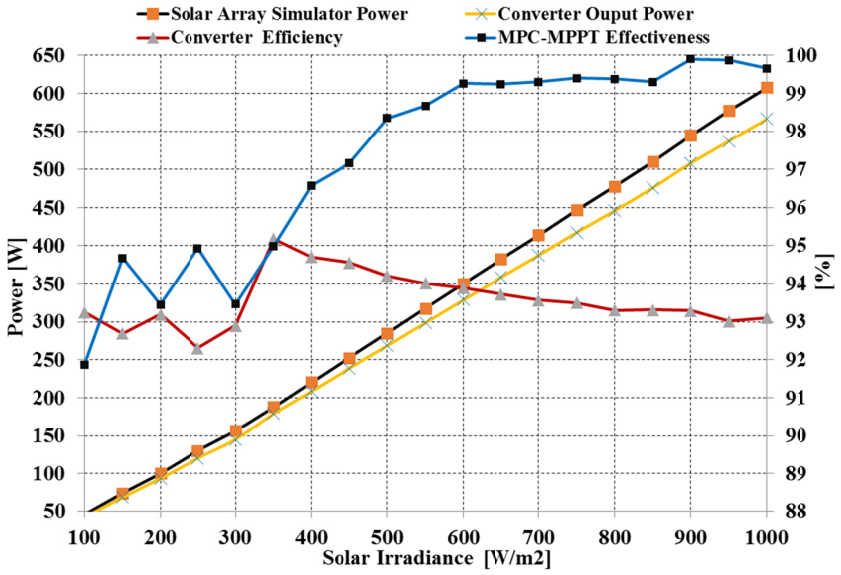

Figure 45: MPC-MPPT control effectiveness, converter efficiency, solar array simulator power, and converter output power for solar irradiance of 100 W/m2 to 1000 W/m2.

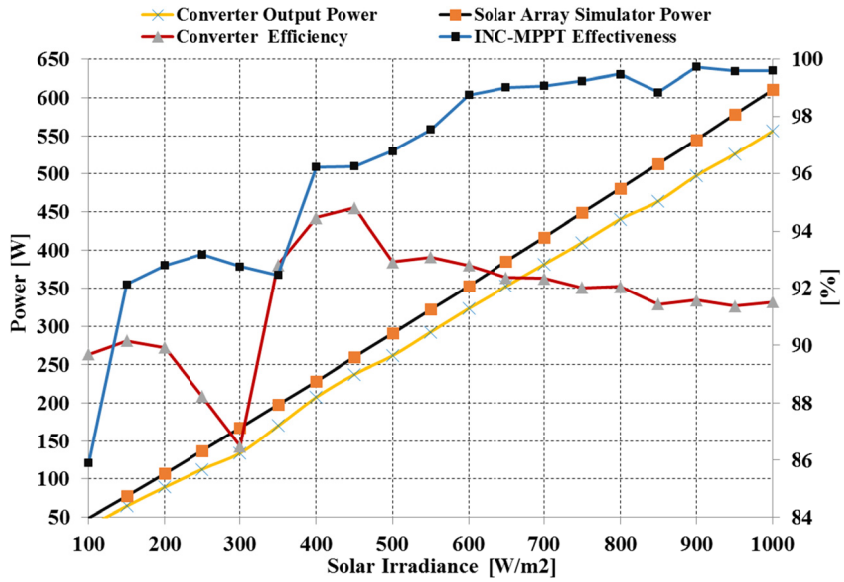

Figure 46: INC-MPPT control effectiveness, converter efficiency, solar array simulator power, and converter output power for solar irradiance of 100 W/m2 to 1000 W/m2.

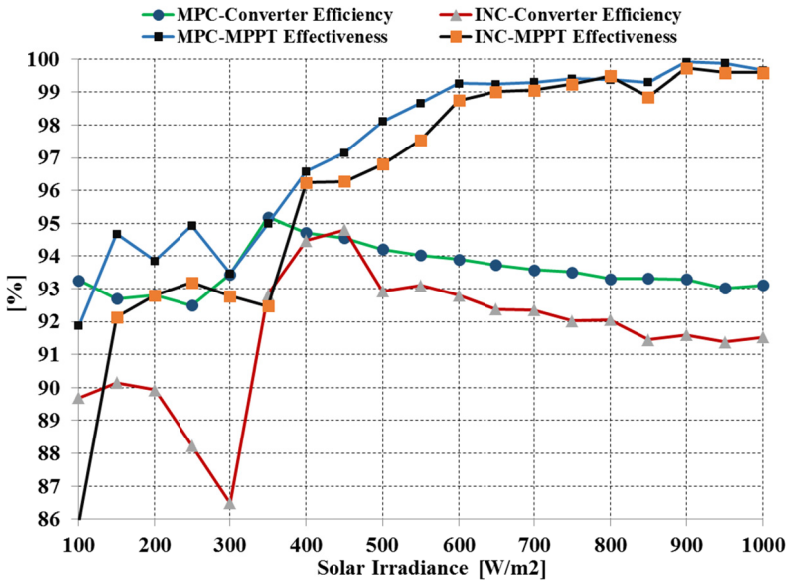

Figure 47: Comparison of INC and MPC control effectiveness and converter efficiency for solar irradiance levels of 100 W/m2 to 1000 W/m2.

more effective especially at low solar irradiance levels, and the tracked power is closer to true maximum power point as illustrated in Figure 47. The solar array simulator side voltage and current ripple at MPP is illustrated in Figure 48, this demonstrates that the oscillation around the maximum power point is very small; as a result high effective MPPT is achieved. Also, the converter output voltage and current ripple for solar irradiance levels of 100 W/m^2 to 1000 W/m^2 are illustrated in Figure 49, the results demonstrate that the ripple are small. Table 6 presents the comparison summary MPC-MPPT and INC-MPPT, as it is demonstrated the proposed method has smaller maximum percentage of overshoot/undershoot, smaller power oscillation around maximum power point, with faster convergence time, and higher control effectiveness.

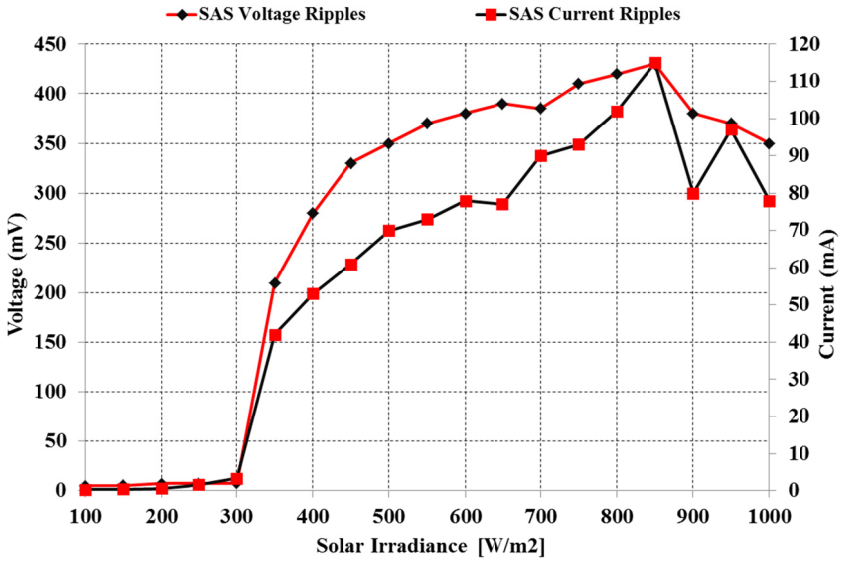

Figure 48: Solar array simulator (SAS) voltage and current ripples for solar irradiance of 100 W/m2 to 1000 W/m2.

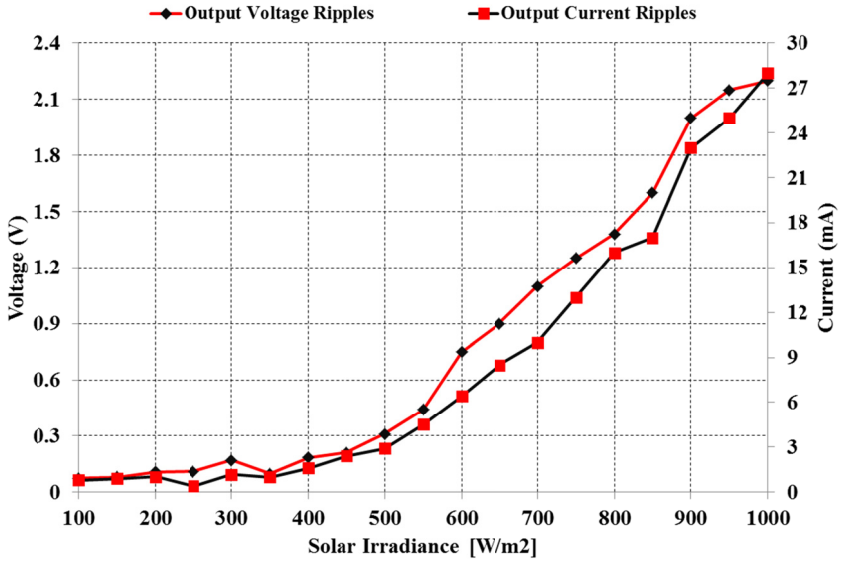

Figure 49: Output voltage and current ripples for solar irradiance of 100 W/m2 to 1000 W/m2.

Table 6. INC-MPPT versus MPC-MPPT comparison of step change dynamic performance (750 W/m2 to 1000 W/m2) and steady state perfomance (1000 W/m2)

Characteristics	INC-MPPT	MPC-MPPT
% of voltage ripple	0.79%	0.63%
% of current ripple	1.06%	0.72%
Steady state power	609.40 W	609.45 W
PV current overshoot/undershoot	11.07%	9.7%
PV voltage overshoot/undershoot	5.51%	4.78%
Convergence time	0.15 s	0.05 s
Control effectiveness	99.60%	99.65%

4.6 Conclusion

This paper presents a high effective MPPT technique based on MPC by predicting the error at next sampling time before applying the switching signal. The proposed predictive MPPT technique is compared to commonly used INC method to show the benefits and improvements in the speed and efficiency of the MPPT. By predicting the future behavior of the PV system, the proposed MPC method in an elegant, embedded controller that has faster response than the conventional INC technique under rapidly changing atmospheric condition without requiring expensive sensing and communication equipment and networks to directly measure the changing solar radiation. The dSpace DS1103 is used for implementing the control technique experimentally. The effectiveness and efficiency of the proposed MPPT controller at different solar irradiance levels are presented.

5. MAXIMUM POWER POINT TRACKING OF GRID-TIED PHOTOVOLTAIC SYSTEMS*

This section presents a maximum power point tracking (MPPT) technique using model predictive control (MPC) for single phase grid connected photovoltaic (PV) systems. The technique exhibits fast convergence, which is ideal for rapidly varying environmental conditions such as changing temperature or insolation or changes in morphology of the PV array itself. The maximum power of PV system is tracked by a high gain DC-DC converter and feeds to the grid through a seven-level inverter. Considering the stochastic behavior of the solar energy resources and the low conversion efficiency of PV cells, operation at the maximum possible power point is necessary to make the system economical.

The main contribution of this section is the development of incremental conductance (INC) method using two-step model predictive control. The multilevel inverter controller is based on fixed step current predictive control with small ripples and low total harmonic distortion (THD). The proposed MPC method for the grid connected PV system speeds up the control loop by sampling and predicting the error two steps before the switching signal is applied. As a result, more energy will be captured from the PV system and injected into grid particularly during partially cloudy sky. A comparison of the developed MPPT technique to the conventional INC method shows significant

*Part of this section is reprinted with permission from M. B. Shadmand, M. Mosa, R. S. Balog, and H. Abu Rub, "Maximum Power Point Tracking of Grid Connected Photovoltaic System Employing Model Predictive Control," Applied Power Electronics Conference & Exposition (APEC), March, 2015, © 2015 IEEE.

improvement in dynamic performance of the PV system. Implementation of the proposed predictive control is presented using the dSPACE DS1103.

5.1 Description of complete system

The PV array can feed power to the grid through a DC/DC converter boosting the output voltage and a grid connected inverter [81, 113-119]. The main contribution of this section is the development of the INC method using a two-step model predictive control for a multilevel boost DC-DC converter. The boost converter output power is fed to the ac grid through a seven level inverter controlled by model based current predictive method. By predicting the future behavior of the PV system, the proposed MPC method in an elegant, embedded controller that has faster response than the conventional INC technique under rapidly changing atmospheric conditions without requiring expensive sensing and communications equipment and networks to directly measure the changing solar insolation.

Figure 50 illustrates the general schematic of the complete grid connected photovoltaic system controlled by predictive methods. As it is shown, the system contains a multilevel DC-DC boost converter to extract the maximum power from the PV arrays and to feed it into the grid through a seven level inverter. Since only one switch is used in the selected multilevel boost DC-DC converter topology, the control procedure is simpler than other topologies such as the switched capacitor converter with a boost stage [112]. The output voltage of the DC-DC converter is proportional to the number of levels, which can be increased by adding two additional capacitors and diodes.

The DC-DC converter in this section has three levels. At the dc-link stage of the system, if the average voltage across the capacitor C_1 is V_{dc}, then the average voltage across capacitors C_2 and C_3 together will be $2V_{dc}$. The detail mode of operation of this DC-DC converter with two levels is presented in [92], this concept can be extended for the three levels topology presented in this paper.

The seven level inverter topology used to feed power to the grid can be divided into two parts: multilevel module and H-bridge inverter. The multilevel module is cascaded with an H-Bridge inverter operating at low frequency to reduce the switching losses. Table 7 demonstrates the summary of the output voltage levels as a function of switching states. The state of the switches can be represented by 0 and 1, where state 0 means the switch is OFF, and state 1 means the switch is ON.

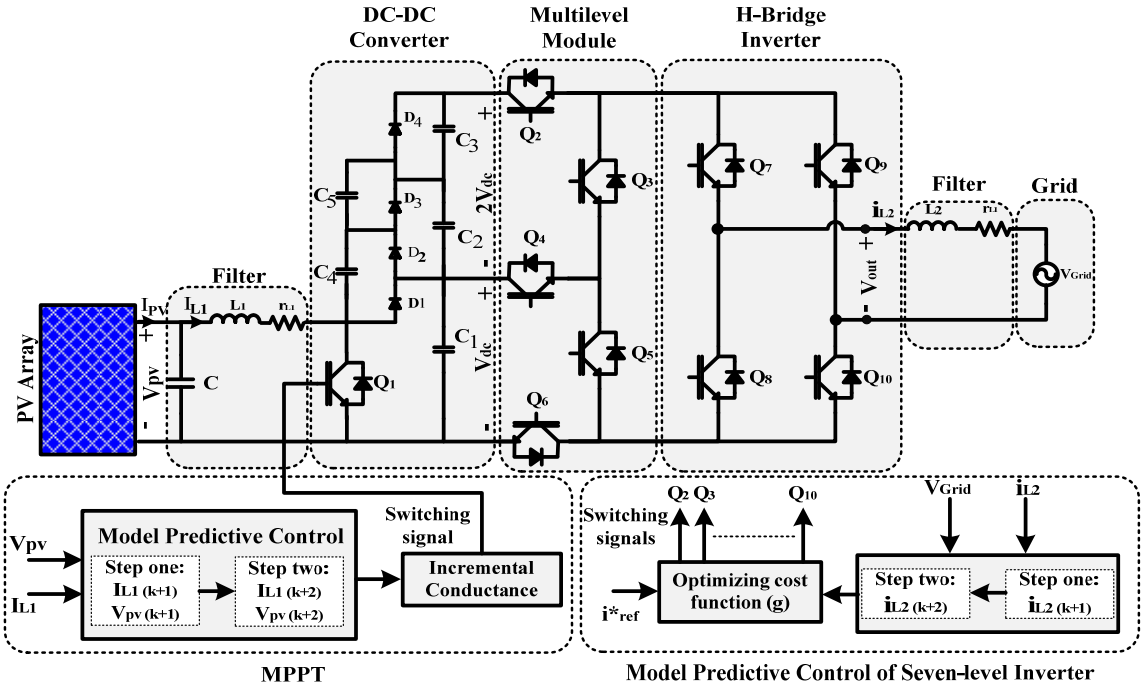

Figure 50: General schematic of the system and proposed model predictive control for grid connected PV system.

Table 7: Summary of output voltage levels as function of switching states.

Output Voltage (V_{out})	Multilevel Inverter Switches States								
	Q_2	Q_3	Q_4	Q_5	Q_6	Q_7	Q_8	Q_9	Q_{10}
$+3V_{dc}$	1	0	0	0	1	1	0	0	1
$+2V_{dc}$	1	0	1	1	0	1	0	0	1
$+V_{dc}$	0	1	1	0	1	1	0	0	1
0	0	1	0	1	0	1	0	0	1
$-V_{dc}$	0	1	1	0	1	0	1	1	0
$-2V_{dc}$	1	0	1	1	0	0	1	1	0
$-3V_{dc}$	1	0	0	0	1	0	1	1	0

5.2 Model predictive control of the system

5.2.1 Predictive maximum power point tracking

The discrete time model of the DC-DC converter is used to determine predicted control variables:

$$I_{L1}(K+n+1) = I_{L1}(K+n)\left[1 - r_{L1} \times \frac{T_s}{L_1}\right] + V_{PV}(K) \times \frac{T_s}{L_1} - (1-S) \times V_C(K+n) \qquad (68)$$

$$V_{PV}(K+n+1) = V_{PV}(K) + \left[I_{PV}(K+n) - I_{L1}(K+n)\right] \times \frac{T_s}{C} \qquad (69)$$

where n+1 is the number of steps in the future being predicted at the current K^{th} step; S is 1 when the switch is ON and 0 when the switch is OFF; and T_S is the sampling time. In this paper the control variables predicted two steps in horizon. Equations (68) and (69) have four inputs I_{L1}, V_{pv}, I_{pv}, and V_C. In order to reduce the number of sensors, these equations can be rearranged by decreasing the number of input variables. Thus (69) can be represented as

$$V_{PV}(K+2) = 2V_{PV}(K+1) - V_{PV}(K) \qquad (70)$$

In order to calculate the value of control variables at time K+2, the estimated value of the current of the inductor, L_1, and PV voltage at time K+1 are used. Thus at

sampling time K+2, four values for control variables are predicted and the optimum value will be selected as illustrated graphically in Figure 51. The derived equations can be expressed in matrix form by (71) and (72) when the switch is ON and OFF respectively

$$\begin{bmatrix} I_{L1}(K+2) \\ V_{PV}(K+2) \end{bmatrix} = \begin{bmatrix} 1-r_{L1}\times\frac{T_s}{L_1} & \frac{T_s}{L_1} \\ 0 & 2 \end{bmatrix} \times \begin{bmatrix} I_{L1}(K+1) \\ V_{PV}(K+1) \end{bmatrix} + \begin{bmatrix} 0 \\ -1 \end{bmatrix} \times V_{PV}(K) \qquad (71)$$

$$\begin{bmatrix} I_{L1}(K+2) \\ V_{PV}(K+2) \end{bmatrix} = \begin{bmatrix} 1 & 0 \\ 0 & 2 \end{bmatrix} \times \begin{bmatrix} I_{L1}(K+1) \\ V_{PV}(K+1) \end{bmatrix} + \begin{bmatrix} 0 \\ -1 \end{bmatrix} \times V_{PV}(K) \qquad (72)$$

The summary of the proposed MPPT algorithm is illustrated in Figure 52.

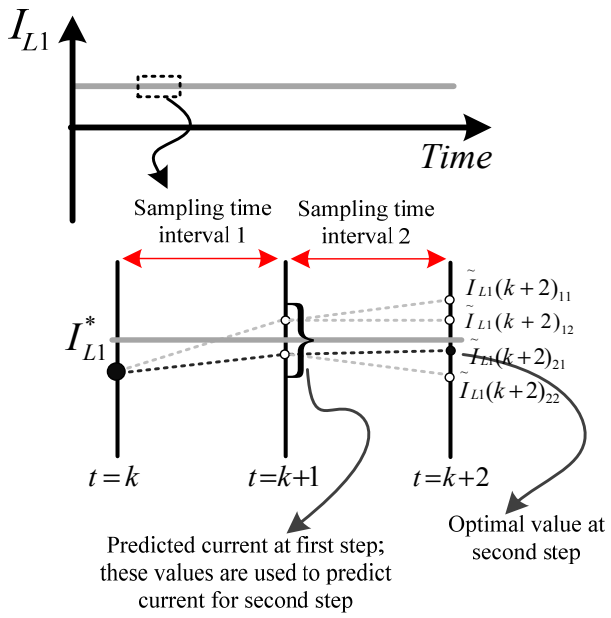

Figure 51: Prediction of PV array side current observation.

5.2.2 Predictive current control

The next step is the current predictive control of the multilevel inverter. The load current in continuous form can be determined using the following expression

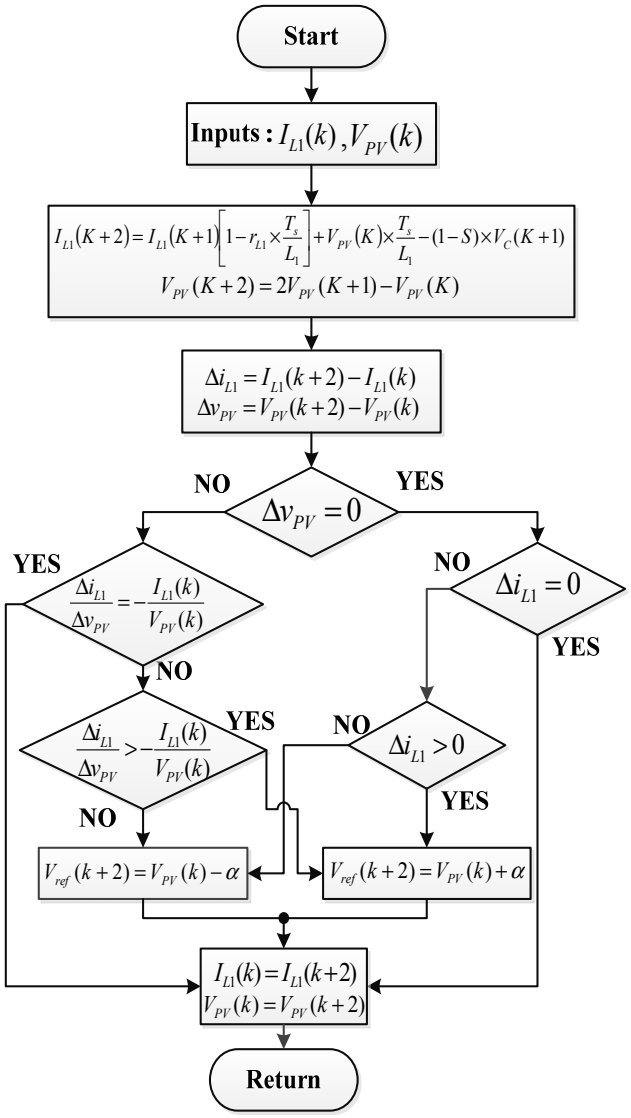

Figure 52: MPC maximum power point tracking procedure.

$$v_{out} = L_2 \frac{di_{L2}}{dt} + r_{L2} i_{L2} + v_{Grid} \tag{73}$$

By using the Euler forward method, the derivative in (73) can be approximately discretize as

$$L_2 \frac{di_{L2}}{dt} = L \frac{i_{L2}(K+1) - i_{L2}(K)}{T_s} \tag{74}$$

where T_s is the sampling period. Based on (73) and (74) the load side current can be predicted for n steps in horizon of time by using

$$i_{L2}(K+n)=\left[1-\frac{r_{L2}T_S}{L_2}\right]i_{L2}(K+n-1)+\frac{T_S}{L_2}(v_{out}(K+n-1)-v_{Grid}(K+n-1)) \qquad (75)$$

where $i_{L2}(K+n)$ is the predicted value of the grid side current at time $K+n$. In this section, i_{L2} is predicted two steps, $n=2$, into the horizon of time as illustrated in Figure 53. The reference current to be tracked and the cost function, g, is given by

$$i^*_{ref}(K+n)=\frac{2}{220\sqrt{2}}I_{PV}(K+n)\times V_{PV}(K+n) \qquad (76)$$

$$g=\left|i^*_{ref}(K+n)-i_{L2}(K+n)\right| \qquad (77)$$

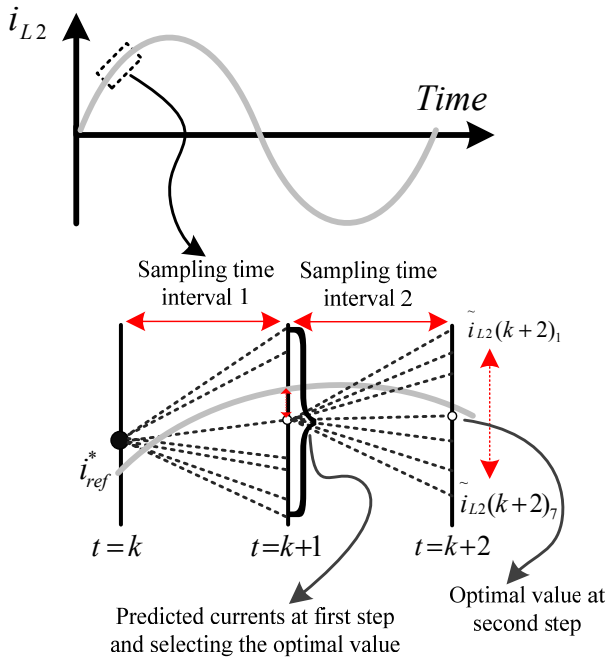

Figure 53: Prediction of grid side current observation.

The cost function needs to be minimized by evaluating all of the possible switching states presented in Table 7 for each step. The summary of optimal switching state selection procedure is illustrated in Figure 54.

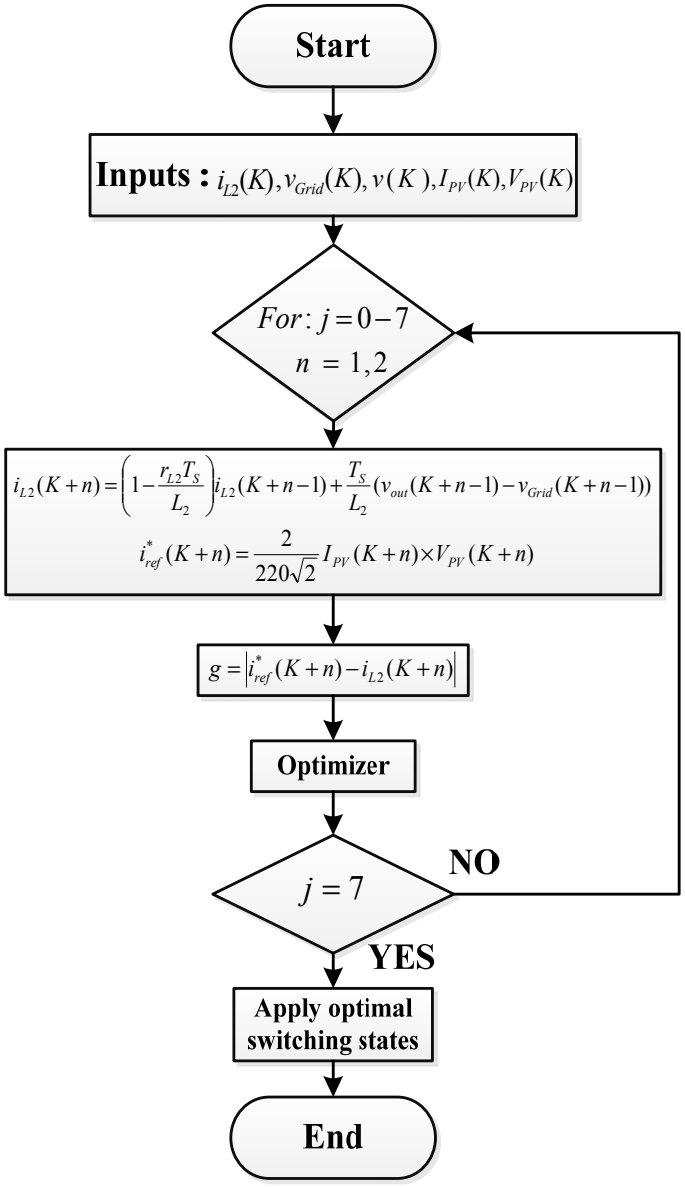

Figure 54: Model predictive control of the multilevel inverter.

5.3 Results and discussion

The proposed controller for the PV system is modeled in MATLAB-Simulink, and implemented in dSPACE DS1103. The I-V and P-V characteristics of the PV system for different irradiance levels are illustrated in Figure 55. The SUNPOWER SPR-305-WHT is used as PV module type. The PV module characteristics under standard test condition (STC: solar irradiance = 1 kW/m2, cell temperature = 25 deg. C) are:

- Open circuit voltage (Voc) = 64.2 V
- Short-circuit current (Isc) = 5.96 A
- Voltage at MPP (VMP) = 54.7 V
- Current at MPP (IMP) = 5.58 A

The sampling time, Ts, is 10 μs. In this paper the MPC for MPPT is compared to the commonly used incremental conductance method. Figure 56 illustrates the simulation results of the proposed MPC and INC method. As it is shown the MPPT is enabled at time 0.1 s, the irradiance decreases gradually at time 0.3 s from 1250 W/m2 to 1000 W/m2, and finally there is a step change in irradiance level at time 0.6 s from 1000 W/m2 to 1250 W/m2. By comparing Figure 56 (d) and (g) to (i) and (h) respectively, it can be noticed that the maximum power is tracked much faster when using two steps in MPC-MPPT than the conventional INC-MPPT method. The maximum power point when using two steps MPC-MPPT is achieved 1 ms after the step change in solar irradiance occurred. Conversely it is about 4 ms for conventional INC-MPPT. By considering continuous operation of the PV systems over the year, the extra amount of

energy captured by the proposed MPPT technique is significant, particularly under the cloudy sky condition such as solar irradiance level of Figure 6.

The simulation results of the grid side voltage and current, using MPC for the multilevel inverter, is illustrated in Figure 57. Figure 57 (a) and (c) show that the unity power factor is achieved and that the controller response to the step change in solar irradiance level at time 0.6 s is very fast.

The simulation results are validated experimentally by real-time implementation of the control strategy with dSPACE DS1103. Figure 58 (a) illustrates the PV side voltage and current, the step change response at time 0.6 s is zoomed in. Figure 58 (b) demonstrates the output voltage of the 7 level grid connected inverter. The grid side voltage and current are illustrated in Figure 58 (c) when the step change occurs in solar irradiance at time 0.6 s. As it is illustrated the injected current to the grid has fast dynamic response. The THD of the grid side current is about 1.8% which is within the IEEE-519 standard [120].

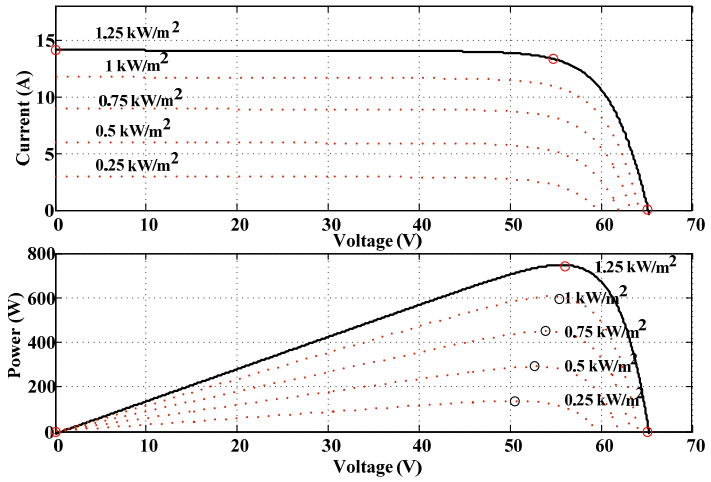

Figure 55: I-V and P-V characteristics of the PV array.

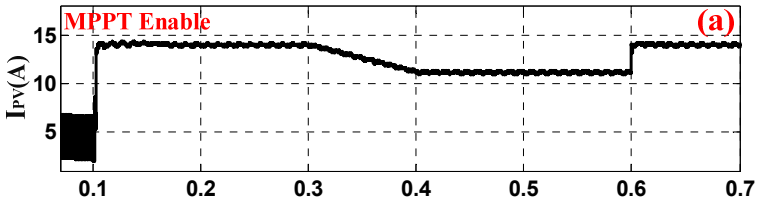

(a) PV current by proposed MPC-MPPT

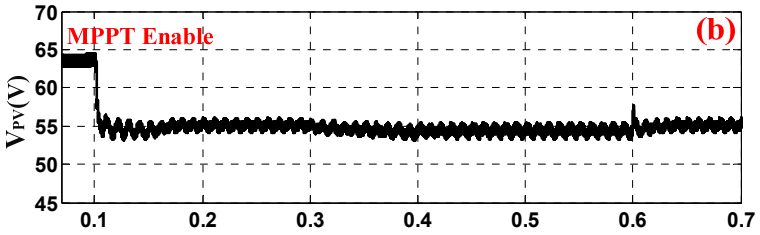

(b) PV voltage by proposed MPC-MPPT

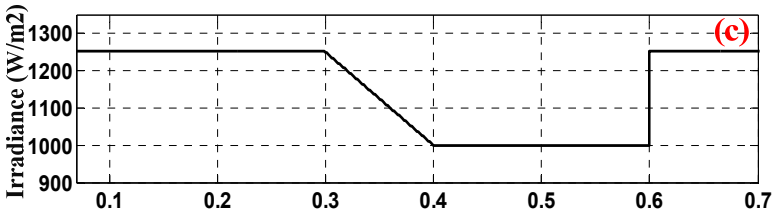

(c) Irradiance level

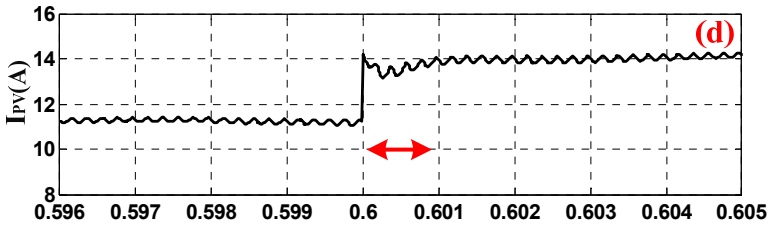

(d) Zoomed in plot of PV current by proposed MPC-MPPT when the step change in irradiance level at time 0.6 s occur

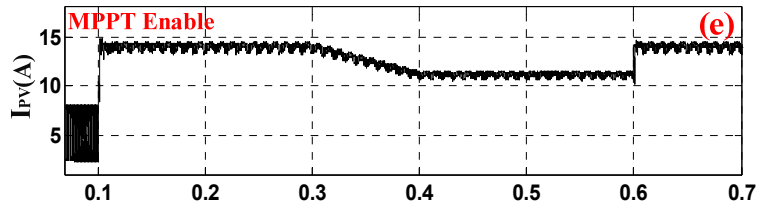

(e) PV current by INC-MPPT

Figure 56: Simulation results of MPPT

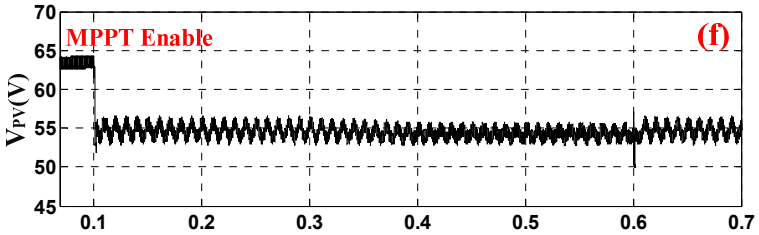

(f) PV voltage by INC-MPPT

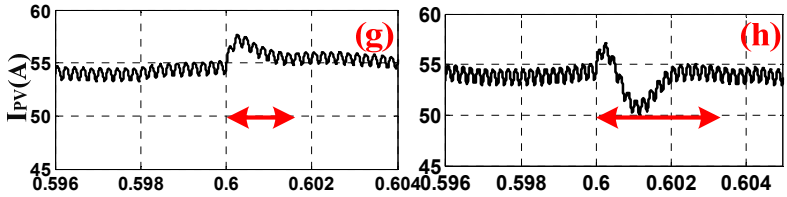

(g) Zoomed in plot of PV voltage by MPC-MPPT at time 0.6 s h) Zoomed in plot of PV voltage by INC-MPPT at time 0.6 s

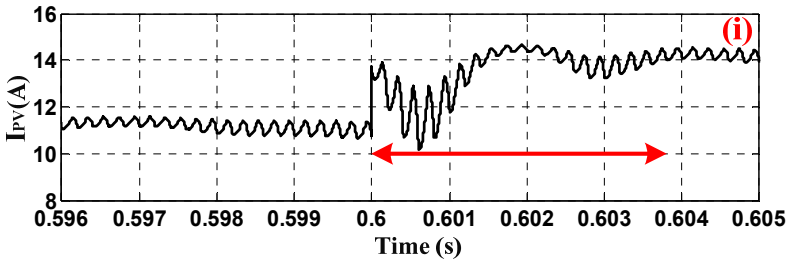

(h) Zoomed in plot of PV current by INC-MPPT at time 0.6 s

Figure 56: Continued

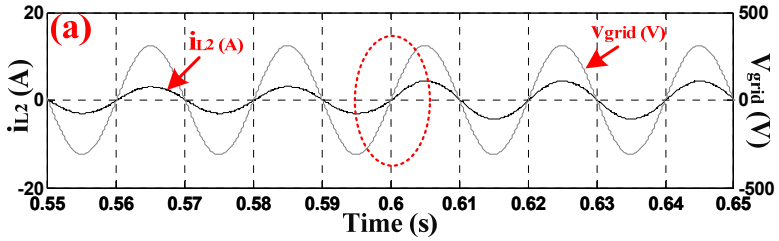

(a) Grid side voltage and injected current

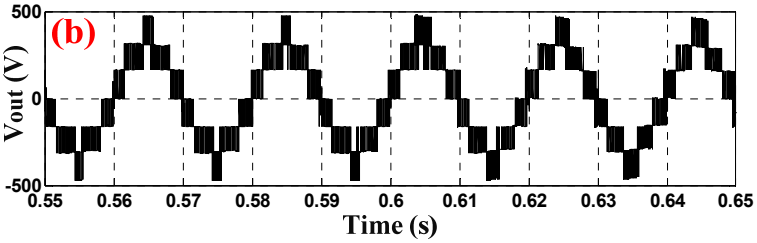

(b) Output voltage of the 7 level inverter

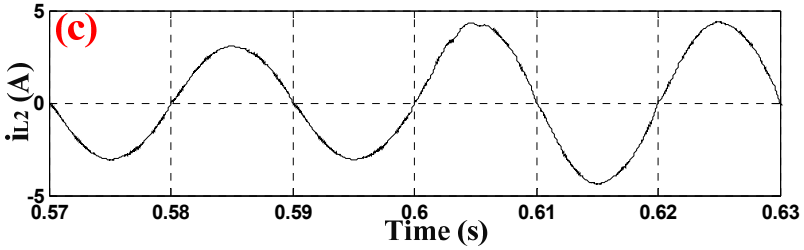

(c) Zoomed in plot of the injected current to the grid by using MPC-MPPT and predictive control of 7 level inverter at time 0.6 s

Figure 57: Simulation result of grid side

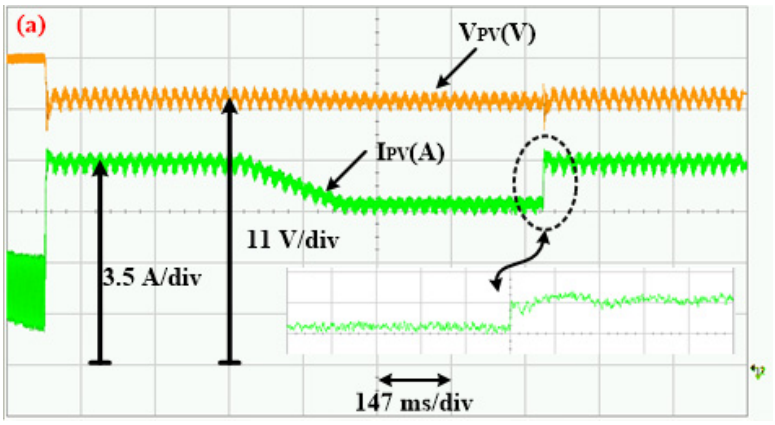

(a) PV voltage and current by proposed MPC-MPPT technique

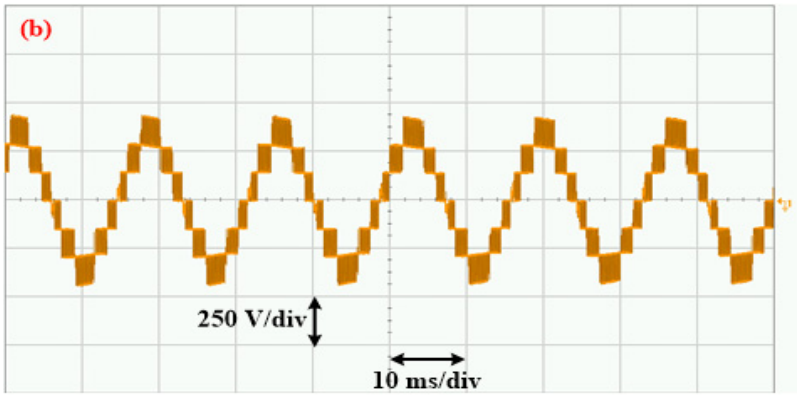

(b) Output voltage of the 7 level grid connected inverter

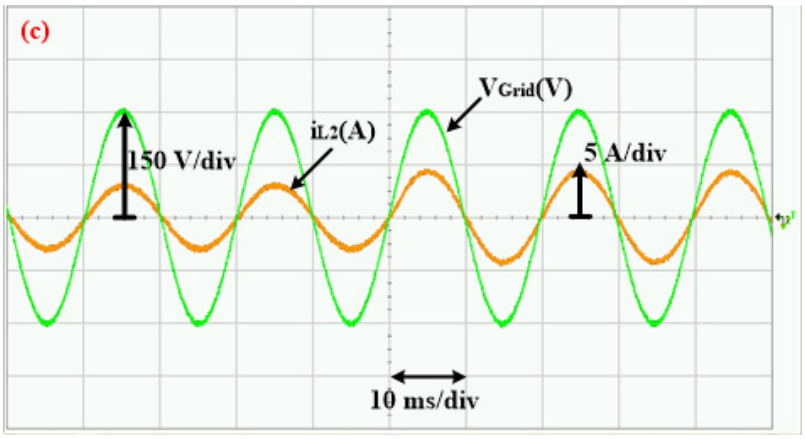

(c) Grid side voltage and injected current

Figure 58: Experimental validation of the control algorithm by real-time implementation

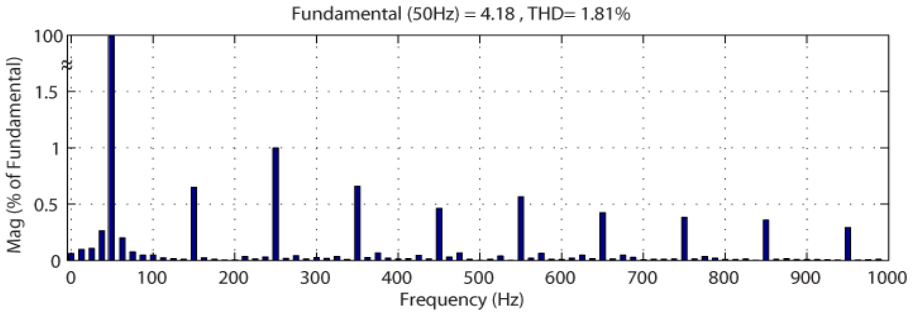

Figure 59: Spectrum analysis of grid side current (i_{L2})

5.4 Conclusion

This paper presents an improved MPPT technique using MPC for grid connected photovoltaic systems by predicting the error at the next sampling time before applying the switching signal. The proposed two steps predictive MPPT technique is compared to the commonly used INC method to show improvement in the dynamic performance and efficiency of the MPPT. The technique exhibits fast convergence, which is ideal for rapidly varying environmental conditions such as changing temperature or insolation or changes in morphology of the PV array itself. As a result, more energy will be captured from the PV system and injected into grid particularly during partially cloudy sky without requiring expensive sensing and communications equipment and networks to directly measure the changing solar insolation.

The maximized captured energy is fed to the grid though a 7 level inverter controlled by means of predictive control. High quality current, with low THD and in-phase with the grid voltage, is achieved and injected into the grid by using the proposed predictive controller. The dSPACE DS1103 is used for implementing the control technique experimentally.

6. MAXIMUM POWER POINT TRACKING USING MODEL PREDICTIVE CONTROL FOR FLYBACK CONVERTER*

This section presents a digital model predictive control technique to employ the MPPT for flyback converter for photovoltaic applications. The main contribution of this section is improvement of the Perturb and Observe (P&O) method through a fixed step predictive control under measured fast solar radiation variation. A characteristic of MPC is the use of system models for selecting optimal actuations, thus evaluating the effect of model parameter mismatch on control effectiveness is of interest. In this section the load model is eliminated from the proposed MPC formulation by using an observer based technique. The sensitivity analysis results indicate a more robust controller to uncertainty and disturbances in the resistive load.

Many standards are developed to ensure the safe and efficient power generation particularly under dynamic weather conditions. The performance of the proposed less sensitive model based MPPT is evaluated on the basis of European Efficiency Test, EN 50530 which evaluates the performance of PV systems under dynamic environment conditions. The proposed MPC-MPPT technique for a flyback converter is implemented using the dSPACE DS1007.

*Part of this section is reprinted with permission from M. B. Shadmand, R. S. Balog, and H. Abu Rub, "Model Predictive Control of PV Sources in a Smart DC Distribution System: Maximum Power Point Tracking and Droop Control," IEEE Transactions on Energy Conversion, November, 2014, © 2014 IEEE and M. B. Shadmand, R. S. Balog, and H. Abu Rub, "Maximum Power Point Tracking using Model Predictive Control of a Flyback Converter for Photovoltaic Applications," Power & Energy Conference at Illinois (PECI), February, 2014, © 2014 IEEE and M. Metry, M. B. Shadmand, R. S. Balog, and H. Abu Rub, "High Efficiency MPPT by Model Predictive Control Considering Load Disturbances for Photovoltaic Applications Under Dynamic Weather Condition," Industrial Electronics Conference (IECON), November, 2015, © 2015 IEEE.

6.1 Current oriented maximum power point tracking by model predictive control

P&O is a well-known technique with relatively good performance; however, P&O method cannot always converge to the true maximum power point. Also, the performance of P&O technique under dynamic weather condition may not be satisfactory. These weather conditions are very common in most part of the world such as the selected geographical location presented in Figure 6. A large variability in the instantaneous PV generation can be seen in Figure 6; in few seconds the power generated dropped almost in half due to transients of cloud coverage. The overall efficiency of PV systems depends on three main factors: the conversion efficiency of the PV module, the efficiency of the dc/dc conversion stage, and the control effectiveness of the MPPT technique. This section presents a highly efficient MPPT technique by using Model Predictive Control (MPC) with low sensitivity to load disturbances. The performance of the proposed controller is validated by considering the European Efficiency test, EN 50530.

A flyback converter is chosen as a DC/DC converter, Figure 60. P&O determines the reference current for the MPC which determines the next switching state as illustrated in Figure 61. This technique predicts the error of the next sampling time and based on optimization of the cost function *g,* illustrated in Figure 62, the switching state will be determined. The inputs to the predictive controller are the PV system current and voltage, and the reference current.

By using the discrete time set of equations, the behavior of control variable can be predicted at the next sampling time k+1. The proposed methodology is based on the

fact that the slope of the PV array power curve is zero at the predicted MPP, positive on the left and negative on the right of the predicted MPP. In continuous conduction mode, the discrete time set of equations of the flyback converter shown in Figure 60 is given by (78) and (79) when switch is "ON" and (80) and (81) when switch is "OFF" [121]:

$$i_{PV}(k+1) = \frac{T_S}{L_m} v_{PV}(k) + i_{PV}(k) \tag{78}$$

$$v_C(k+1) = \left(1 - \frac{T_S}{RC}\right) v_C(k) \tag{79}$$

$$i_{PV}(k+1) = i_{PV}(k) - \frac{T_S}{L_m n} v_C(k) \tag{80}$$

$$v_C(k+1) = \frac{T_S}{nC} i_{PV}(k) + \left(1 - \frac{T_S}{RC}\right) v_C(k) \tag{81}$$

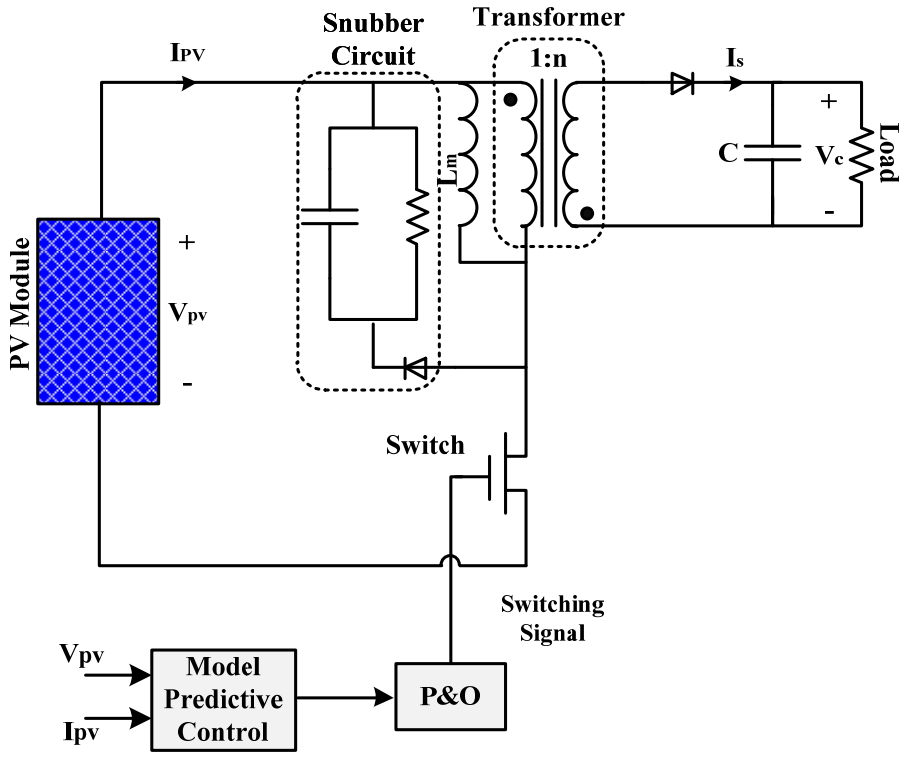

Figure 60: Flyback converter with snubber circuit.

The PV current $i_{pv}(k+1)$ is determined from (78), (80) and the reference current, i_{ref}, found using the procedure illustrated in Figure 61. The cost function for the MPC algorithm is

$$g_{S=0,1} = \left| i_{PV_{S=0,1}}(k+1) - i_{ref} \right| \qquad (82)$$

The switching state for the MPPT controller is determined by minimizing the cost function g using the procedure in Figure 62.

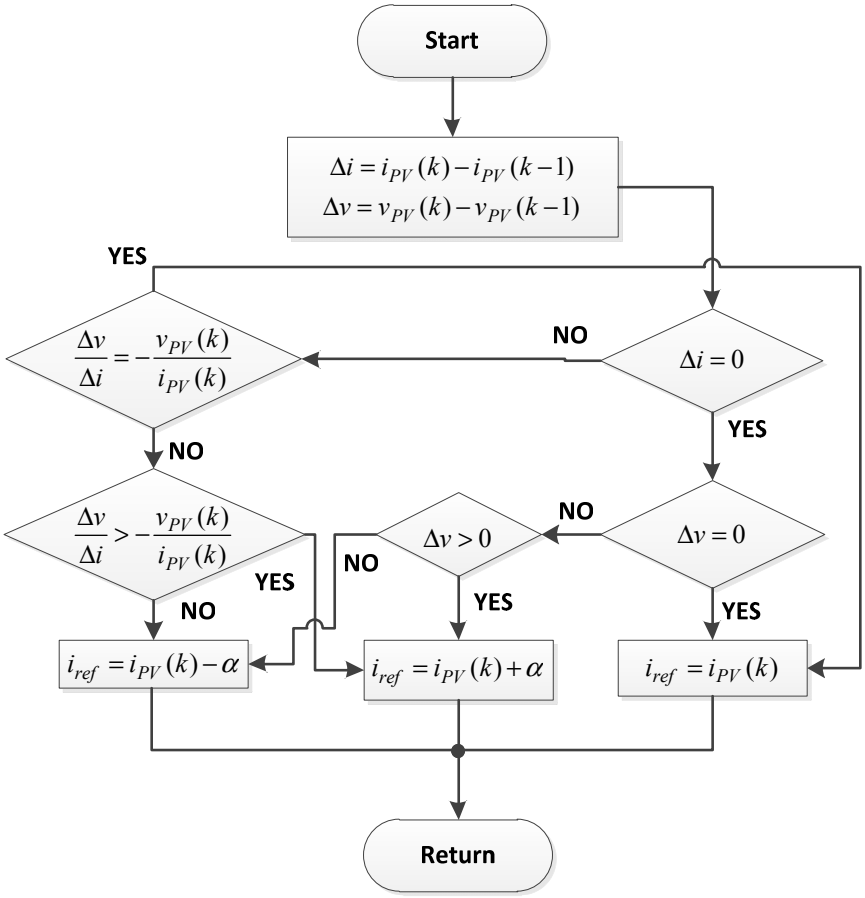

Figure 61: MPC procedure to determine reference current using P&O.

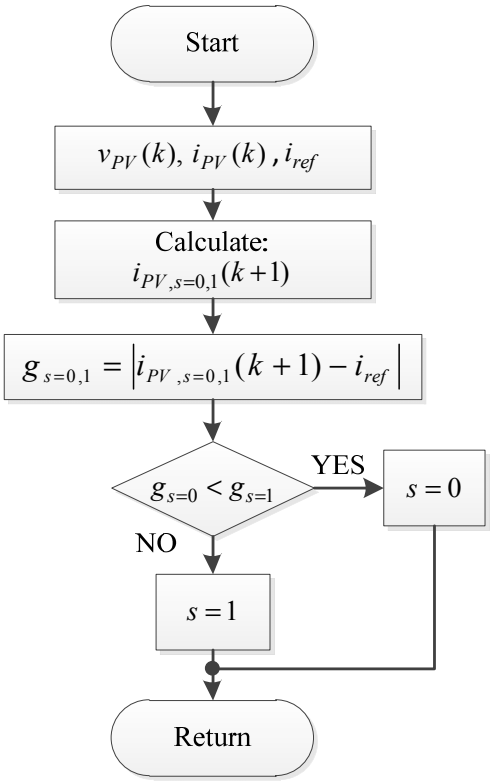

Figure 62: MPC-MPPT procedure.

However in this section we consider MPC-MPPT for one step in the horizon. Generalizing the concept, the discrete time equation can be extended to n-step in the horizon as following

$$i_{PV}(k+n+1) = i_{PV}(k+n) - S\frac{T_S}{L}v_{PV}(k) + (1-S)\frac{T_S}{Ln}v_C(k+n) \quad (83)$$

$$v_C(k+n+1) = S\left(1-\frac{T_S}{RC}\right)v_C(k) + (1-S)\frac{T_S}{Cn}i_{PV}(k+n) \quad (84)$$

where S is the switching state and T_s is the sampling time. By increasing the number of steps to two or three, the computation time will be increased but better control performance will be achieved.

The I-V and P-V characteristic of the PV systems used in this paper for different irradiance levels are illustrated in Figure 55. In this section the model predictive control for MPPT is compared to the commonly used perturb and observed method. The sampling time T_s is 10 μs. Figure 63 illustrate the simulation results of the proposed MPC and conventional P&O method. The system is tested under three irradiance level changes, the irradiance level is initially 750 W/m^2 then decreases gradually at time 0.7 s to 500 W/m^2, and finally there is a step change in irradiance level at time 1.5 s from 500 W/m^2 to 750 W/m^2. As illustrated in Figure 63 the dynamic performance of the MPC method is better than the conventional P&O method. More specifically by applying a step change in the irradiance at time 1.5 s, when using the proposed MPC method the MPP is tracked at time 1.52 s, conversely when using the P&O method the MPP is tracked at time 1.60 s. The detail descriptive plots are illustrated in Figure 63. Matlab/Simulink and dSPACE DS1103 is used for the experimental implementation.

Figure 64 and Figure 65 illustrate the implementation of the MPC-MPPT and Figure 66 demonstrates the implementation of conventional P&O-MPPT method. As it is shown, they confirm the simulation results.

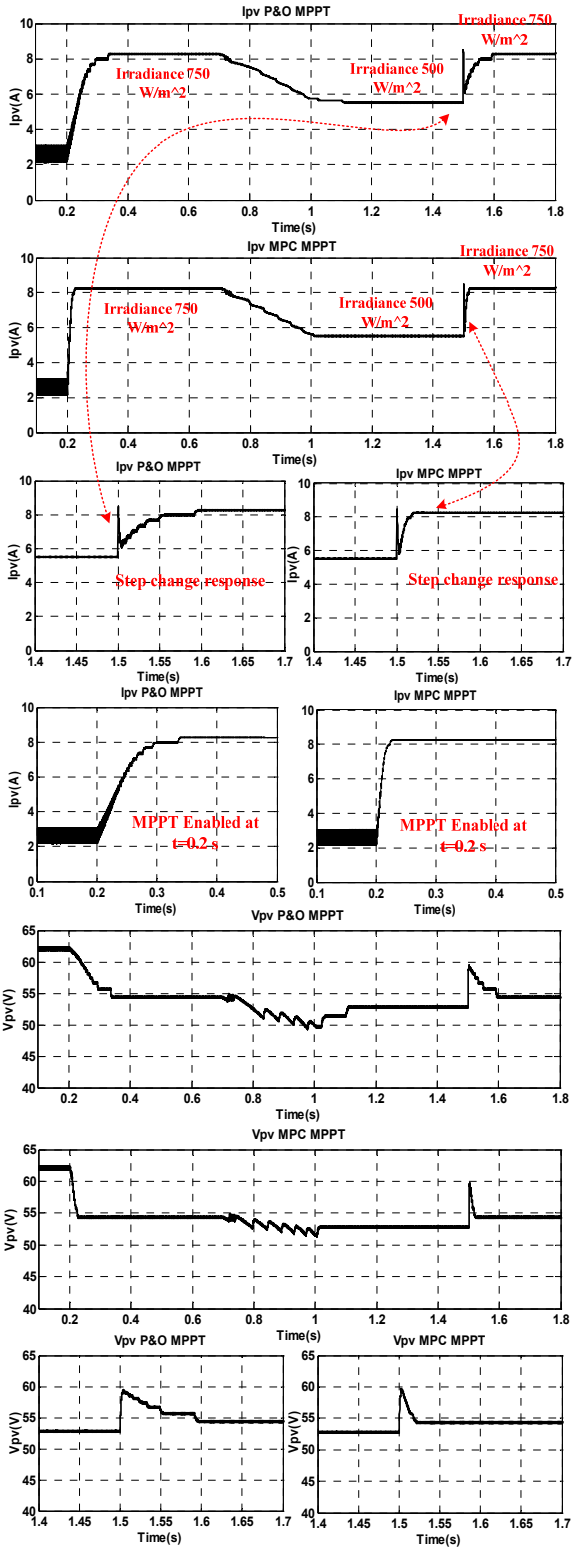

Figure 63: Comparison of proposed MPC-MPPT to conventional P&O-MPPT.

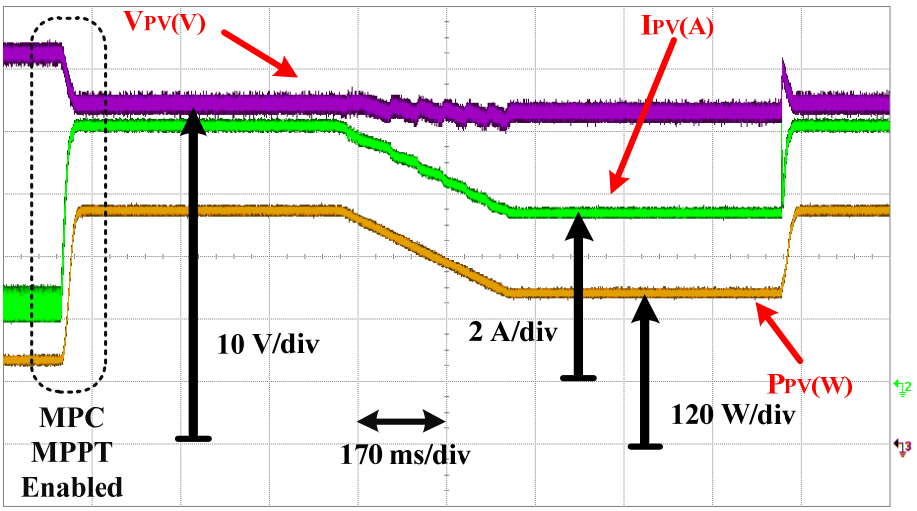

Figure 64: PV current, voltage, and power of MPC-MPPT.

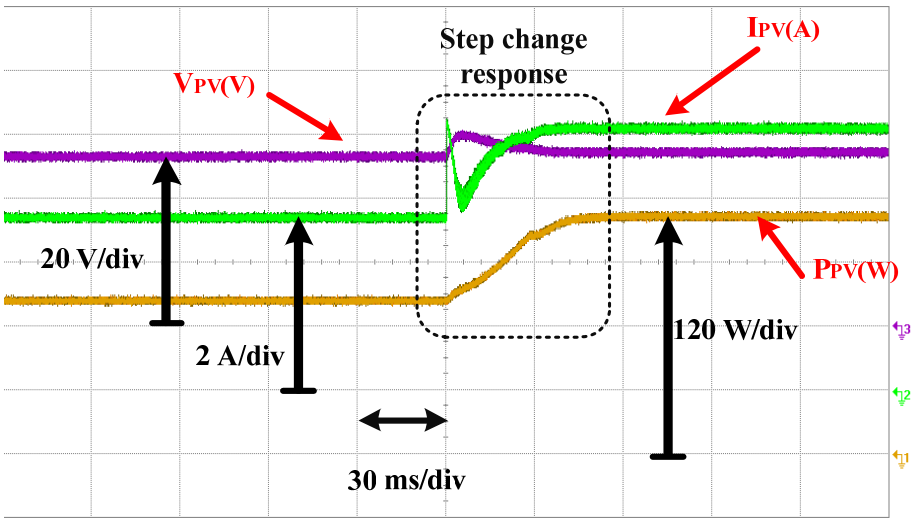

Figure 65: PV current, voltage, and power response to step change in the irradiance from 500 W/m^2 to 750 W/m^2 when using MPC-MPPT method.

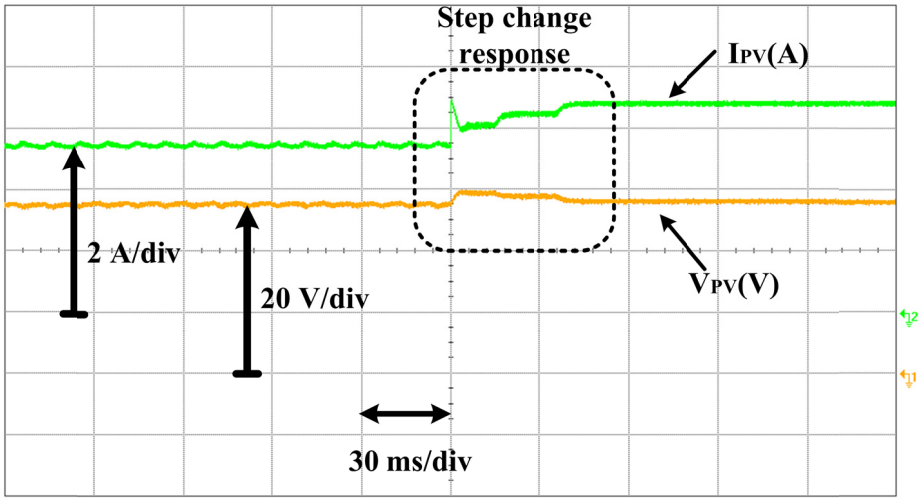

Figure 66: MPC-MPPT procedure.

6.2 Elimination of load model

Figure 67 illustrates the general diagram of the proposed MPC technique for MPPT of PV system. The Flyback converter, as a DC/DC boosting stage converter, is controlled using 2-step MPC-MPPT. In the proposed technique, the measured PV voltage and current as well as capacitor voltage are used to estimate the voltage and current of PV at sampling time *k+2*. Plant 1 and 2 in Figure 67 demonstrate the model of the converter when the switch (S) is ON and OFF respectively. Then the outputs of the predictive model of the converter are the input for MPPT algorithm. This algorithm uses this predicted information to determine the reference current to track. This reference current with predicted parameters are the input to a cost function subject to minimization that determines the switching action for the converter switch. A more detail procedure of the proposed technique is presented in Figure 71 and will be explained in this section.

From Figure 68 and Figure 69, model equations are derived as (85) when the switch is closed, and (86) when the switch is open.

$$L_m \frac{di_{Lm}}{dt} = V_{PV} \quad , \quad C\frac{dv_c}{dt} = \frac{-V_C}{R} \tag{85}$$

$$L_m \frac{di_{Lm}}{dt} = \frac{-V_C}{n} \quad , \quad C\frac{dv_c}{dt} = \frac{DI_{PV}}{n} - \frac{V_C}{R} \tag{86}$$

The discrete time model for the topology can be obtained by using the Euler approximation technique in (3).

$$\frac{di_{Lm}}{dt} = \frac{i_{Lm,k+1} - i_{Lm,k}}{T_s} \quad , \quad \frac{dv_c}{dt} = \frac{v_{c,k+1} - v_{c,k}}{T_s} \tag{87}$$

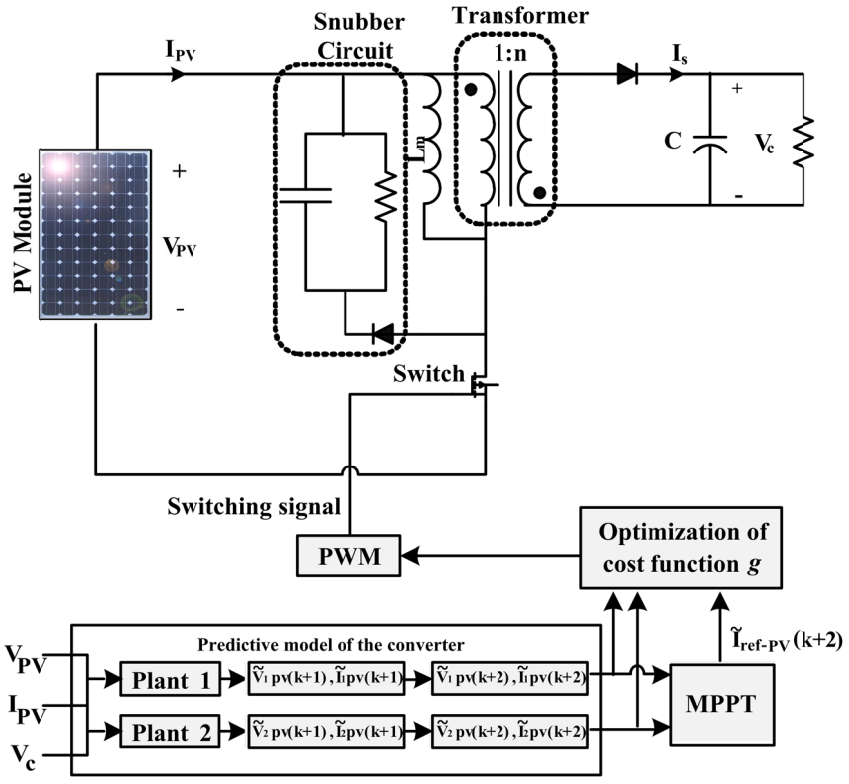

Figure 67: General schematic of the system and proposed model predictive control for flyback converter.

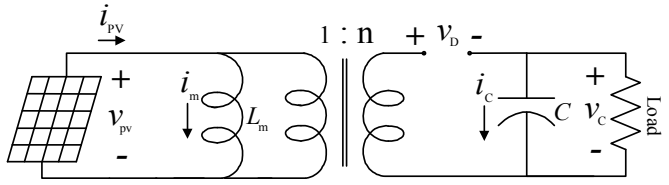

Figure 68: Flyback converter when the switch is ON (S).

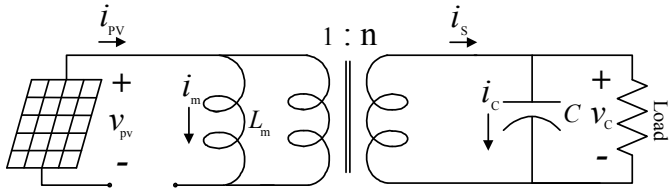

Figure 69: Flyback converter when the switch is OFF (1-S).

By deriving the discrete time set of equations, the behavior of control variable can be predicted at next sampling time *k+1*. The proposed methodology is based on the fact that the slope of the PV array power curve is zero at the predicted MPP, positive on the left and negative on the right of the predicted MPP. Applying the approximations in (87) to relations in (85) and (86) yields: (88) and (89) when the switch is closed, and (90) and (91) when the switch is open.

$$I_{PV}(k+1) = \frac{T_S}{L} V_{PV}(k) + I_{PV}(k) \tag{88}$$

$$V_{PV}(k+1) = \left[V_{PV}(k) - \left(\frac{T_S}{RC} \right) V_C(k) \right] \left(\frac{1-D}{nD} \right) \tag{89}$$

$$I_{PV}(k+1) = I_{PV}(k) - \frac{T_S}{Ln} V_C(k) \tag{90}$$

$$V_{PV}(k+1) = \left[\frac{DT_S}{nC} I_{PV}(k) - \frac{T_S}{RC} V_C(k) + V_{PV}(k) \right] \left(\frac{1-D}{nD} \right) \tag{91}$$

While model-based relations offer greater robustness, a drawback of such system, in general, is its dependence on the model variables. Load resistance is highly variable and sudden perturbation in the load can render the full system unstable. Hence, a simple, yet effective solution is to provide better monitoring on the load using an observer based approach that uses the already existing sensors in the flyback converter model. Relations for the resistor value can be inferred using the same flyback converter models (Figure 68 and Figure 69).

The relation between input and output current is given by:

$$i_c = I_{PV}\left(\frac{1-D}{D}\right)\frac{1}{n} \tag{92}$$

The load resistance relation can then be estimated as:

$$\gamma = R(k) = \frac{V_c}{i_c} = \frac{V_c(k)}{I_{PV}(k)\left(\frac{1-D}{D}\right)\frac{1}{n}} \tag{93}$$

Therefore, using the already existing input current and output voltage sensors, equation (93) for load resistance provides an accurate estimation of the load wihout directly sensing it. In which case γ, an observer based estimator for the load, can be applied to equations (88)-(91) to determine the predicted value for $V_{PV}(k+1)$ and $I_{PV}(k+1)$ which then summarize to (94) and (95).

$$I_{PV}(k+1) = I_{PV}(k) + [\frac{T_S}{L}V_{PV}(k)]S - [\frac{T_S}{Ln}V_C(k)](1-S) \tag{94}$$

$$V_{PV}(k+1) = \left[V_{PV}(k) - \left(\frac{T_S}{\gamma C}\right)V_C(k) + [\frac{DT_S}{nC}I_{PV}(k)](1-S)\right]\left(\frac{1-D}{nD}\right) \tag{95}$$

where S is the status of the switch.

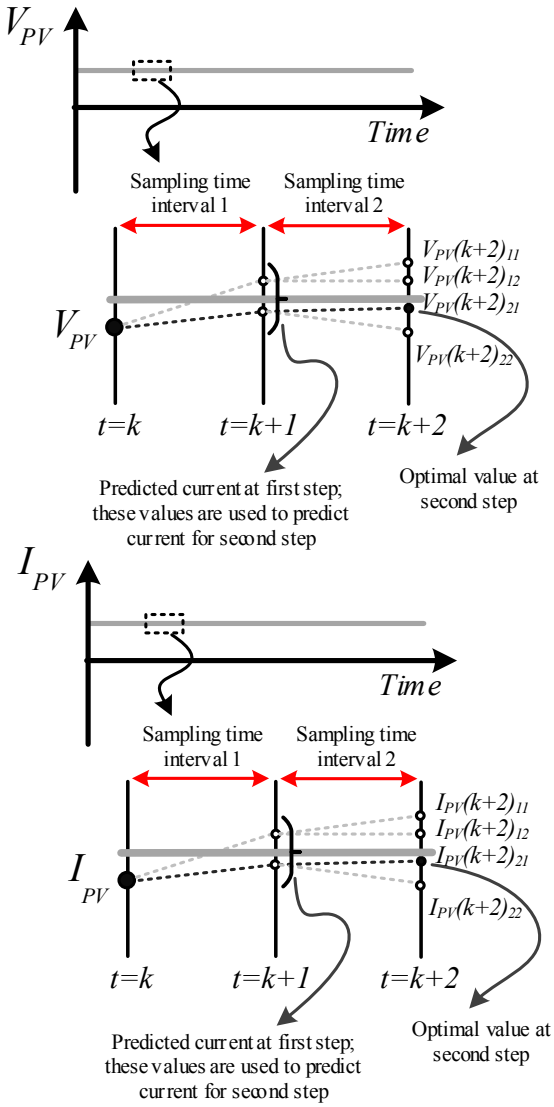

Figure 70: Prediction of PV array side current and voltage observation.

While, the model-based relations add great perfomance improvements as discussed in [122-124], previous work has suggested the addition of a second stage of predictive control for even better system perfomance and model accuracy [125]. In order to predict the control variables at time *k*+2, the estimated value of the PV current, PV voltage and output voltage at time *k*+1 are used. Thus at sampling time *k*+2, four

values for control variables are predicted and the optimum value is selected as illustrated graphically in Figure 70. Equations (94), (95) are adjusted to get (96), (97) for two-stage MPC.

$$I_{PV}(k+2) = I_{PV}(k+1) + [\frac{T_S}{L} V_{PV}(k+1)]S - [\frac{T_S}{Ln} V_C(k+1)](1-S) \qquad (96)$$

$$V_{PV}(k+2) = \left[V_{PV}(k+1) - \left(\frac{T_S}{\gamma C}\right) V_C(k+1) + [\frac{DT_S}{nC} I_{PV}(k+1)](1-S) \right] \left(\frac{1-D}{nD}\right) \qquad (97)$$

The model used for prediction is a discrete-time model, which can be presented as state space model:

$$\begin{bmatrix} I_{PV}(k+2) \\ V_{PV}(k+2) \end{bmatrix} = \begin{bmatrix} 1 & \frac{T_s S}{L} & \frac{T_s(1-S)}{Ln} \\ \frac{DT_s(1-S)}{nC}\left(\frac{1-D}{nD}\right) & \left(\frac{1-D}{nD}\right) & \frac{-T_s}{\gamma C}\left(\frac{1-D}{nD}\right) \end{bmatrix} \times \begin{bmatrix} I_{PV}(k+1) \\ V_{PV}(k+1) \\ V_C(k+1) \end{bmatrix} \qquad (98)$$

After determination of the reference voltage using the procedure shown in Figure 71, the cost function subject to minimization can be obtained as in (99).

$$g_{S=0,1} = \left| V_{PV_{S=0,1}}(k+2) - V_{ref} \right| \qquad (99)$$

This model can then be generalized to m-stage MPC as formulated in (100).

$$\begin{bmatrix} I_{PV}(k+m+1) \\ V_{PV}(k+m+1) \end{bmatrix} = \begin{bmatrix} 1 & \frac{T_s S}{L} & \frac{T_s(1-S)}{Ln} \\ \frac{DT_s(1-S)}{nC}\left(\frac{1-D}{nD}\right) & \left(\frac{1-D}{nD}\right) & \frac{-T_s}{\gamma C}\left(\frac{1-D}{nD}\right) \end{bmatrix} \times \begin{bmatrix} I_{PV}(k+m) \\ V_{PV}(k+m) \\ V_C(k+m) \end{bmatrix} \qquad (100)$$

m ϵ 0, 1, 2,…N

The system is implemented using SUNPOWER SPR-305-WHT as PV module type. The PV module characteristics under standard test condition (STC: solar irradiance = 1 kW/m2, cell temperature = 25 deg. C) are: Open circuit voltage (V_{OC}) = 64.2 V, Short-circuit current (I_{SC}) = 5.96 A, Voltage at MPP (V_{MP}) = 54.7 V, and Current at MPP (I_{MP}) = 5.58 A.

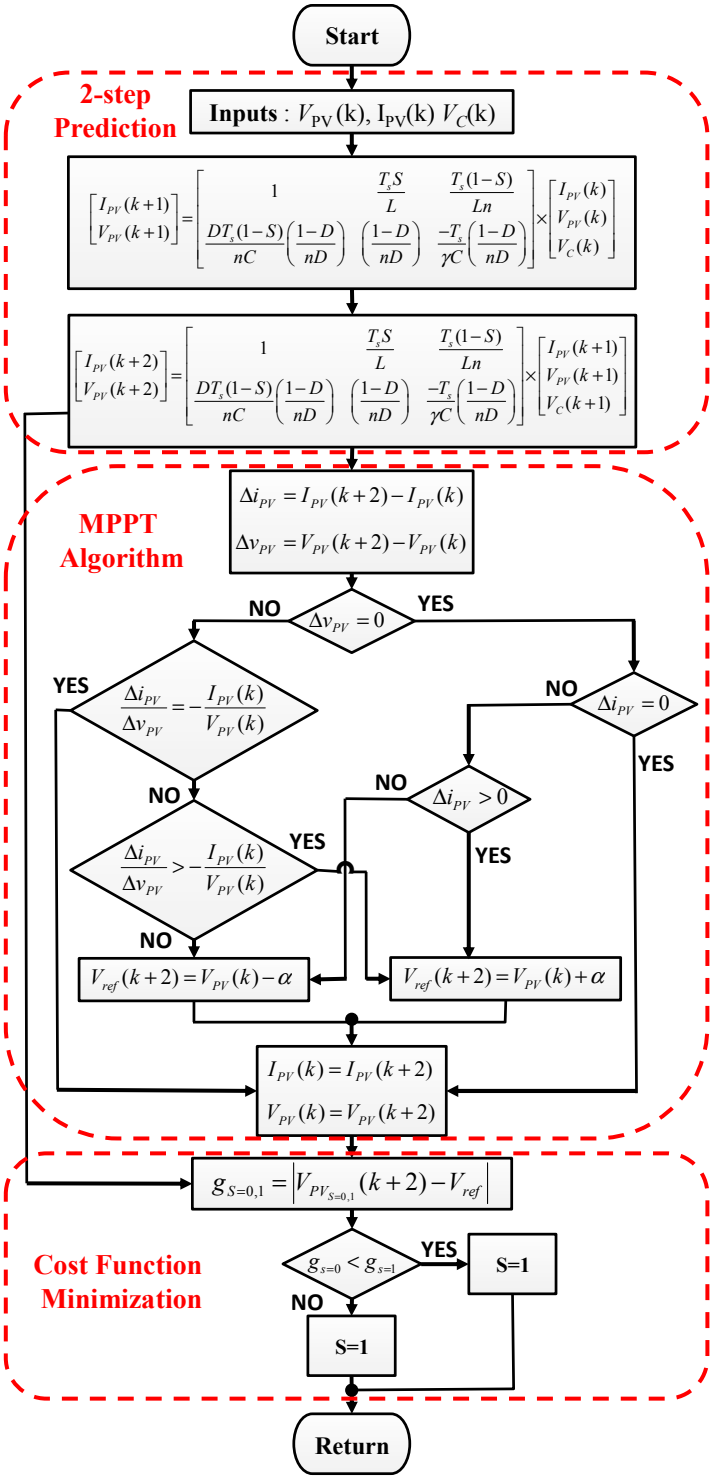

Figure 71: MPC-MPPT procedure to determine reference voltage, and determination of switching state using cost function minimization.

Two modules are connected in parallel with the I-V and P-V characteristic of the string illustrated in Figure 55. Voltage, current and power outputs in response to steps in the characteristics of Figure 72 are plotted in Figure 73, Figure 74, and Figure 75 respectively. Step response of PV power when irradiance is changed from 500 to 750 W/m^2 is shown in Figure 76. And finally power ripple at STC (1000 W/m^2) is 0.082% and is shown in Figure 77.

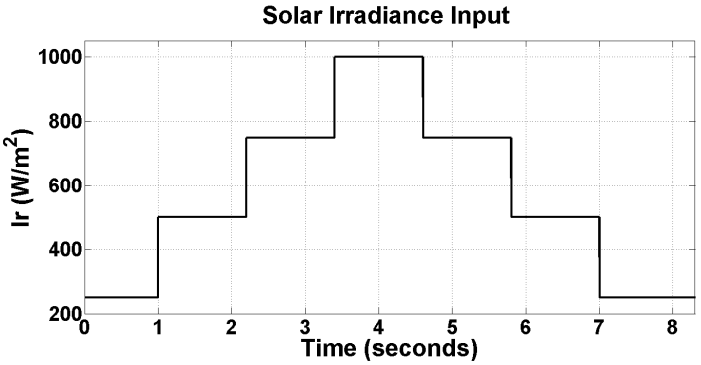

Figure 72: Solar Irradiance Applied Steps.

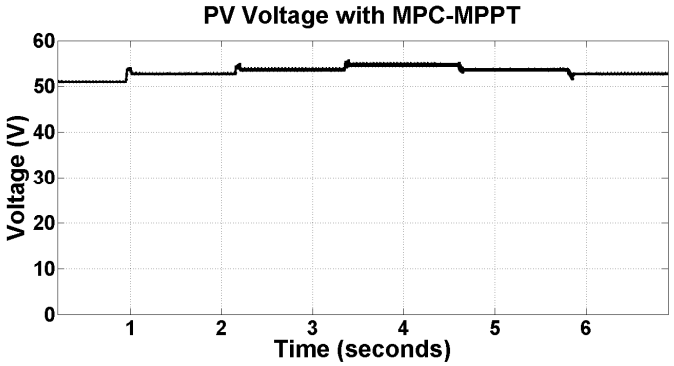

Figure 73: PV Voltage using MPC-MPPT.

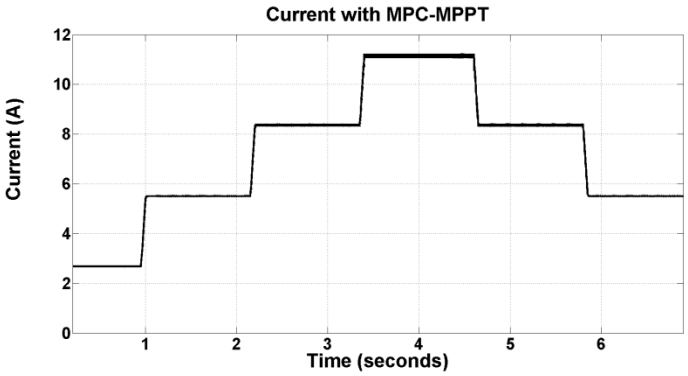

Figure 74: PV Current using MPC-MPPT.

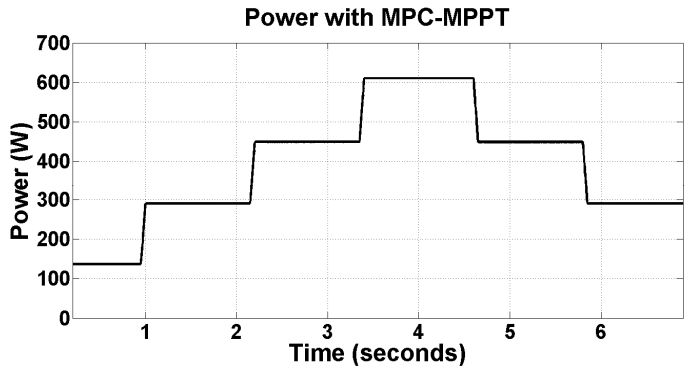

Figure 75: PV Power using MPC-MPPT.

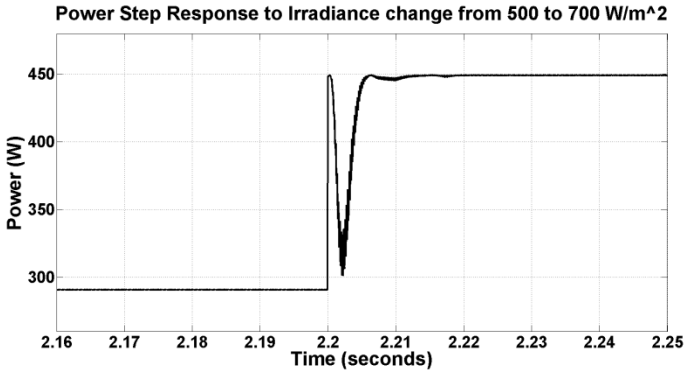

Figure 76: PV Power step response to irradiance change.

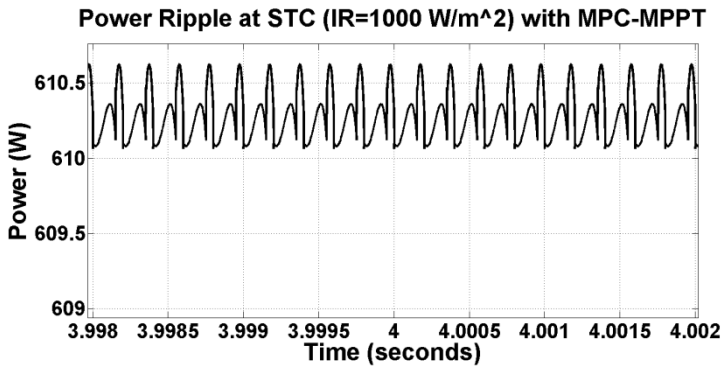

Figure 77: PV Power ripple at STC.

The proposed controller is implemented in real time experimentally by using dSPACE DS1007 plat form; the step change response and the current and voltage ripple at 750 W/m^2 of the proposed MPPT technique in real time are illustrated in Figure 78 and Figure 79 respectively.

To further illustrate the capabilities of 2-steps MPC-MPPT without the *R* model, some parameters were varied in the circuit and the system performance is evaluated. Figure 80 shows the response to uncertainty in transformer leakage inductance value on the error in voltage and current at MPP. The inductance value is underestimate and overestimated 50%. Figure 81 shows the response to uncertainty in transformer leakage resistance value for 50% underestimate and overestimate.

Then to illustrate the operation of the surrogate to the *R* model in MPC, a comparison was made for the error percentage comparing the conventional MPC with the *R* model and the MPC with the observer based estimation of the *R* model. As presented in Figure 82, the proposed MPC with observer based estimation of *R* model is much less sensitive to disturbances in the resistive load.

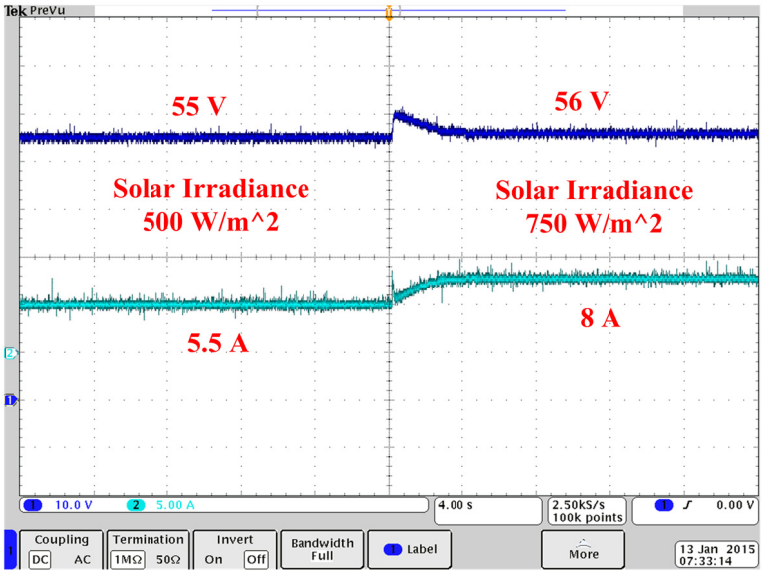

Figure 78: PV voltage and current step response.

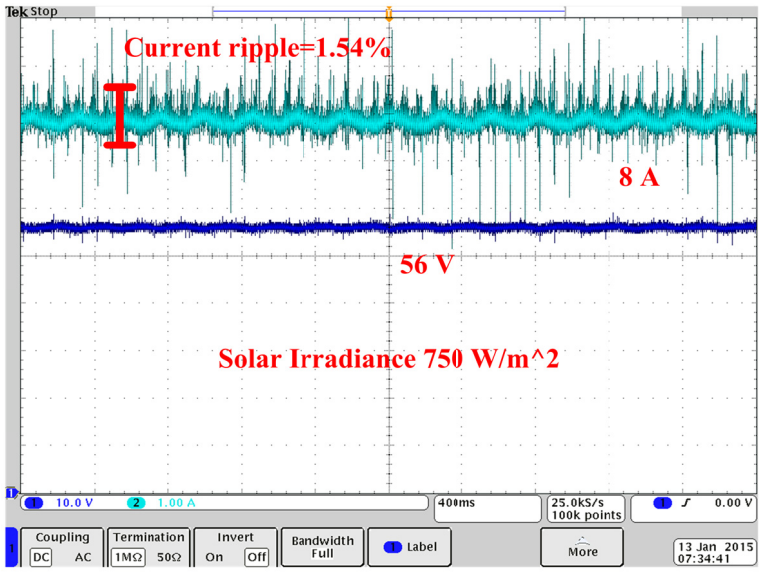

Figure 79: PV voltage and current ripple at 750 W/m^2.

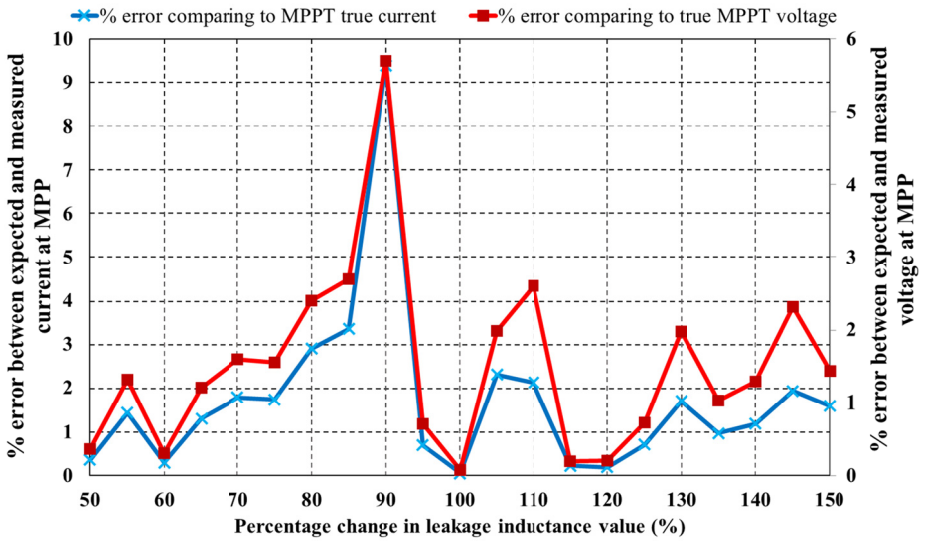

Figure 80: The effect of varying transformer leakage inductance value.

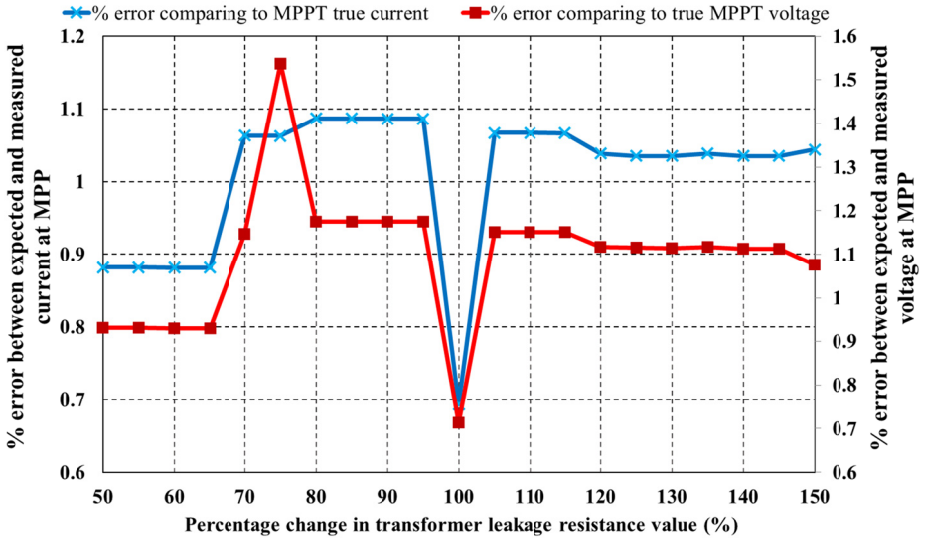

Figure 81: The effect of varying transformer leakage resistor value.

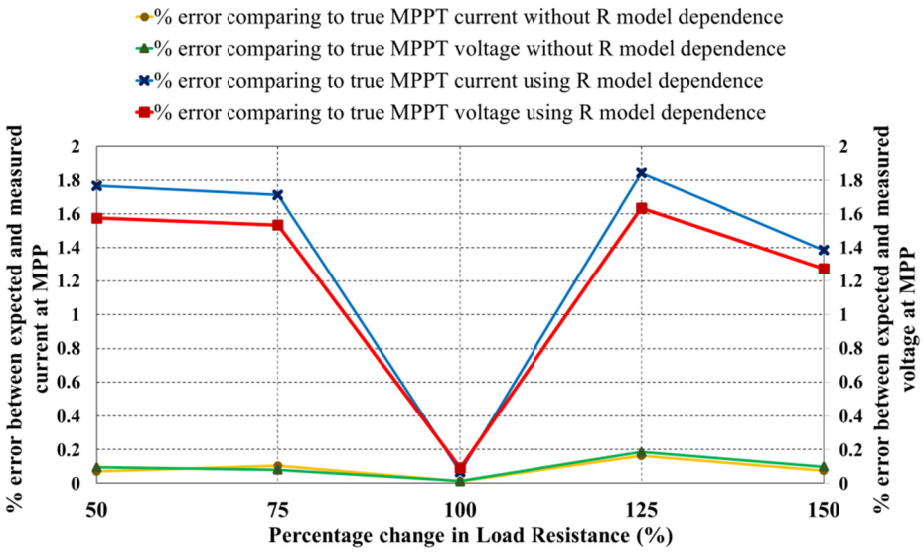

Figure 82: A comparison on varying load resistance between MPC with R dependence and MPC without R dependence.

Thus in this section a two-step MPC was studied and generalized for m-stage MPC. Then an observer based estimation of the resistive load is derived to eliminate the *R* model from the MPC and reduce the sensitivity of the controller to disturbances in the load. Effect of model parameter mismatch on the performance of the controller is presented. The simulation results indicate that the sensitivity of modified formulation of MPC is reduced to disturbances and uncertainty in load.

6.3 Efficiency analysis under dynamic weather condition

Performance evaluation of MPPT techniques depends largely on the test being conducted. Different literature suggests different test types like step changes. While, such tests may prove the effectiveness of the system during such test, they fail to follow a standardized acceptance [126]. Therefore, using a globally accepted test for MPPT is essential to evaluate a system's performance.

To overcome the inconsistency in performance tests, an international working group was set up in late 2006 to develop a standardized test that takes into account both MPPT accuracy and conversion efficiency [126]. The test was accepted as a standard in the European union by the end of 2009 and published as The Standard EN 50530 Test [126].

The dynamic EN 50530 standard tests are run under rapidly changing weather conditions. It combines rising and falling ramp profiles with different slopes to represent insolation levels [126]. The principle of test sequence is illustrated in Fig. 7 parametrically. The slope of each ramp is named ζ_n which is incrementally increasing by a factor of ε, this sequence is repeated n times during the period under the test. The test is made of three components as in Fig. 8: (A) Low to medium insolation (150-500W/m^2), (B) medium to high insolation (300-1000W/m^2) and (C) startup and shutdown insolation (2-100W/m^2). Slopes for (A) vary from 0.5 W/m^2/s to 50 W/m^2/s, while slopes for (B) vary from 10 W/m^2/s to 100 W/m^2/s.

According to the standard, the test looks into both MPPT accuracy and conversion efficiency of grid connected PV systems [126]. Since the target of this efficiency test is the control effectiveness of the MPPT technique not the conversion stage, inverter, of PV system, this test is also valid for the MPPT accuracy of the off-grid PV system [127]. In this paper this test is applied to the proposed MPC technique to validate its performance. By which case the inverter efficiency calculation is not made and segment (C) of the test is disregarded [127].

To assess the dynamic performance of the MPPT accuracy, the output power calculated from the measured voltage and measured current is compare to the ideal maximum power point. Then the control effectiveness is determined.

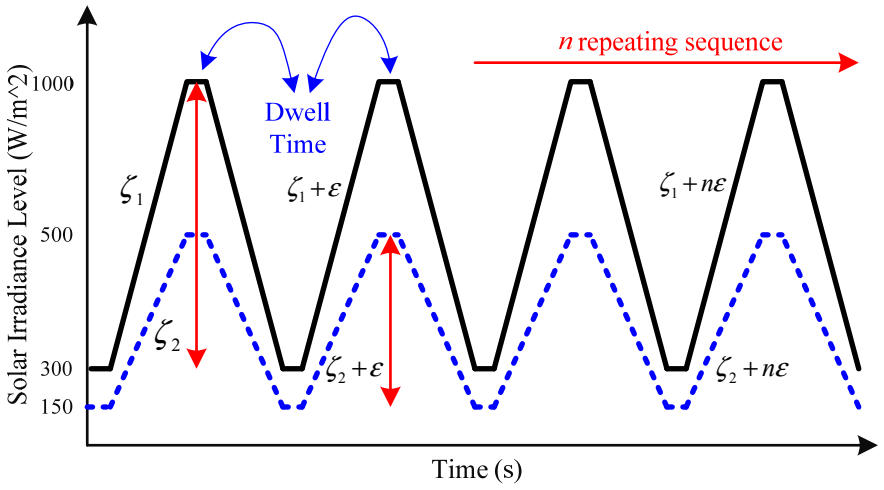

Figure 83: Test sequence principle, medium to high solar irradiance level (black solid line) and low to medium solar irradiance level (blue dashed line).

The EN 50530 test is run on the system and performance results for duty cycle, power, voltage and current are as shown in Figs. 10-13. The sampling time of the controller is 1μs, the switching frequency is 5 kHz, and the sampling time for recording the data is 1 ms. Due to highly effective MPPT, the real expected power from the PV is not added to the curve since they are overlapping and it is not clear how much the error is at each test segment. Thus the control effectiveness is determined for the duration under the test and plotted in Fig. 13 and 14. Fig. 14 demonstrates the control effectiveness of the proposed MPC-MPPT during 183 minutes of the test run. The

control effectiveness versus the power at the MPP for different value of ζ during the test run is plotted in Fig. 9. As it is illustrated in these two plots, the lowest control effectiveness during the run test is 97%. The average of the control effectiveness is 98.8% percent for different power and ζ values. However it can be seen that in most of the time the proposed MPPT technique gives control effectiveness of more than 99.5% which demonstrate the accuracy and fast convergence of the proposed technique.

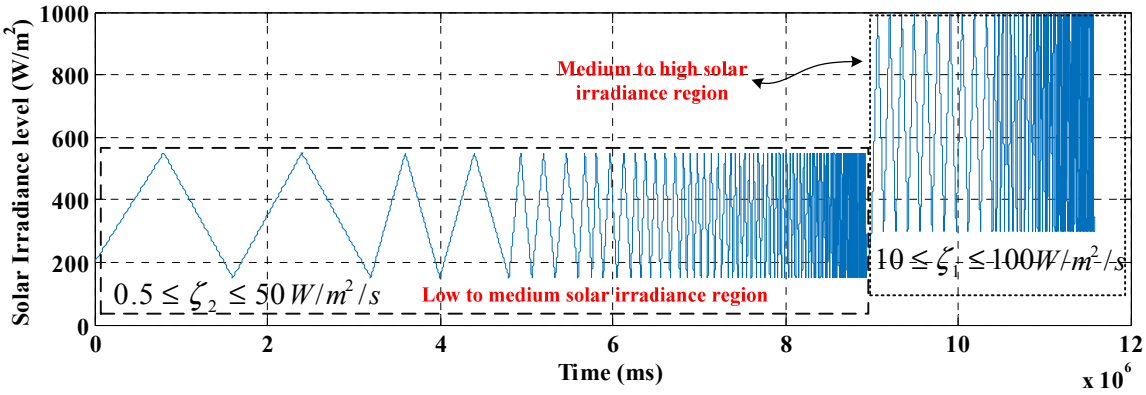

Figure 84: The two components of the EN 50530 standard test.

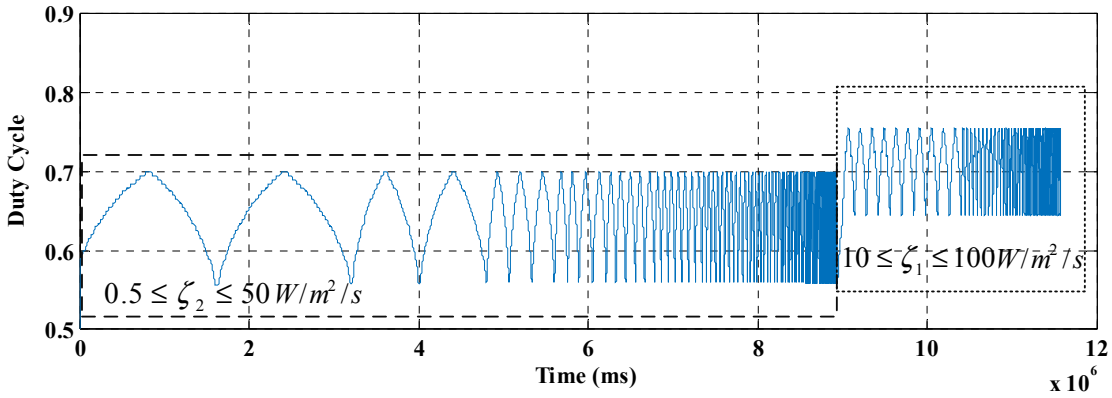

Figure 85: Duty cycle of the flyback converter under dynamic test.

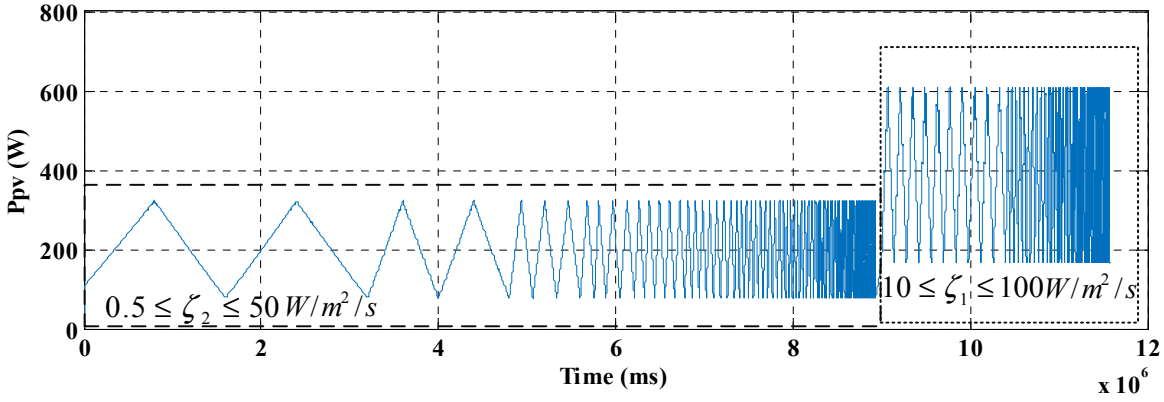

Figure 86: PV power under dynamic test.

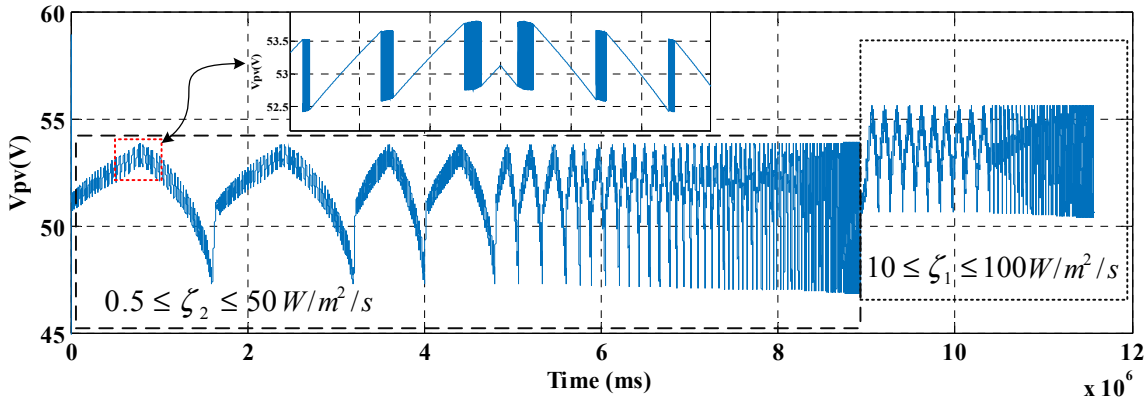

Figure 87: PV voltage under dynamic test.

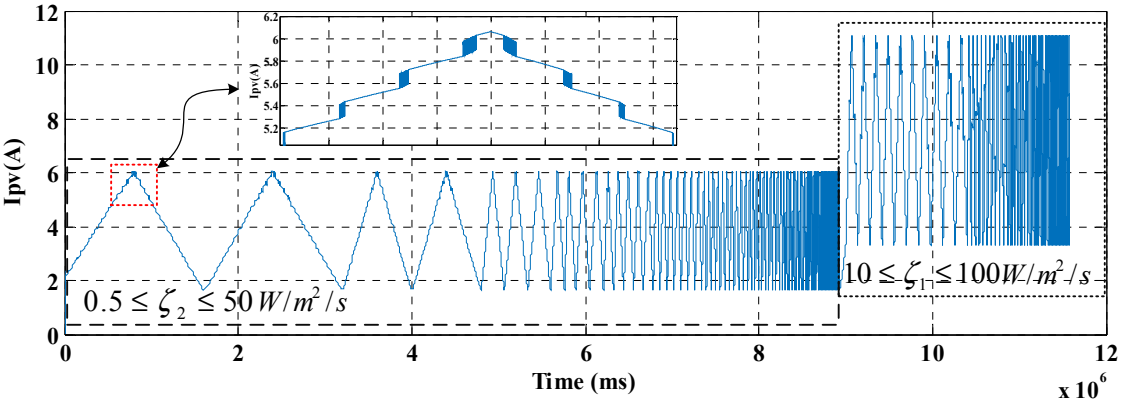

Figure 88: PV current under dynamic test.

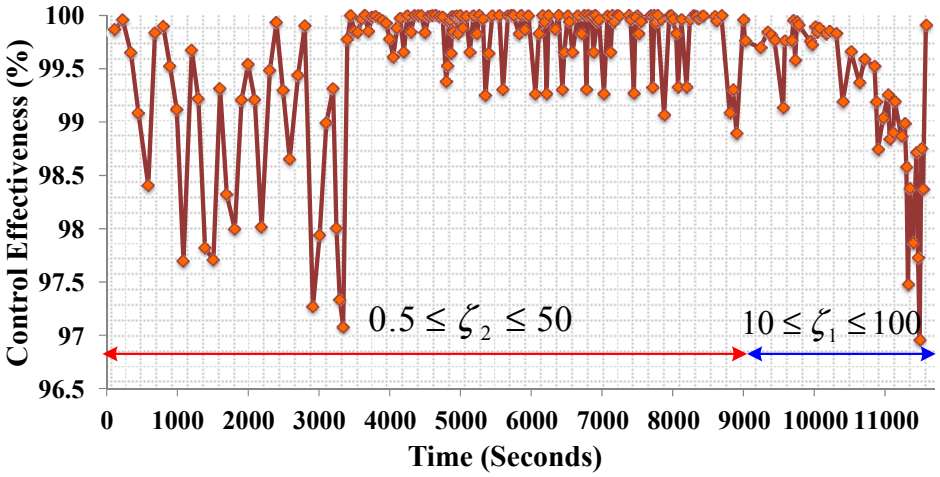

Figure 89: Control effectiveness of the proposed MPC-MPPT under EN 50530 standard test for 183 minutes..

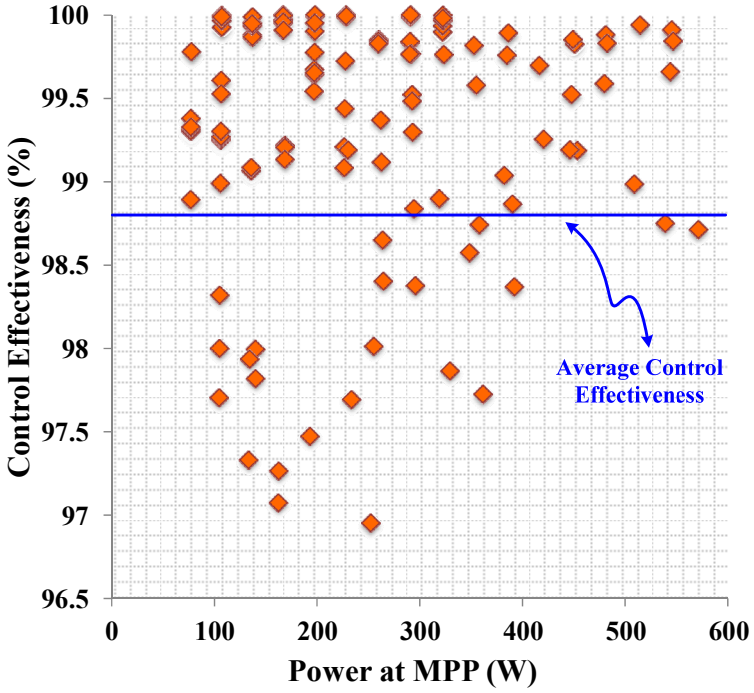

Figure 90: Control effectiveness of the proposed MPC-MPPT.

6.4 Conclusion

This section presented a performance evaluation on an efficient MPPT technique that predicts the error at next sampling time before applying the switching signal using MPC. A two-step MPC was studied and generalized for m-stage MPC. Then an observer based estimation of the resistive load is derived to eliminate the *R* model from the MPC and reduce the sensitivity of the controller to disturbances in the load. Results of system's performance using the EN 50530 test are presented in this paper. Performance results met and surpassed the requirements for the system and validate such system in a globally accepted performance evaluation.

7. DROOP PREDICTIVE CONTROL IN DC MICROGRID SYSTEM*

In a DC distribution system, where multiple power sources supply a common bus, current sharing is an important issue. When renewable energy resources are considered, such as photovoltaic (PV), DC/DC converters are needed to decouple the source voltage, which can vary due to operating conditions and Maximum Power Point Tracking (MPPT), from the DC bus voltage. Since different sources may have different power delivery capacities that may vary with time, coordination of the interface to the bus is of paramount importance to ensure reliable system operation. Further, since these sources are most likely distributed throughout the system, distributed controls are needed to ensure a robust and fault tolerant control system. This section presents a Model Predictive Control-based droop (MPC-DROOP) current regulator to interface PV in smart DC distribution systems. Back-to-back DC/DC converters control both the input current from the PV module, known as maximum power point tracking, and the droop characteristic of the output current injected into the distribution bus. The predictive controller speeds up both of the control loops since it predicts and corrects error before the switching signal is applied to the respective converter.

Direct current (DC) electrical systems are gaining popularity due in part to high efficiency, high reliability and ease of interconnection of the renewable sources compared to alternating current (AC) systems [1, 2]. DC microgrids have been proposed

*Part of this section is reprinted with permission from M. B. Shadmand, R. S. Balog, and H. Abu Rub, "Model Predictive Control of PV Sources in a Smart DC Distribution System: Maximum Power Point Tracking and Droop Control," IEEE Transactions on Energy Conversion, November, 2014, © 2014 IEEE.

to improve point-of-load energy availability and to integrate disparate renewable energy sources with energy storage [3]. Various renewable energy sources such as PV systems have natural dc couplings; therefore it is more efficient to connect these sources directly to DC microgrid by using DC/DC converters.

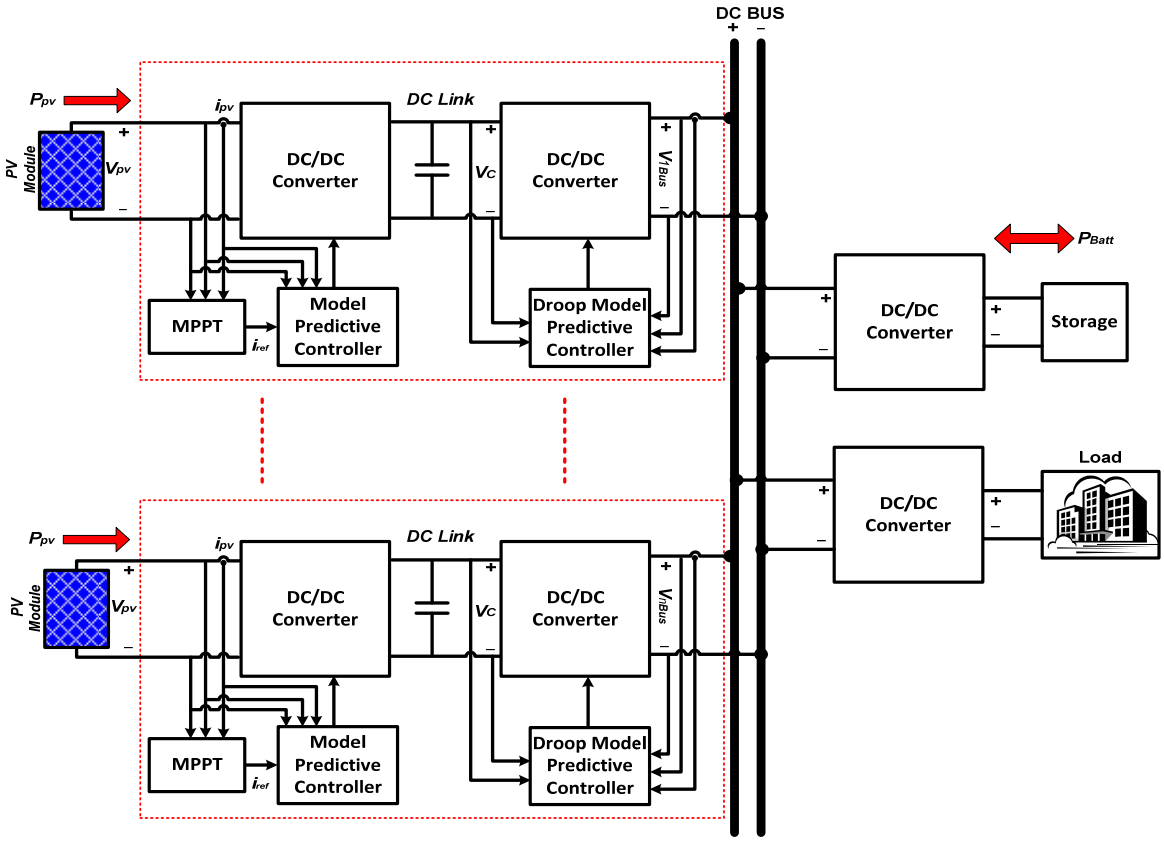

Figure 91: Multiple-sourced DC distribution system with central storage.

A DC microgrid system with distributed PV and centralized battery storage, illustrated in Figure 91 as part of hybrid distribution system of Figure 1, is an attractive technology solution for communities to "go-green" while simultaneously ensures reliable electricity. The PV arrays can delivery power to the system through a DC/DC converter boosting the output voltage. A maximum power point tracking (MPPT) control

technique presented earlier is required for the PV system to operate at the maximum power point [105, 128, 129] but produces output voltage that is not constant. Thus a second DC/DC converter is added to control the current and voltage fed into the DC bus [130]. Although power from the PV is now processed twice, DC/DC converters have very high efficiency and the back-to-back converters (Figure 91) would have comparable, if not better efficiency, than ac systems based on a contemporary, best-in-class inverter of comparable power rating [6, 131, 132].

In a DC microgrid system where multiple PV source converters supply the same bus, current sharing is an important consideration [1]. Theoretically, identical supply converters will share the load current equally. However, mismatches in components and feedback networks as well as different impedances at different locations on the DC bus can cause imbalance in current sharing. If significant, this imbalance can result in overload and thermal stresses which could jeopardize system reliability. The reliability of a single-bus DC system can be improved by using autonomous local controls rather than a central controller [133]. Droop control is one of such control technique that controls the output current from the source in response to the sensed bus voltage [134]. Since no communication is needed to coordinate controllers, the system is robust and cyber-secure [135]. The contribution of this section is to develop the conventional droop control methodology by means of MPC for smart DC distribution systems. The developed droop control by MPC proposed in this section enables a stable process control due to the nature of MPC that is predicting the error before the control signal applied to the converter.

Figure 91, as part of hybrid distribution system of Figure 1, illustrates the general schematic of the proposed smart DC microgrid. Multiple PV arrays using MPC-MPPT to supply power through a MPC-DROOP converter into the DC distribution bus is presented. According to the availability of power from PV sources, the MPC-DROOP adjusts the droop characteristics of the DC/DC converter. In practice, the MPC-MPPT and MPC-DROOP would be integrated into a single system component, delineated by the dotted line in Figure 91.

7.1 Methods of load sharing

Whenever sources are operated in parallel, for fault-tolerant design or higher output power, current sharing is an important consideration. The methods for load sharing reported in the literature fall into two groups: active sharing and droop control [136, 137]. Droop control uses the sensed bus voltage at the output of each source to automatically share current. The focus of this section is droop control by using model predictive control principles because it is form of autonomous local control. The reliability of a single-bus dc microgrid system, such as the system illustrated in Figure 1, can be improved by using autonomous local controls for both supply-side and load-side management.

Active current-sharing techniques involve a control structure and a method of programming individual converters with a reference current. One implementation is to use a master/slave configuration such that one dc source is designated as the *master* and is used to control the bus voltage.

The remaining dc sources, designated as *slaves*, operate as current sources. This strategy produces a stiff bus voltage and controlled load dispatch at each source. There are two main limitations of this technique: high-speed communication is required and a single point failure can disable the entire system [138]. In practice, active current sharing techniques are best suited for physically small systems, such as paralleled voltage regulator module (VRM) applications. If the topology were fixed and known a priori, more sophisticated controls such as interleaving can be used to reduce ripple [139].

7.2 Supply-side: droop predictive control

In droop control, the output voltage of the source drops as current increases. This is a form of local control since converters autonomously share load current by sensing the local bus voltage. Droop control can be as simple as a series resistance or a more efficient closed-loop controller such as a phase-angle controller in a rectifier source converter. This scheme has been proposed for use in large-scale distributed systems [140] with dynamically changing topologies since it supports plug-and-play reconfiguration and system scaling, and is robust to component failures.

In this section MPC is used for the droop control. MPC can forecast the error using the model of the system behavior, thus speed up stabilization process. In the proposed control scheme by using the predicted parameters and locally measured reference voltage, the reference current for each parallel converters is determined. Consequently no communication between converters is required; as a result the reliability of the system increases. Then the determined reference current is used as an input to a hysteresis current controller [141] for tracking the reference current and

generating the switching signal. The complete control procedure is illustrated in Figure 92. Since the second DC/DC converter for droop control is flyback converter, the discrete time model derived in previous section for MPPT can be used here.

The predicted variables I_o and V_{Bus} are the current and voltage at the output terminals of the converter at next sampling time. The voltage at the output, the bus voltage, is low-pass filtered and used to close a feedback loop. The droop gain K converts the voltage error into a current command for the source converter; it is included in the compensator block in Figure 92. Assuming the converter current perfectly tracks the reference current, the steady state droop relationship is

$$I_{ref} = K\left(V_{ref} - v_{Bus}\right) \qquad (101)$$

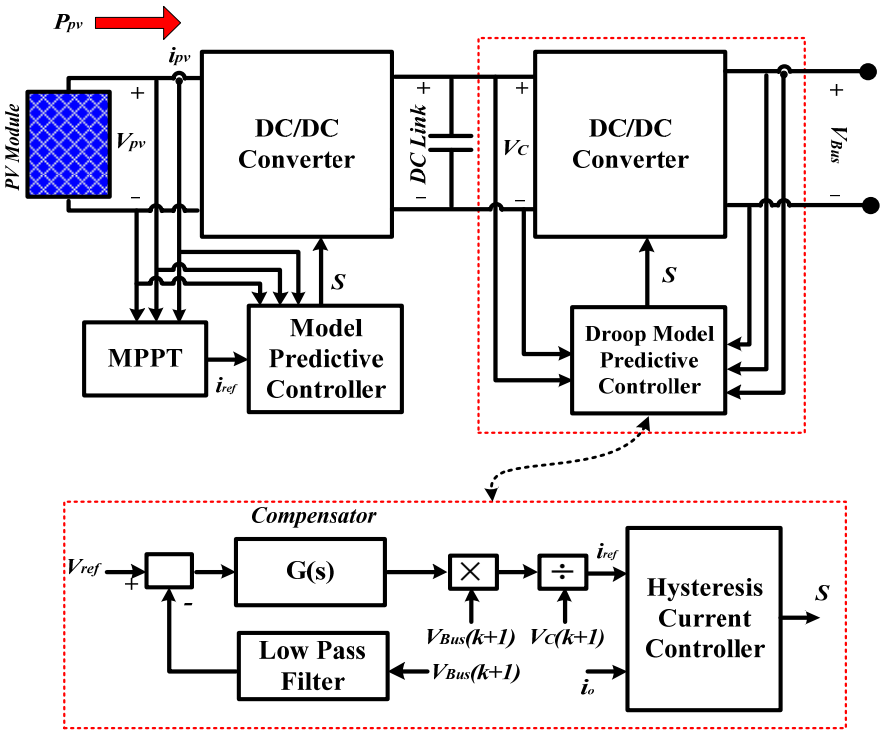

Figure 92: Droop MPC control of the DC/DC converters.

The proposed distributed system controlled by droop MPC is inherently robust because droop control automatically shares current among the available converters without the need for a central controller to redispatch the source converters. If a converter turns off or fails, the remaining converters sense a decrease in bus voltage and increase their respective output current to compensate for the lost source.

Consider a system (Figure 93) comprised of five PV arrays on a common dc bus supplying 1500 W of total load. Each PV source converter has a load-line that describes the *v-i* terminal characteristics (Figure 93). Assuming negligible bus impedance, the solution to the base case (where all converters are operational) results in the bus voltage V_{OP1} with each converter supplying I_{OP1} current. The analytical solution for the operating point is found by solving the load-flow equations for n source converters and m constant-power loads:

$$V_{oc,n} - I_n \frac{1}{K_n} = V_{bus}, \forall n, \quad \sum_n I_n = \sum_m \frac{P_m}{V_{bus}} \qquad (102)$$

Contingency analysis is shown graphically in Figure 93. As the number of PV (source) converters decreases, the bus voltage drops. Since the load is now shared by fewer sources, the current from each remaining source increases. The analytical solutions for two case contingencies and the base case are presented in Table 8. It is observed that the droop gain is the slope of the *v*-i curve and modifies the actual source impedance. So a simple model for a source converter is

$$V_S = V_{OC} - \frac{1}{K} i_S \qquad (103)$$

where the droop gain K can be defined in terms of a resistance $K = 1/R_{droop}$.

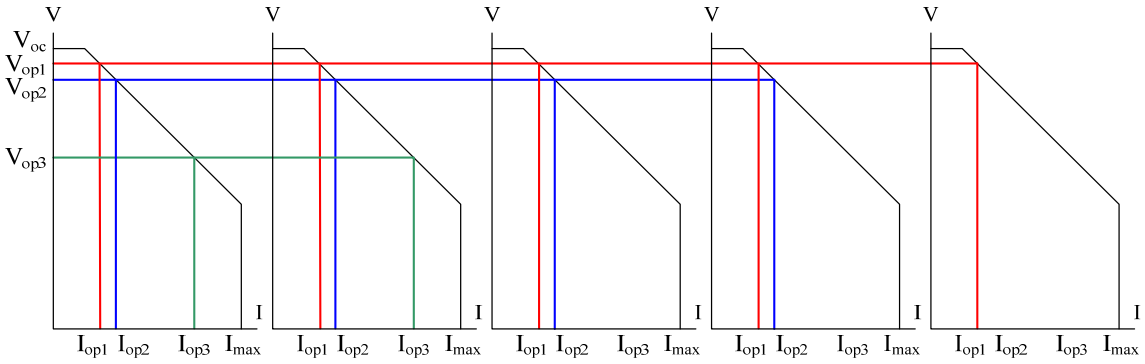

Figure 93: Illustration of supply current-sharing using droop-control. The droop characteristic of the output convertor regulates the current supplied into the bus. If all supplies are identical, with the same supply capability, then current is evenly shared. Adjusting the droop characteristic can allows current to be shared automatically in arbitrary proportion, as in the case of unequal supply capabilities.

Table 8. Current sharing under droop-control as the number of source converters decreases.

	Number of sources		
	5	4	2
V_{OP}	48V	45.50 V	37.50 V
I_{OP}	6.25 A	8.24 A	20 A
I_{bus}	31.25 A	32.96 A	40 A
P_{load}	1,500 W	1,500 W	1,500 W

Although droop control can be as simple as a series resistance, a more energy efficient choice is a closed-loop controller, such as MPC used in this section. For an arbitrary source converter, the permissible droop resistance is lower bounded by the actual source resistance of the converter:

$$R_s \leq R_{droop} \qquad (104)$$

In the previous example, the PV converters are assumed to be identical with identical droop characteristics. Thus the total load current is shared equally. In general, however, each converter can have an arbitrary droop characteristic representing its operating parameters, power limits, or preferred dispatch:

$$R_{droop} = \frac{1}{1-\varphi} R_s, \text{ where } 0 \le \varphi < 1 \qquad (105)$$

Thus, droop controller result in current sharing and directly affect the system dynamic behavior.

7.3 Load-side: dynamic load interruption

In a power system in steady state, the supply is matched to the load and the system is stable. However, many dc distribution systems are electrically weak and do not have the spinning reserves or other stability mechanisms. The bus voltage can sag for a number of reasons such as partial loss of generation, increase in load, or topological reconfiguration. Further, tight voltage regulation in dc-dc converters makes them operate as constant power loads which draw increasing current for decreasing bus voltage, possibly leading to further voltage sag or even voltage collapse.

Demand-side management is a suite of techniques that control the loads so that they become integral components in system stability. Interruptible load is one method that provides curtailment of demand to promote system security. Autonomous local control is investigated to perform this load-side control and improve system reliability.

7.3.1 The P-V curve

The P-V curve is a useful tool to visualize the operation of a power system. Figure 94 illustrates a family of the familiar *p-v* system curve. Maximum power

transmission (MPT) occurs at the nose were the source impedance and load impedance are equal. In a dc system, the bus voltage drops as the load increases due to voltage-divider action of the source impedance and the load impedance.

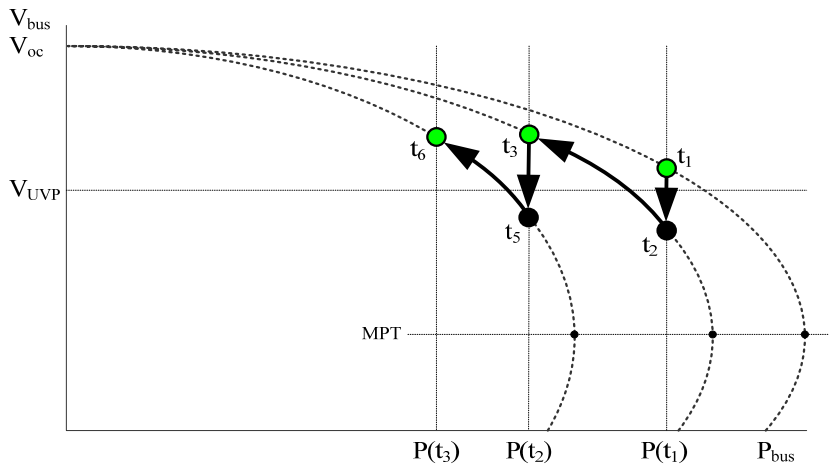

Figure 94: P-V curve showing operating points as the system impedance increases and loads are interrupted.

A system is initially in steady state with voltage $V(t_1)$ delivering total load power of $P(t_1)$. The system impedance suddenly increases, perhaps due to a partial loss of generation or topological reconfiguration, and the operating point moves to a new p-v curve at time t_2. However, the voltage $V(t_2)$ is below the undervoltage limit and load is shed, moving to a new operating point on the same p-v curve at t_3. The time-domain waveforms in Figure 95 reveal that these changes in operating points do not occur instantaneously. The trajectories on the two figures, however, are idealized to improve clarity of the system response and do not include the dynamics associated with the inductance of the bus, the input filter, and the constant-power dc-dc converters.

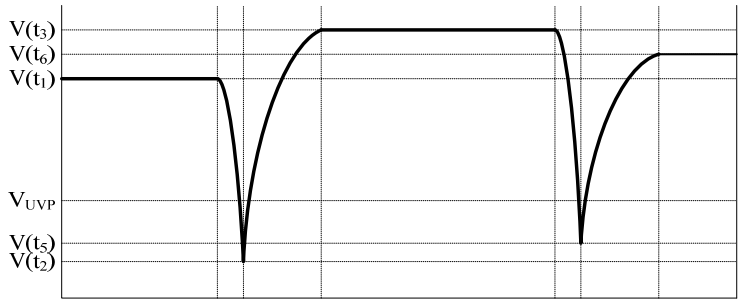

(a) Bus voltage decreases in response to increased system impedance at t1 to reach the operating point on the new p-v curve at t2. The new bus voltage is below the UVP limit, so control action cause load to be shed, moving to a new operating point on the same p-v curve at t3 with a higher bus voltage.

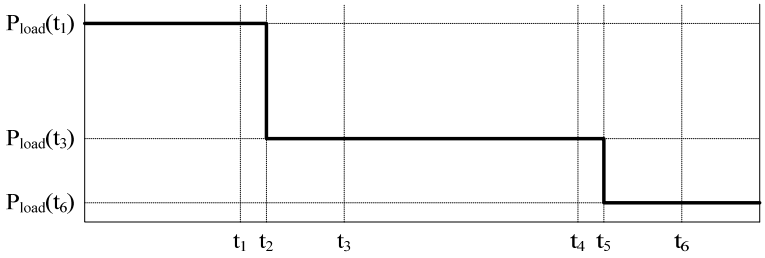

(b) Load power in the system changes as point-of-load converters are turned-off to reduce total system load when the bus voltage drops below the UVP.

Figure 95: Ideal bus voltage and load power as system impedance increases and loads are interrupted to prevent voltage collapse.

7.4 Results and discussion

The smart DC microgrid system illustrated in Figure 91 is implemented in Matlab/Simulink. The case study is done for three PV array systems. The MPPT of each array is carried out using the procedure presented in previous section. In this section two case studies will be presented to show the effectiveness of the proposed droop MPC. The first case study evaluates the DC bus voltage response to a step change in the power drained by the load from 340 W to 440 W at time 0.5 s, and then from 440 W to 520 W

at time 0.7 s. The reference DC bus voltage is assumed 188 V in this paper. The detail behavior during load variation of DC microgrid bus voltage and supplied power by each converter is illustrated in Figure 96. The input PV sources are assumed to be in balance operating point; this means the solar irradiance is assumed to be constant and equal to 750 W/m^2 for all of the three first stage DC/DC converters in this case study. The bus voltage regulation has fast dynamic response to the step change in power drained by load, though the bus voltage dropped to 187.1 V at time 0.55 s and 186.5 at time 0.75 s. Thus as shown, the bus voltage regulation is perfectly done with 0.80% error.

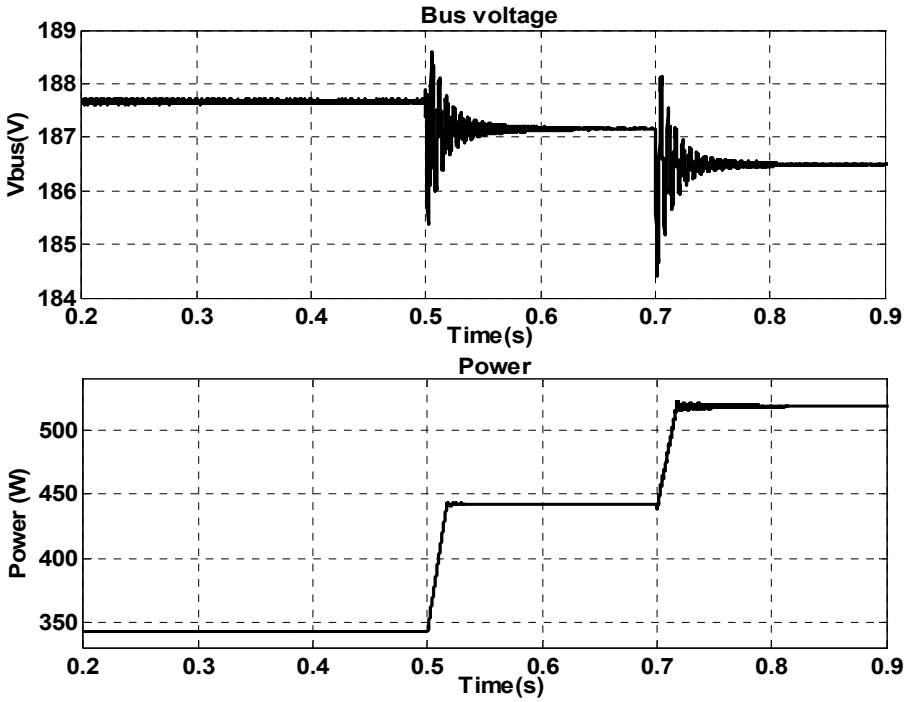

Figure 96: Response of DC bus voltage to step changes in the power drained by load.

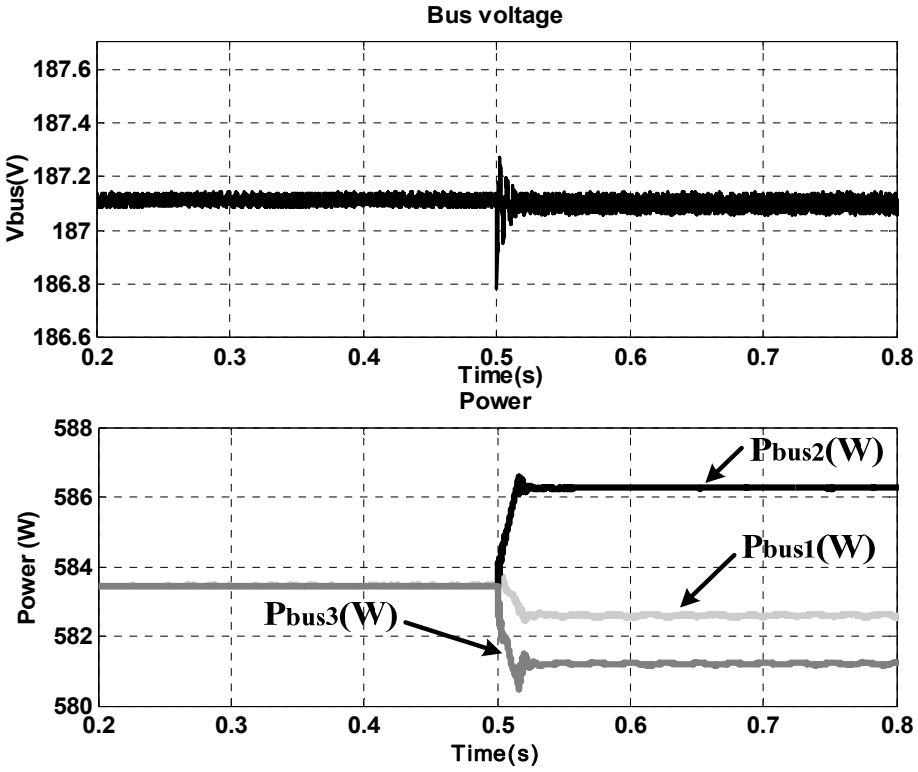

Figure 97: Response of DC bus voltage and output power to imbalanced input PV sources.

The simulation results of this case study are implemented using dSPACE DS1103 and verified as shown in Figure 98. These results demonstrate that the proposed approach is valid for a step change in the power drained by load. The second case study evaluates the droop MPC under imbalanced input PV sources. The solar irradiance level for all three input PV sources are 750 W/m^2 before time 0.5 s, at this time the irradiance level of PV source 1 and 3 dropped to 400 W/m^2 and 300 W/m^2 respectively and the irradiance level of PV source 2 increased 850 W/m^2. Figure 97 illustrates the bus voltage and the power supplied to the bus for this case study. The implementation of the droop control is done for this case, as illustrated in Figure 99. Figure 100 illustrates the

response of DC bus voltage and output power to the input PV sources of Figure 63. The variation of the power supplied to the bus during the time interval 0.7 s to 1.0 s is due to the gradually reduction of solar irradiance level from 750 W/m^2 to 500 W/m^2. Also, as illustrated earlier in Figure 63, a step change in solar irradiance from 500 W/m^2 to 750 W/m^2 occurred at time 1.5 s which is also appeared in Figure 100.

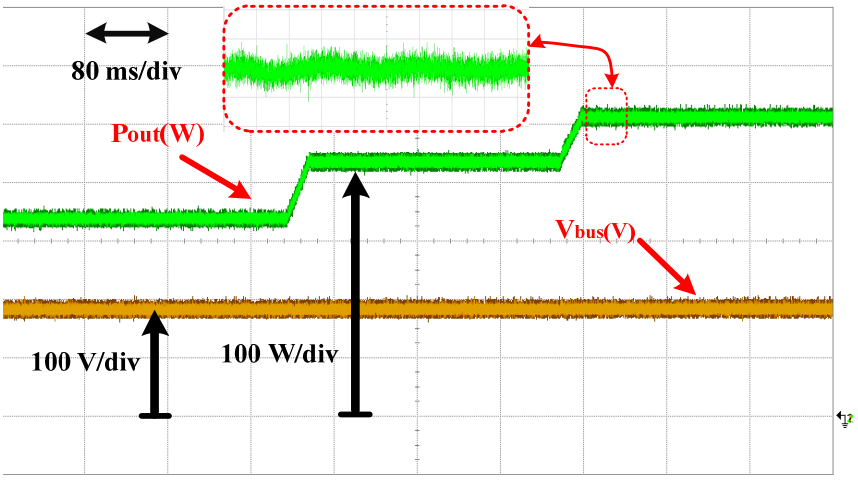

Figure 98: Response validation of DC bus voltage to step changes in the power drained by load.

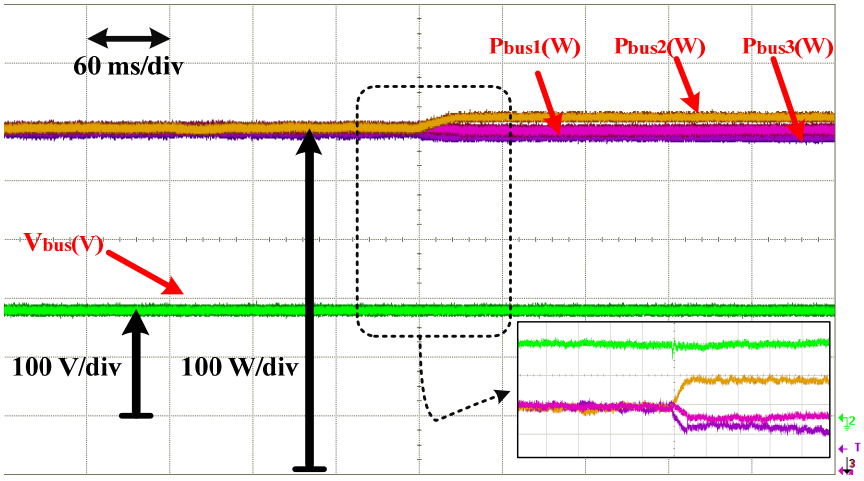

Figure 99: Response validation of DC bus voltage and output power to imbalanced input PV sources.

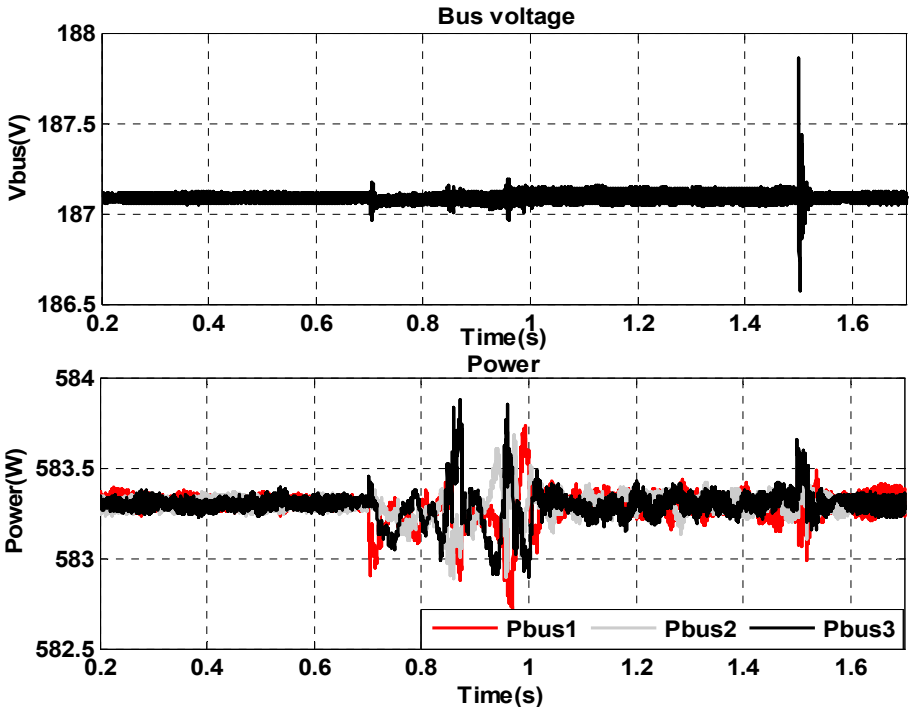

Figure 100: Response of DC bus voltage and output power to the input PV sources of Figure 63.

7.5 Conclusion

In a smart DC distribution system for microgrid community, parallel DC/DC converters are used to interconnect the sources, load, and storage systems. Equal current sharing between the parallel DC/DC converters and low voltage regulation is required. The proposed droop MPC can achieve these two objectives. The proposed droop control improved the efficiency of the DC distribution system, because of the nature of MPC which predicts the error one step in horizon before applying the switching signal. The effectiveness of the proposed MPPT-MPC and droop MPC is verified through detailed simulation of case studies. Implementation of the MPPT-MPC and droop MPC using dSPACE DS1103 validates the simulation results.

8. CAPACITOR-LESS VAR COMPENSATION BY MODEL PREDICTIVE CONTROL OF MATRIX CONVERTER*

This section presents a reactive power compensation technique using model predictive control (MPC) of a matrix converter. This technique compensates lagging power factor loads using inductive energy storage elements instead of electrolytic capacitors (e-caps). Although ubiquitous in power electronic converters, e-caps have well-known failure modes and wear-out mechanisms. Therefore, the capacitors used to store energy in a voltage-sourced inverter (VSI) reactive power compensator require continuous monitoring and periodic replacement, both of which significantly increase the cost of the traditional load compensation technique. MPC of the matrix converter provides reactive power compensation by controlling the input reactive power and the output current to the inductive storage elements. Thus, compared to VSI techniques, the proposed reactive power compensation technique is more reliable and has a longer expected service life that is not limited by failure and wear-out modes of capacitors.

8.1 System description

Reactive power, denoted as volt ampere reactive (VAR) power, brings several undesirable consequences to an AC power system network such as the reduction of power transferring capability and increases in transmission line losses if not controlled

*Part of this section is reprinted with permission from M. B. Shadmand, R. S. Balog, and H. Abu Rub, "Model Predictive Control of a Capacitor-less VAR Compensator Based on a Matrix Converter," Industrial Electronics Conference (IECON), November, 2014, © 2014 IEEE and M. B. Shadmand, R. S. Balog, and H. Abu Rub, "Auto Tuning Approach of Cost Function Weight Factors in Model Predictive Control for Matrix Converter VAR Compensator Application," Energy Conversion Congress and Exposition (ECCE), September, 2015, © 2014 IEEE.

appropriately [142-144]. VAR compensation is a technique to control reactive power by supplying or absorbing VARs respectively to or from the AC network.

Within the literature, several compensation techniques have been proposed to supply or consume VARs to/from loads and transmission lines. Considering the reactive power compensation techniques listed in [145], candidate techniques include mechanically switched capacitors and reactors [145], synchronous condensers [146], static VAR compensators (SVCs) [143, 147], static synchronous compensators (STATCOMs) [148], and compensation using thyristor-based cycloconverters [149]. The STATCOM technique is based on a voltage-source inverter which performs as a controllable AC source in the network. Direct AC-AC cycloconverters [150] can be used instead of inverters; they can operate in the AC network to draw only reactive power by using a passive tank at the input side of the converter. However, although the cycloconverter is a compact solution for VAR compensation, one of the main drawbacks of the cycloconverter is the requirement of a large number of thyristor: 36 switches for a three-phase converter. The matrix converter (MC) [151, 152] also performs as an AC-AC converter which consists of an array of bidirectional switches. It is gaining popularity for different applications due to the following characteristics [152, 153]:

a. Compact and simple structure
b. It does not contain a DC link capacitor
c. High quality voltage and current delivery to load without frequency restriction
d. Regenerative load characteristics: it allows power to flow from source to the load and vice versa

e. Operation with unity power factor

As a silicon-intensive converter, the matrix converter also lends itself to integration, which improves the reliability and reduces cost over discretely built converter topologies. Thus, MCs are well-suited for power system applications.

Inductive loads which operate with lagging power factor consume VARs. Load compensation techniques employing capacitor banks locally supply VARs needed by the load. Capacitors are known to be unreliable components due to their inevitable aging an associated failure modes of increased leakage currents and electrolytic leakage, open circuits, short circuits, and open vents [154, 155]. The most frequent failure types are listed in [156]. Yet due to the high energy density and reasonable voltage rating of DC electrolytic capacitors, they are widely used in power electronics converters for VAR compensations. But approximately 60% of power electronic devices failures are due to the use of aluminum electrolytic DC capacitors [157]. The voltage-source inverter based STATCOM which uses DC electrolytic capacitors is vulnerable to this high-rate failure mode. Capacitors need to be replaced periodically and their health monitored [157-159] which adds additional cost to the system and decreases the reliability of the VAR compensation technique. Realizing a capacitor-less VAR compensation method is the chief motivation of the proposed section.

This section presents a STATCOM capacitor-less reactive power compensation technique that uses only inductors combined with a model predictive controlled matrix converter (MPC-MC). Inductors are known to be robust and reliable elements, but they consume reactive power and their operating behavior is opposite of capacitors. The

proposed technique interfaces a 3×3 direct matrix converter to the inductor bank, which is controlled by MPC. The general schematic of the proposed system is illustrated in Figure 101. The matrix converter is appropriately controlled by MPC to enable the input to output current phase inversion. By using the property of current phase reversal, the converter absorbs leading currents from the AC network while the inductor absorbs lagging current at the output side of the converter. As a result, the proposed VAR compensation by the matrix converter is achieved without using capacitors and provides a more reliable and robust technique for long service life of the device.

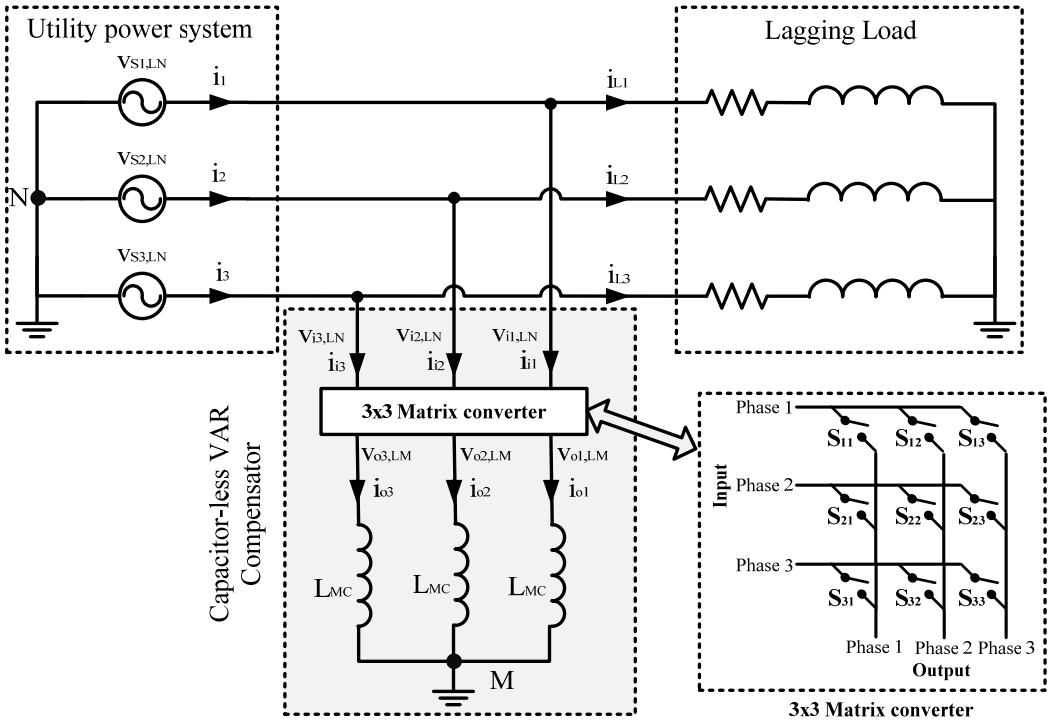

Figure 101: Proposed capacitor-less VAR compensator employing a matrix converter for the lagging load.

The system illustrated in Figure 101 consists of the three phase AC power network, an inductive lagging load, and the proposed reactive power compensator. The

AC system is assumed to operate at angular frequency ω. The line-neutral AC network voltages are denoted by $v_{S1,LN}$, $v_{S2,LN}$, and $v_{S3,LN}$, while the currents are given by i_1, i_2, and i_3. The currents drawn by the lagging load are denoted by i_{L1}, i_{L2}, and i_{L3}. The reactive power compensator consists of the inductors L_{MC} connected to the AC network through a 3×3 matrix converter. The line-neutral input voltages of the matrix converter are denoted by $v_{i1,LN}$, $v_{i2,LN}$, and $v_{i3,LN}$, while the output voltages are given by $v_{o1,LM}$, $v_{o2,LM}$, and $v_{o3,LM}$. The currents drawn by the matrix converter from the network are i_{i1}, i_{i2}, and i_{i3}, while the currents drawn by the choke from the matrix converter are given by i_{o1}, i_{o2}, and i_{o3}.

8.2 Matrix converter model

The matrix converter can be modeled as a mathematical transfer function, the *modulation matrix or instantaneous transfer matrix* **H**, which relates the input and output voltages:

$$\begin{bmatrix} v_{o1,LM} \\ v_{o2,LM} \\ v_{o3,LM} \end{bmatrix} = \mathbf{H} \times \begin{bmatrix} v_{i1,LN} \\ v_{i2,LN} \\ v_{i3,LN} \end{bmatrix}, \text{ where } \mathbf{H} = \mathbf{H}^T = \begin{bmatrix} H_1 & H_2 & H_3 \\ H_2 & H_3 & H_1 \\ H_3 & H_1 & H_2 \end{bmatrix} \qquad (106)$$

The modulation matrix $\boldsymbol{H}$ is symmetric constructed by three basic functions $\boldsymbol{H_1}$, $\boldsymbol{H_2}$, and $\boldsymbol{H_3}$ [160]:

$$\begin{aligned} H_1 &= \frac{1}{3}\left(1 + 2\left(\frac{V_o}{V_i}\right)\cos(2\omega t)\right) \\ H_2 &= \frac{1}{3}\left(1 + 2\left(\frac{V_o}{V_i}\right)\cos\left(2\omega t - \frac{2\pi}{3}\right)\right) \\ H_3 &= \frac{1}{3}\left(1 + 2\left(\frac{V_o}{V_i}\right)\cos\left(2\omega t + \frac{2\pi}{3}\right)\right) \end{aligned} \qquad (107)$$

The instantaneous powers are equal on the input and output sides because there are no energy storage elements in the matrix converter, and as a result, we can assume that there is no power loss in the converter. Consequently, by applying Kirchhoff's current law, the relationship between the input and output currents of the MC is given by

$$\begin{bmatrix} i_{i1} \\ i_{i2} \\ i_{i3} \end{bmatrix} = \mathbf{H}^T \times \begin{bmatrix} i_{o1} \\ i_{o2} \\ i_{o3} \end{bmatrix} \qquad (108)$$

where $\mathbf{H}^T$ is the transpose of the modulation matrix **H**.

The bidirectional switches turn "ON" and "OFF", operating with a high switching frequency, to generate a low frequency voltage with adjustable amplitude and frequency. The comprehensive working principle of MC is available in [152, 153].

Several papers in literature have investigated the model predictive control for MCs [22, 161-167]. The model predictive control for this MC is simple and based on the instantaneous relation of the input and output voltages/currents given by (106) and (107). The state of the switches should never short circuit input lines because this switching state will create short circuit currents. The output phase also cannot be open circuited. By keeping in mind these restrictions we can say that the 3×3 MC has 27 possible switching states to be considered during the prediction of variables and optimization of the cost function by MPC.

8.3 Inductive load model

A load model needs to be obtained in order to predict the value of the load current at the next step sampling interval for all 27 possible switching states. The inductive load at the output side of the MC can be represented as

$$L_{MC}\frac{di_o(t)}{dt} = v_{oLM}(t) - e(t) \qquad (109)$$

where L_{MC} is the inductance and e is the electromotive force (emf). By using the Euler forward method, the derivative in (109) can be approximated as

$$\frac{di_o(t)}{dt} \approx \frac{i_o(k+1) - i_o(k)}{T_S} \qquad (110)$$

where T_s is the sampling period. From (8) and (9) we can obtain:

$$\tilde{i}_o(k+1) = i_o(k) + \frac{T_S}{L_{MC}}(v_{oLM}(k) - \hat{e}(k)) \qquad (111)$$

Equation (111) estimates the value of the output current of MC for the next sampling interval, ($k+1$), and the corresponding voltage, $v_{o,LM}$, which is calculated for the 27 possible switching states of the MC. The value of the emf at the present sampling interval, $e(t)$, can be estimated to be approximately $e(t-1)$ for sufficiently small sampling time.

8.4 Model predictive control for the matrix converter

Control of reactive power and the output current are the objectives for the MPC in this work. The reactive power can be determined by

$$Q = \mathrm{Im}\left\{v_{iLN}(t).\bar{i}_i(t)\right\} \qquad (112)$$

Where $\bar{i}_i(t)$ is the complex conjugate of $i_i(t)$. The current phase reversal property of the matrix converter indicates that the $i_i(t)$ and $i_o(t)$ are out of phase, this property will be proved in next section of this paper. The reactive power can be predicted by using

$$\begin{aligned}\tilde{Q}(k+1) &= \mathrm{Im}\left\{v_{iLN}(k+1).\bar{i}_i(k+1)\right\} \\ &= v_{iLN\beta}(k+1)i_{i\alpha}(k+1) - v_{iLN\alpha}(k+1)i_{i\beta}(k+1)\end{aligned} \qquad (113)$$

where α and β correspond to the real and imaginary components of the associated vector. The value of $v_{iLN}(k+1)$ can be approximated to be $v_{iLN}(k)$ because the line voltages are low frequency signals compared to the switching frequency. By keeping in mind the current phase reversal property of the matrix converter and (10), the $i_i(t)$ can be calculated.

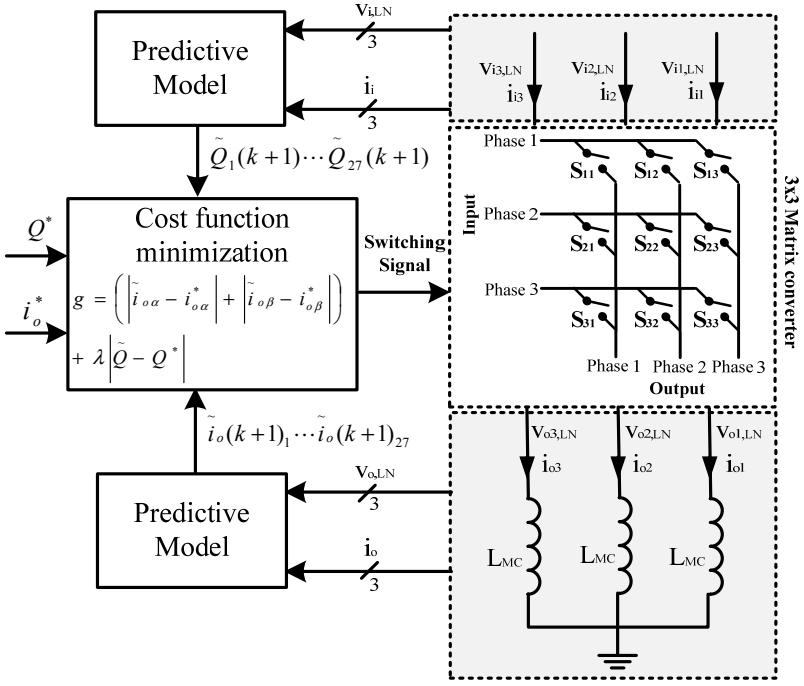

Figure 102: VAR compensator predictive control block diagram.

From (5), (10), and (12), the cost function *g* can be formed as

$$g = \left(\left|\tilde{i}_{o\alpha} - i^*_{o\alpha}\right| + \left|\tilde{i}_{o\beta} - i^*_{o\beta}\right|\right) + \lambda\left|\tilde{Q} - Q^*\right| \qquad (114)$$

The weight factor λ is needed in order to be deal with different units of the variables in the cost function; it also implies that a higher λ gives more priority to the

reactive power control. A block diagram of the predictive reactive control and current control strategy is illustrated in Figure 102. Weight factor is the only parameter in the cost function of the MPC that needs to be adjusted. The auto tuning of the weight factor is still an open topic for research [15, 168]. In this section the branch and bound technique is used to reduce the number of simulations and to obtain a suitable solution for the weight factor design [168]. In this procedure, first we assume a couple of initial values for λ, for example [(0.001,0.5),(1,10)]. Then, two measurements are conducted for the four values of λ to make sure that the controller accomplishes the system requirement. From the cost function (114) we can see that the current error can be measured in terms of total harmonic distortion (THD). The instantaneous reactive power is the second measurement. The two measurements evaluate the system behavior for each corresponding λ. Then these measurements are compared with maximum acceptable error; the weighting factor can be fitted into two intervals such as (0.001, 0.5). After that the measurements should be compared with a weighting factor equal to half of the new interval (λ=0.25). This procedure can be continued until an appropriate λ is determined. The procedure for determination of λ is briefly illustrated in Figure 103. In the following sections of this section, an auto tuning approach for weight factor will be presented.

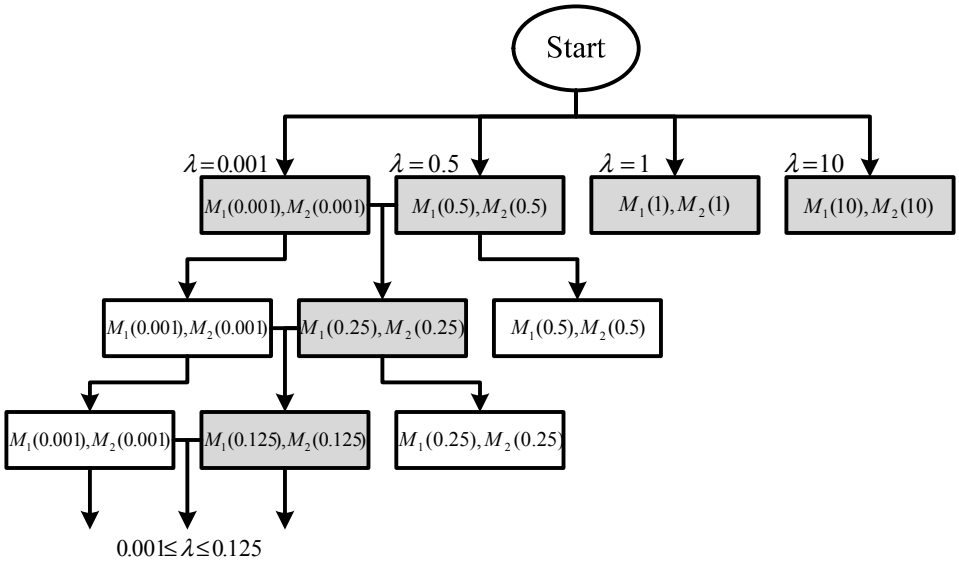

Figure 103: Procedure for weight factor (λ) selection.

The MPC algorithm for the matrix converter is detailed in Figure 104. Inside this loop we can see, after the determination of the cost function *g* for all 27 switching states, that an optimization should be performed to apply the optimal switching state. Figure 105 illustrates the prediction observation of the two control variables. As it is shown for each control variable, we have 27 different predictions at time (*k+1*). The distance of each of these points to the reference value is called the cost function at unity weight factor. The nearest point to the reference value which minimizes the cost function is the optimal value. Finally the optimizer will choose the optimal state according to the summation of the cost function (114) outputs in each round as shown in Figure 104.

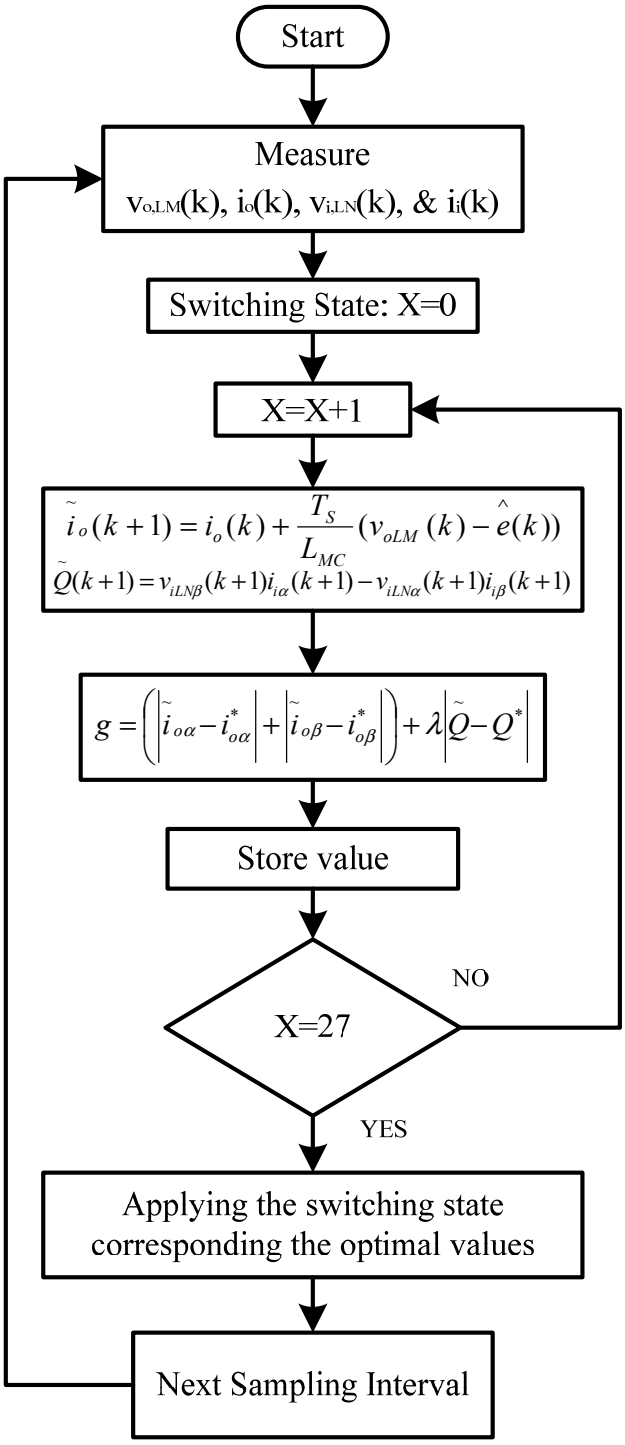

Figure 104: Model predictive control algorithm of the matrix converter.

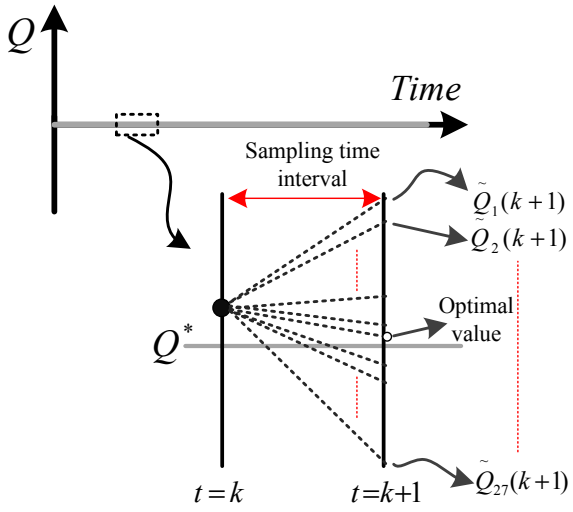

(a) Reactive power

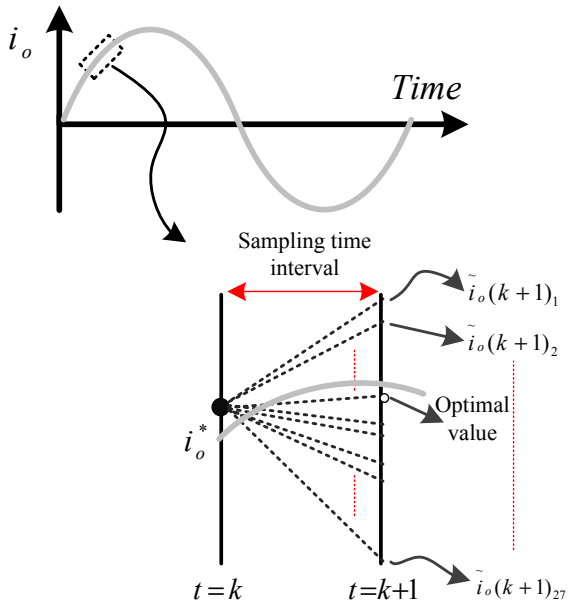

(b) Output current

Figure 105: Prediction observation.

8.5 Current phase reversal property

Let the AC utility power system voltages be given by (115) which are equal to input side MC voltages where $V_{LN,rms}$ is the line-neutral rms voltage.

$$
\begin{aligned}
v_{S1,LN} &= v_{i1,LN} = \sqrt{2}\times V_{LN,rms}\cos(\omega t) \\
v_{S2,LN} &= v_{i2,LN} = \sqrt{2}\times V_{LN,rms}\cos(\omega t - 2\pi/3) \\
v_{S3,LN} &= v_{i3,LN} = \sqrt{2}\times V_{LN,rms}\cos(\omega t + 2\pi/3)
\end{aligned}
\qquad (115)
$$

By using equation (116) and (117), application of the ***H*** matrix to the system in Figure 101, results in output voltages [160]:

$$
\begin{aligned}
v_{o1,LM} &= \sqrt{2}\times\frac{V_o}{V_i}\times V_{LN,rms}\cos(\omega t) \\
v_{o2,LM} &= \sqrt{2}\times\frac{V_o}{V_i}\times V_{LN,rms}\cos(\omega t - 2\pi/3) \\
v_{o3,LM} &= \sqrt{2}\times\frac{V_o}{V_i}\times V_{LN,rms}\cos(\omega t + 2\pi/3)
\end{aligned}
\qquad (116)
$$

The currents drawn by the inductor L_{MC} from the output of the MC are given by (117). Similarly by using equation (107) and (108), the input currents drawn by the MC from the AC network is determined and given by (118).

$$
\begin{aligned}
i_{o1} &= \sqrt{2}\times\frac{V_o}{V_i}\times\frac{V_{LN,rms}}{\omega L_{MC}}\times\cos(\omega t - \pi/2) \\
i_{o2} &= \sqrt{2}\times\frac{V_o}{V_i}\times\frac{V_{LN,rms}}{\omega L_{MC}}\times\cos(\omega t - \pi/2 - 2\pi/3) \\
i_{o3} &= \sqrt{2}\times\frac{V_o}{V_i}\times\frac{V_{LN,rms}}{\omega L_{MC}}\times\cos(\omega t - \pi/2 + 2\pi/3)
\end{aligned}
\qquad (117)
$$

$$
\begin{aligned}
i_{i1} &= \sqrt{2}\times\left(\frac{V_o}{V_i}\right)^2\times\frac{V_{LN,rms}}{\omega L_{MC}}\times\cos(\omega t + \pi/2) \\
i_{i2} &= \sqrt{2}\times\left(\frac{V_o}{V_i}\right)^2\times\frac{V_{LN,rms}}{\omega L_{MC}}\times\cos(\omega t + \pi/2 - 2\pi/3) \\
i_{i3} &= \sqrt{2}\times\left(\frac{V_o}{V_i}\right)^2\times\frac{V_{LN,rms}}{\omega L_{MC}}\times\cos(\omega t + \pi/2 + 2\pi/3)
\end{aligned}
\qquad (118)
$$

The output current i_{o1} can be expressed as a phasor by

$$
i_{o1} = \mathrm{Re}\left\{\sqrt{2}\times I_o\times e^{j(\omega t - \pi/2)}\right\} = \mathrm{Re}\left\{\sqrt{2}\times I_o e^{j\omega t}\times e^{-j\pi/2}\right\} \qquad (119)
$$

Where $I_o = \left(\frac{V_o}{V_i}\right) \times \frac{V_{LN,rms}}{\omega L_{MC}}$

$$\therefore \quad \tilde{I}_{o1} = I_o \angle -\pi/2 \tag{120}$$

Similarly, the input current i_{i1} can be expressed as a phasor

$$i_{i1} = \mathrm{Re}\left\{\sqrt{2} \times I_i \times e^{j(\omega t + \pi/2)}\right\} = \mathrm{Re}\left\{\sqrt{2} \times I_i e^{j\omega t} \times e^{j\pi/2}\right\} \tag{121}$$

where $I_i = \left(\frac{V_o}{V_i}\right)^2 \times \frac{V_{LN,rms}}{\omega L_{MC}} = qI_o$

$$\therefore \quad \tilde{I}_{i1} = \left(\frac{V_o}{V_i}\right) I_o \angle \pi/2 \tag{122}$$

The input and output voltages are in-phase from (115)-(116), the input currents of each phase indeed lead their corresponding phase input voltages by π/2 , thus power factor reversal from output to input side of MC is achieved. By comparing (119) and (121), it is obvious that there is a reversal in the sign of the phase angles of the output and input currents – the *current phase reversal property*. Comparing the voltage and current expressions, it can be seen that while the output currents lag the corresponding output voltages by π/2 radians, the input currents lead the corresponding input voltages by π/2 radians. This demonstrates that while the inductor L_{MC} draws VARs from the MC, the MC actually supplies VARs to the AC network – exhibiting the behavior of a capacitor.

The instantaneous input power of the compensator is given by:

$$p(t) = \left(\sqrt{2}\left(\frac{V_o}{V_i}\right)^2 \frac{V_{LN,rms}}{\omega L_{MC}} \times \cos(\omega t + \frac{\pi}{2})\right) \times \left(\sqrt{2} \times V_{LN,rms} \cos(\omega t)\right) \tag{123}$$

Using trigonometric identities, equation (123) can be re-arranged as:

$$p(t) = \frac{\left(\frac{V_o}{V_i}\right)^2 \left(V_{LN,rms}\right)^2}{\omega L_{MC}} \times (-) \sin(2\omega t) \tag{124}$$

The instantaneous input power of the compensator given by (124) indicates that the MC doesn't consume any real power, while it supplies required reactive power by the load to the AC network. The total three phase reactive power supplied by the MC to the AC network is given by

$$Q = 3 \times \frac{\left(\frac{V_o}{V_i}\right)^2 \left(V_{LN,rms}\right)^2}{\omega L_{MC}} \qquad (125)$$

Equation (125) presents that in order to compensate the lagging load with Q reactive power; an inductance of L_{MC} is required at the output of the MC. Thus considering (125), the required value of inductance at the output of MC can be determined for reactive power compensation.

8.6 Results of conventional optimization of the cost function

The system is mathematically modeled and simulated in Simulink-MATLAB. The MPC algorithm is implemented in an embedded MATLAB function in Simulink. The sampling time (T_S) of the MPC is 60 μs, other system parameters are given in Table 9.

Table 9. Parameters for the system in Figure 101.

PARAMETER	VALUE
Line-to-neutral grid voltage $V_{LN,rms}$	277.13 V
Angular frequency of grid voltage ω	2π*50 rad/s
Per-phase resistance of load $R_{Load,\ per\ phase}$	10 Ω
Per-phase inductance of load $L_{Load,\ per\ phase}$	30 mH
Total rated real power of load P_{Load}	2.2 kW
Power factor at the load side *p.f.*	0.9
Total maximum load reactive power requirement Q_{load}	2 kVAR
MC output-side inductance L_{MC}	30 mH
Sampling time (T_s)	60 μs
Weight factor λ	0.008

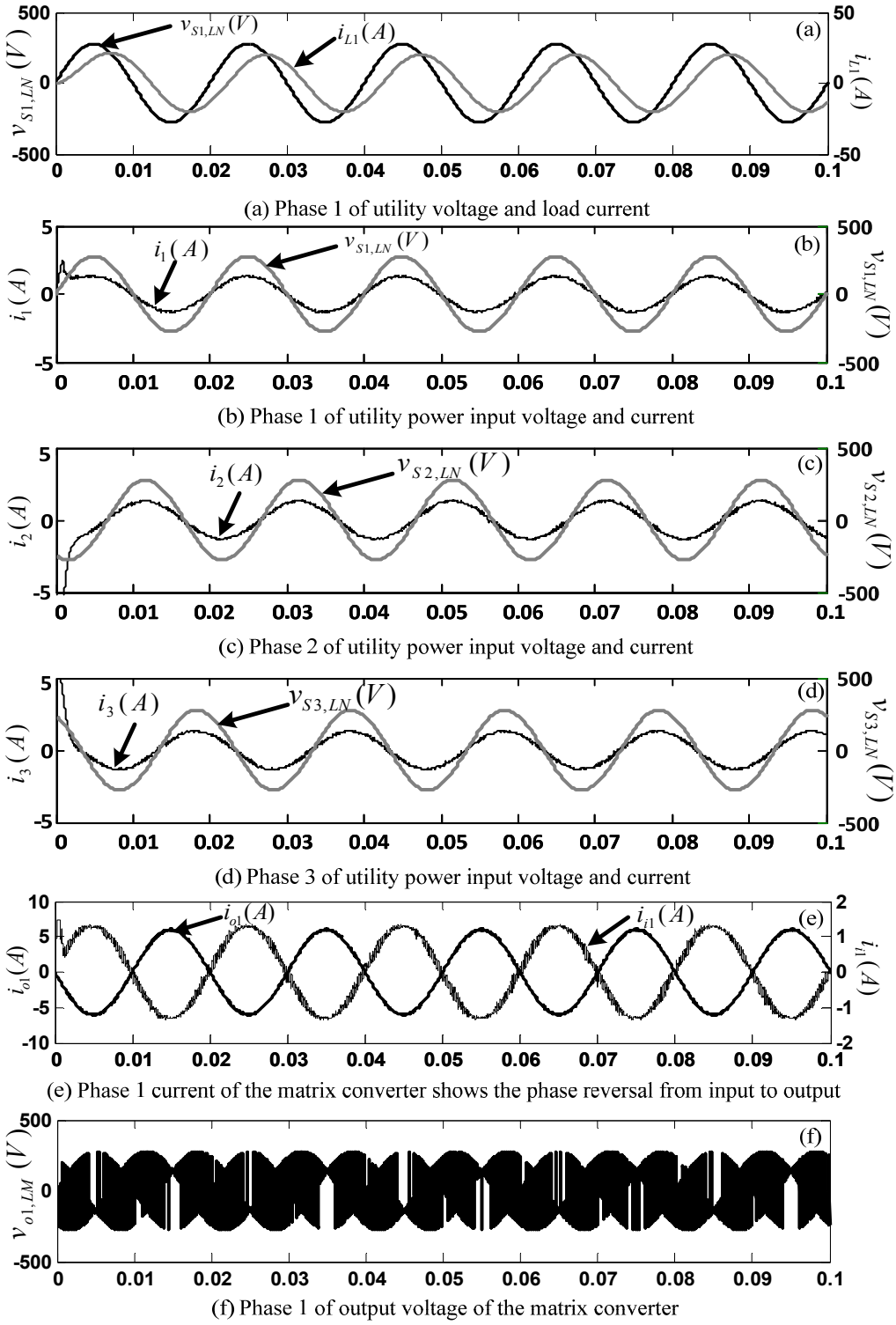

Figure 106: Simulation results.

By using the procedure of branch and bound explained earlier, the weight factor λ is determined to be 0.008, and the reference reactive power Q^* is zero VAR (unity PF). The lagging load power factor is illustrated in Figure 106 (a). Phase 1-3 of the utility voltage and load current are illustrated in Figure 106 (b-d) respectively. As it is shown and required for the VAR compensation they are in-phase. Thus the objective of capacitor-less VAR compensation is achieved. The current phase reversal property is illustrated in Figure 106 (e) which shows the input and output current of the matrix converter. The phase 1 of output voltage of the matrix converter is illustrated in Figure 106 (f). The simulation results are verified experimentally by implementing the control algorithm using dSPACE DS1006 and matrix converter hardware.

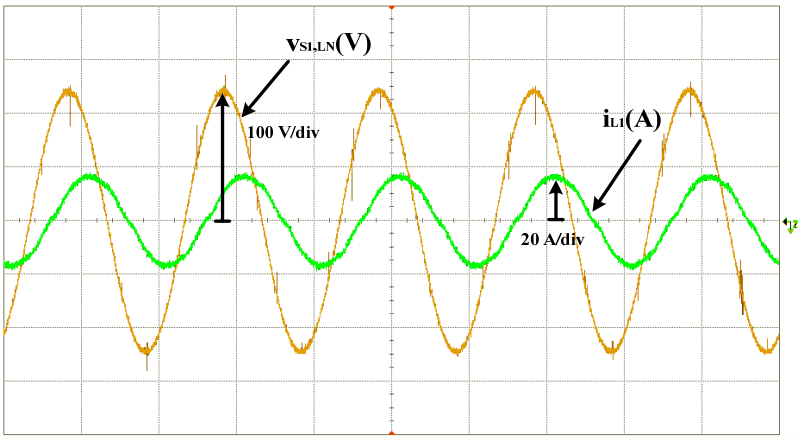

Figure 107: Experimental result of the system in Fig. 1, phase 1 of utility voltage and load current. The inductive load current lags the voltage.

Figure 107 illustrates the experimental results of phase 1 of the utility power input voltage and load current. Figure 108 and Figure 109 respectively demonstrate the experimental verification of output voltage of the 3x3 matrix converter, phase 1 of the

utility voltage and current. As it is illustrated in Fig. 10 the utility current is in-phase with utility voltage as a result they verify the MPC VAR compensation technique and simulation results.

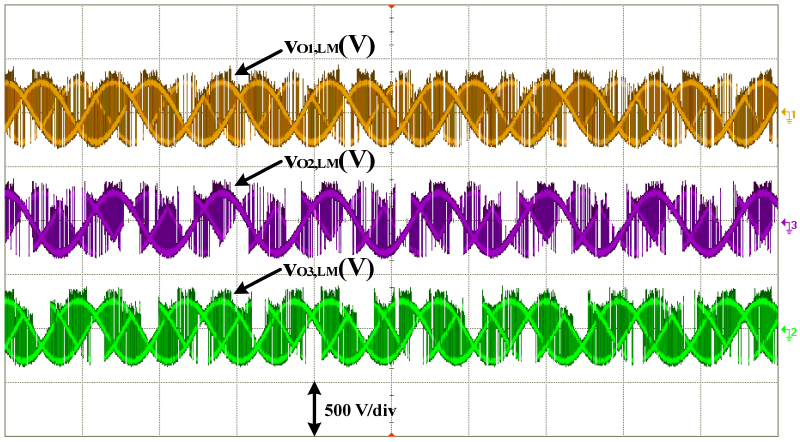

Figure 108: Experimental result of output voltages of matrix converter.

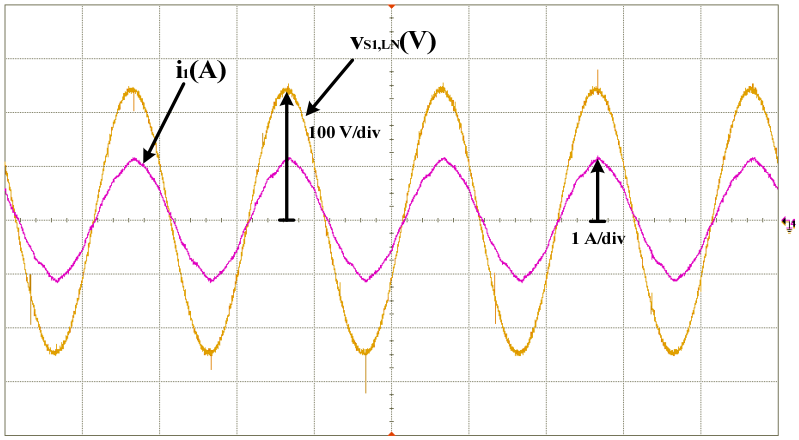

Figure 109: Experimental result showing the utility voltage and current. The utility current is in-phase with the voltage due to the VAR compensation of MPC-matrix converter.

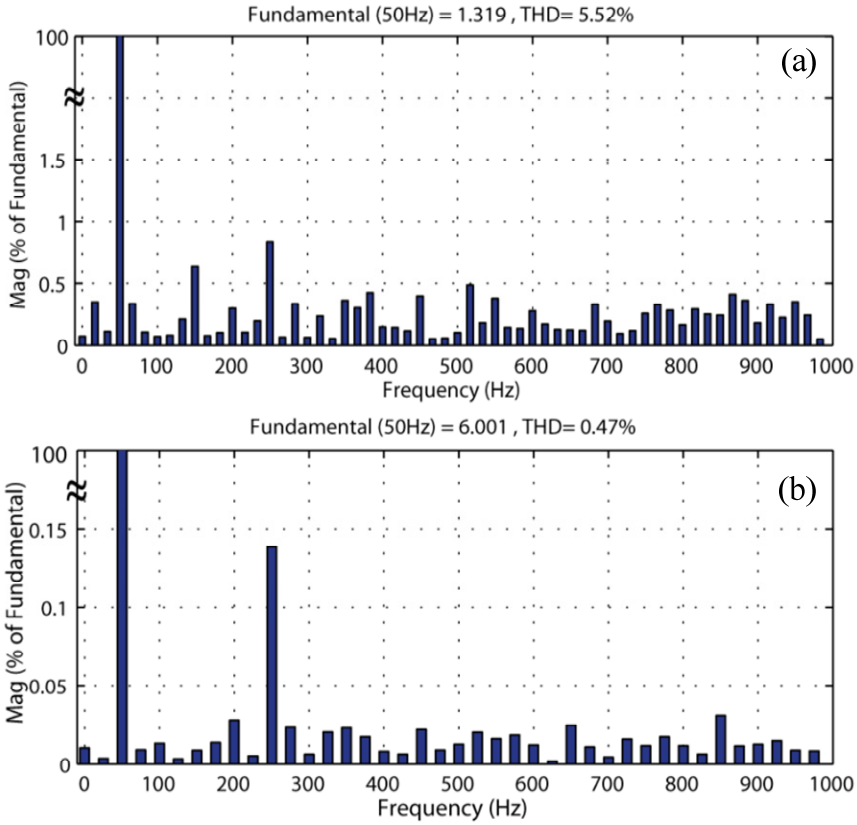

Figure 110: (a) Spectrum analysis of phase 1 of utility side current (i_1), (b) Spectrum analysis of phase 1 of matrix converter output current (i_{o1})

The spectrum analysis of phase 1 of the utility side current (i_1) and output current of the matrix converter (i_{o1}) are illustrated in Figure 110. These THD analyses are used to evaluate the performance of the current control. As it is shown, they have THD of 5.52% and 0.48% respectively which indicates good quality waveforms and meets the IEEE 519 standards [120].

8.7 Optimization of cost function by auto tuning of weight factor

This section presents an auto tuning technique for online selection of the cost function weight factors in model predictive control (MPC). The weight factors in the

cost function with multiple control objectives directly affect the performance and robustness of the MPC. The proposed method in this section determines the optimum weight factors of the cost function for each sampling time; the optimization of the weight factors is done based on the prediction of the absolute error of the optimization objective and the corresponding constraints. Without loss of generality, this technique is applied to the application considered in this section, a reactive power compensation technique using MPC of a direct matrix converter. The result demonstrates that the proposed auto tuning approach of cost function weights makes the control algorithm robust to parameter variation and other uncertainties such as load variation. The proposed capacitor-less reactive power compensator based on auto tuned MPC cost function weight factor is implemented experimentally using dSpace DS1007.

One of the important characteristics of MPC is the use of system models for optimal selection of switching state at each sampling time. This is one of the drawbacks of the MPC, because in some systems the parameters may vary and it is difficult to obtain their exact modeling. This issue reduces the performance of MPC with constant weight factor procedure. Weight factors in the cost function accommodate different units and scales as well as enable prioritization of specific control variables. However, selection of these weight factors is not straight forward [15]. Several empirical approaches to determine a fix weight factor using trial and error have been investigated in the literature [99]. However, a fixed weight factor is not robust to parameter variation and other uncertainties of the system.

The proposed dynamic weight factor selection of MPC algorithm for the matrix converter is detailed in Figure 111. The previously defined cost function (114) is divided into two parts as

$$g_1 = \left(\left| \tilde{i}_{o\alpha} - i^*_{o\alpha} \right| + \left| \tilde{i}_{o\beta} - i^*_{o\beta} \right| \right) \tag{126}$$

$$g_2 = \left| \tilde{Q} - Q^* \right| \tag{127}$$

In algorithm of auto selection of weight factor λ, indifference strategy between both objectives g_1 and g_2 is assumed. Constraint on the acceptable error of each term within the cost function can be considered in the control loop. The acceptable error in the tracking of current and reactive power is denoted by Ψ_1 and Ψ_2 respectively as following

$$g_1 = \left(\left| \tilde{i}_{o\alpha} - i^*_{o\alpha} \right| + \left| \tilde{i}_{o\beta} - i^*_{o\beta} \right| \right) \le \Psi_1 \tag{128}$$

$$g_2 = \left| \tilde{Q} - Q^* \right| \le \Psi_2 \tag{129}$$

Inside this loop, after the determination of the cost function g_1 and g_2 for all 27 switching states, the minimum value of g_2 will be selected.

$$\xi = \min g_2 \tag{130}$$

The next step is to evaluate the magnitude of minimum g_2 with a sufficiently small number ε_1 as following

$$\xi \le \varepsilon_1 \Rightarrow \lambda = \varepsilon_2 \tag{131}$$

The statement (131) is presenting that, if g_2 is small enough (less than a defined small number ε_1), then the weight factor λ is determined to be equal to a sufficiently small number ε_2, considering the fact that the g_2 is within an acceptable error range Ψ_2.

If the condition in (131) is not satisfied, a larger value for weight factor λ should be selected in order to give higher value to g_2 for minimization at the next sampling time k+1. This evaluation of ξ when its value is more than ε_1 is as following

$$\begin{aligned} &\xi \le 2\varepsilon_1 \Rightarrow \lambda = 2\varepsilon_2 \\ &\xi \le 3\varepsilon_1 \Rightarrow \lambda = 3\varepsilon_2 \\ &\quad \vdots \\ &\xi \le n\varepsilon_1 \Rightarrow \lambda = n\varepsilon_2 \\ &where: n \in \{1,2,3,\ldots,N\} \end{aligned} \qquad (132)$$

The statements in (132) quantized the ξ, which corresponds to the magnitude of g_2, the weight factor λ is determined based on ξ magnitude when comparing to n multiples of ε_1 till the statement in (132) is satisfied. The corresponding value of λ is multiplication of n by ε_2. This strategy for selecting the weight factor λ, based on the absolute error of g_2 is illustrated in right hand side of Figure 111.

After optimal determination of λ, the general form of cost function (114) will be constructed. Then an optimization should be performed to apply the optimal switching state. This procedure will be repeated every sampling time, thus during every sampling period the weight factor will be modified based on the predicted performance of the system at the next sampling time.

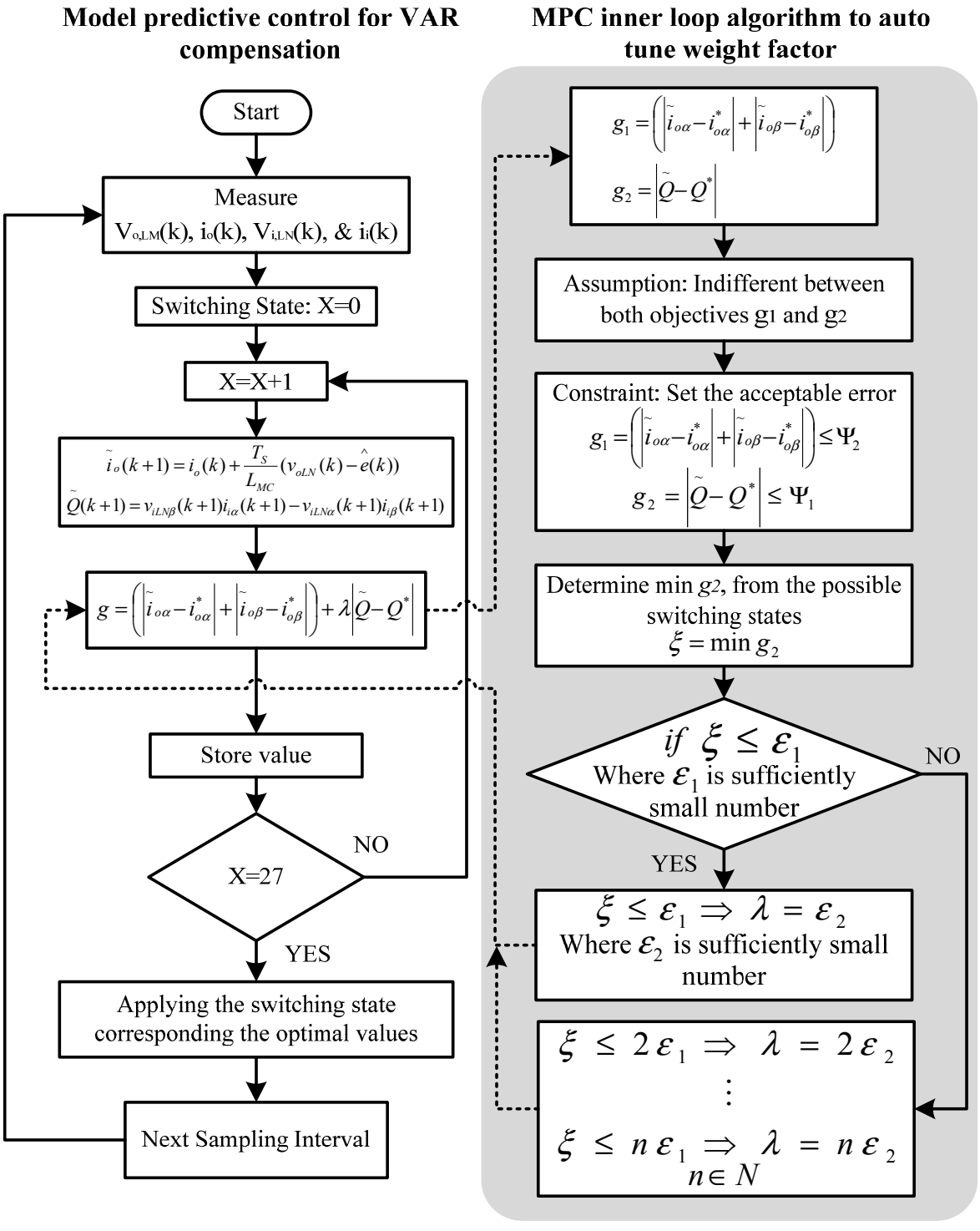

Figure 111: Model predictive control algorithm of the matrix converter for VAR compensation with dynamic weight factor selection

The system is mathematically modeled and simulated in Simulink-MATLAB. The sampling time (T_S) of the MPC is 60 μs, and other system parameters are given in Table 9. The proposed dynamic weight factor selection in this section illustrates that the effectiveness of model parameter errors on performance of the system is significantly reduced. In order to demonstrate this fact, the matrix converter output-side inductance is changed from 30 mH to 15 mH, while the nominal value is 30 mH.

The simulation results illustrated in Figure 112 demonstrate the MPC performance of reactive power compensation of matrix converter with conventional fixed weight factor selection based on try and error tuning method. The optimum weight factor based on conventional try and error approach is determined as 0.008 and the reference reactive power Q^* set as zero VAR (unity PF). Figure 112a and 112b demonstrate the phase 1 of utility side voltage and current which are required to be in-phase, in addition to the output voltage of matrix converter. At time 60 ms the inductance at the output side of the matrix converter dropped to 15 mH from its nominal value (30 mH), as it is shown in Figure 112a and 112b. After this parameter variation, the current became highly distorted.

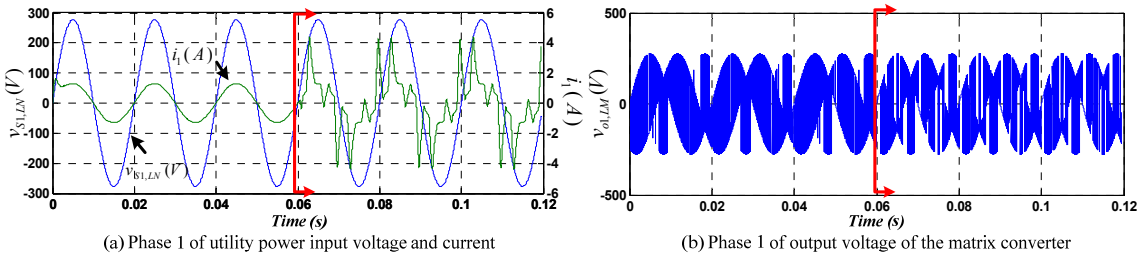

(a) Phase 1 of utility power input voltage and current

(b) Phase 1 of output voltage of the matrix converter

Figure 112: Simulation results of the conventional fixed weight factor for MPC cost function for VAR compensation by matrix converter.

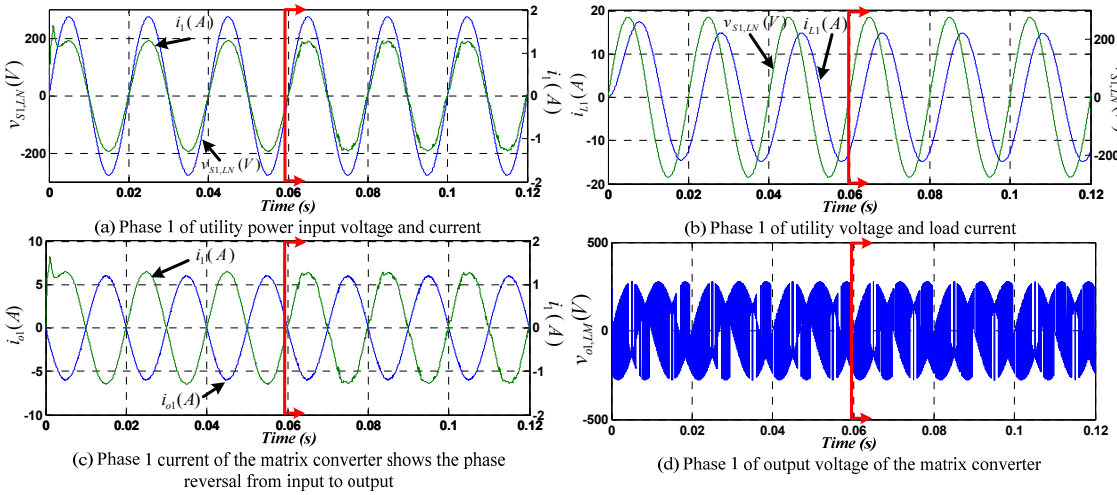

Figure 113: Simulation results of the proposed auto tuning approach of weight factor for MPC cost function for VAR compensation by matrix converter.

Now by using the proposed auto tuning approach of weight factor of MPC the distortion can be significantly reduced after inductance variation. The simulation results in Figure 114 demonstrate this fact. The cost function weight factor is updated instantaneously at each sampling time. Phase 1 of the utility voltage and load current are illustrated in Figure 114a, and the lagging load power factor is illustrated in Figure 114b. As it is shown and required for the VAR compensation the grid side voltage and current are in-phase with very small distortion after time 60 ms. Thus, a robust MPC with auto tuned cost function weight factor for the objective of capacitor-less VAR compensation is achieved. The current phase reversal property is illustrated in Figure 114c which shows the input and output current of the matrix converter. The phase 1 of output voltage of the matrix converter is illustrated in Figure 114d.

The simulation results are verified experimentally by real time implementing the control algorithm using dSPACE DS1007. Figure 115 illustrates the utility side voltage

and current and output voltage of matrix converter with fixed cost function weight factor under inductance variation. Figure 115 and Figure 116 demonstrate the utility side voltage and current, the output current of the matrix converter, the lagging power factor of the load, and the output voltage of the matrix converter with auto tuned cost function weight factor under inductance variation. It can be seen that not only with parameter variation and uncertainty the proposed approach shows better performance, but also before parameter variation with the proposed method the control objective is achieved with less absolute error. The spectrum analysis of phase 1 of the utility side current (i_1) before and after inductance change is illustrated in Figure 117 and Figure 118. These THD analyses are used to evaluate the performance of the current control. However after the inductance change the THD is increased from 1.67% to 4.37% but it meets the IEEE 519 standards limits [120].

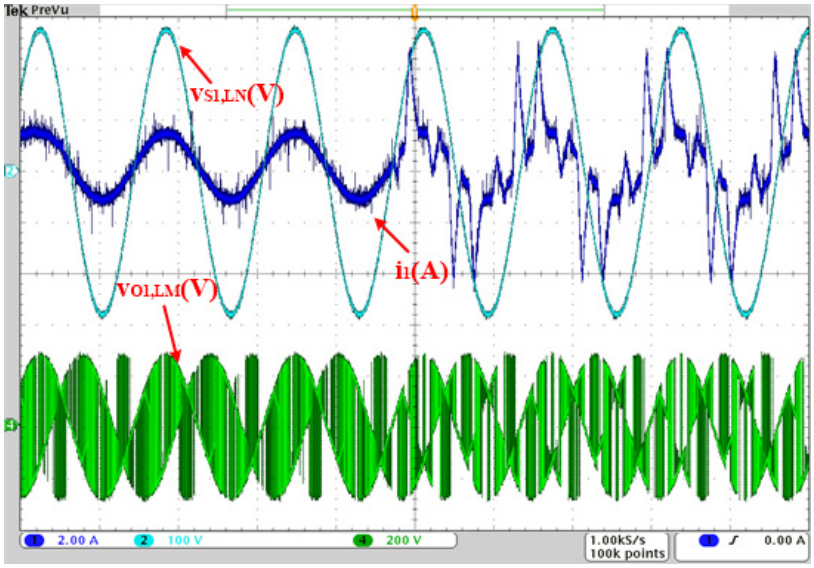

Figure 114: Phase 1 of grid side voltage and current and output voltage of matrix converter with fixed cost function weight factor under inductance variation.

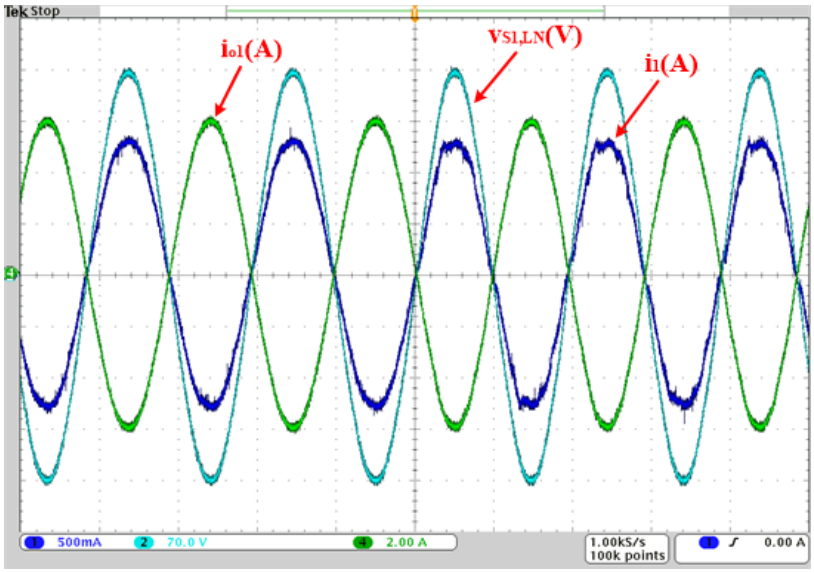

Figure 115: Phase 1 of grid side voltage and current and output current of matrix converter with auto-tuned cost function weight factor under inductance variation.

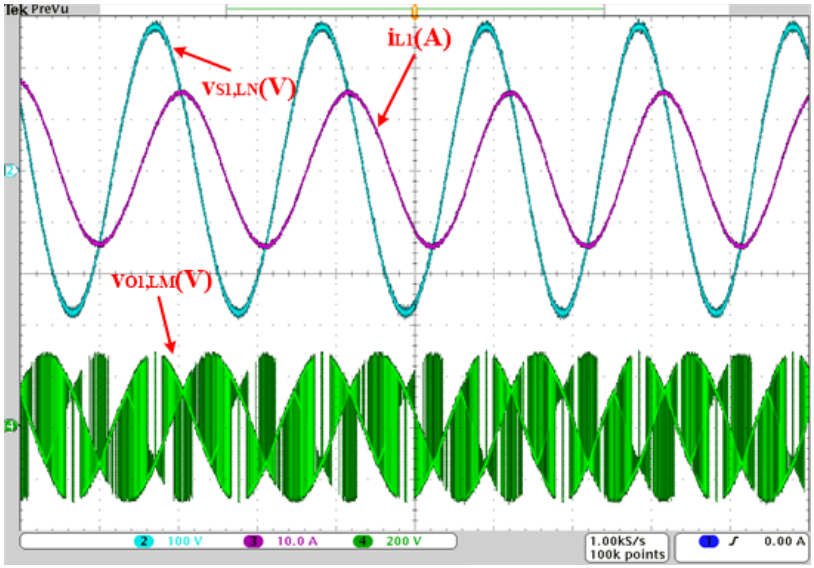

Figure 116: Phase 1 of grid side voltage, load current, and output voltage of matrix converter with auto-tuned cost function weight factor under inductance variation.

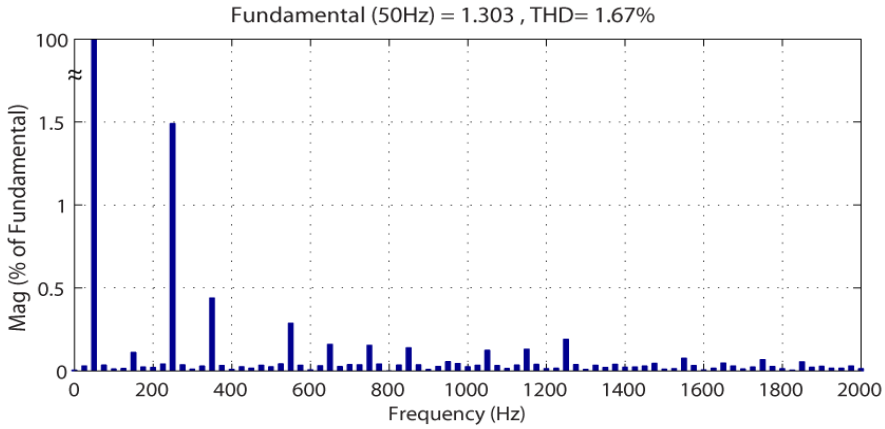

Figure 117: Spectrum analysis of phase 1 of utility side current (i_1), before change in inductance at time 60 ms.

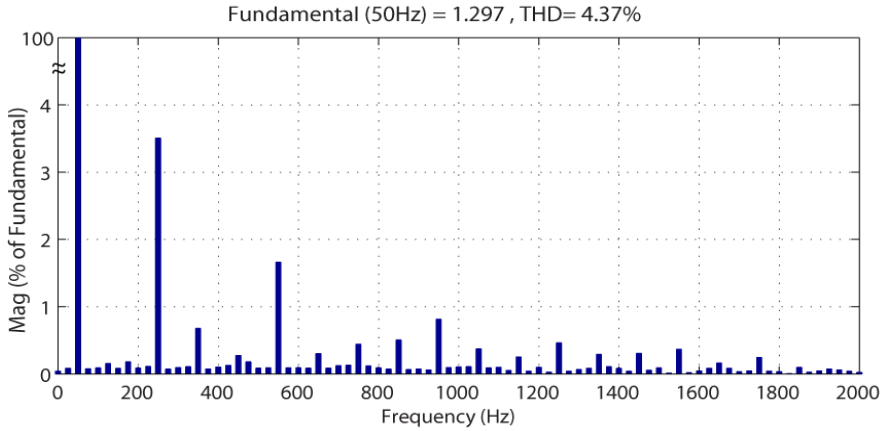

Figure 118: Spectrum analysis of phase 1 of utility side current (i_1), after change in inductance at time 60 ms.

8.8 Conclusion

Reactive power in the AC power system network, while fundamental to the system, is detrimental to the reliability, efficiency and overall performance of the AC network. This section presents a capacitor-less VAR compensation technique by using MPC of a direct matrix converter. Mathematical modeling of the matrix converter and the principle of MPC is presented. MPC of the matrix converter provides reactive power compensation by controlling the input reactive power and the output current into the inductive storage elements. The detailed algorithm of the predictive control for the VAR compensator matrix converter is proposed. The results show that the VAR compensation is achieved without using e-caps. The performance of MPC with multiple objectives in the cost function is directly affected by the weight factors. The proposed method in this section determines the optimum weight factor of the cost function at each sampling time, the optimization of weight factor is done based on the prediction of objectives absolute error and their corresponding constraints. Simulation results are validated experimentally using dSPACE DS1006 to implement the MPC for the direct matrix converter hardware to achieve capacitor-less VAR compensation.

9. HARMONICS CONSTRAINT MINIMUM ENERGY CONTROLLER FOR GRID-TIED INVERTER BY MEANS OF MODEL PREDICTIVE CONTROL*

Control of ac power in a grid-tied inverter often involves synchronous reference frame transformation, a process which requires phase-angle information typically provided by a Phase-Looked Loop (PLL). This section presents a decoupled real and reactive power control technique, for a single phase grid-tied inverter, using Model Predictive Control (MPC). The proposed technique does not use a PLL, PWM nor a synchronization transform, which makes the control algorithm well suited for an all-digital implementation. This section explores the proposed controller performance under distorted grid conditions and variations of system parameters. The results show that the proposed controller keeps good power tracking performance with small error in steady state and the grid side current Total Harmonic Distortion (THD) is within the IEEE-519 standards limits, which allows a much smaller dc-link capacitor to improve system's reliability and power density.

The dynamic performance and steady state stability of the proposed predictive controller are evaluated in this section. The tracking performance of the proposed controller is compared to the conventional PLL-based method, the result demonstrate significant improvement in the steady state power tracking when using the proposed

*Part of this section is reprinted with permission from X. Li, M. B. Shadmand, R. S. Balog, and H. Abu Rub, "Model Predictive Control for a single-phase Grid-tied Inverter," Power & Energy Conference at Illinois, February, 2014, © 2014 IEEE and X. Li, M. B. Shadmand, R. S. Balog, and H. Abu Rub, "Harmonics Constraint Minimum Energy Controller for Grid-tied Inverter by Means of Model Predictive Control Technique," Energy Conversion Congress and Exposition (ECCE), September, 2015, © 2015 IEEE.

controller. The simulation result is validated by implementing the control algorithm experimentally using dSPACE 1007.

9.1 System description

Interest in renewable energy resources like solar energy continues to gain popularity [5]. However, higher penetration of these systems will likely necessitate the regulation of the active and reactive power produced to maintain high power quality and reliable operation of the electrical grid. Many power control strategies for the single-phase inverter have been proposed over the past few decades [169-172]. In general, the control process requires the amplitude and phase angle information of the AC mains voltage captured by the phase-looked loop (PLL) [173]. However, the loop dynamics of the PLL module, a nonlinear subsystem, may prevent the inverter output current from adequately tracking the mains voltage [4]. In addition, some other control subsystems are necessary for PLL-based techniques including a properly tuned synchronous reference frame (SRF) and proportional-integral (PI) controller, pulse width modulation (PWM), and dc-link capacitor voltage control. Tuning and designing these modules to get the desired performance, trading off steady-state and transient performance, is challenging. Thus a control algorithm that eliminates the need for the PLL and SRF results in a system that overcomes the limitations of PLL-based methods.

The proposed MPC-based method in this paper is straightforward and completely eliminates the need for PI controllers and PWM modulation. In this paper, the MPC concept is applied for decoupled real and reactive power control of single-phase grid-tied inverter. Active power and reactive power of the inverter are controlled

independently. In addition, the synchronization function is embedded into the power control process, thus the PLL is not required.

The conventional H-bridge grid-tied inverter configuration is illustrated in Figure 119. Without loss of generality the dc bus could be fed by renewable energy resources such as photovoltaic or wind systems. There are numerous examples in the literature of inverter topologies capable of feed power produced from renewable sources to the ac power grid [118, 119, 174-176]. Table 10 provides a list of the output voltage V_o as a function of switching states and the function $\psi(t)$ which provides the desired polarity of the output voltage. The state of the switches are represented by 0 and 1, where state 0 means the switch is OFF, and state 1 means the switch is ON.

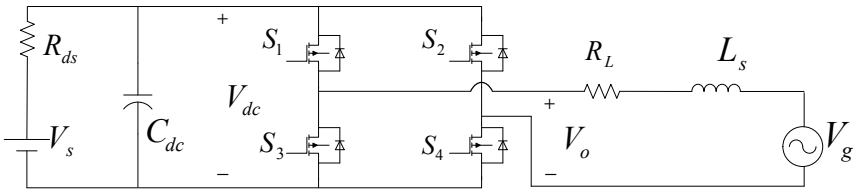

Figure 119: H-bridge grid-tied inverter configuration.

Table 10. Switching states of the grid-tied inverter.

	S_1	S_2	S_3	S_4	Ψ	V_o
State 1	0	0	1	1	0	0
State 2	1	1	0	0	0	0
State 3	1	0	0	1	1	V_{dc}
State 4	0	1	1	0	-1	$-V_{dc}$

The grid-connected inverter is controlled with MPC method. The reactive power reference command is typically provided by the grid operator or user. This can be set to

zero for unity, negative for leading, and positive for the lagging power factor. The active power reference is determined by the user or related with the instantaneous output power value feed to the system at the dc-link stage. As an example, for PV system application, the active power reference should be the maximum power point determined from maximum power point tracking (MPPT) algorithm [92].

9.2 Mathematical model of the system

In the stationary frame, the grid-connected inverter, illustrated in Figure 119, is modeled by the following equation, neglecting the effect of inductor resistor:

$$\frac{d}{dt} i_l(t) = \frac{1}{L_s}(V_o(t) - V_g(t)) \tag{133}$$

where i_l is the inductor current, V_o and V_g are the inverter output voltage and grid voltage respectively, L_s is grid side filter inductance. The inverter output voltage can be expressed in terms of a tri-state function and the dc-link voltage:

$$V_o = \psi(t) \times V_{dc} \tag{134}$$

where $\psi(t)$ is composed from the individual switching functions:

$$\psi(t) = S_1(t)S_4(t) - S_2(t)S_3(t) \tag{135}$$

By using the Euler forward method, the derivative in (133) can be approximated as

$$\frac{di_l(t)}{dt} \approx \frac{i_l(k+1) - i_l(k)}{T_S} \tag{136}$$

where T_s is the sampling period and k is discretized t. From (133)-(136), the discrete-time model of the inverter, now taking into consideration the series resistance of the inductor is given by

$$i_g(k+1) = \frac{T_s}{L_s}(V_o(k) - V_g(k) - i_g(k) \cdot R_L) + i_g(k) \qquad (137)$$

In order to control the output reactive power of the single-phase grid-connected inverter, orthogonal signal generation (OSG) sub-systems are used to create two orthogonal reference signals for each of the grid voltage and grid current. As such, the two voltage signals are orthogonal to each other, as are the two current signals, but there is no constrained relationship of the current to voltage yet. From these reference signals, the grid reactive power values are calculated as

$$P = \frac{1}{2}(V_{g-\alpha} \times I_{g-\alpha} + V_{g-\beta} \times I_{g-\beta}) \qquad (138)$$

$$Q = \frac{1}{2}(V_{g-\beta} \times I_{g-\alpha} - V_{g-\alpha} \times I_{g-\beta}) \qquad (139)$$

where $V_{g\text{-}\alpha}$ and $V_{g\text{-}\beta}$ are the output signals of the OSG module with V_g input, $I_{g\text{-}\alpha}$ and $I_{g\text{-}\beta}$ are the output signals of the OSG module with I_g input.

9.3 Model predictive decoupled power control

9.3.1 Controller design

Control of real and reactive power using MPC is the objective for this paper. The instantaneous real and reactive power are defined as

$$\begin{aligned} P &= \mathrm{Re}\left\{ v_g(t) . \bar{i}_g(t) \right\} \\ Q &= \mathrm{Im}\left\{ v_g(t) . \bar{i}_g(t) \right\} \end{aligned} \qquad (140)$$

where $\bar{i}_g(t)$ is the complex conjugate of $i_g(t)$. The reactive power can be predicted using the OSG reference signals

$$\tilde{P}(k+1) = v_{g-\alpha}(k+1)i_{g-\alpha}(k+1) + v_{g-\beta}(k+1)i_{g-\beta}(k+1)$$
$$\tilde{Q}(k+1) = v_{g-\beta}(k+1)i_{g-\alpha}(k+1) - v_{g-\alpha}(k+1)i_{g-\beta}(k+1) \quad (141)$$

where α and β are the orthogonal signals and represent the real and imaginary components of the associated voltage and current. The value of $v_g(k+1)$ can be approximated to be $v_g(k)$ because the line voltage varies at low frequency compared to the switching frequency and thus is approximately constant from switch event to switch event.

The cost function g, which is to be minimized, is formulated from active and reactive power terms:

$$g(k+1) = \frac{1}{P_{rated}}\left|P_{ref}(k+1) - P_{out}(k+1)\right| + \lambda\frac{1}{Q_{rated}}\left|Q_{ref}(k+1) - Q_{out}(k+1)\right| \quad (142)$$

where λ is the weighting factor of reactive power . Weighting factor is the only parameter in the cost function of the MPC that needs to be selected.

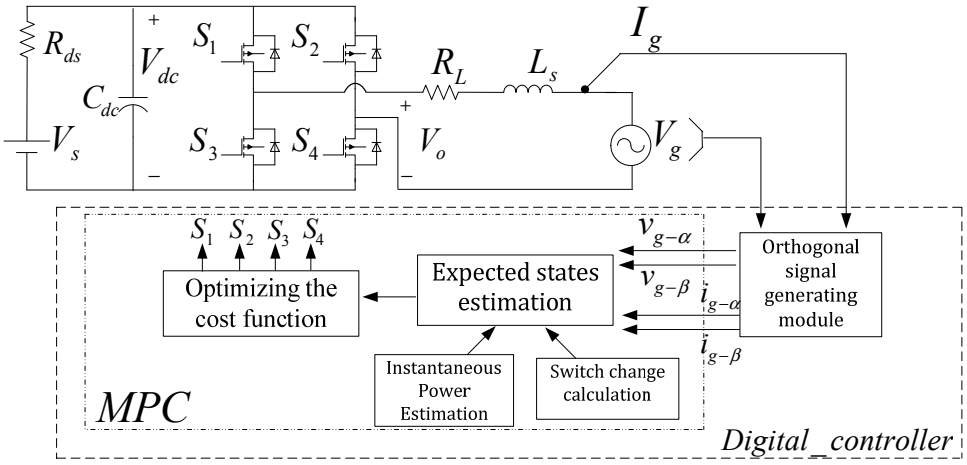

Figure 120: Block diagram of MPC for grid-tied inverter.

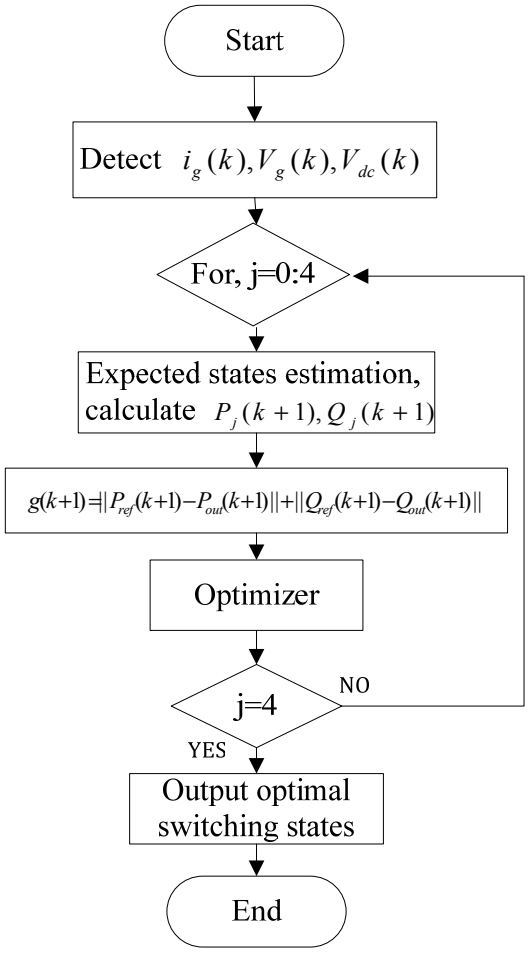

Figure 121: Structure of MPC controller for grid-tied inverter.

The block diagram of MPC for grid-tied inverter is illustrated in Figure 120. The summary of control algorithm is illustrated in Figure 121 and can be described as:

- Detect grid current and voltage.
- Use discrete-time model of the system to predict the grid current and voltage of the next sampling in horizon of time.
- Based on predicted grid current and voltage values, calculate the predicted real and reactive power for each possible switching state using equation (142).

- Determine cost function *g* for each possible switching state.
- Determine the switching state that minimize the cost function *g*, and apply the optimal switching state to the inverter.

9.3.2 Results and discussion

The proposed controller is modeled in MATLAB-Simulink; the parameters of the system are given in the Table 11. The performance of the proposed controller is compared to the conventional PLL-based method for three different case studies: ideal grid voltage without distortion, distorted grid voltage, and pulsating dc-link voltage. In addition, the effect of system model parameter variation on the current THD and power ripple is studied.

Table 11. System parameters.

Parameters	Value
V_{dc}	400 V
L_s	11mH
R_L	0.5 ohm
V_g	300 V
f_g	60 Hz
T_S	15 µs

For the first case study, the simulation results of conventional PLL-based method and proposed MPC-based method are presented in Figure 122 and Figure 123 respectively. In order to study the dynamic performance, at time 0.15 s, the reference active and reactive power changed from 0 VAR to 200 VAR and from 800 W to 500 W respectively. The results demonstrate, however both controller techniques have almost similar dynamic behavior, but the proposed predictive controller has much better steady state performance with smaller power ripple and tracking error.

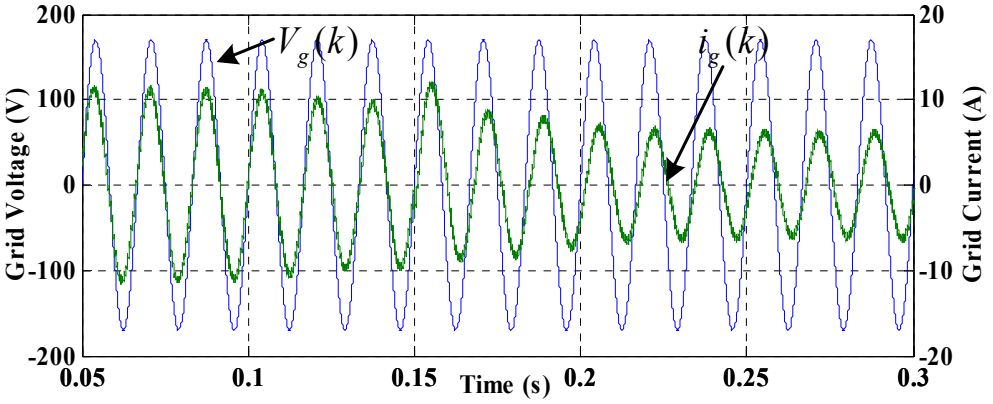

(a) Grid-side voltage and current

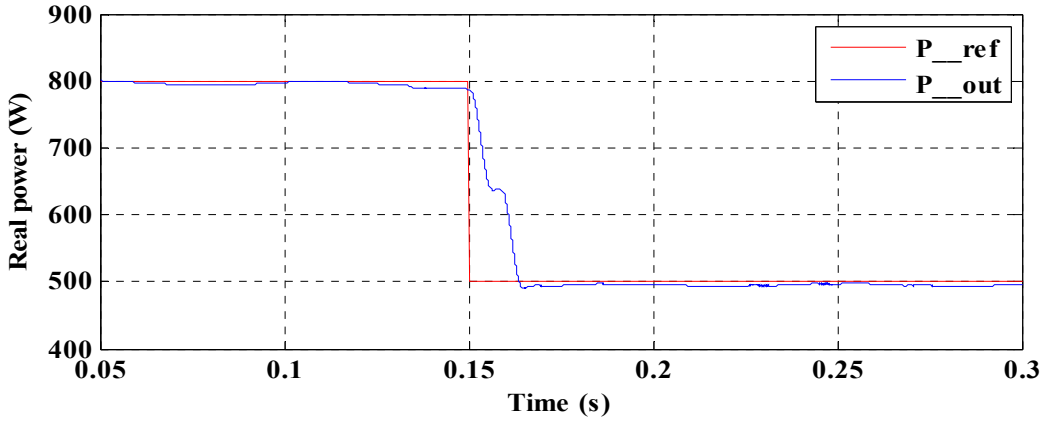

(b) Real power

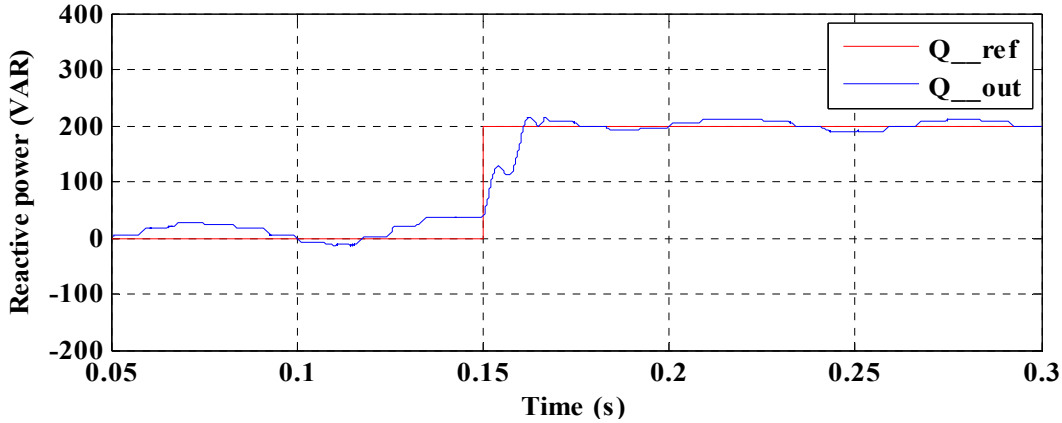

(c) Reactive power

Figure 122: Conventional PLL controller for ideal grid voltage (case study 1).

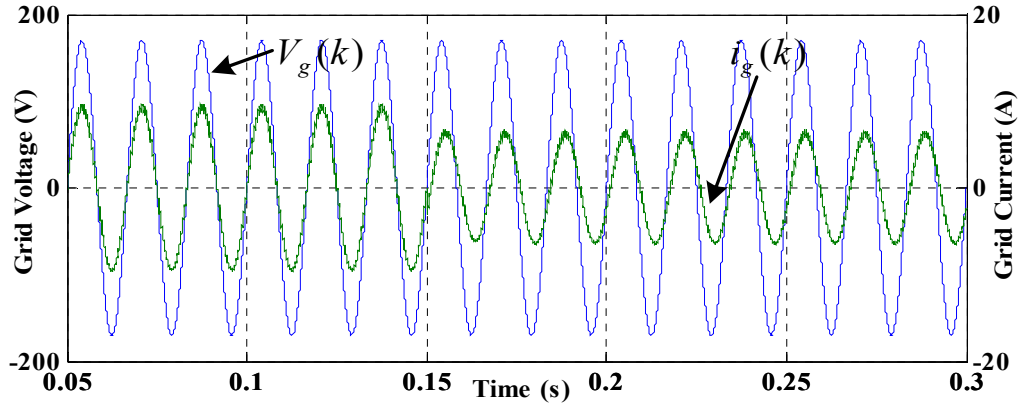

(a) Grid-side voltage and current

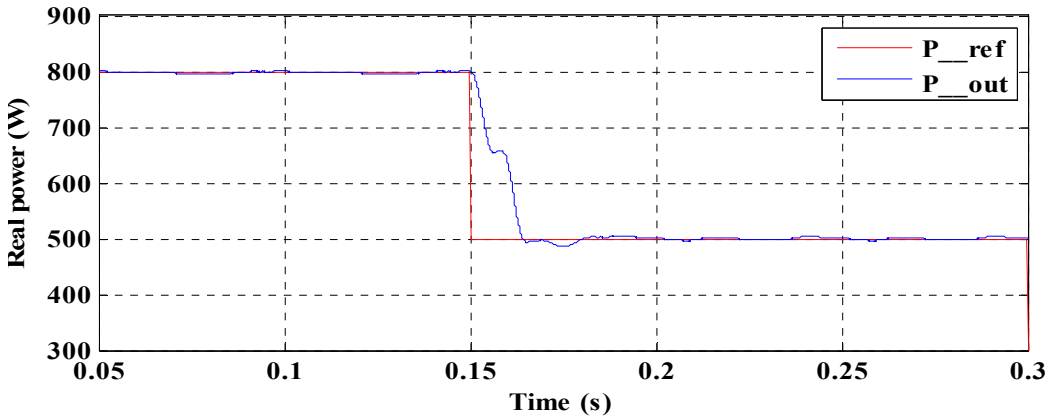

(b) Real power

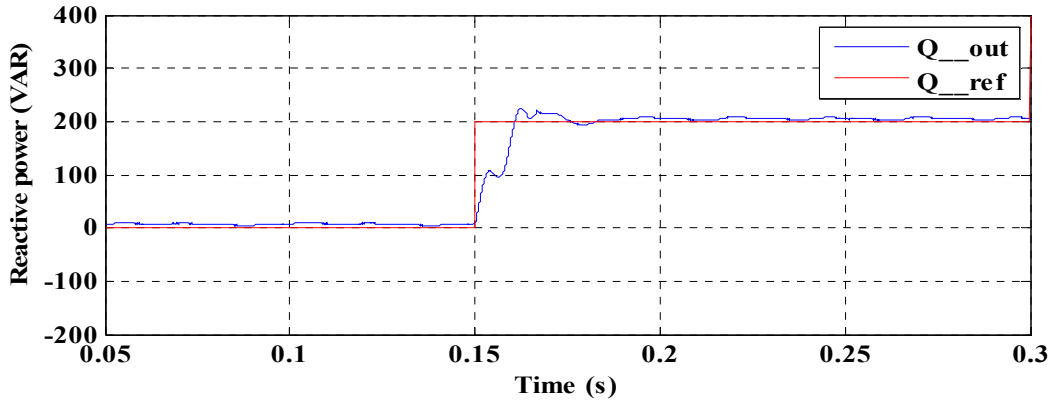

(c) Reactive power

Figure 123: MPC for ideal grid voltage (case study 1).

The second case study is to investigate the performance of proposed controller and PLL-based controller when the grid side voltage is distorted. The simulation results are presented in Figure 124 and Figure 125. The grid voltage is initially ideal without any distortion, then at time 0.5 s to 0.6 s, the ideal grid is combined with 4% 3^{rd}, 4% 5^{th}, 3% 7^{th} and 3% 11^{th} order harmonics. At time 0.6 s the grid resumes to the ideal condition without these harmonic components. The simulation result of this case study presents that the grid current is highly distorted with PLL technique and the power tracking error is high compared to the proposed predictive controller.

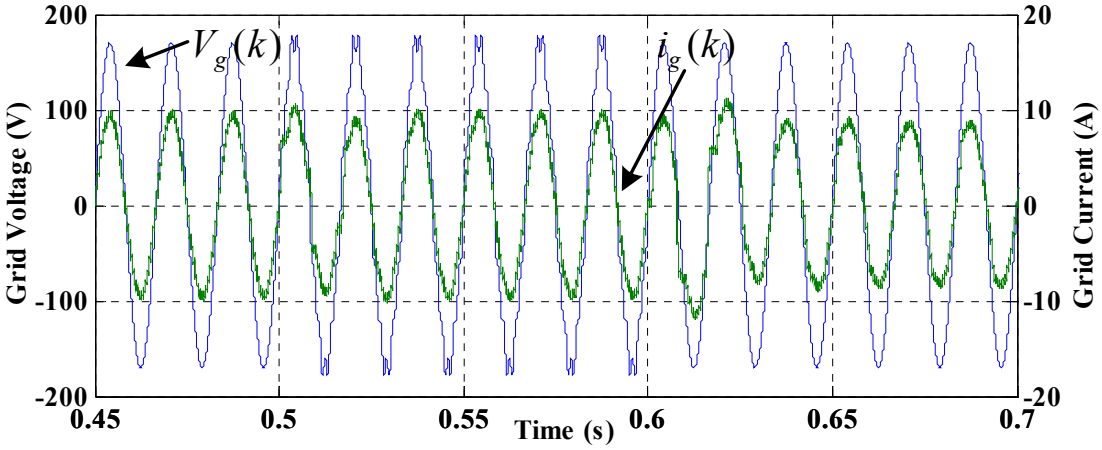

(a) Grid-side voltage and current

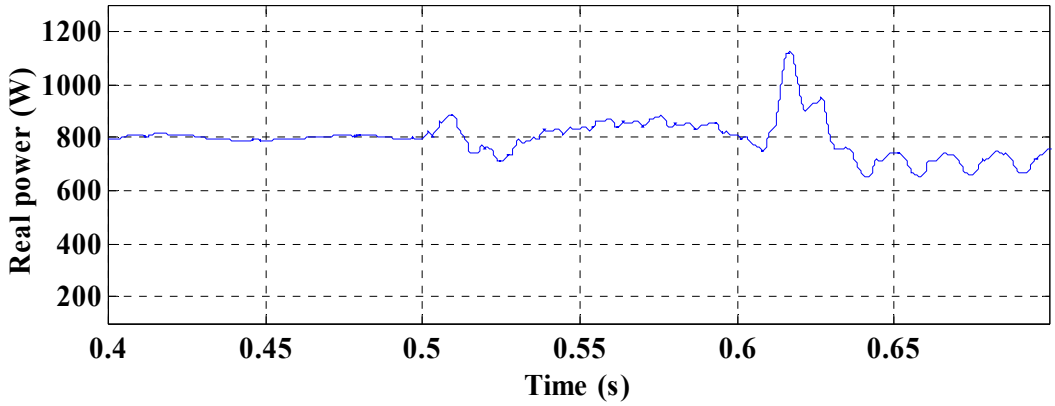

(b) Real power

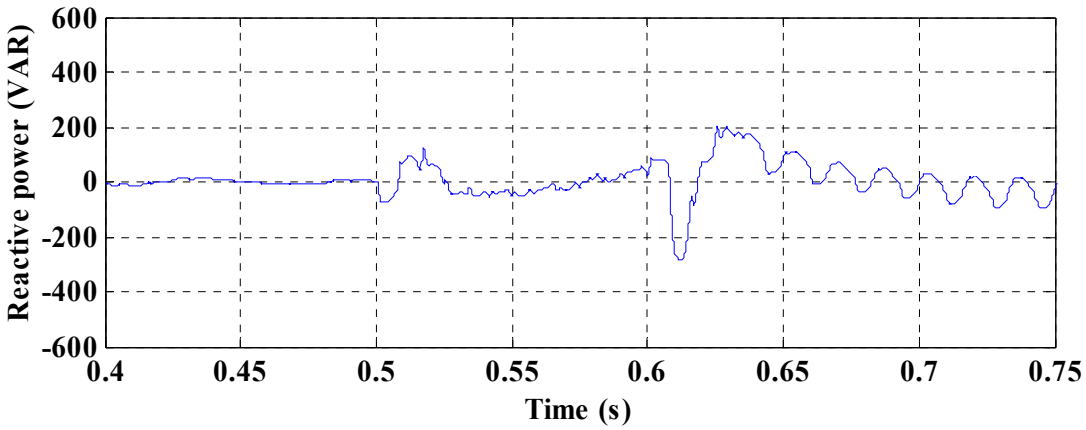

(c) Reactive power

Figure 124: Conventional PLL controller for distorted grid voltage (case study 2).

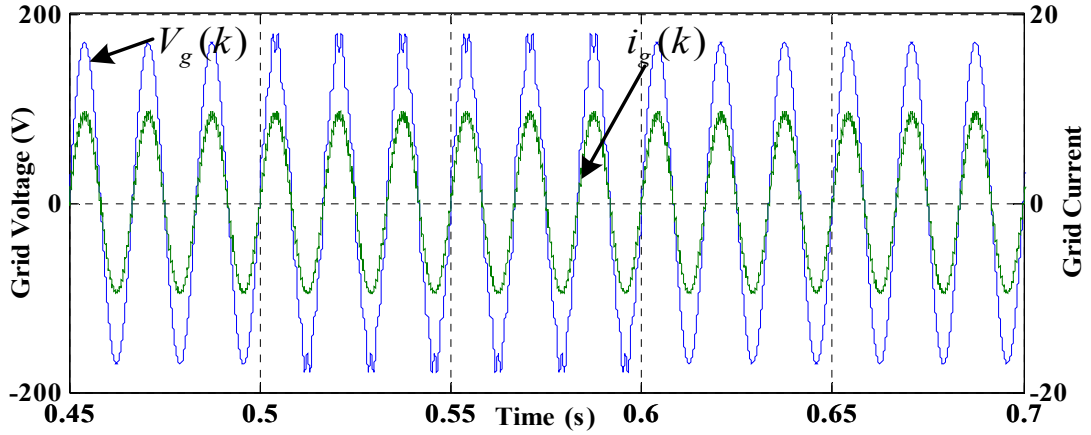

(a) Grid-side voltage and current

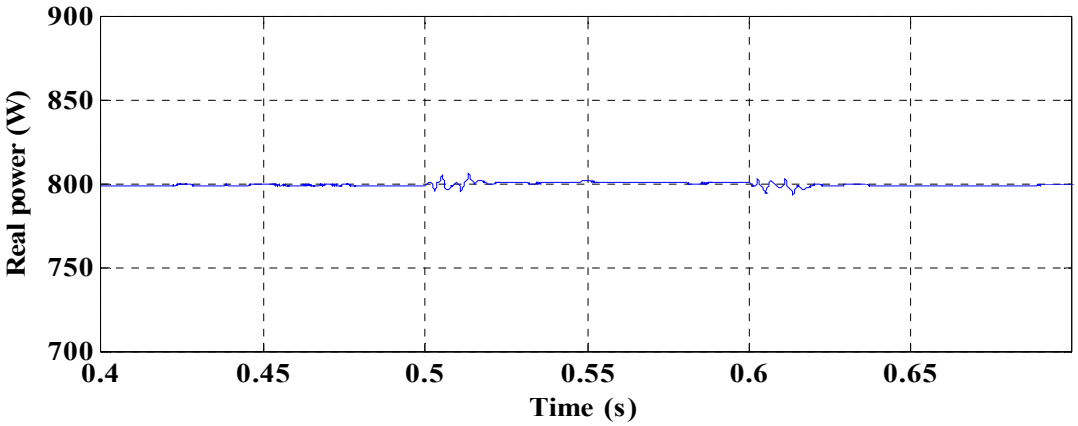

(b) Real power

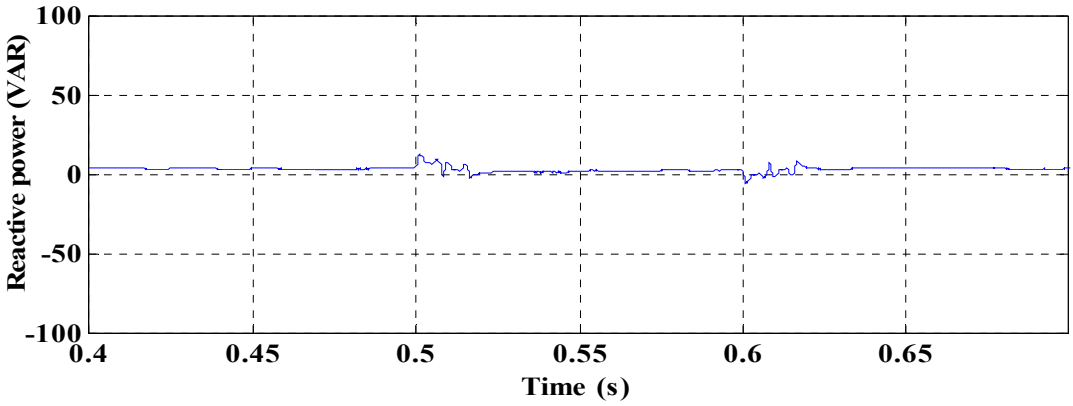

(c) Reactive power

Figure 125: MPC for distorted grid voltage (case study 2).

The spectral analyses of the grid side current for distorted grid voltage are illustrated in Figure 126 and Figure 127 to evaluate the performance of the current control. The THD is 1.98% which is within the IEEE-519 standards limits [120].

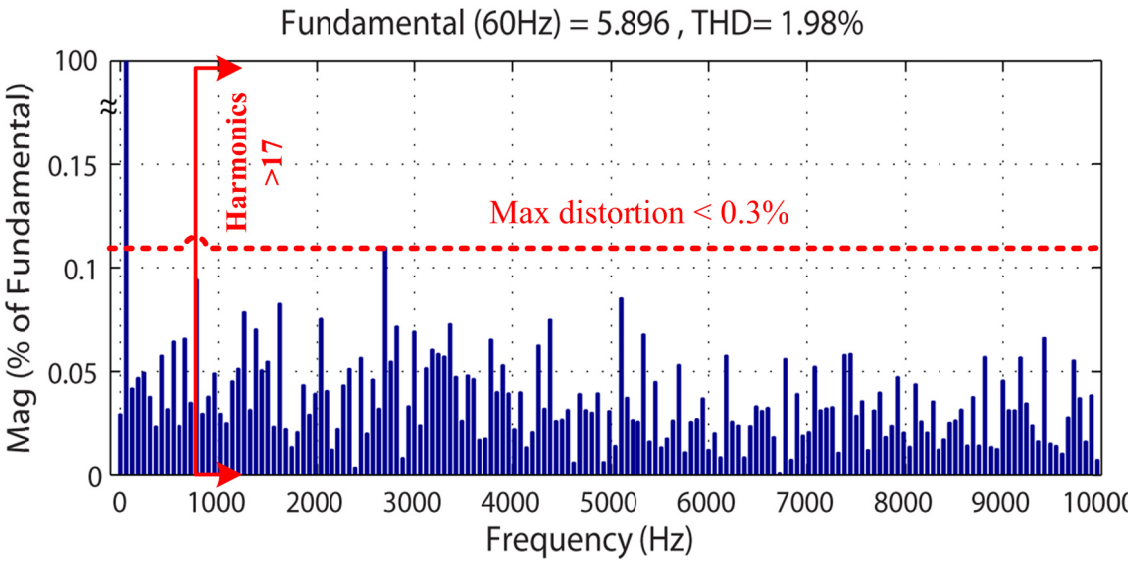

Figure 126: Spectral analysis of grid side current for distorted grid-side voltage (case study 2)

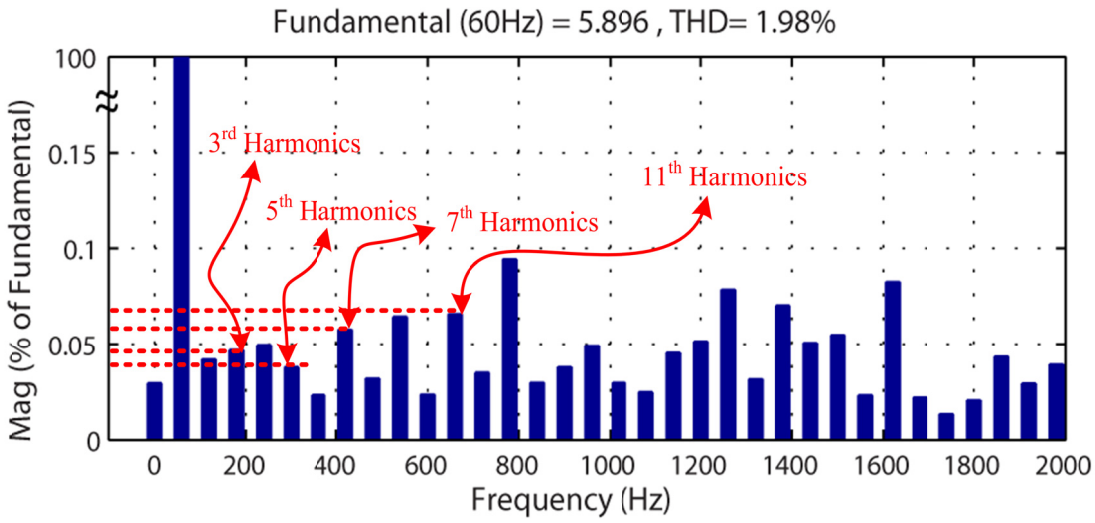

Figure 127: Spectral analysis of grid side current at low frequency for distorted grid-side voltage (case study 2).

The third case study is to determine the proposed MPC performance for the pulsating dc-link voltage. The dc-link voltage in this case is not pure constant and has some variation as presented in Figure 128. The simulation results of dynamic performance and steady state are presented in

Figure 129. A step change is applied to the reference values of active and reactive power at time 0.15 s. The reactive power reference value is changed from 200 VAR to 400 VAR and real power reference value is changed from 600 W to 0 W. However in this case, the steady state error of the control variables is larger than the ideal case, but still both the dynamic and steady state performance are comparable to the ideal case.

One of the main drawbacks of MPC is the effect of model parameters error on the performance of the system. In this paper, the effect of uncertainty in the filter inductance value L_s and its resistance value R_L are studied. The effect of inductor resistance value on the grid side current THD and power ripple is illustrated in Figure 130. The R_L of 100% means that there is no error in R_L value and as a result the THD and power ripple had the minimum possible value. Then THD and power ripple for R_L of 50% to 150% of its nominal value (100%) are evaluated and presented in Fig. 13.

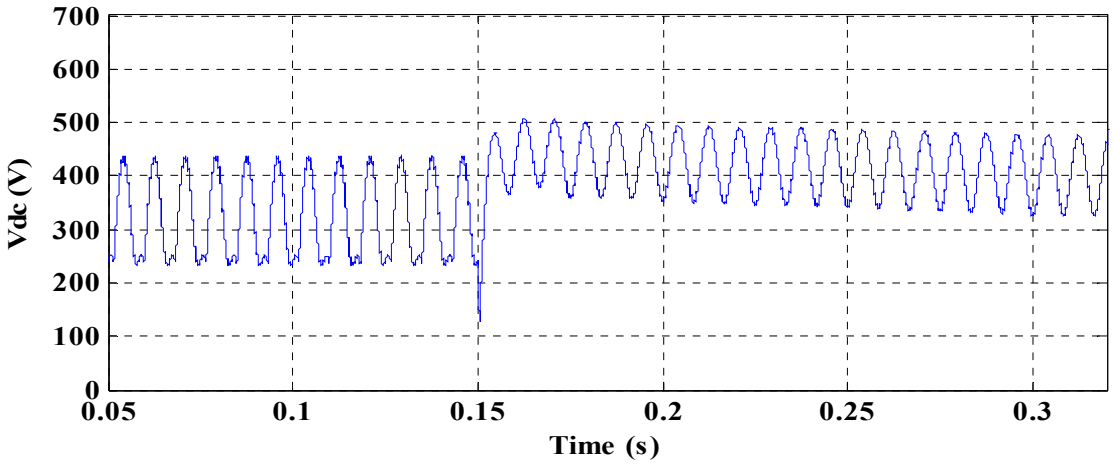

Figure 128: Case study 3: pulsating dc-link voltage

Fig. 14 presents the inductance parameter uncertainty effect on THD and power ripple, similarly the 100% inductance means there is no error or variation in this parameter. At this point the power ripple is minimum only, but the THD is not minimum. This is due to the fact that higher inductance value will result in smoother grid current. The THD and power ripple of 50% to 150% of inductance nominal value (100%) are investigated and presented in Fig. 14. The results demonstrate the model parameter error may decrease the performance of the proposed MPC technique, but the grid side current THD is still within the IEEE-519 standards [120].

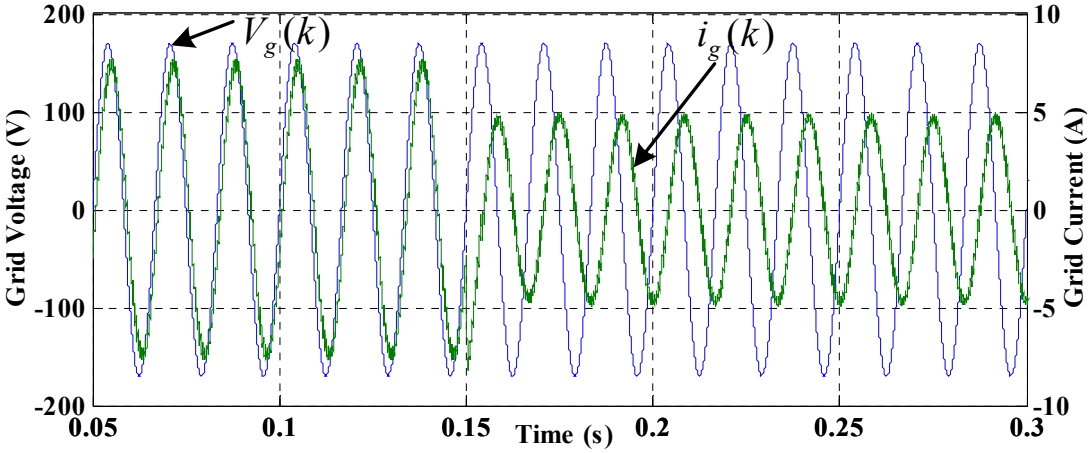

(a) Grid-side voltage and current

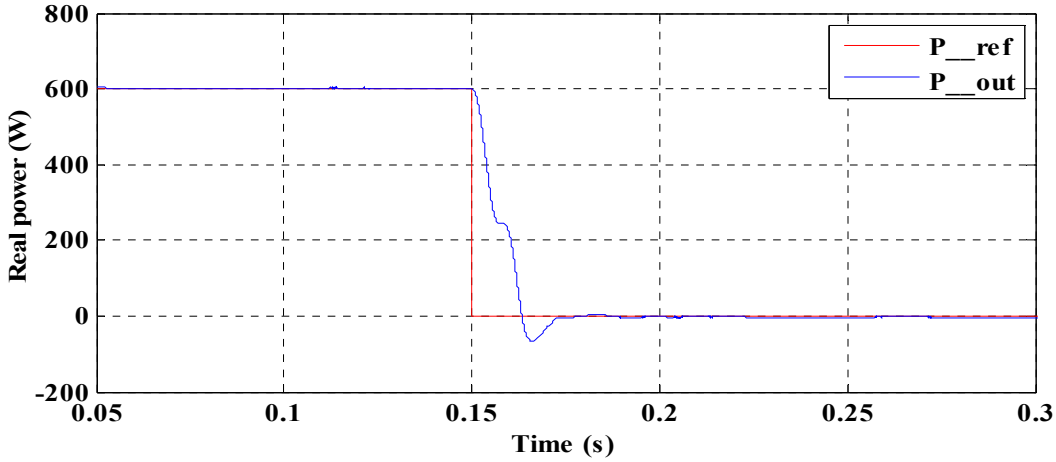

(b) Real power

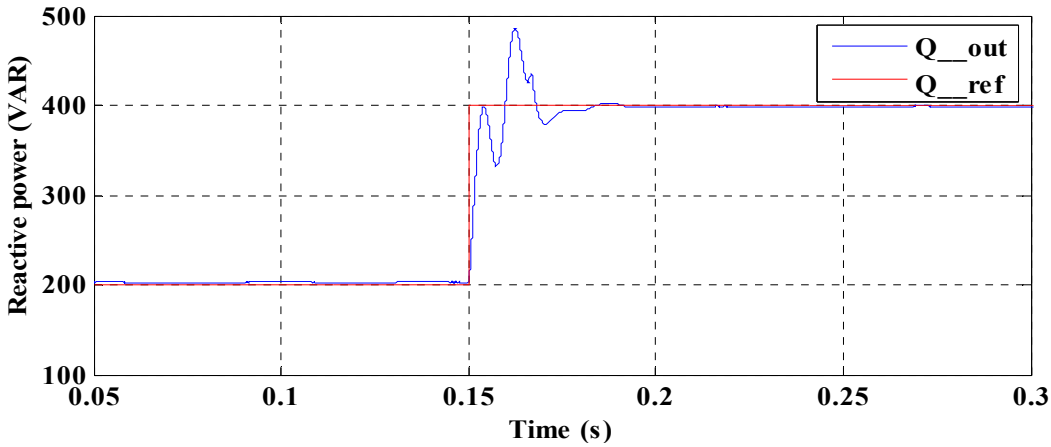

(c) Reactive power

Figure 129: MPC for pulsating dc-link voltage (case study 3).

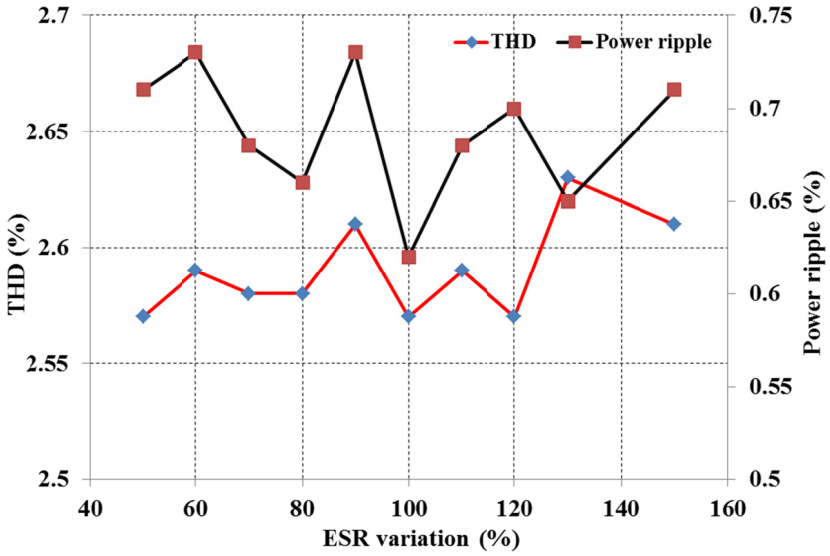

Figure 130: Error effect of inductor resistance (R_L) value on the THD and power ripple.

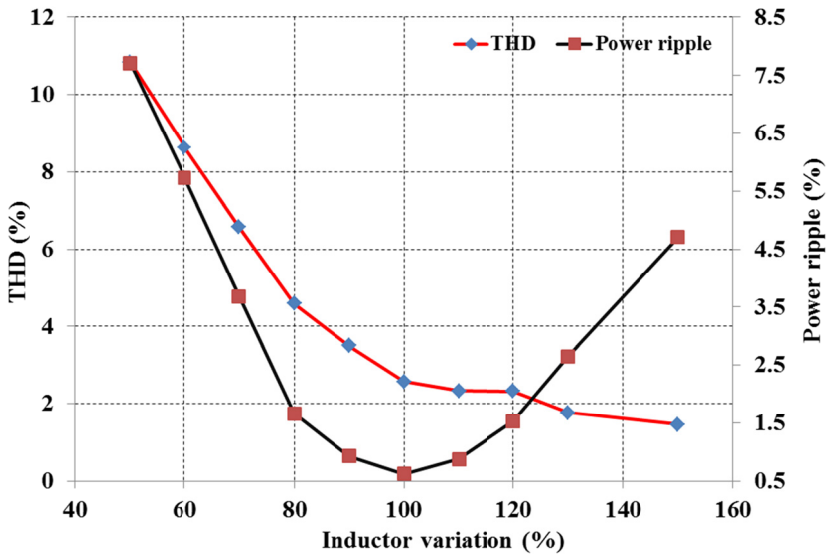

Figure 131: Error effect of inductance value on the THD and power ripple.

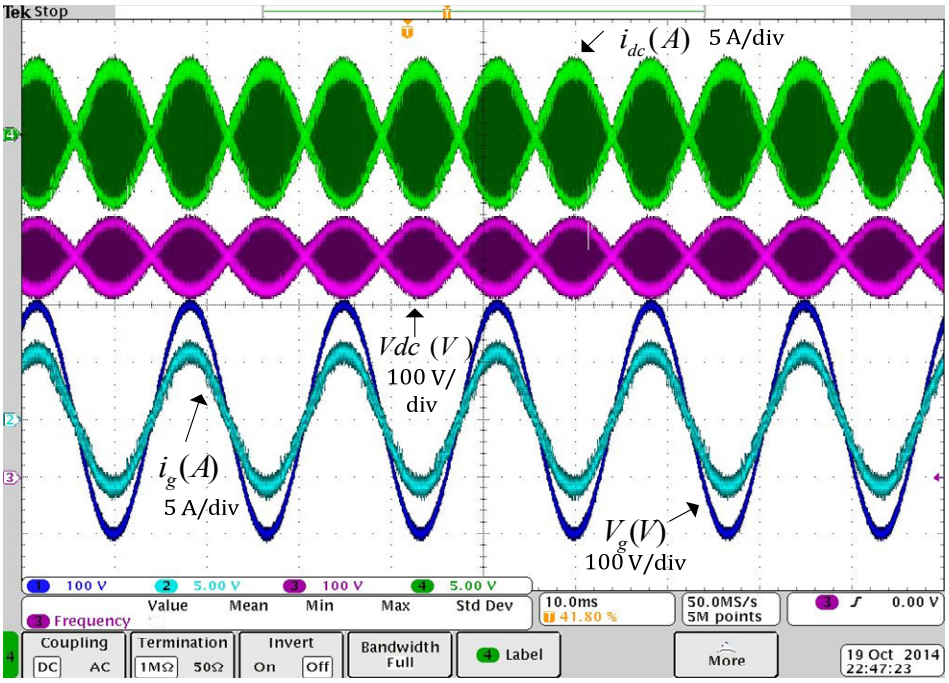

Figure 132: Steady state performance of grid-side voltage, current and the dc-link voltage and current for pulsating dc-link voltage.

The simulation results are validated experimentally by real-time implementation of the control strategy with DS1007 platform of dSPACE. Figure 133 demonstrates the system performance in steady state condition for pulsating dc-link voltage. Fig. 16 illustrates the dynamic performance of the proposed MPC decoupled control when applying a step change to reference value of active power from 500 W to 0 W and to reference value of reactive power from 0 VAR (unity power factor) to -200 VAR. The FFT analysis of grid side current is illustrated in Fig. 17.

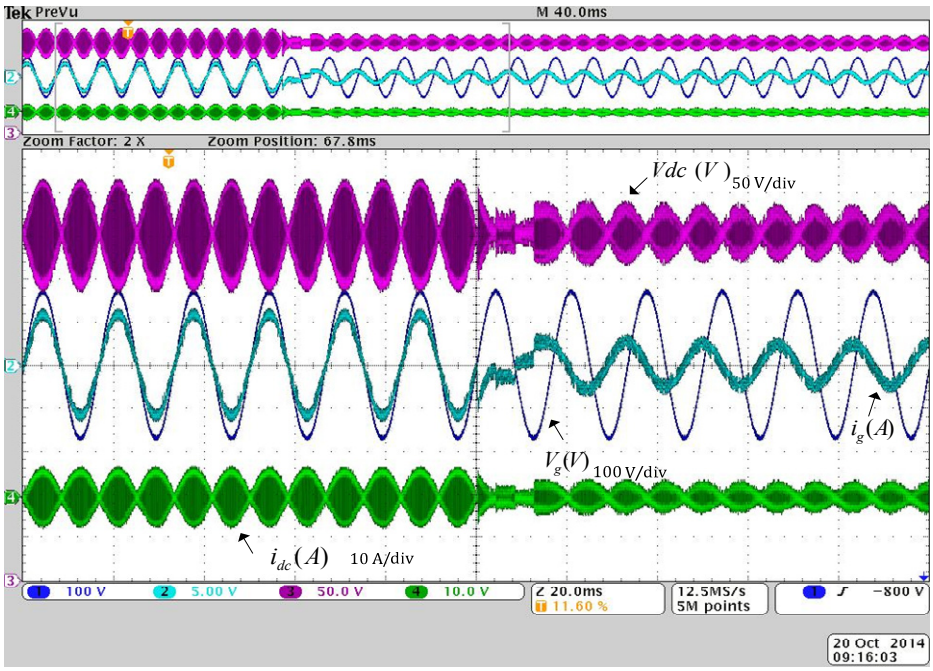

Figure 133: Dynamic performance of grid-side voltage, current and the dc-link voltage and current for pulsating dc-link voltage.

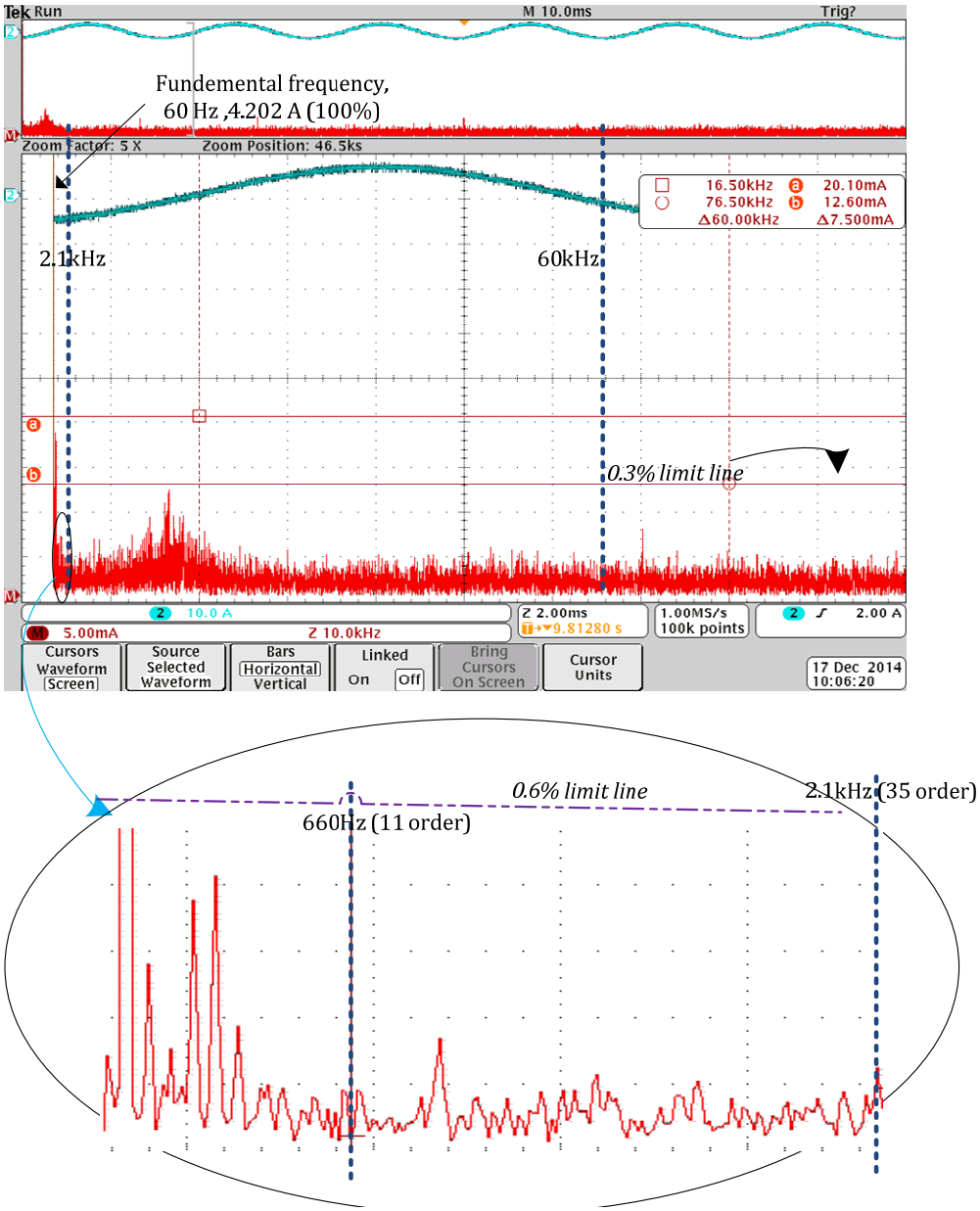

Figure 134: FFT analysis of grid side current.

9.4 Harmonics constraint minimum energy decoupled power control

This section presents a predictive controller to minimize the energy loss per switching event for decoupled power control of grid-tied inverter. The proposed

predictive controller is in a form of cost function subject to minimization with an adaptive weight factor. Total harmonic distortions (THD) of grid side current are the constraint of the proposed control technique for reducing the pack of energy loss per switching event. The goal of proposed dynamic reduction in the switching event by MPC is to optimize the controller objectives priority at each sampling period by the commanded constaints. The proposed controller demonstrates that the inverter have a stable performance under pulsating dc-link voltage, which allows a smaller dc-link capacitor connected in the system. The results demonstrate that an engineering tradeoff should be done between the current THD and switching frequency to optimize the cost function weight factor in steady state.

9.4.1 Controller design

The control effectiveness for power converters can be evaluated by the switching frequency, the energy losses per switching event, and the voltage and current harmonics [177]. The MPC technique has this ability to include all of these control efforts into a single cost function subject to minimization. Due to variable switching frequency scheme of MPC technique [178], the high switching frequecny may be obtained during some sampling periods. This problem is unwanted in application dealing with switching losses, therefore in many power convrter applications, it is important to minimize the energy loss per switching event to improve the efficiency due to switching losses. However the main draw back of reducing the switching event is increase in distortion of current. The goal of proposed dynamic reduction in the switching event by MPC is to optimize the controller objectives priority at each sampling period by the commanded

constaints. The optimized weight factor of the cost function gives more priority to decoupled power control during the transient process due to large absolute error in power tracking. In steady state when the absolute error in power tracking is sufficiently small enough, the minimization of switching event is taken into account with more weight in the cost function.

In the proposed technique, instead of using a PWM module, each switching state change should be predicted in order to obtain a minimum number of switch change event. An adaptive cost function subject to minimization is designed to have fast dynamic response for active and reactive power tracking and minimizing the pack of energy loss per switching event in steady state.

Using the previously defined formulation (141), the sub-cost function for this objective can be formulated as

$$g'(k+1) = |P_{ref}(k+1) - P_{out}(k+1)| + |Q_{ref}(k+1) - Q_{out}(k+1)| \qquad (143)$$

As illustrated in Figure 135, the total number of switching events required to move from one state to other through possible switching paths is fixed, a look-up table (LUT) is constructed to store these information. Thus the number of switching events from current sampling time to next sampling time can be directly presented as

$$g'' = S_c(n_{k-1}, n_k) \qquad (144)$$

The implementation of predictive control is highly dependent on required computation time; it is always desired to reduce the computational time of MPC process [178]. A state elimination is considered in this section in order to minimize the computational time of control algorithm. There are two possible switching states with

zero voltage, S_3 and S_4. By eliminating one of these states in each half cycle, the computation time can be reduced.

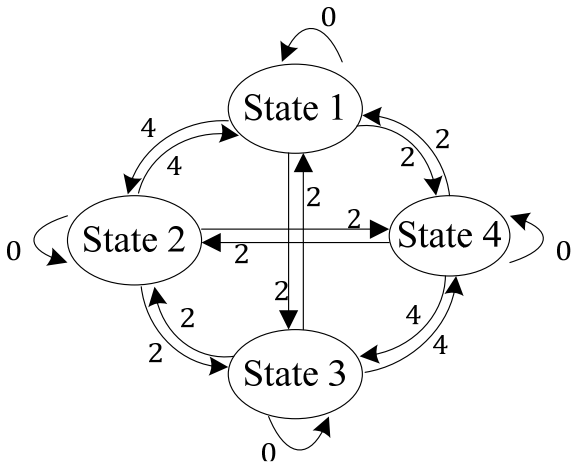

Figure 135: Switching changes between states.

The final cost function can be presented as

$$g_1(k+1)=\frac{1}{P_{rating}}|P_{ref}(k)-P_{out}(k+1)|+\frac{1}{Q_{rating}}|Q_{ref}(k)-Q_{out}(k+1)|+\lambda\cdot S_c(n_{k-1},n_k) \quad (145)$$

In the transient process, the main goal of the controller is set to track the commanded power with fast dynamic response by using the dynamic behavior of the cost function weight factor. When in the steady-state, the power control tracking errors are within determined constraints, the energy loss per switching event minimization can be considered into account. The summary of this process is illustrated in Figure 136, which uses the absolute error in power tracking as a measurement tool as well as the contour plots of the system performance versus weight factor which is discussed in the next section. The step by step procedure for adaptive minimization of the cost function is as follow:

- Detect the present value of P_r, which represents the power ripple limitation value set by user or system organizer.
- Calculate the instantaneous real and reactive power values and power ripple value.
- Compare the detected power ripple value with its limitation value P_r. If it is higher than Pr, set weighting factor to 0. Otherwise, set it with value based on trading-off between the desired performance and analysis of contour plots of xxxx.

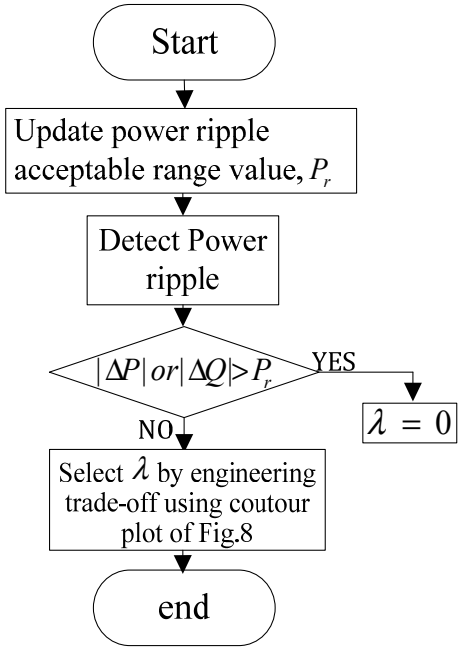

Figure 136: Flowchart of dynamic selection of weight factor (λ).

9.4.2 Results and discussion

The system in Figure 120 is modeled in Simulink-MATLAB. As a case study, the initial commanded real and reactive power is set to be 500 W and 0 VAR respectively, the steady state performance is illustrated in Figure 137 (a), the tracking

error is sufficiently small. The dynamic performance of proposed system is evaluated. At time 0.15 s, the reference values of real and reactive power changed to 0 W and -200 VAR. Finally at time 0.3 s, the reference value for real and reactive power changed to -200 W and 200 VA. These step changes are selected to evaluate the proposed system with the flexible decoupled power control ability and bidirectional power flow capability. The dynamic response to these step changes in reference active and reactive power is illustrated in Figure 137 (b).

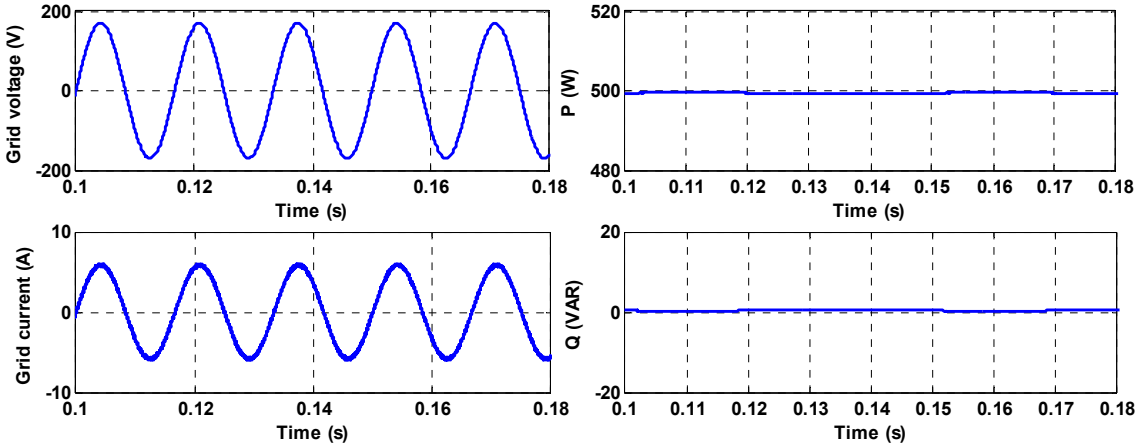

(a) Steady state performance (real power reference of 500 W and unity power factor)

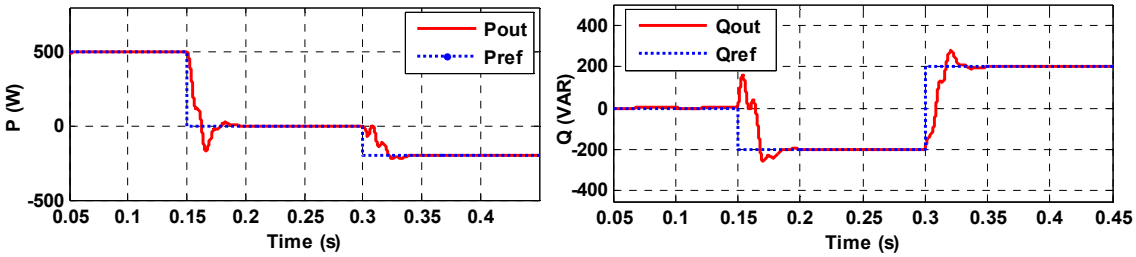

(b) Step response of real and reactive power (The command of real and reactive power is shown by blue dotted line and the response in read)

Figure 137: Steady state and dynamic performance of the proposed controller

The system performance under distorted grid condition with harmonics is evaluated. In this case study, the ideal grid is combined with 4% 3th, 4% 5th, 3% 7th and 3% 11th order harmonics beginning at time 0.08 s, then at time 0.15 s the grid resumes to the ideal condition without these harmonic components. The grid side voltage and current as well as active and reactive power of this case study is illustrated in Figure 138. The THD of grid side current is 3.89% under the distorted case study by using the proposed adaptive predictive direct power control with minimum switching event. The tracking error of real and reactive power during this period is higher. This is due to the proposed harmonics constrained controller which tries to reduce the grid side current harmonics, thus in the multi-objective controller less prioritization is given to real and reactive power control.

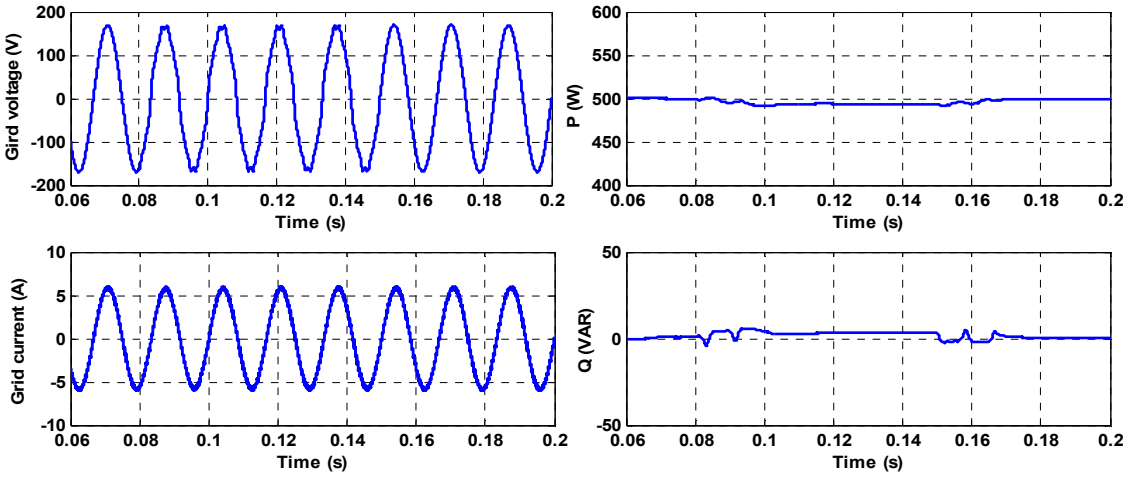

Figure 138: Controller performance with distorted grid from 0.08s to 0.15s.

The effect of pulsating dc-link voltage on the system performance is investigated. In this case study, the voltage source of the inverter is a single-phase diode rectifier with

a dc-link capacitor. Figure 139 demonstrates the simulation results with a 120 μF dc-link capacitor. The steady state control performance is comparable with the case study results shown in Figure 137 (a) where an ideal input dc source is used as the input source to the grid-tied inverter. A step change is applied to the real and reactive power reference at time 0.15 s to evaluate the dynamic performance with the pulsating dc-link voltage.

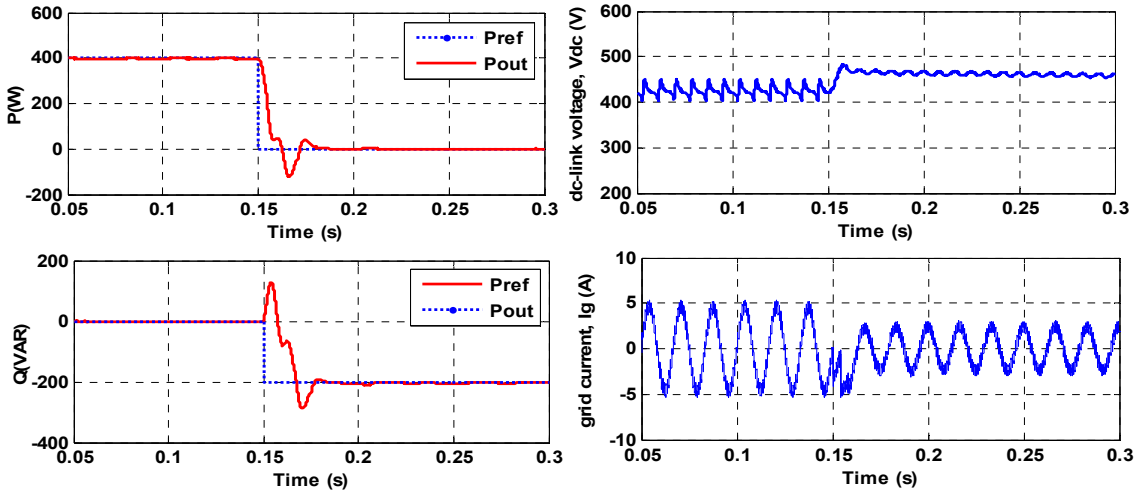

Figure 139: Controller performance with a small dc-link capacitor (120 uf), the figure shows two things: first only real power is commanded, then only reactive power is commanded, command (reference) is shown in dotted blue and response in read line

The final evaluation is the effectiveness of minimizing the energy loss per switching state change. Effect of reduction in pack of energy per switching state change is illustrated in the contour plots of Figure 140. The results of Figure 140 (a) demonstrate that the relation between the weight factor, switching frequency, and absolute error in apparent power tracking is not linear, however the relation of the THD versus weight factor is more trivial as illustrated in Figure 140 (b). An engineering trade-off should be applied to determine the optimum operation point of the system in steady

state. These visualizations demonstrate that the proposed approach to minimize the energy controller, by optimization of the switching events, results in reduction of average switching frequency. The adaptive selection of the weight factor in the formulated cost function leads to set of optimal solutions in form of "pareto frontier" illustrated in Figure 140. A final solution for the weight factor can be determined by trading-off between the THD, switching frequency, and apparent power absolute error. This weight factor will be used for the algorithm in Figure 136 when it should be non-zero.

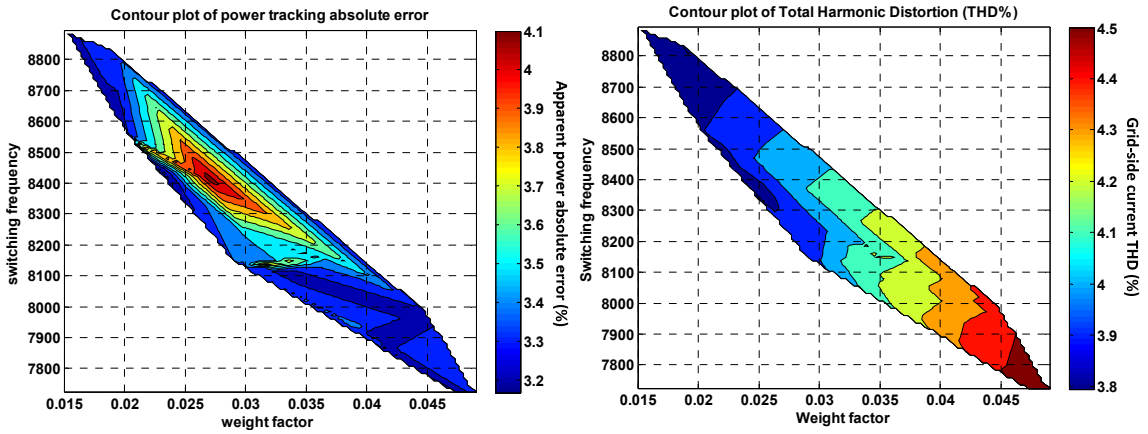

Figure 140: Effect of switching reduction algorithm on performance of system and switching frequecny

Using the set of optimal solutions presented in Figure 140 as reference, two design scenarios are selected for purpose of evaluating and comparing the performance of the proposed controller with conventional multi-loop PI based controller. Table III presents the comparison summary between traditional multi-loop PI based power control method, MPC based controller with only decoupled power control and the proposed MPC based controller with two different design scenarios by trading-off between THD

and switching event using Figure 140 as a tool. The steady-state performance is done in the case with power reference values as P_r=500 W; Q_r=200 VAR. The dynamic performance is done in the case with power reference values Pr steps change from 800 W to 0 W; Qr steps change from 0 VAR to 200 VAR. As demonstrated, the proposed method has smaller overshoot/undershoot value in the dynamic process, with faster convergence time compared with traditional PI based method. The proposed MPC decoupled power minimum energy controller with harmonics constraint results in switching frequency reduction when comparing to other two techniques as presented in Table 12, this leads to minimizing switching losses per switching event.

Table 12. Comparison summary of performance.

	Method 1	**Method 2**	**Method 3, case 1**	**Method 3, case 2**
Real power ripple (%)	1.5%	0.8%	1.0%	1.1%
Reactive power ripple (%)	5%	1.5%	1.7%	1.8%
Switching frequency (Hz)	10K	9790	8690	8230
Grid Current THD	2.5%	1.6%	1.8%	2.2%
Convergence time(s)	0.20	0.10	0.09	0.09
Apparent power overshoot	21.2%	6.5%	7.3%	7.5%

Note: Method 1- Traditional multi-loop PI based power control method;
Method 2- MPC based controller with only decoupled power control
Method 3,case 1-Proposed controller with weight factor as 0.02
Method 4,case 2-Proposed controller with weight factor as 0.04

The proposed control strategy is verified experimentally by real-time implementation using DS1007 platform of dSPACE. Figure 141 (a) demonstrates the

system performance in steady state condition for 500 W reference real power and 200 VAR reference reactive power, and Figure 141 (b) demonstrate the steady state performance when the reference reactive power is -200 VAR and reference real power is 500 W. Figure 142 presents the dynamic performance of proposed system for change in the real power reference value from 800 W to 500 W. Simultaneously, the reactive power reference value changed from 0 VAR to 200 VAR. These results show the proposed decoupled power predictive control ability with fast dynamic performance and low absolute error at steady state.

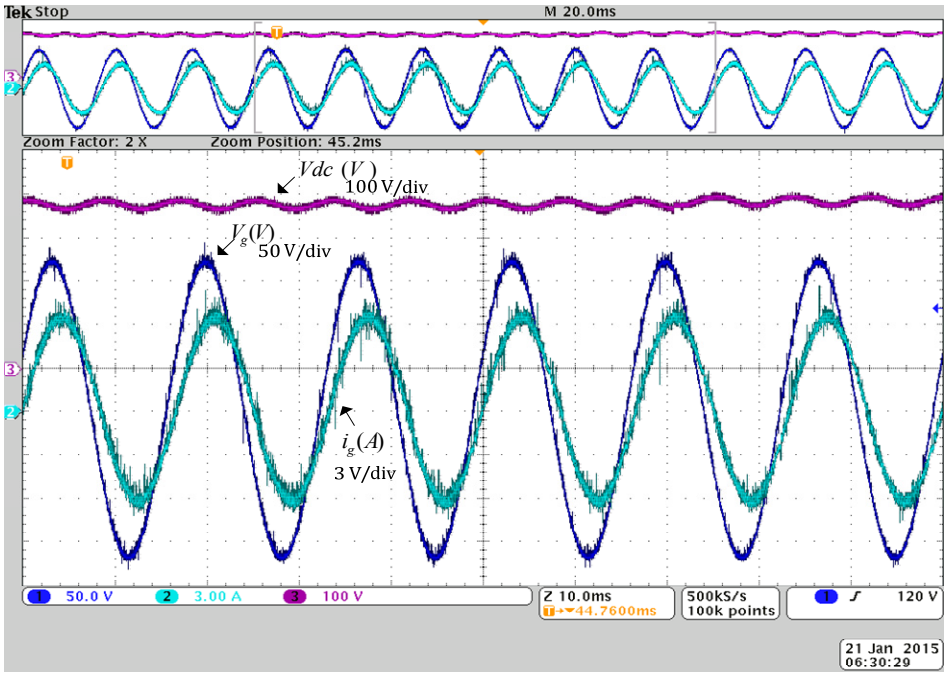

(a) Pref=500 W ; Qref=200 VAR

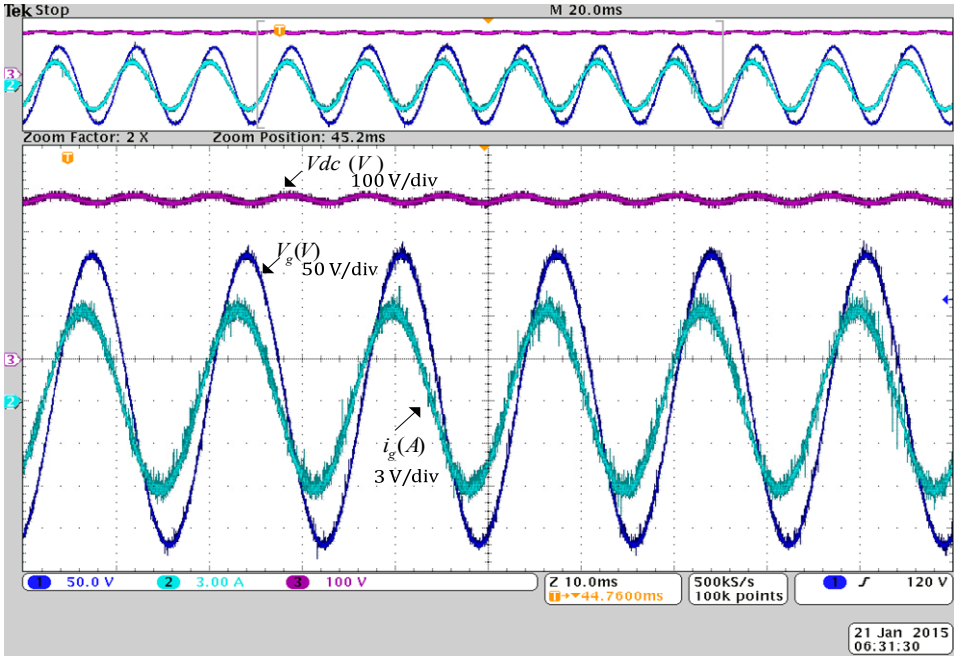

(b) Pref=500 W; Qref= -200 VAR

Figure 141: Steady-state performance

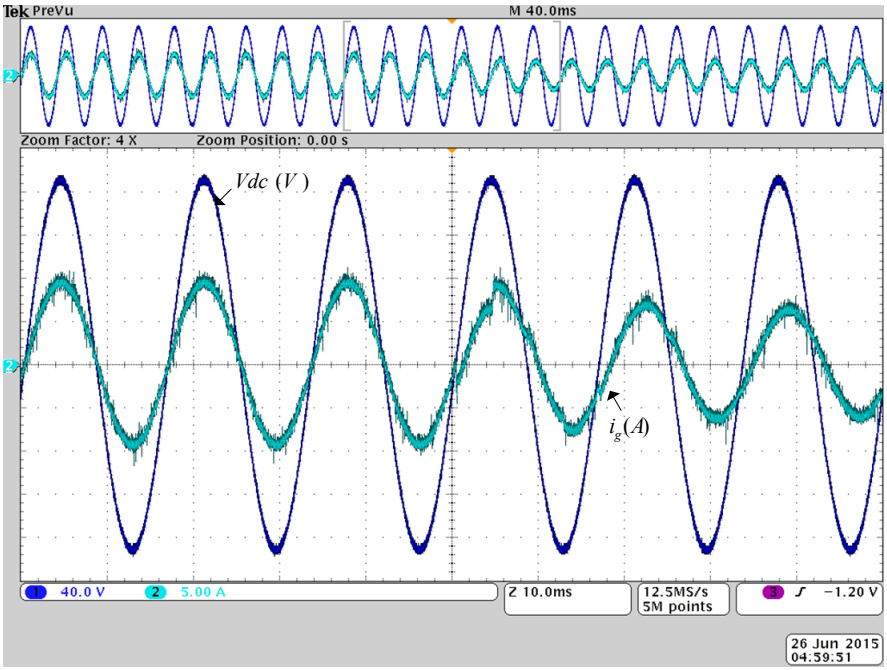

Figure 142: Dynamic performance (Pref: 800 W change to 500 W; Qref:0 VAR changed to 200 VAR)

9.5 Conclusion

This section presents a decoupled power control by MPC for grid-tied inverter and a formulation for harmonic constraints decoupled power control with minimizing the pack of energy loss per switching state change. The proposed control has adjustable capability to change the priority of the control objectives in real time. In order to reduce switching loss in inverter system, an adaptive switching frequency reduction algorithm with a flexible weighting factor is proposed. The weighting factor of switching frequency reduction part is adjusted based on the power tracking error constraints and instantaneous power ripple value. Thus, the functionality of switching event reduction can be maximized when the power ripple is within the defined limits. The results

demonstrate that the grid-tied inverter system can achieve decoupled power control with switching frequency reduction by keeping the grid side current harmonics below the standards.

10. CONCLUSION AND FUTURE WORK

This dissertation focused on two main aspects of hybrid distribution system of future: multi-criteria design and optimization of the hybrid system, model predictive control of power electronics interfaces in the hybrid distribution system. A techno-economic optimization of the proposed hybrid distribution system is studied and energy availability as well as energy variability is investigated. A system structure is proposed by using non-planar photovoltaic systems and geographical distribution of photovoltaic arrays in community microgrid to mitigate the energy variability of the system. The power electronics interfaces considered for model predictive control are: maximum power point tracking, droop predictive control for the dc microgrid, MPC of grid interaction inverter, and MPC of a capacitor-less VAR compensator based on a matrix convert. The main contributions of this dissertation can be listed as following:

- Techno-economic multi-objective optimization using Prado Front for hybrid power and energy system design,
- Auto tuning methodology for the weight factors in the model predictive control (MPC) cost function,
- MPC technique for maximum power point tracking (MPPT),
- Reduce sensitivity (improved robustness) of MPC-MPPT to load disturbances,
- Hysteresis-based mode predictive droop control in dc microgrid,
- Grid-tied photovoltaic model predictive maximum power point tracking and decoupled power control,
- Harmonics constrained, minimum switching loss controller for grid-tied inverter,

- Capacitor-less VAR compensator by MPC techniques for matrix converter.

The studies in this dissertation opened new challenges that require further investigation as future work. These challenges can be listed as:

- Modifying the proposed MPPT algorithm for partially shaded PV system
- Proposing integrated distributed model predictive maximum power point tracking
- Parallel processing and optimization of the proposed auto tuned weight factor for model predictive control
- Adaptive variation of the duty cycle in the proposed model predictive maximum power pint tracking
- Considering the transition states in the proposed harmonics constraint minimum energy controller
- Design of predictive control for power converters with guaranteed performance: considering Lyapunov stability concepts, considering design performance in the cost function

REFERENCES

[1] W. Baochao, M. Sechilariu, and F. Locment, "Intelligent DC Microgrid With Smart Grid Communications: Control Strategy Consideration and Design," *IEEE Transactions on Smart Grid,* vol. 3, pp. 2148-2156, 2012.

[2] R. Majumder, "A Hybrid Microgrid With DC Connection at Back to Back Converters," *IEEE Transactions on Smart Grid,* vol. 5, pp. 1-9, 2013.

[3] R. Lasseter, A. Akhil, C. Marnay, J. Stephens, J. Dagle, R. Guttromson*, et al.*, "Integration of distributed energy resources. The CERTS Microgrid Concept," *Technical Report, US Department of Energy,* 2002.

[4] A. Toliyat, A. Kwasinski, and F. M. Uriarte, "Effects of high penetration levels of residential photovoltaic generation: Observations from field data," in *IEEE International Conference on Renewable Energy Research and Applications (ICRERA)*, 2012, pp. 1-6.

[5] B. Fahimi, A. Kwasinski, A. Davoudi, R. S. Balog, and M. Kiani, "Charge It!," *IEEE Power and Energy Magazine,* vol. 9, pp. 54-64, 2011.

[6] S. Xu, A. Q. Huang, S. Lukic, and M. E. Baran, "On Integration of Solid-State Transformer With Zonal DC Microgrid," *IEEE Transactions on Smart Grid,* vol. 3, pp. 975-985, 2012.

[7] S. Bhattacharya, Z. Tiefu, W. Gangyao, S. Dutta, B. Seunghun, D. Yu*, et al.*, "Design and development of Generation-I silicon based Solid State Transformer," in *IEEE Applied Power Electronics Conference and Exposition (APEC)*, 2010, pp. 1666-1673.

[8] A. Bidram and A. Davoudi, "Hierarchical Structure of Microgrids Control System," *IEEE Transactions on Smart Grid,* vol. 3, pp. 1963-1976, 2012.

[9] J. A. Peas Lopes, C. L. Moreira, and A. G. Madureira, "Defining control strategies for MicroGrids islanded operation," *IEEE Transactions on Power Systems,* vol. 21, pp. 916-924, 2006.

[10] G. T. Heydt, "The Next Generation of Power Distribution Systems," *IEEE Transactions on Smart Grid,* vol. 1, pp. 225-235, 2010.

[11] G. T. Heydt, B. H. Chowdhury, M. L. Crow, D. Haughton, B. D. Kiefer, M. Fanjun*, et al.*, "Pricing and Control in the Next Generation Power Distribution System," *IEEE Transactions on Smart Grid,* vol. 3, pp. 907-914, 2012.

[12] J. Irwin, M. P. Kazmierkowski, R. Krishnan, and F. Blaabjerg, *Control in power electronics: selected problems*: Academic press, 2002.

[13] N. Mohan and T. M. Undeland, *Power electronics: converters, applications, and design*: John Wiley & Sons, 2007.

[14] A. Linder, R. Kanchan, R. Kennel, and P. Stolze, *Model-based predictive control of electric drives*: Cuvillier, 2010.

[15] J. Rodriguez and P. Cortes, *Predictive control of power converters and electrical drives* vol. 37: John Wiley & Sons, 2012.

[16] J. Holtz, "Pulsewidth modulation for electronic power conversion," *Proceedings of the IEEE,* vol. 82, pp. 1194-1214, 1994.

[17] T. Ohnishi, "Three phase PWM converter/inverter by means of instantaneous active and reactive power control," in *IEEE Conference on Industrial Electronics, Control and Instrumentation (IECON)*, 1991, pp. 819-824.

[18] I. Takahashi and T. Noguchi, "A new quick-response and high-efficiency control strategy of an induction motor," *IEEE Transactions on Industry Applications,* pp. 820-827, 1986.

[19] M. P. Kazmierkowski and L. Malesani, "Current control techniques for three-phase voltage-source PWM converters: a survey," *IEEE Transactions on Industrial Electronics,* vol. 45, pp. 691-703, 1998.

[20] F. Blaschke, "The principle of field orientation as applied to the new transvektor closed-loop control system for rotating field machines," 1972.

[21] J. Holtz and S. Stadtfeld, "A predictive controller for the stator current vector of AC machines fed from a switched voltage source," in *International Power Electronics Conference (IPEC)*, 1983, pp. 1665–1675.

[22] J. Rodriguez, M. P. Kazmierkowski, J. R. Espinoza, P. Zanchetta, H. Abu-Rub, H. A. Young*, et al.*, "State of the Art of Finite Control Set Model Predictive Control in Power Electronics," *IEEE Transactions on Industrial Informatics,* vol. 9, pp. 1003-1016, 2013.

[23] H. Abu-Rub, J. Guzinski, Z. Krzeminski, and H. A. Toliyat, "Predictive current control of voltage-source inverters," *IEEE Transactions on Industrial Electronics,* vol. 51, pp. 585-593, 2004.

[24] P. Cortes, A. Wilson, S. Kouro, J. Rodriguez, and H. Abu-Rub, "Model Predictive Control of Multilevel Cascaded H-Bridge Inverters," *IEEE Transactions on Industrial Electronics,* vol. 57, pp. 2691-2699, 2010.

[25] M. B. Shadmand, M. Mosa, R. S. Balog, and H. Abu-Rub, "An Improved MPPT Technique of High Gain DC-DC Converter by Model Predictive Control for Photovoltaic Applications," in *IEEE Applied Power Electronics Conference & Exposition (APEC)*, 2014.

[26] P. Eichenberger and M. Junger, "Predictive vector control of the stator voltages for an induction machine drive with current source inverter," in *IEEE Power Electronics Specialists Conference (PESC)*, 1997, pp. 1295-1301 vol.2.

[27] J. Holtz and S. Stadtfeld, "A predictive controller for the stator current vector of ac machines fed from a switched voltage source," in *JIEE IPEC-Tokyo Conf*, 1983, pp. 1665-1675.

[28] R. Kennel and A. Linder, "Predictive control of inverter supplied electrical drives," in *Proc. of the Power Electronics Specialists Conference (PESC 00)*, 2000, pp. 761-766.

[29] P. Mutschler, "A new speed-control method for induction motors," in *Conf. Record of PCIM'98*, 1998, pp. 131-136.

[30] M. Depenbrock, "Direct self-control (DSC) of inverter-fed induction machine," *IEEE Transactions on Power Electronics,* vol. 3, pp. 420-429, 1988.

[31] E. Flach, R. Hoffmann, and P. Mutschler, "Direct mean torque control of an induction motor," in *European Conference on Power Electronics and Applications*, 1997, pp. 3.672-3.677.

[32] O. Kukrer, "Discrete-time current control of voltage-fed three-phase PWM inverters," *IEEE Transactions on Power Electronics,* vol. 11, pp. 260-269, 1996.

[33] L. Malesani, P. Mattavelli, and S. Buso, "Robust dead-beat current control for PWM rectifiers and active filters," in *IEEE IAS Annual Meeting*, 1998, pp. 1377-1384.

[34] S. Buso, S. Fasolo, and P. Mattavelli, "Uninterruptible power supply multiloop control employing digital predictive voltage and current regulators," *IEEE Transactions on Industry Applications,* vol. 37, pp. 1846-1854, 2001.

[35] S. Saggini, W. Stefanutti, E. Tedeschi, and P. Mattavelli, "Digital deadbeat control tuning for dc-dc converters using error correlation," *IEEE Transactions on Power Electronics,* vol. 22, pp. 1566-1570, 2007.

[36] E. F. Camacho and C. Bordons, "Model Based Predictive Controllers," in *Model Predictive Control*, ed: Springer, 1999, pp. 13-31.

[37] S. J. Qin and T. A. Badgwell, "A survey of industrial model predictive control technology," *Control engineering practice,* vol. 11, pp. 733-764, 2003.

[38] D. Q. Mayne, J. B. Rawlings, C. V. Rao, and P. O. Scokaert, "Constrained model predictive control: Stability and optimality," *Automatica,* vol. 36, pp. 789-814, 2000.

[39] C. E. Garcia, D. M. Prett, and M. Morari, "Model predictive control: theory and practice—a survey," *Automatica,* vol. 25, pp. 335-348, 1989.

[40] A. Linder and R. Kennel, "Model predictive control for electrical drives," in *IEEE Power Electronics Specialists Conference*, 2005, pp. 1793-1799.

[41] *Emerge Alliance*. Available: http://www.emergealliance.org/

[42] A. Mohamed and O. Mohammed, "Connectivity of DC microgrids involving sustainable energy sources," in *IEEE Industry Applications Society Annual Meeting (IAS)*, 2011, pp. 1-8.

[43] S. E. R. Gelman, "2013 Renewable Energy Data Book," U. S. D. Energy, Ed., ed. United States: U.S. Department of Energy's National Renewable Energy Laboratory (NREL), 2013.

[44] J. W. Kimball, B. T. Kuhn, and R. S. Balog, "A System Design Approach for Unattended Solar Energy Harvesting Supply," *IEEE Transactions on Power Electronics,* vol. 24, pp. 952-962, April 2009 2009.

[45] M. B. Shadmand and R. S. Balog, "Optimization of photovoltaic-wind hybrid system for apartment complexes and other community living environments by minimizing excess capacity," in *IEEE Photovoltaic Specialists Conference (PVSC)*, 2012, pp. 000531-000536.

[46] C. M. Fonseca and P. J. Fleming, "Genetic Algorithms for Multiobjective Optimization: FormulationDiscussion and Generalization," in *ICGA*, 1993, pp. 416-423.

[47] G. Ying, S. Lei, and Y. Pingjing, "Study on multi-objective genetic algorithm," in *IEEE World Congress on Intelligent Control and Automation*, 2000, pp. 646-650 vol.1.

[48] K. Deb, A. Pratap, S. Agarwal, and T. Meyarivan, "A fast and elitist multiobjective genetic algorithm: NSGA-II," *IEEE Transactions on Evolutionary Computation,* vol. 6, pp. 182-197, 2002.

[49] M. M. H. Bhuiyan and M. Ali Asgar, "Sizing of a stand-alone photovoltaic power system at Dhaka," *Renewable Energy,* vol. 28, pp. 929-938, 2003.

[50] L. Fernandes and J. Figueiredo, "An economic analysis of a power production hybrid system," in *International Conference on European Electricity Market* 2008, pp. 1-6.

[51] D. Abbes, A. Martinez, and G. Champenois, "Eco-design optimisation of an autonomous hybrid wind-photovoltaic system with battery storage," *IET Renewable Power Generation,* vol. 6, pp. 358-371, 2012.

[52] W. D. Kellogg, M. H. Nehrir, G. Venkataramanan, and V. Gerez, "Generation unit sizing and cost analysis for stand-alone wind, photovoltaic, and hybrid wind/PV systems," *IEEE Transactions on Energy Conversion,* vol. 13, pp. 70-75, 1998.

[53] Sa, x, V. nchez, J. M. Ramirez, and G. Arriaga, "Optimal sizing of a hybrid renewable system," in *IEEE International Conference on Industrial Technology (ICIT)*, 2010, pp. 949-954.

[54] A. M. Leite da Silva, L. C. Nascimento, M. A. da Rosa, D. Issicaba, Pe, x00E*, et al.*, "Distributed Energy Resources Impact on Distribution System Reliability Under Load Transfer Restrictions," *IEEE Transactions on Smart Grid,* vol. 3, pp. 2048-2055, 2012.

[55] S. V. Dhople and A. D. Dominguez-Garcia, "Estimation of Photovoltaic System Reliability and Performance Metrics," *IEEE Transactions on Power Systems,* vol. 27, pp. 554-563, 2012.

[56] SolarAgs. *The Home of Current Solar Projects at Texas A&M University*. Available: http://solarags.tamu.edu/

[57] U. D. o. Energy. *Zoning Issues and Wind Energy in Virginia*. Available: http://www.windpoweringamerica.gov/pdfs/small_wind/va_zoning.pdf

[58] W. Finder. *Wind Reports/Forecast*. Available: http://www.windestimator.com

[59] D. E. Goldberg and J. H. Holland, "Genetic algorithms and machine learning," *Machine learning,* vol. 3, pp. 95-99, 1988.

[60] P. C. Fishburn, "Utility theory for decision making," DTIC Document1970.

[61] R. L. Keeney, *Decisions with multiple objectives: preferences and value trade-offs*: Cambridge University Press, 1993.

[62] Y. V. Makarov, D. Pengwei, M. C. W. Kintner-Meyer, J. Chunlian, and H. F. Illian, "Sizing Energy Storage to Accommodate High Penetration of Variable Energy Resources," *IEEE Transactions on Sustainable Energy,* vol. 3, pp. 34-40, 2012.

[63] R. Tonkoski, D. Turcotte, and T. H. M. El-Fouly, "Impact of High PV Penetration on Voltage Profiles in Residential Neighborhoods," *IEEE Transactions on Sustainable Energy,* vol. 3, pp. 518-527, 2012.

[64] Y. Riffonneau, S. Bacha, F. Barruel, and S. Ploix, "Optimal Power Flow Management for Grid Connected PV Systems With Batteries," *IEEE Transactions on Sustainable Energy,* vol. 2, pp. 309-320, 2011.

[65] J. P. Storey, P. R. Wilson, and D. Bagnall, "Improved Optimization Strategy for Irradiance Equalization in Dynamic Photovoltaic Arrays," *IEEE Transactions on Power Electronics,* vol. 28, pp. 2946-2956, 2013.

[66] E. Drury, T. Jenkin, D. Jordan, and R. Margolis, "Photovoltaic Investment Risk and Uncertainty for Residential Customers," *IEEE Journal of Photovoltaics,* vol. 4, pp. 278-284, 2014.

[67] J. Traube, L. Fenglong, D. Maksimovic, J. Mossoba, M. Kromer, P. Faill*, et al.*, "Mitigation of Solar Irradiance Intermittency in Photovoltaic Power Systems With Integrated Electric-Vehicle Charging Functionality," *IEEE Transactions on Power Electronics,* vol. 28, pp. 3058-3067, 2013.

[68] N. Kawasaki, T. Oozeki, K. Otani, and K. Kurokawa, "An evaluation method of the fluctuation characteristics of photovoltaic systems by using frequency analysis," *Solar Energy Materials and Solar Cells,* vol. 90, pp. 3356-3363, 2006.

[69] R. A. Gansler, S. A. Klein, and W. A. Beckman, "Investigation of minute solar radiation data," *Solar Energy,* vol. 55, pp. 21-27, 1995.

[70] A. Karavadi and R. S. Balog, "Novel non-flat photovoltaic module geometries and implications to power conversion," in *IEEE Energy Conversion Congress and Exposition (ECCE)*, 2011, pp. 7-13.

[71] H. Zhang and R. S. Balog, "Experimental Verification of Energy Harvest from Non-Planar Photovoltaic Surfaces," in *Energy Conversion Congress and Exposition (ECCE 2013)*, Denver, CO, 2013.

[72] R. S. Balog, "Design Considerations for Photovoltaic Systems Installed on Curved Surfaces," in *Photovoltaic Specialist Conference (PVSC)*, Tampa, FL, USA, 2013.

[73] M. Pagliaro, G. Palmisano, and R. Ciriminna, *Flexible Solar Cells*. Weinheim Germany: Wiley-VCH, 2008.

[74] J. L. Cruz-Campa, G. N. Nielson, P. J. Resnick, C. A. Sanchez, P. J. Clews, M. Okandan*, et al.*, "Ultrathin Flexible Crystalline Silicon: Microsystems-Enabled Photovoltaics," *IEEE journal of Photovoltaics,* vol. 1, pp. 3-8, 2011.

[75] M. S. Shur, S. L. Rumyantsev, and R. Gaska, "Nanostructures on flexible substrates," in *Proceedings of The International Society for Optical Engineering (SPIE)*, 2002, pp. 553-557.

[76] M. Powalla, W. Witte, P. Jackson, S. Paetel, E. Lotter, R. Wuerz*, et al.*, "CIGS Cells and Modules With High Efficiency on Glass and Flexible Substrates," *IEEE Journal of Photovoltaics,* vol. 4, pp. 440-446, 2014.

[77] W.-Y. Chang, T.-H. Fang, H.-J. Lin, Y.-T. Shen, and Y.-C. Lin, "A Large Area Flexible Array Sensors Using Screen Printing Technology," *IEEE Journal of Display Technology,* vol. 5, pp. 178-183, June 2009 2009.

[78] A. Bedeloglu, A. Demir, Y. Bozkurt, and N. S. Sariciftci, "A Photovoltaic Fibre Design for Smart Textiles," *Textile Research Journal,* October 29, 2009 2009.

[79] A. Elasser, "Photovoltaics Systems: Overview, Status, and Future Prospects," presented at the Rensselaer Polytechnic Institute October 7th 2010.

[80] S. Tucker, "Flexible Photovoltaics: Mission Power from the Sun," ARMY Natick Soldier Research Development and Engineering Center MA, Shelter Technology Engineering and Fabrication Directorate report no A749415, Nov 2009 2009.

[81] R. Ahmadi, A. Kashyap, A. Berrueta Irigoyen, A. Rayachoti, C. Wright, and J. Kimball, "Selective source power converter for improved photovoltaic power utilization," in *IEEE Power and Energy Conference at Illinois (PECI)*, 2013, pp. 247-252.

[82] N. Farokhnia, S. H. Fathi, N. Yousefpoor, and M. K. Bakhshizadeh, "Minimisation of total harmonic distortion in a cascaded multilevel inverter by regulating voltages of dc sources," *IET Power Electronics,* vol. 5, pp. 106-114, 2012.

[83] L. Chia-Hung, H. Wei-Lin, C. Chao-Shun, H. Cheng-Ting, K. Te-Tien, and T. Cheng-Ta, "Financial Analysis of a Large-Scale Photovoltaic System and Its

Impact on Distribution Feeders," *IEEE Transactions on Industry Applications,* vol. 47, pp. 1884-1891, 2011.

[84] A. M. Latham, R. Pilawa-Podgurski, K. M. Odame, and C. R. Sullivan, "Analysis and Optimization of Maximum Power Point Tracking Algorithms in the Presence of Noise," *IEEE Transactions on Power Electronics,* vol. 28, pp. 3479-3494, 2013.

[85] S. Kuszamaul, A. Ellis, J. Stein, and L. Johnson, "Lanai High-Density Irradiance Sensor Network for characterizing solar resource variability of MW-scale PV system," in *IEEE Photovoltaic Specialists Conference (PVSC)*, 2010, pp. 000283-000288.

[86] T. Golnas, R. Aghatehrani, and J. Bryan, "PV Plant Variability, Aggregation, and Impact on Grid Voltage," presented at the PV Grid Integration Workshop Belmont, California April 2012.

[87] K. Otani, J. Minowa, and K. Kurokawa, "Study on areal solar irradiance for analyzing areally-totalized PV systems," *Solar Energy Materials and Solar Cells,* vol. 47, pp. 281-288, 1997.

[88] A. Mills, "Understanding Variability and Uncertainty of Photovoltaics for Integration with the Electric Power System," ed, 2010.

[89] D. Lew, M. Milligan, G. Jordan, L. Freeman, N. Miller, K. Clark*, et al.*, "How do wind and solar power affect grid operations: The western wind and solar integration study," in *8th international Workshop on large scale integration of wind power and on transmission networks for Offshore wind farms*, 2009, pp. 14-15.

[90] Z. Hradílek and T. Šumbera, "Stochastic production of photovoltaic power plant," *Przegląd Elektrotechniczny Selected full texts,* vol. 88, pp. 112-115, 2012.

[91] P. Chen, "Stochastic modeling and analysis of power system with renewable generation," Department of Energy Technology, Aalborg University, 2010.

[92] M. B. Shadmand, M. Mosa, R. S. Balog, and H. A. Rub, "An Improved MPPT Technique of High Gain DC-DC Converter by Model Predictive Control for Photovoltaic Applications," in *IEEE Applied Power Electronics Conference & Exposition (APEC)*, 2014, pp. 2993 - 2999.

[93] M. Mosa, H. Abu-Rub, and J. Rodriguez, "High performance predictive control applied to three phase grid connected Quasi-Z-Source Inverter," in *IEEE Industrial Electronics Society Annual Conference (IECON)*, 2013, pp. 5812-5817.

[94] M. Mosa, O. Ellabban, A. Kouzou, H. Abu-Rub, and J. Rodriguez, "Model Predictive Control applied for Quasi-Z-source inverter," in *IEEE Applied Power Electronics Conference and Exposition (APEC)*, 2013, pp. 165-169.

[95] M. Shadmand, R. S. Balog, and H. Abu Rub, "Maximum Power Point Tracking using Model Predictive Control of a flyback converter for photovoltaic applications," in *IEEE Power and Energy Conference at Illinois (PECI)*, 2014, pp. 1-5.

[96] A. G. Beccuti, S. Mariéthoz, S. Cliquennois, S. Wang, and M. Morari, "Explicit model predictive control of DC–DC switched-mode power supplies with extended Kalman filtering," *IEEE Transactions on Industrial Electronics,* vol. 56, pp. 1864-1874, 2009.

[97] S. Mariéthoz and M. Morari, "Explicit model-predictive control of a PWM inverter with an LCL filter," *IEEE Transactions on Industrial Electronics,* vol. 56, pp. 389-399, 2009.

[98] S. Mariéthoz, A. Domahidi, and M. Morari, "Sensorless explicit model predictive control of permanent magnet synchronous motors," in *IEEE Electric Machines and Drives Conference (IEMDC)*, 2009, pp. 1250-1257.

[99] P. Cortes, S. Kouro, B. La Rocca, R. Vargas, J. Rodriguez, J. I. Leon*, et al.*, "Guidelines for weighting factors design in Model Predictive Control of power converters and drives," in *IEEE International Conference on Industrial Technology (ICIT)*, 2009, pp. 1-7.

[100] Z. Lin, C. Yan, G. Ke, and J. Fangcheng, "New Approach for MPPT Control of Photovoltaic System With Mutative-Scale Dual-Carrier Chaotic Search," *IEEE Transactions on Power Electronics,* vol. 26, pp. 1038-1048, 2011.

[101] N. Femia, G. Petrone, G. Spagnuolo, and M. Vitelli, "Optimization of perturb and observe maximum power point tracking method," *IEEE Transactions on Power Electronics,* vol. 20, pp. 963-973, 2005.

[102] R. Khanna, Z. Qinhao, W. E. Stanchina, G. F. Reed, and M. Zhi-Hong, "Maximum Power Point Tracking Using Model Reference Adaptive Control," *IEEE Transactions on Power Electronics,* vol. 29, pp. 1490-1499, 2014.

[103] J. Shuai, C. Dong, L. Yuan, and P. Fang Zheng, "Grid-Connected Boost-Half-Bridge Photovoltaic Microinverter System Using Repetitive Current Control and Maximum Power Point Tracking," *IEEE Transactions on Power Electronics,* vol. 27, pp. 4711-4722, 2012.

[104] S. L. Brunton, C. W. Rowley, S. R. Kulkarni, and C. Clarkson, "Maximum Power Point Tracking for Photovoltaic Optimization Using Ripple-Based Extremum Seeking Control," *IEEE Transactions on Power Electronics,* vol. 25, pp. 2531-2540, 2010.

[105] T. Esram and P. L. Chapman, "Comparison of photovoltaic array maximum power point tracking techniques," *IEEE Transactions on Energy Conversion,* vol. 22, pp. 439-449, June 2007 2007.

[106] A. Bidram, A. Davoudi, and R. S. Balog, "Control and Circuit Techniques to Mitigate Partial Shading Effects in Photovoltaic Arrays," *IEEE Journal of Photovoltaics,* vol. 2, pp. 532-546, 2012.

[107] K. A. Kim, R. M. Li, and P. T. Krein, "Voltage-offset resistive control for DC-DC converters in photovoltaic applications," in *IEEE Applied Power Electronics Conference and Exposition (APEC)*, 2012, pp. 2045-2052.

[108] D. Sera, T. Kerekes, R. Teodorescu, and F. Blaabjerg, "Improved MPPT Algorithms for Rapidly Changing Environmental Conditions," in *IEEE Power Electronics and Motion Control Conference (EPE-PEMC)*, 2006, pp. 1614-1619.

[109] T. Esram, J. W. Kimball, P. T. Krein, P. L. Chapman, and P. Midya, "Dynamic Maximum Power Point Tracking of Photovoltaic Arrays Using Ripple Correlation Control," *IEEE Transactions on Power Electronics,* vol. 21, pp. 1282-1291, 2006.

[110] M. Mousa, M. E. Ahmed, and M. Orabi, "New converter circuitry for high v applications using Switched Inductor Multilevel Converter," in *IEEE International Telecommunications Energy Conference (INTELEC)*, 2011, pp. 1-8.

[111] J. C. Rosas-Caro, J. M. Ramirez, and P. M. Garcia-Vite, "Novel DC-DC Multilevel Boost Converter," in *IEEE Power Electronics Specialists Conference (PESC)*, 2008, pp. 2146-2151.

[112] D. Maksimovic and S. Cuk, "Switching converters with wide DC conversion range," *IEEE Transactions on Power Electronics,* vol. 6, pp. 151-157, 1991.

[113] S. Harb, Z. Haiyu, and R. S. Balog, "AC-link, single-phase, photovoltaic Module Integrated Inverter," in *IEEE Applied Power Electronics Conference and Exposition (APEC)*, 2013, pp. 177-182.

[114] H. Keyhani, H. A. Toliyat, M. H. Todorovic, R. Lai, and R. Datta, "A Step-Up/Down Three-Phase Resonant High-Frequency AC-Link Inverter," in *IEEE Applied Power Electronics Conference and Exposition (APEC)*, 2013.

[115] A. Amirahmadi, C. Lin, U. Somani, H. Haibing, N. Kutkut, and I. Bartarseh, "High Efficiency Dual-Mode Current Modulation Method for Low-Power DC/AC Inverters," *IEEE Transactions on Power Electronics,* vol. 29, pp. 2638-2642, 2014.

[116] B. Farhangi and S. Farhangi, "Comparison of z-source and boost-buck inverter topologies as a single phase transformer-less photovoltaic grid-connected power conditioner," in *IEEE Power Electronics Specialists Conference (PESC)*, 2006, pp. 1-6.

[117] M. Hamzeh, S. Farhangi, and B. Farhangi, "A new control method in PV grid connected inverters for anti-islanding protection by impedance monitoring," in *IEEE Workshop on Control and Modeling for Power Electronics (COMPEL)*, 2008, pp. 1-5.

[118] S. Sajadian and E. C. dos Santos, "Three-phase DC-AC converter with five-level four-switch characteristic," in *Power and Energy Conference at Illinois (PECI)*, 2014, pp. 1-6.

[119] E. C. dos Santos Junior and S. Sajadian, "Energy conversion unit with optimized waveform generation," in *IEEE Industry Applications Society Annual Meeting*, 2013, pp. 1-6.

[120] C. K. Duffey and R. P. Stratford, "Update of harmonic standard IEEE-519: IEEE recommended practices and requirements for harmonic control in electric power systems," *IEEE Transactions on Industry Applications,* vol. 25, pp. 1025-1034, 1989.

[121] R. W. Erickson and D. Maksimovic, *Fundamentals of power electronics*: Kluwer Academic Pub, 2001.

[122] M. B. Shadmand, R. S. Balog, and H. Abu-Rub, "Model Predictive Control of PV Sources in a Smart DC Distribution System: Maximum Power Point Tracking and Droop Control," *Energy Conversion, IEEE Transactions on,* vol. 29, pp. 913-921, 2014.

[123] M. B. Shadmand, R. S. Balog, and H. Abu-Rub, "Maximum Power Point Tracking using Model Predictive Control of a flyback converter for photovoltaic applications," presented at the Power and Energy Conference at Illinois (PECI) 2014, Champaign, IL, 2014.

[124] M. Mosa, H. Abu Rub, M. E. Ahmed, and J. Rodriguez, "Modified MPPT with using model predictive control for multilevel boost converter," in *IECON 2012 - 38th Annual Conference on IEEE Industrial Electronics Society*, 2012, pp. 5080-5085.

[125] M. B. Shadmand, M. Mosa, R. S. Balog, and H. A. Rub, "Maximum Power Point Tracking of Grid Connected Photovoltaic System Employing Model Predictive Control," *IEEE Applied Power Electronics Conference & Exposition (APEC),* 2015.

[126] N. H. R. Bründlinger, H. Häberlin, B. Burger, A. Bergmann, F. Baumgartner, "prEN 50530 - The New European Standard for Performance Characterisation of PV Inverters," in *24th European Photovoltaic Solar Energy Conference*, Hamburg, Germany, 2009, pp. 3105 - 3109.

[127] Z. S. Kashif Ishaquea, George Laussc, "The performance of perturb and observe and incremental conductance maximum power point tracking method under dynamic weather conditions," *Applied Energy,* vol. 119, pp. 228-236, 15 April 2014 2014.

[128] C. Chian-Song, "T-S Fuzzy Maximum Power Point Tracking Control of Solar Power Generation Systems," *IEEE Transactions on Energy Conversion,* vol. 25, pp. 1123-1132, 2010.

[129] Z. Fan, K. Thanapalan, A. Procter, S. Carr, and J. Maddy, "Adaptive Hybrid Maximum Power Point Tracking Method for a Photovoltaic System," *IEEE Transactions on Energy Conversion,* vol. 28, pp. 353-360, 2013.

[130] Y. C. Chang, C. L. Kuo, K. H. Sun, and T. C. Li, "Development and Operational Control of Two-String Maximum Power Point Trackers in DC Distribution Systems," *IEEE Transactions on Power Electronics,* vol. 28, pp. 1852-1861, 2013.

[131] L. Ching-Ming, P. Ching-Tsai, and C. Ming-Chieh, "High-Efficiency Modular High Step-Up Interleaved Boost Converter for DC-Microgrid Applications," *IEEE Transactions on Industry Applications,* vol. 48, pp. 161-171, 2012.

[132] J. B. Wang, "Parallel DC/DC converters system with a novel primary droop current sharing control," *IET Power Electronics,* vol. 5, pp. 1569-1580, 2012.

[133] R. S. Balog, W. W. Weaver, and P. T. Krein, "The Load as an Energy Asset in a Distributed DC SmartGrid Architecture," *IEEE Transactions on Smart Grid,* vol. 3, pp. 253-260, 2012.

[134] A. Ghazanfari, M. Hamzeh, H. Mokhtari, and H. Karimi, "Active Power Management of Multihybrid Fuel Cell/Supercapacitor Power Conversion System in a Medium Voltage Microgrid," *IEEE Transactions on Smart Grid,* vol. 3, pp. 1903-1910, 2012.

[135] F. Katiraei, R. Iravani, N. Hatziargyriou, and A. Dimeas, "Microgrids management," *IEEE Power and Energy Magazine,* vol. 6, pp. 54-65, 2008.

[136] S. Luo, Z. Ye, R.-L. Lin, and F. C. Lee, "A classification and evaluation of paralleling methods for power supply modules," in *Power Electronics Specialists Conference (PESC)*, 1999, pp. 901-908.

[137] Z. Moussaoui, I. Batarseh, H. Lee, and C. Kennedy, "An overview of the control scheme for distributed power systems," in *Southcon/96*, Orlando, FL, USA, 1996, pp. 584-591.

[138] Z. Ye, D. Boroyevich, K. Xing, and F. C. Lee, "Design of parallel sources in DC distributed power systems by using gain-scheduling technique," in *Power Electronics Specialist Conference*, 1999, pp. 161-165.

[139] X. Zhou, P.-L. Wong, P. Xu, F. C. Lee, and A. Q. Huang, "Investigation of candidate VRM topologies for future microprocessors," *IEEE Transactions on Power Electronics,* vol. 15, pp. 1172-1182, Nov. 2000 2000.

[140] B. K. Johnson, R. H. Lasseter, F. L. Alvarado, and R. Adapa, "Expandable multiterminal DC systems based on voltage droop," *IEEE Transactions on Power Delivery,* vol. 8, pp. 1926-1932, Oct. 1993 1993.

[141] B. K. Bose, "An adaptive hysteresis-band current control technique of a voltage-fed PWM inverter for machine drive system," *IEEE Transactions on Industrial Electronics,* vol. 37, pp. 402-408, 1990.

[142] S. Xu, A. Q. Huang, W. Fei, and R. Burgos, "Wind Energy System With Integrated Functions of Active Power Transfer, Reactive Power Compensation, and Voltage Conversion," *IEEE Transactions on Industrial Electronics,* vol. 60, pp. 4512-4524, 2013.

[143] L. An, S. Zhikang, Z. Wenji, and Z. J. Shen, "Combined System for Harmonic Suppression and Reactive Power Compensation," *IEEE Transactions on Industrial Electronics,* vol. 56, pp. 418-428, 2009.

[144] R. S. Herrera and P. Salmeron, "Instantaneous Reactive Power Theory: A Reference in the Nonlinear Loads Compensation," *IEEE Transactions on Industrial Electronics,* vol. 56, pp. 2015-2022, 2009.

[145] J. Dixon, L. Moran, J. Rodriguez, and R. Domke, "Reactive Power Compensation Technologies: State-of-the-Art Review," *Proceedings of the IEEE,* vol. 93, pp. 2144-2164, 2005.

[146] S. Teleke, T. Abdulahovic, T. Thiringer, and J. Svensson, "Dynamic Performance Comparison of Synchronous Condenser and SVC," *IEEE Transactions on Power Delivery,* vol. 23, pp. 1606-1612, 2008.

[147] R. S. Kemerer and L. E. Berkebile, "Directly connected static VAr compensation in distribution system applications," *EEE Transactions on Industry Applications,* vol. 35, pp. 176-182, 1999.

[148] R. Majumder, "Reactive Power Compensation in Single-Phase Operation of Microgrid," *IEEE Transactions on Industrial Electronics,* vol. 60, pp. 1403-1416, 2013.

[149] L. Gyugyi, "Reactive Power Generation and Control by Thyristor Circuits," *IEEE Transactions on Industry Applications,* vol. IA-15, pp. 521-532, 1979.

[150] W. Bin, J. Pontt, J. Rodriguez, S. Bernet, and S. Kouro, "Current-Source Converter and Cycloconverter Topologies for Industrial Medium-Voltage Drives," *IEEE Transactions on Industrial Electronics,* vol. 55, pp. 2786-2797, 2008.

[151] J. W. Kolar, T. Friedli, J. Rodriguez, and P. W. Wheeler, "Review of Three-Phase PWM AC-AC Converter Topologies," *IEEE Transactions on Industrial Electronics,* vol. 58, pp. 4988-5006, 2011.

[152] J. Rodriguez, M. Rivera, J. W. Kolar, and P. W. Wheeler, "A Review of Control and Modulation Methods for Matrix Converters," *IEEE Transactions on Industrial Electronics,* vol. 59, pp. 58-70, 2012.

[153] P. W. Wheeler, J. Rodriguez, J. C. Clare, L. Empringham, and A. Weinstein, "Matrix converters: a technology review," *IEEE Transactions on Industrial Electronics,* vol. 49, pp. 276-288, 2002.

[154] H. Keyhani, M. Johnson, and H. A. Toliyat, "A soft-switched highly reliable grid-tied inverter for PV applications," in *IEEE Applied Power Electronics Conference and Exposition (APEC)*, 2014, pp. 1725-1732.

[155] S. Harb and R. S. Balog, "Reliability of Candidate Photovoltaic Module-Integrated-Inverter (PV-MII) Topologies-A Usage Model Approach," *IEEE Transactions on Power Electronics,* vol. 28, pp. 3019-3027, 2013.

[156] A. S. Farag, C. Wang, T. C. Cheng, G. Zheng, Y. Du, L. Hu*, et al.*, "Failure analysis of composite dielectric of power capacitors in distribution systems," *IEEE Transactions on Dielectrics and Electrical Insulation,* vol. 5, pp. 583-588, 1998.

[157] A. M. Imam, D. M. Divan, R. G. Harley, and T. G. Habetler, "Real-Time Condition Monitoring of the Electrolytic Capacitors for Power Electronics Applications," in *IEEE Applied Power Electronics Conference (APEC)*, 2007, pp. 1057-1061.

[158] P. Venet, H. Darnand, and G. Grellet, "Detection of faults of filter capacitors in a converter. Application to predictive maintenance," in *IEEE Telecommunications Energy Conference (INTELEC)*, 1993, pp. 229-234 vol.2.

[159] A. Braham, A. Lahyani, P. Venet, and N. Rejeb, "Recent Developments in Fault Detection and Power Loss Estimation of Electrolytic Capacitors," *IEEE Transactions on Power Electronics,* vol. 25, pp. 33-43, 2010.

[160] D. Balakrishnan and R. S. Balog, "Capacitor-less VAR compensator based on matrix converter," in *IEEE North American Power Symposium (NAPS)*, 2010, pp. 1-7.

[161] R. Vargas, J. Rodriguez, U. Ammann, and P. W. Wheeler, "Predictive Current Control of an Induction Machine Fed by a Matrix Converter With Reactive Power Control," *IEEE Transactions on Industrial Electronics,* vol. 55, pp. 4362-4371, 2008.

[162] M. Rivera, C. Rojas, Rodri, x, J. guez, P. Wheeler*, et al.*, "Predictive Current Control With Input Filter Resonance Mitigation for a Direct Matrix Converter," *IEEE Transactions on Power Electronics,* vol. 26, pp. 2794-2803, 2011.

[163] M. Rivera, A. Wilson, C. A. Rojas, J. Rodriguez, J. R. Espinoza, P. W. Wheeler*, et al.*, "A Comparative Assessment of Model Predictive Current Control and Space Vector Modulation in a Direct Matrix Converter," *IEEE Transactions on Industrial Electronics,* vol. 60, pp. 578-588, 2013.

[164] M. Rivera, J. L. Elizondo, M. E. Macias, O. M. Probst, O. M. Micheloud, J. Rodriguez*, et al.*, "Model predictive control of a Doubly Fed Induction Generator with an Indirect Matrix Converter," in *Annual Conference of the IEEE Industrial Electronics Society (IECON)*, 2010, pp. 2959-2965.

[165] M. Rivera, J. Rodriguez, J. R. Espinoza, and H. Abu-Rub, "Instantaneous Reactive Power Minimization and Current Control for an Indirect Matrix Converter Under a Distorted AC Supply," *IEEE Transactions on Industrial Informatics,* vol. 8, pp. 482-490, 2012.

[166] M. Rivera, J. Rodriguez, W. Bin, J. R. Espinoza, and C. A. Rojas, "Current Control for an Indirect Matrix Converter With Filter Resonance Mitigation," *IEEE Transactions on Industrial Electronics,* vol. 59, pp. 71-79, 2012.

[167] F. Villarroel, J. R. Espinoza, C. A. Rojas, J. Rodriguez, M. Rivera, and D. Sbarbaro, "Multiobjective Switching State Selector for Finite-States Model Predictive Control Based on Fuzzy Decision Making in a Matrix Converter," *IEEE Transactions on Industrial Electronics,* vol. 60, pp. 589-599, 2013.

[168] P. Cortes, S. Kouro, B. La Rocca, R. Vargas, J. Rodriguez, J. I. Leon*, et al.*, "Guidelines for weighting factors design in Model Predictive Control of power converters and drives," in *IEEE International Conference on Industrial Technology,*, 2009, pp. 1-7.

[169] M. Aleenejad, H. Iman-Eini, and S. Farhangi, "Modified space vector modulation for fault-tolerant operation of multilevel cascaded H-bridge inverters," *IET Power Electronics,* vol. 6, pp. 742-751, 2013.

[170] R. Bojoi, L. R. Limongi, D. Roiu, and A. Tenconi, "Enhanced power quality control strategy for single-phase inverters in distributed generation systems," *IEEE Transactions on Power Electronics,* vol. 26, pp. 798-806, 2011.

[171] S. Xu, J. Wang, and J. Xu, "A current decoupling parallel control strategy of single-phase inverter with voltage and current dual closed-loop feedback," *IEEE Transactions on Industrial Electronics,* vol. 60, pp. 1306-1313, 2013.

[172] M. Aleenejad, R. Ahmadi, and P. Moamaei, "Selective harmonic elimination for cascaded multicell multilevel power converters with higher number of H-Bridge modules," in *IEEE Power and Energy Conference at Illinois (PECI)*, 2014, pp. 1-5.

[173] Z. Qi, S. Xiang-Dong, Z. Yan-Ru, M. Matsui, and R. Bi-Ying, "Analysis and Design of a Digital Phase-Locked Loop for Single-Phase Grid-Connected Power Conversion Systems," *IEEE Transactions on Industrial Electronics,* vol. 58, pp. 3581-3592, 2011.

[174] B. Farhangi and S. Farhangi, "Application of Z-source converter in photovoltaic grid-connected transformer-less inverter," *Electrical Power Quality and Utilisation, Journal,* vol. 12, 2006.

[175] M. Aleenejad, R. Ahmadi, and P. Moamaei, "A modified selective harmonic elimination method for fault-tolerant operation of multilevel cascaded H-bridge inverters," in *Power and Energy Conference at Illinois (PECI)*, 2014, pp. 1-5.

[176] S. Harb, M. Kedia, Z. Haiyu, and R. S. Balog, "Microinverter and string inverter grid-connected photovoltaic system-A comprehensive study," in *IEEE Photovoltaic Specialists Conference (PVSC)*, 2013, pp. 2885-2890.

[177] J. Hu, J. Zhu, and D. G. Dorrell, "Model-predictive control of grid-connected inverters for PV systems with flexible power regulation and switching frequency reduction," in *IEEE Energy Conversion Congress and Exposition (ECCE)*, 2013, pp. 540-546.

[178] S. Kouro, P. Cortes, R. Vargas, U. Ammann, and J. Rodriguez, "Model Predictive Control-A Simple and Powerful Method to Control Power Converters," *IEEE Transactions on Industrial Electronics,* vol. 56, pp. 1826-1838, 2009.